



HAL
open science

Large Eddy Simulations of the interactions between flames and thermal phenomena: application to wall heat transfer and combustion control

Dario Maestro

► **To cite this version:**

Dario Maestro. Large Eddy Simulations of the interactions between flames and thermal phenomena: application to wall heat transfer and combustion control. Physics [physics]. Institut National Polytechnique de Toulouse - INPT, 2018. English. NNT : 2018INPT0074 . tel-04217427

HAL Id: tel-04217427

<https://theses.hal.science/tel-04217427>

Submitted on 25 Sep 2023

HAL is a multi-disciplinary open access archive for the deposit and dissemination of scientific research documents, whether they are published or not. The documents may come from teaching and research institutions in France or abroad, or from public or private research centers.

L'archive ouverte pluridisciplinaire **HAL**, est destinée au dépôt et à la diffusion de documents scientifiques de niveau recherche, publiés ou non, émanant des établissements d'enseignement et de recherche français ou étrangers, des laboratoires publics ou privés.



Université
de Toulouse

THÈSE

En vue de l'obtention du

DOCTORAT DE L'UNIVERSITÉ DE TOULOUSE

Délivré par :

Institut National Polytechnique de Toulouse (Toulouse INP)

Discipline ou spécialité :

Energétique et Transferts

Présentée et soutenue par :

M. DARIO MAESTRO

le jeudi 27 septembre 2018

Titre :

Large Eddy Simulations of the interactions between flames and thermal phenomena: application to wall heat transfer and combustion control

Ecole doctorale :

Mécanique, Energétique, Génie civil, Procédés (MEGeP)

Unité de recherche :

Centre Européen de Recherche et Formation Avancées en Calcul Scientifique (CERFACS)

Directeur(s) de Thèse :

M. THIERRY POINSOT

M. GABRIEL STAFFELBACH

Rapporteurs :

M. BENOIT FIORINA, CENTRALESUPELEC GIF SUR YVETTE

M. PASCAL BRUEL, CNRS

Membre(s) du jury :

Mme DEANNA LACOSTE, KING ABDULLAH UNIVERSITY OF SC&TECH, Président

Mme BENEDICTE CUENOT, CERFACS, Membre

M. OSKAR Haidn, TECHNISCHE UNIVERSITAT MUNICH, Membre

M. THIERRY POINSOT, CNRS TOULOUSE, Membre

Abstract

Interactions between flames and thermal phenomena are the guiding thread of this work. Flames produce heat indeed, but can also be affected by it. Large Eddy Simulations (LES) are used here to investigate these interactions, with a focus on two main topics: wall heat transfer and combustion control. In a first part, wall heat transfer in a rocket engine sub-scale CH_4/O_2 burner is studied. In the context of launchers re-usability and cost reduction, which are major challenges, new propellant combinations are considered and wall heat fluxes have to be precisely predicted. The aim of this work is to evaluate LES needs and performances to simulate this kind of configuration and provide a computational methodology permitting to simulate various configurations. Numerical results are compared to experimental data provided by the Technische Universität München (Germany). In a second part, combustion control by means of Nanosecond Repetitively Pulsed (NRP) plasma discharges is studied. Modern gas turbine systems use indeed lean combustion with the aim of reducing fuel consumption and pollutant emissions. Lean flames are however known to be prone to instabilities and combustion control can play a major role in this domain. A phenomenological model which considers the plasma discharges as a heat source is developed and applied to a swirl-stabilized CH_4/Air premixed lean burner. LES are performed in order to evaluate the effects of the NRP discharges on the flame. Numerical results are compared with experimental observations made at the King Abdulla University of Science and Technology (Saudi Arabia).

Keywords: Large Eddy Simulations, Interactions between flames and thermal phenomena, Methane combustion, Wall heat transfer, Combustion control, Nanosecond Repetitively Pulsed plasma discharges

Résumé

Les interactions entre les flammes et les phénomènes thermiques sont le fil conducteur de ce travail. En effet, les flammes produisent de la chaleur, mais peuvent aussi être affectées par des transferts ou des sources de chaleur. La Simulation aux Grandes Échelles (SGE) est utilisée ici pour étudier ces interactions, en mettant l'accent sur deux sujets principaux: le transfert de chaleur aux parois et le contrôle de la combustion. Dans un premier temps, on étudie le transfert de chaleur aux parois dans un modèle de brûleur CH_4/O_2 de moteur-fusée. Dans un contexte de réutilisabilité et de réduction des coûts des lanceurs, qui constituent des enjeux majeurs, de nouveaux couples de propergols sont envisagés et les flux thermiques à la paroi doivent être précisément prédits. Le but de ce travail est d'évaluer les besoins et les performances des SGE pour simuler ce type de configuration et de proposer une méthodologie de calcul permettant de simuler différentes configurations. Les résultats numériques sont comparés aux données expérimentales fournies par la Technische Universität München (Allemagne). Dans un deuxième temps, le contrôle de la combustion au moyen de décharges de plasma de type NRP (en anglais Nanosecond Repetitively Pulsed) est étudié. Les systèmes de turbines à gaz modernes utilisent en effet une combustion pauvre dans le but de réduire la consommation de carburant et les émissions de polluants. Les flammes pauvres sont connues pour être sujettes à des instabilités et le contrôle de la combustion peut jouer un rôle majeur dans ce domaine. Un modèle phénoménologique qui considère les décharges de plasma comme une source de chaleur est développé et appliqué à un brûleur pauvre avec prémélange CH_4/Air stabilisé par un swirler. Les SGE sont réalisées afin d'évaluer les effets des décharges NRP sur la flamme. Les résultats numériques sont comparés aux observations expérimentales faites à la King Abdulla University of Science and Technology (Arabie Saoudite).

Mots-clés: Simulation aux Grandes Échelles, Interactions entre les flammes et les phénomènes thermiques, Combustion du méthane, Transfert de chaleur aux parois, Contrôle de combustion, Décharges de plasma de type NRP

Acknowledgments

First of all, I would like to thank Pascal Bruel and Benoît Fiorina for accepting to review my work as well as Deanna Lacoste and Oskar Haidn, for the positive comments and the pleasant discussion during my defense. A special thanks to Prof. Haidn and all the members of the Institute for Flight Propulsion of the Technische Universität München for their hospitality during the Summer Program and the long discussions since then. A special thanks also to Prof. Lacoste for providing the PACCI experimental configuration and associated discussions for the NRP model calibration.

Un grand merci à mes encadrants de thèse, Thierry et Bénédicte. Merci Thierry pour cette belle opportunité, pour ton suivi constant et pour les directions intéressantes (et souvent inattendues) que tu as su donner à mon parcours. J'ai pu apprendre beaucoup de choses et grandir énormément. Et merci Bénédicte, ça a été un vrai plaisir de travailler ensemble !! Un plaisir tout d'abord professionnel, car tu m'as appris beaucoup de choses et tu as su me remettre sur la bonne route à chaque hésitation ou difficulté que j'ai dû surmonter. A chaque point de thèse je sortais rechargé de positivité et d'envie de continuer mon travail, même si jusqu'à 30 minutes avant j'étais au fond du seau. Et un plaisir aussi personnel, car c'était toujours dans la bonne humeur et c'est beaucoup plus facile de travailler dans cet esprit. Un gros merci également à tous les seniors, vous êtes d'une aide précieuse pour l'équipe et votre disponibilité est vraiment remarquable ! Un merci particulier à Gab, tout d'abord pour m'avoir prêté ton nom à mettre sur tous les papiers MEGeP :) mais surtout pour ton aide énorme dans la gestion d'AVBP. Sans toi les thèses au CERFACS ne seraient surement pas les mêmes ! Merci beaucoup à toute l'équipe CSG pour votre aide au quotidien, votre réactivité et gentillesse. Et merci beaucoup à Michèle, Marie, Chantal et Nicole pour votre support administratif mais surtout pour votre bonne humeur qui anime le CERFACS au jour le jour.

Ce fut 4 années et demie très plaisantes au CERFACS et ceci surtout grâce aux gens qui y travaillent. L'ambiance est vraiment cool et beaucoup de collègues sont devenus aussi des amis, avec qui partager beaucoup plus qu'une journée de travail mais aussi diners, soirées, vacances et beaux moments de vie. Donc un grand merci à tous les thésards, stagiaires (aka QuentinMalés) et post-docs que j'ai pu rencontrer durant ces années. Merci en particulier aux thésards de ma période. Merci à César pour ton accueil et ton aide pendant mes premiers temps au CERFACS, tu m'as tout appris,

ACKNOWLEDGMENTS

du terminal que je n'avais jamais ouvert à l'utilisation de toutes les moyennes informatiques, et sans toi ça aurait été beaucoup plus dur. Merci aux autres 2/3 du trio magique, Majoud et Mélissa, pour nos soirées cartes, tisanes et quatre quarts, pour nos vacances inoubliables, les mangues carottés, les soirées reggae music, les sorties escalade, et tout simplement pour tout le reste. Rappelez vous, vous êtes vraiment une belle bande d'e*****s !! Merci Romain pour ta constante bonne humeur (enfin bon c'était pas drôle en vrai), Laura et l'inoubliable tram, Pierre et ton Pierre, feuille ciseaux géant, Grosnick et nos discussions moto et VR46, Omar (merci poulet!!), Félix et l'encore plus inoubliable tas de pailles, Valou et tes enseignement de foot (je sais c'est une cause perdue), Luis pour nos discussions en espagnol et nos voyages improbables dans toute l'Europe, le duo AVSP Aïcha et Franchine pour vos brunchs et interminables bons plans resto, Luc pour être tout simplement toi même, tu nous as fait beaucoup rêver, JarJar pour être toujours la #ilestlaJarJar, Lulu pour ta matraque attitude, Astoul pour nos sorties escalade, Maxou pour tes gâteaux, ils me manquent déjà !! Merci et bon courage aux prochains sur la liste, Bizz aka le président dictateur et à tous les jeunes qui ont encore un bout de chemin à faire. Et merci aux "vieux", et particulièrement à mon premier co-bureau Abdulla pour ton aide précieuse.

Merci aux post-docs, avec une mention spéciale pour ma co-bureau Laure, ça a été un vrai plaisir de partager cette année avec toi !! Merci au parisien Nico la Frite pour la bonne humeur et l'ambiance que t'as su ramener et pour nos vacances #rotooooooom. Sans oublier Pierre, Lola, Quentin, Lucas et tous les autres.

Merci beaucoup à Miss banane aka "la même un petit peu plus" pour ton soutien constant, pour notre symbiose et nos fou-rires, ça n'aurait pas été la même chose sans toi !!

Merci à l'EAC, premier club de mon histoire. Jamais je n'aurais pensé jouer au foot un jour mais le CERFACS a réussi ça aussi.

E infine un enorme GRAZIE alla mia famiglia per il vostro sostegno costante e incondizionato. Grazie per avermi insegnato la passione, ma soprattutto per avermi insegnato a inseguirla sempre e comunque. Senza di voi di sicuro non sarei arrivato fino a qui! Grazie a Diego per esserci sempre, grazie mamma, grazie papà.

Pour conclure je voudrais partager le plus grand enseignement de ces 4 ans en France: "On peut survivre sans bidet. Ce ne sera jamais la même chose et on s'habituera jamais. Mais on peut survivre !"

A mio papà

Contents

1	Introduction: flames and heat	1
1.1	Actual context and needs	1
1.2	Thermal aspects of flames	4
1.2.1	Heat transferred to the flame	5
1.2.2	Heat coming from the flame	8
1.2.3	Flame-wall interaction	13
1.3	Thesis objectives and outline	14
I	Theoretical background and modeling of turbulent reactive flows via Large Eddy Simulation	17
2	Governing equations of turbulent reactive flows	19
2.1	Thermodynamics of a multispecies mixture	19
2.2	Navier-Stokes equations	20
2.3	Transport properties	21
2.4	Chemical kinetics	23
3	Theoretical concepts of turbulence and combustion	25
3.1	Basics of turbulence	25
3.2	Premixed combustion	28
3.2.1	Laminar premixed flames	28
3.2.2	Turbulent premixed flames	31
3.3	Non-premixed combustion	33
3.3.1	Laminar diffusion flames	33
3.3.2	Turbulent diffusion flames	37
4	Modeling of turbulent reactive flows via Large Eddy Simulation	39
4.1	Numerical simulation approaches: DNS, LES, RANS	40
4.2	Large Eddy Simulation	41
4.2.1	Filtered viscous fluxes	42
4.2.2	Subgrid fluxes closure	43
4.3	Turbulent viscosity models	44
4.4	Combustion modeling	46

ACKNOWLEDGMENTS

4.4.1	Thickened Flame model	46
4.5	Chemistry description	48
4.5.1	Methane chemistry	49
4.6	The LES code AVBP	50
4.6.1	Numerical methods	50
4.6.2	Artificial viscosity	51
4.6.3	Boundary conditions	51
II Wall heat flux prediction in rocket combustors		53
5 LES of a single element GO_x/GCH_4 combustor		55
5.1	Combustion and heat transfer in rocket engines	56
5.2	Wall modeling	57
5.2.1	Standard wall law	58
5.2.2	Coupled wall law	59
5.3	Combustion modeling	60
5.4	Paper <i>Int. J. Heat Mass Transfer</i>	61
5.5	Additional material	80
5.5.1	Effect of the mesh	80
5.5.2	Possible causes for the heat flux underestimation	82
5.6	Few words about CPU time	86
III Plasma assisted combustion in gas turbines		87
6 Bibliographical review on plasma assisted combustion		89
6.1	Combustion instabilities	89
6.1.1	Driving and damping of instabilities	93
6.2	Combustion instabilities control	95
6.2.1	Passive methods	95
6.2.2	Active methods	96
6.3	Plasma assisted combustion	97
6.3.1	Effects of an NRP discharge on the mixture	99
6.3.2	Enhancing combustion by means of NRP discharges	100
6.4	Modeling of NRP discharges	106
7 LES of a premixed swirl-stabilized burner		111
7.1	The PACCI experimental configuration	112
7.1.1	Available experimental data	114
7.1.2	Numerical setup	114
7.2	Non-reacting flow in the PACCI burner	118
7.2.1	Flow characteristics and flow pattern	118
7.2.2	Mean flow velocity profile	120
7.2.3	Flow instability	125
7.3	Reacting flow in the PACCI burner	126
7.3.1	Validation of the kinetic schemes	127

7.3.2	LES using the BFER 2-steps global chemistry	131
7.3.3	Impact of the kinetic scheme: LES using the LU13 ARC chemistry	140
7.4	Acoustically pulsating the PACCI burner	150
7.4.1	Forced response method for the dynamic analysis of flames . . .	150
7.4.2	Dynamic response of the PACCI burner	151
7.5	Conclusion	161
8	Phenomenological model for NRP discharges	163
8.1	Building up a phenomenological model	163
8.2	Test case setup	166
8.2.1	Model calibration using the BFER kinetic scheme	170
8.3	Increasing the complexity of the kinetic scheme: from BFER to LU13 .	176
8.3.1	Influence of the deposit size	179
8.3.2	Influence of the number of consecutive discharges	183
8.4	Influence of the plasma chemistry	185
8.4.1	The PLASMA-LU kinetic scheme	187
8.5	Few words about CPU time	194
8.6	Conclusion	195
9	LES of plasma assisted combustion for a premixed swirl-stabilized burner	197
9.1	LES of the PACCI burner with NRP discharges	197
9.1.1	LES using the BFER 2-steps global chemistry	197
9.1.2	Impact of the kinetic scheme: LES using the LU13 ARC chemistry	211
9.1.3	Few words about CPU cost	221
9.1.4	Concluding remarks	222
9.2	Acoustically pulsating the PACCI burner with NRP discharges	222
9.2.1	Dynamic response of the PACCI burner	222
9.3	Conclusion	232
	Conclusions and perspectives	233
	Publications and Communications	237
	Bibliography	239

Nomenclature

Roman characters

Symbol	Description
a	Strain rate
a_{sgs}	Sub-grid-scale strain rate
\mathcal{A}_j	Pre-exponential factor of reaction j
C_p	Heat capacity at constant pressure
C_s	Smagorinsky model constant
C_σ	Sigma model constant
C_{vd}	Van Driest constant
D_{inj}^E	PACCI burner injection tube diameter
D_k	Diffusion coefficient of species k
D_t	Turbulent diffusion coefficient
D_{th}	Thermal diffusion coefficient
D_{TCI}	TCI model diffusion coefficient
E	Total energy
E_{aj}	Activation energy of reaction j
E_p	Plasma energy
\mathcal{E}	Efficiency function
f	Frequency
f_p	Plasma frequency
\mathcal{F}	Thickening factor
h_s	Sensible enthalpy
HRR	Heat Release Rate
$J_{i,k}$	i -th component of the diffusive flux of species k
k	k -th species

NOMENCLATURE

Symbol	Description
K_{fj}	Forward reaction rate of reaction j
K_{rj}	Reverse reaction rate of reaction j
$K_{eq,j}$	Equilibrium constant
l	Characteristic dimension
l_t	Integral length
\dot{m}	Mass flow rate
N	Flame Transfer Function gain
P	Pressure
P_p	Plasma power
q_i	i -th component of the energy flux
q_w	Wall heat flux
Q_{sp}	External energy source
\mathcal{R}	Ideal gas constant
t	Time
S_c	Flame consumption speed
S_{ij}	Deformation tensor
S_L^0	Premixed laminar flame speed
\mathcal{S}	Flame sensor for premixed flame TFLES
T	Temperature
T_τ	Friction temperature
u_j	j -th component of velocity
u_τ	Friction velocity
V_i^c	Correction velocity
V_ψ	Volume of 3-D NRP plasma discharges distribution
W_k	Molar mass of species k
X_k	Molar fraction of species k
y_τ	Friction distance
Y_k	Mass fraction of species k
z	Mixture fraction
(x, y, z)	Spatial coordinates

Greek characters

Symbol	Description
χ	Scalar dissipation rate
δ_{ij}	Kronecher symbol
δ_L^0	Premixed laminar flame thermal thickness
δ_L^d	Diffusion flame thickness
Δ	Characteristic length scale of a grid cell
Δt_p	Plasma time duration
ϵ	Turbulence dissipation rate
η_K	Kolmogorov length scale
κ	Von Karman constant
κ_f	Relaxation coefficient
λ	Thermal conductivity
λ_t	Turbulent thermal conductivity
μ	Molecular (dynamic) viscosity
ν	Kinematic viscosity
$\nu_t (\mu_t)$	Turbulent viscosity
ϕ	Equivalence ratio
φ	2-D NRP discharges energy distribution
ψ	3-D NRP discharges energy distribution
Ψ	Integrated value of 3-D NRP discharges energy distribution
σ	Standard deviation
τ	Flame Transfer Function time delay
τ_c	Chemical time scale
τ_{conv}	Convective time scale
τ_{ij}	Viscous tensor
τ_w	Wall shear stress
θ	Flame sensor for diffusion flame TFLES
ϑ	NRP discharges angle
ρ	Density
ω	Angular frequency
$\dot{\omega}_k$	species k source term
$\dot{\omega}_T$	energy source term
Ξ	Flame wrinkling (Charlette efficiency function)

NOMENCLATURE

Dimensionless numbers

Symbol	Description
Da	Damköhler number
Ka	Karlovitz number
Le	Lewis number
Pr	Prandtl number
Pr_t	Turbulent Prandtl number
Re	Reynolds number
Re_t	Turbulent Reynolds number
Sc	Schmidt number
Sc_t	Turbulent Schmidt number

Indices and superscripts

Symbol	Description
+	Superscript of quantities written in wall units
K	Index of a quantity at Kolmogorov scale
g	Index of a Gaseous quantity
p	Index of a Plasma quantity
sgs	Index of a Sub-grid-scale quantity
st	Index of a quantity at Stoichiometric equivalence ratio
w	Index of a quantity located at Wall

Acronyms

Symbol	Description
ARC	Analytically Reduced Chemistry
AV	Artificial Viscosity
CFD	Computational Fluid Dynamics
CFL	Courant-Friedrichs-Lewy
CSP	Computational Single Perturbation
DNS	Direct Numerical Simulation
DRG	Directed Relation Graph method
FTF	Flame Transfer Function
FWHM	Full Width at Half Maximum
FWI	Flame-Wall Interaction
HFRM	Harmonic Flame Response Model
HPC	High Performance Computing
KAUST	King Abdulla University of Science and Technology
LES	Large Eddy Simulation
LPP	Lean Pre-mixed Pre-vaporized
LW	Lax-Wendroff numerical scheme
NRP	Nanosecond Repetitively Pulsed (plasma discharges)
NSCBC	Navier-Stokes Characteristic Boundary Conditions
PEA	Pre-Exponential Adjustment
PIV	Particle Image Velocimetry
PDF	Probability Distribution Function
PSD	Power Spectral Density
PVC	Precessing Vortex Core
QSS	Quasi-Steady State
RANS	Reynolds Averaged Navier-Stokes
RMS	Root-Mean-Square
TCI	Turbulence Combustion Interaction
TFLES	Thickened Flame model for LES
TTGC	Two-step Taylor-Galerkin scheme version C
TUM	Technische Universität München
UHC	Unburnt HydroCarbons
WL	Wall Law

Chapter 1

Introduction: flames and heat

Contents

1.1	Actual context and needs	1
1.2	Thermal aspects of flames	4
1.2.1	Heat transferred to the flame	5
1.2.2	Heat coming from the flame	8
1.2.3	Flame-wall interaction	13
1.3	Thesis objectives and outline	14

1.1 Actual context and needs

Combustion is nowadays, and will be in the next future, the primary source of energy for ground power systems as well as for aeronautical and aerospace applications. The market of gas turbines for electricity generation is indeed in continuous growth thanks to their high efficiency (which can reach 60 % in combined cycle power plants), as well as to their high flexibility. Gas turbines can be switched on and off relatively easily in order to adapt to the network demand and they can play a major role in a market which tends toward a high integration of renewable-high unsteady supply sources.

At the same time some sectors, like aerial transportation and space systems, are far from becoming independent from fossil fuels. The energy density required to fly that can provide kerosene or methane is still not reachable with alternative solutions like batteries or electric engines, which are more and more used in the ground transportation systems.

However the scarcity of fossil fuel, as well as environmental issues and global warming, are pushing the engine manufacturers to go towards systems which reduce the specific fuel consumption and the pollutant emissions. In parallel, due to the high competitive market, cost has become a key parameter for the design of the energy generation and propulsion systems.

Focusing on gas turbines (either for electricity generation or for aero-engines), the systems operating today are different by far from the first demonstrating jet

1. INTRODUCTION: FLAMES AND HEAT

powering ones. The combustion chambers have moved towards LPP (lean-premixed-prevaporized) systems in order to minimize pollutant emissions [Lefebvre, 2010]. The exhaust gases of a gas turbine are composed of CO_2 , H_2O , CO , NO_x , unburned hydrocarbons (UHC), particulate matter and excess O_2 and N_2 . CO_2 and H_2O are final combustion products and can be reduced only by means of a reduction of fuel consumption. On the contrary, the concentration of other pollutants depends on the combustion process and flame characteristics as illustrated in Fig. 1.1, where the dependency of CO and NO_x concentration with flame temperature is shown. Temperature is by far the

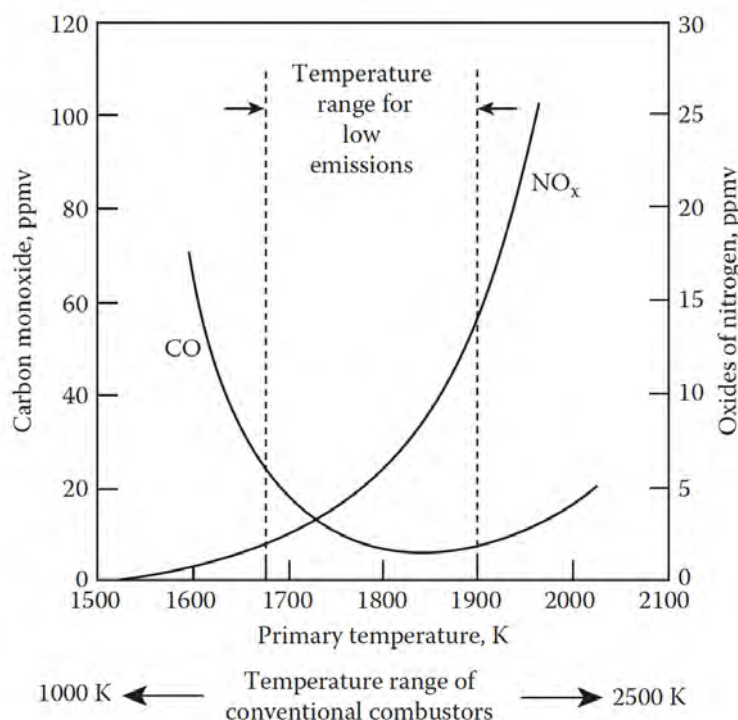


Figure 1.1: Influence of temperature of combustion zone on pollutant formation [Lefebvre, 2010]

most important factor in pollutant emissions and an optimal range of flame temperature exists. A huge effort has been made to keep combustion in this zone and eliminate all possible hot or cold spots which will increase the pollutant emissions. The LPP concept represents the ultimate solution in this regard. Its working principle is to supply to the flame a completely homogeneous lean mixture of fuel and air to burn it at an equivalence ratio as close as possible to the blowout limit. Temperature inhomogeneities are therefore ideally eliminated and combustion proceeds at a uniform, very low temperature with a minimum production of NO_x . The flame is stabilized by one or various recirculation zones in which combustion is completed. The resulting products flow then through a dilution zone. By designing the combustion chamber in order to have high residence times, the oxidation of CO and UHC is completed and their emission is minimized (especially in ground systems where dimensions are less problematic). This is also made possible by the fact that, for flames with a maximum temperature

lower than 1900 K, NO_x formation is independent of residence time. Another huge advantage of LPP systems is that with a uniform, pre-vaporized mixture the soot formation is very low, leading to a decrease of particles emission and to less radiative heat transfer at liner walls. This permits a reduction in cooling air and a further increase in engine efficiency.

Lean combustion has been found as the key for lower fuel consumption and lower pollutant emissions but brought with it some severe drawbacks of dynamical nature [Lieuwen, 2003]. Lean combustors work close to the lean flammability limit of the fuel and so close to the stability line. This makes the flame strongly subject to all the phenomena which happen around it and at this regime small perturbations can lead to strong responses. In particular, being on the stability line means that the flame can blow-off or be subject to combustion-driven oscillations. This is facilitated also by the fact that, as high velocity of the cold flow are needed in order to avoid flashback the flame is generally situated at a pressure maximum: in this position a variation of the heat release rate is more prone to add energy to the acoustic field. Moreover, as mentioned before, the combustors are in general long to facilitate CO burnout. This makes the flame very short relative to an acoustic wavelength, resulting in a concentrated heat release. Mechanisms leading to combustion instabilities will be presented in detail in chapter 6. The effects of this thermoacoustic oscillations can be tragic for the combustion chamber, leading to mechanical and thermal stress of walls up to the failure of the system. Research in this field is so very active in order to fully understand its phenomenology, with the aim of avoid their appearance or manage to control them. In particular, control attracts an increasing attention. Research in this field is active since the 90's [Lang et al., 1987; Poinso et al., 1989, 1992; Candel, 1992; McManus et al., 1993], has never been out-of-date in the 21th century [Candel, 2002; Docquier and Candel, 2002] and is still a very present topic [Poinso, 2017]. Among other techniques, plasma discharges have been found very promising in controlling combustion, thanks to its thermal and chemical effects on the fresh gases (see for example Starikovskiy and Aleksandrov [2013]; Ju and Sun [2015]). Combustion control techniques as well as a complete review of plasma assisted combustion in gas turbines will be presented in chapter 6.

If we focus now on space propulsion, until now, cost has never been a big issue. The primary goal has always been to manage to keep the desired load into orbit and the rocket used to do so has always been designed to burn up in reentry. With the shift of this last years from governmental agencies to private companies, cost has become one of the design parameters of future space propulsion systems. The declared objective is to fly reusable combustion chambers and reduce costs at least by a factor of 10 [Iannetti et al., 2017], as shown in Fig. 1.2 regarding the new gas generator Prometheus for the future European launcher Ariane 6. This will be achieved by means of several technological breakthrough [Iannetti et al., 2017]. The components production will be in part performed using additive manufacturing (3D impression). Digital control and engine diagnostics will be fully implemented to fly at variable thrust regimes. A shift from classical liquid hydrogen-liquid oxygen propellant towards hydrocarbons is also underway: the Prometheus engine will be powered with liquid oxygen and methane and the Merlin engines which equip the Falcon 9 launcher of SpaceX are powered with

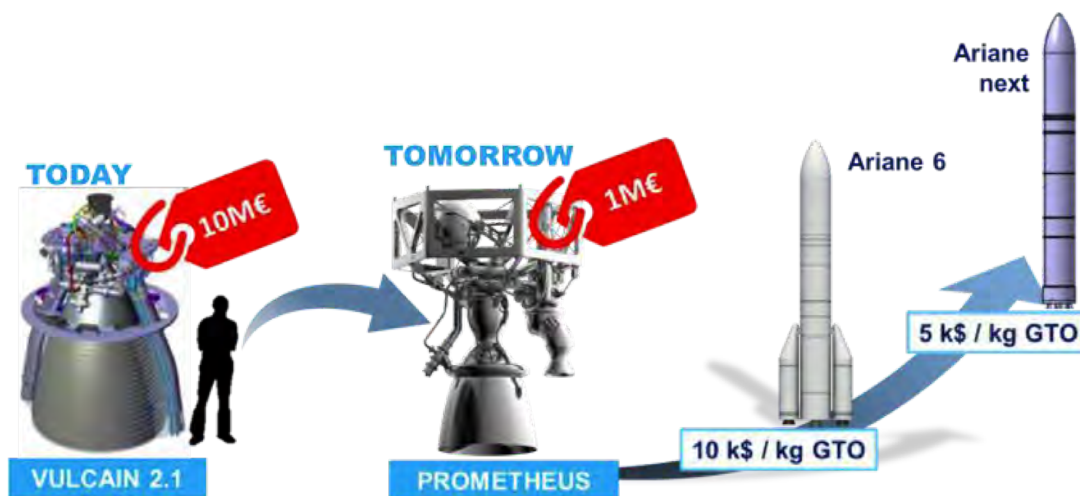


Figure 1.2: Prometheus cost objectives [Iannetti et al., 2017]

liquid oxygen and rocket-grade kerosene (RP-1).

Moreover, a new keyword has appeared in the rocket engines world: reusability.

If one can figure out how to effectively reuse rockets just like airplanes, the cost of access to space will be reduced by as much as a factor of a hundred. A fully reusable vehicle has never been done before. That really is the fundamental breakthrough needed to revolutionize access to space.

— Elon Musk

The main launch cost is to build the rocket, which only flies once. If we consider that the building cost of a commercial airplane is similar to the one of a Falcon 9 launcher¹ and that an airplane can fly several times per day and tens of thousands of times during its life cycle, the point is quite clear. Reusability means of course that a system to recover the launcher has to be conceived, but most of all it means that it is mandatory to build an engine which can sustain multiple launches, which is not the case nowadays. This needs an increasing attention in combustion process and a deep knowledge and control of thermal stresses on walls, which cannot be subject anymore to extreme loads leading to plastic deformations.

The current energy and propulsion scenario brings the interactions between flame and heat under the spotlights, whether from the point of view of using the sensitivity of flames to heat in order to control them or from the point of view of studying the effect of heat generated by the flames on the engine structure.

1.2 Thermal aspects of flames

In a combustion chamber, flame and heat interact in several ways. This section is dedicated to investigate the principal mechanisms through which flames affect and are

¹www.spacex.com

affected by the thermal state of the combustion chamber. A schematic summary is given in Fig. 1.3. White arrows identify the mechanisms in which heat is added to the flame and black ones the mechanisms in which heat is subtracted from the flame; the gray arrow identifies the mechanism in which there is a simultaneous subtraction and addition of heat from (to) the flame.

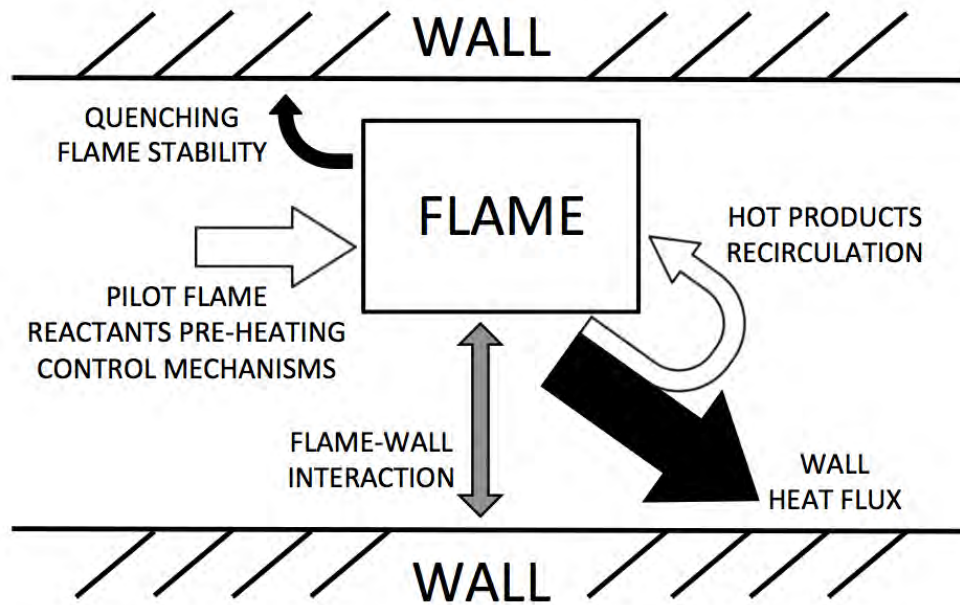


Figure 1.3: Interactions between flame and heat

1.2.1 Heat transferred to the flame

Starting with the mechanisms in which heat is added to the flame, we will immediately see how they are responsible for flame stabilization. In a gas turbine combustor, and specially in aircraft engines, the flame must be sustained over a wide range of operating conditions. Combustion must be initiated and must operate in an air-stream which is highly turbulent and is flowing in general at a speed much higher than the nominal burning velocity of the fuel employed. The usual way to remedy this problem is to create a zone at the upstream end of the combustion zone in which hot products recirculate and mix with the fresh incoming gases. This provides favorable conditions for ignition and flame stabilization.

The most simple way to do so is to use bluff body flame-holders (Fig. 1.4). They are commonly used to stabilize flowing combustible mixtures (see for example [Sanquer et al. \[1998\]](#)) and their main application is for scramjets and turbojets afterburners. Different theories are available for the mechanisms through which the recirculation zone acts as a flame stabilizer [[Lefebvre, 2010](#)]. According to [Longwell et al. \[1953\]](#), the recirculation zone works as an homogeneous chemical reactor. As long as the time to heat up the fresh gases is lower than the time needed for chemical reaction, combustion occurs. On the contrary, [Zukoski and Marble \[1955\]](#) assume that fresh gases ignition occurs in the shear layer, where hot combustion products from the recirculation zone

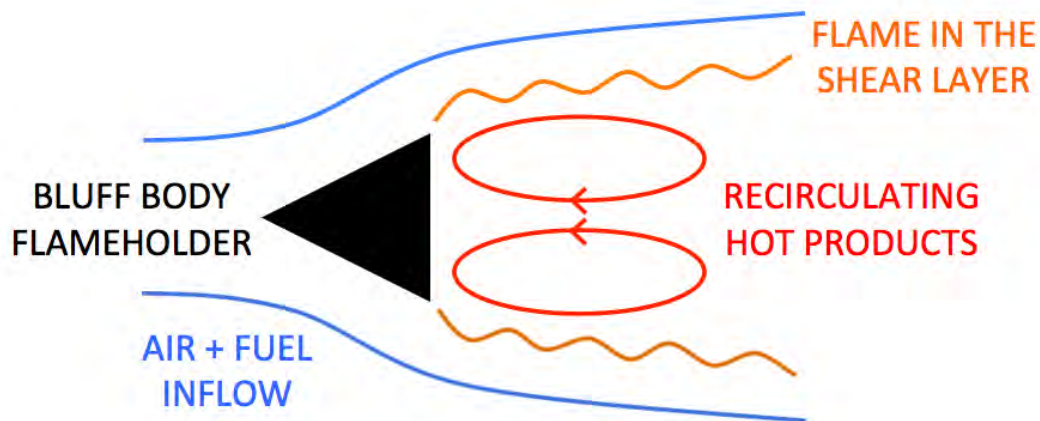


Figure 1.4: Bluff body flame-holder schematic view

are mixed with fresh gases. The burning mixture then flows down in the shear layer zone, igniting neighboring mixture kernels. At the end of the recirculation zone, some of the burning mixture continues to flow downstream, whereas some other is trapped in the recirculation zone. It is clear how in both cases the heat transfer from the hot gases to the flame plays a crucial role.

Due to the difficulty in controlling the amount of hot products trapped in the wake of a bluff body flame-holder, which varies with incoming temperature and velocity [Lefebvre et al., 1966], gas turbine combustors are generally stabilized by means of swirling flows (Fig. 1.5). Swirlers impose a rotating component to the incoming flow.

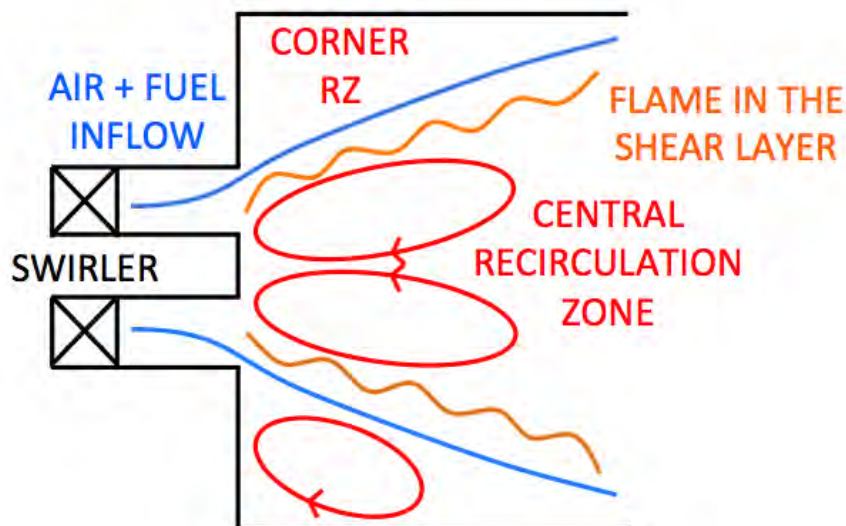


Figure 1.5: Swirler as a flame-holder schematic view

This results in the creation of a central recirculation zone in the combustion chamber which is filled with hot products. By this means, a source of continuous ignition is

established and combustion can be easily controlled over a large range of operating points. Corner recirculation zones also generally appear, filled with burnt gases or with a mixture of fresh and burnt gases. Depending on the temperature of the corner recirculation zone, different flame shapes can appear (V-shaped or M-shaped flames, see for example [Guiberti et al. \[2015\]](#)). This introduces another sensibility of the flames to heat, which will be detailed in the following.

Hot products recirculation is the key stabilization mechanism in gas turbine combustors, but additional stabilization mechanisms can be necessary when operating the system close to the flammability limit, at which instabilities can appear. Among other techniques, some of them employ the supply of heat to the fresh gases.

A first example is the use of the so called "staged" combustion. The principle of staged combustion is illustrated in Fig. 1.6, from [Lefebvre \[2010\]](#). It features a pilot

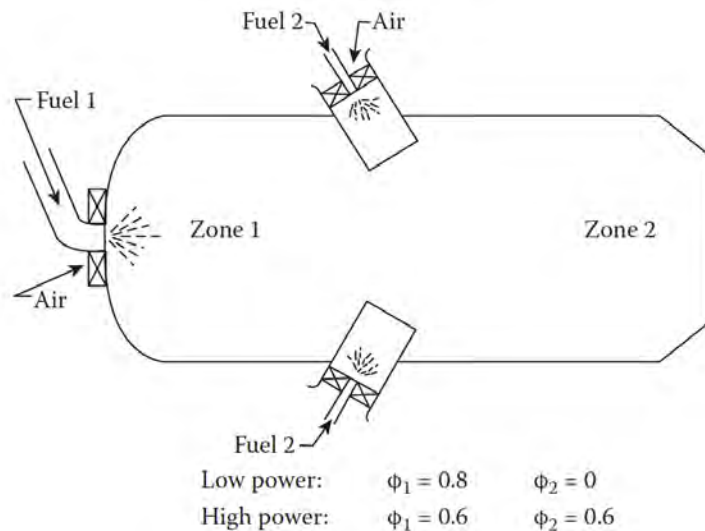


Figure 1.6: Principle of axial staging [[Lefebvre, 2010](#)]

zone (Zone 1 in Fig. 1.6) which is operated at a fairly high equivalence ratio (around 0.8) to ensure flame stability. This stage provides the temperature rise necessary at low power. At high power the fuel is supplied to the main stage (Zone 2 in Fig. 1.6) which is operated lean (at an equivalence ratio of about 0.6) to reduce pollutant emissions. Combustion in the main zone is initiated and sustained by the hot gases emanating from the pilot zone.

A second possible stabilization mechanism is reactant pre-heating, whose effects have been studied in a wide range of configurations. Some examples are given here. The dependency of the laminar flame speed with the reactants temperature for a H_2/CO mixture (syngas for gas turbines) has been studied by [Natarajan et al. \[2007\]](#). They found how the measured flame speeds increase rapidly with the unburned gases temperature for all the equivalence ratios studied. Model predictions are in accordance with this dependency. The role of reactants preheating on syngas production has been investigated by [Smith et al. \[2013\]](#), who found how the operating limits for a flat flame

1. INTRODUCTION: FLAMES AND HEAT

burner increase substantially with increased reactant temperature. That allows the stable operation of the burner at richer equivalence ratios (where syngas yields are greater) than those achievable with unheated reactants. Effects of preheating on stabilization and stability limits of a non-premixed methane jet flame have been studied in the work of [Lamige et al. \[2013\]](#). They have shown that flame stability is substantially increased with preheating, since an attached flame is able to sustain much higher jet velocities with higher initial reactant temperatures. They also investigated the combined effect of reactants preheating and dilution with burnt gases, showing how dilution limits are directly modified with preheating thanks to the flame speed increase. [Erickson and Soteriou \[2011\]](#) have studied the impact of reactant temperature increase on the dynamics of bluff body stabilized premixed flames using numerical simulations. They found how the wake behavior changes completely depending on the reactants temperature switching from a relatively symmetrical one to an asymmetric one characterized by a coherent vortices shed at a particular frequency. The flame stability also changes, denoting a non-monotonic behavior: as the reactant temperature increases the flame response first increases slightly, then decreases to finally increase again. Finally, we cite combustion control by means of plasma discharges. One of the effects of plasma discharges is of thermal nature: the energy deposit acts as a heat source on the fresh gases. This will not be detailed here and a complete review of plasma assisted combustion in gas turbines will be presented in chapter 6.

1.2.2 Heat coming from the flame

We now switch to all those phenomena through which heat is subtracted from flames or, more generally, through which the heat generated by flames is transported away from them. The first, obvious, mechanism to consider is heat transfer to solid components of the engine.

In gas turbines, the thermal efficiency and power output of the engine increase with increasing turbine rotor inlet temperatures. Following [Terzis \[2014\]](#), an increase of 50 K in turbine firing temperature can provide a corresponding increase of 8-9 % in power output and 2-4 % improvement in cycle efficiency. Temperatures that engine constructors have reached nowadays are far higher than the maximum temperatures that the materials of combustion chamber walls and turbine blades can sustain, as can be seen in Fig 1.7. In order to prevent the chamber walls and turbine blades to melt, thermal coatings and cooling systems have to be used. In combustion chambers, multi-perforated plates are commonly employed in order to generate a film cooling on the liner walls. For turbine blades, several systems are used and among them we cite internal cooling channels, film cooling, impinging jets, etc. (a complete overview of gas turbine cooling technologies can be found in [Lakshminarayana \[1995\]](#) or [Han et al. \[2012\]](#)). Whatever cooling system is used, it is clear how it is vital to accurately predict the thermal loads on the engine components in order to avoid local hot spots and properly design the cooling systems. This is stressed by the fact that the life of a turbine blade can be reduced by 50 % if the blade metal temperature prediction is off by only 50 °F [[Han et al., 2012](#)].

1. INTRODUCTION: FLAMES AND HEAT

material not to melt. However it is clear that the plastic deformations and the fatigue induced by cyclic application of very high thermal loads are unacceptable for reusable engines, which are the objective for the near future. Innovative cooling technologies have to be designed and the thermal loads on walls have to be accurately predicted. Doing so, the life cycle of the combustor structure can be correctly estimated.

When the flame is close to a solid boundary, which is often the case, it is subject to the influence of the wall from a thermal point of view. The solid structure being often at temperatures at which combustion can not sustain, quenching phenomena occur. Moreover, if the solid boundary is in the flame root zone (as it is the case for flame-holders), the flame root dynamics is modified. This may have an impact on the overall flame dynamics. Quenching phenomena due to heat losses at walls have been extensively studied, mostly in the case of flames in tubes or channels (see for example [Jarosiński \[1983\]](#); [Hackert et al. \[1998\]](#); [Daou and Matalon \[2002\]](#)) and will not be detailed here. Flame-walls interaction phenomena will be presented in subsection 1.2.3. The modification of the flame dynamics due to heat losses at walls is now addressed. [Kedia and Ghoniem \[2012\]](#) studied flame stabilization and blow-off mechanisms in methane-air flames anchored on heat conducting perforated-plates burners through numerical tools. The aim was to highlight the role of heat loss in the burner on the stabilization and blow-off mechanisms. They found how, during blow-off, the recirculation zone size, the flame displacement speed and the flame stand-off distance increase while the plate cools down, until the flame cannot anchor anymore. The flame blows-off. The same mechanisms were studied again by [Kedia and Ghoniem \[2014\]](#) for a bluff-body stabilized laminar premixed flame with unsteady, fully resolved two-dimensional numerical simulations. This work points out how the majority of Direct Numerical Simulations (DNS) investigations use artificial anchoring conditions because of the wrong temperature at the flame holder location. Here conversely no artificial flame anchoring boundary conditions were imposed and the flame was free to naturally choose an anchoring location. The flame anchoring mechanism is investigated, focusing on the impact of heat exchange and preferential diffusion. The anchoring location is shown in this work to vary non-linearly with the thermal conductivity and to strongly depend on the conjugate² heat transfer between the bluff body and the reacting flow. [Kedia and Ghoniem \[2015\]](#) investigate also the unsteady response of a bluff body stabilized premixed flame to harmonic forcing. The heat release rate response has been found to vary significantly depending on the bluff body material: this has been found to be due to the direction of the total heat flux. The latter is different for the ceramic and the metal cases: in the first case the net flux is directed to the solid body, while in the second case it is directed from the solid body to the reacting flow during an excitation cycle. This behavior explains the weaker response in the case with a ceramic bluff body, because part of the energy is used in heating up the body. The configuration of [Kedia and Ghoniem \[2014\]](#) has been numerically studied by [Berger et al. \[2016\]](#). The study relies on direct numerical simulations in which the bluff-body wall thermal condition is varied. The impact of the wall temperature has been found to

²conjugate heat transfer: the heat transfer between body and flow over or inside it as a result of interaction of two objects

be huge. The flame stabilizes further and further upstream as the wall temperature is increased, as can be seen in Fig. 1.9. The flame anchoring mechanism switches from a lifted flame in which the recirculation zone provides the heat necessary to maintain it, to an anchored flame where fresh gas preheating is assured almost entirely by the walls or, for very hot temperatures, to a bowed flame where combustion sustains through a pseudo auto-ignition process. Another example of the influence of solid temperature in

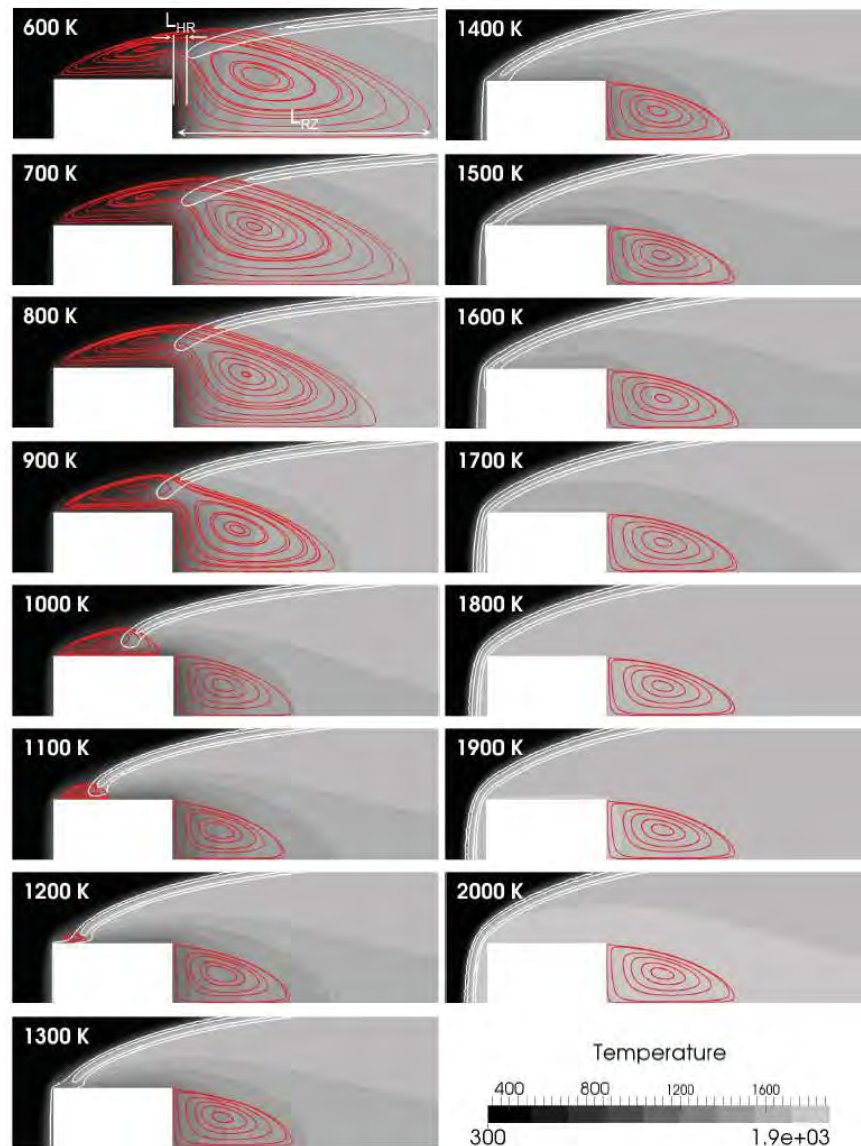


Figure 1.9: Temperature field with heat release rate contours (white) and flow streamlines within the recirculation zone (red) in the vicinity of the flame holder on the top half of the domain. [Berger et al., 2016]

flame anchoring is provided by Kaess et al. [2008], who performed simulations of thermoacoustics stability for a laminar premixed flame. Varying the boundary condition on the face plate of the burner from adiabatic to isothermal, they found that where there

1. INTRODUCTION: FLAMES AND HEAT

is no heat loss to the plate the flame attaches on the plate surface. On the contrary, for the isothermal case, a lifted flame appears due to the quenching of the chemical reactions close to the wall. This difference in the reaction rate field has an impact on the Flame Transfer Function (FTF) behavior: FTF calculated with adiabatic or isothermal boundary conditions slightly differs in phase, but differs quantitatively and qualitatively for the gain. The FTF calculated with the isothermal boundary condition shows the characteristic overshoot in amplitude often found (e.g. [Birbaud et al. \[2006\]](#)) and is closer to the experimental data of [Noiray et al. \[2007\]](#), denoting the importance of the thermal boundary condition. The influence of the thermal boundary condition at the combustor wall and combustor confinement on the dynamic flame response of a perfectly premixed axial swirl burner was investigated by [Tay-Wo-Chong and Polifke \[2013\]](#). They found that the flow field immediately downstream of the burner outlet and the flame configuration depend strongly on the combustor boundary conditions. With adiabatic walls the flame was shorter due to the flame stabilization in both shear layers, while with isothermal walls the stabilization is present almost only in the inner shear layer. This leads to different FTFs for the two cases, who showed that the level of adiabacity of the walls has an influence on the flame response due to the different flow fields and the different shapes of the flame. An analogous effect of the heat loss on the FTF of turbulent flames has been found by [Bauerheim et al. \[2015\]](#), who performed a numerical study of azimuthal unstable modes in the annular combustor of Cambridge [[Worth and Dawson, 2013](#)]. Large Eddy Simulation (LES) has been used to compute a Harmonic Flame Response Model (HFRM) and the overall stability of the combustor has been predicted with a Helmholtz solver. They found how, with a heat loss condition on bluff body walls, the flame anchoring point was lifted and its base oscillated near the injector tip. This different dynamic of the flame has been found to change both the amplitude and the time-delay of the HFRM, which decrease compared to the adiabatic case. [Mejia et al. \[2014\]](#) performed an experimental investigation of combustion instabilities for a laminar premixed flame stabilized on a slot burner. Their

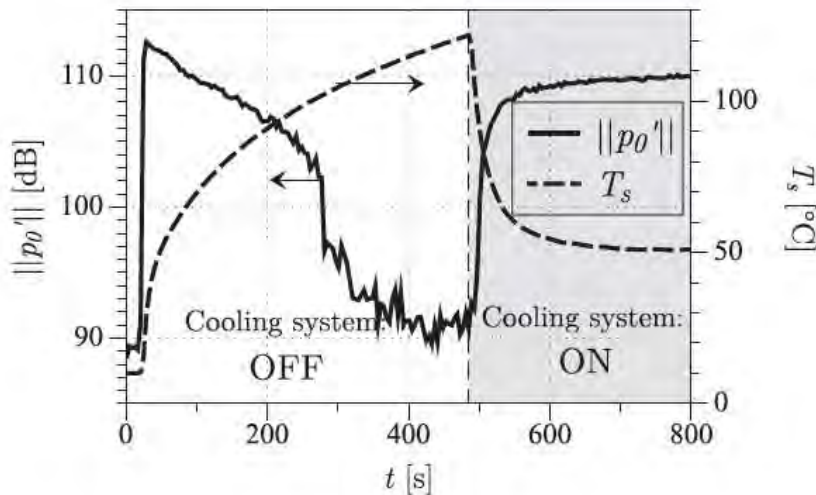


Figure 1.10: Experimental evidence of the effect of wall temperature on the amplitude of combustion instabilities [[Mejia et al., 2014](#)].

study focused on the impact of heat transfer to the slot on the flame response, starting from the observation that many systems have a different behavior at cold start and in permanent regime. They measured the response of the flame varying the temperature of the burner at the flame anchoring point. In Fig. 1.10, is presented the temporal evolution of the test. At $t=0$ s, the system is at ambient temperature and at $t=20$ s the combustion starts producing immediately an instability at the frequency of the Helmholtz mode of the burner. The pressure fluctuation then decreases as the slot heats up and the flame is fully stable after $t=400$ s. At $t=480$ s, the cooling system is activated and the slot is cooled by means of water at $T_W=3^\circ\text{C}$ and so the slot temperature T_S falls down, "reactivating" the instability that reaches a steady state around $t=800$ s.

The same qualitative results have been found in the work of [Mejia et al. \[2018\]](#), in which the influence of the flame-holder temperature has been studied for a laminar flame stabilized on a cylindrical bar.

1.2.3 Flame-wall interaction

Design of modern combustors underlines not only restrictions in fuel consumption and pollutant emissions but also in engine dimensions. Modern combustors have high confinement ratios, causing the flame to operate in a wall-bounded environment in which walls can be very close to the flame. This raises questions about the interactions between the flame and the walls. Flame-wall interaction (FWI) have an impact in fuel consumption and pollutant emissions since the flame is strongly influenced by the presence of the wall. The wall limits indeed the flame wrinkling and may cause the flame front to quench. The flame propagation in the low velocity regions of the boundary layer is also indicated as one of the possible causes for flame flashback from the combustion chamber to the mixing zone [\[Fritz et al., 2001\]](#). Moreover, the flame has a significant effect on the flow in the vicinity of the wall: viscosity is greatly increased in the burned gases, inhibiting turbulence. FWI are also the cause of locally higher heat fluxes at walls.

Two generic FWI cases must be considered for laminar premixed flames (Fig. 1.11 from [Poinsot and Veynante \[2011\]](#)):

- Head on quenching (HOQ): it is observed when the premixed flame propagates towards the wall. The flame quenches at a certain distance y_Q from the wall (of the order of the flame thickness) and the maximum wall flux Φ_Q^p (reached when the flame quenches) is of the order of one third of the total flame power $\rho_1 S_L^0 C_p (T_2 - T_1)$, where ρ_1 is the fresh gas density, S_L^0 is the flame speed and $C_p (T_2 - T_1)$ is the enthalpy jump through the flame [\[Poinsot and Veynante, 2011\]](#).
- Side wall quenching (SWQ): it is observed when the premixed flame propagates along the wall. The distance y_Q between wall and flame is larger than for HOQ and the flux slightly lower.

FWI have been studied theoretically [\[Wichman and Bruneaux, 1995\]](#), experimentally [\[Jarosinski, 1986; Ezekoye et al., 1992; Dreizler and Böhm, 2015; Xavier et al., 2017\]](#) and numerically [\[Poinsot et al., 1993; Bruneaux et al., 1996, 1997; Alshaalan](#)

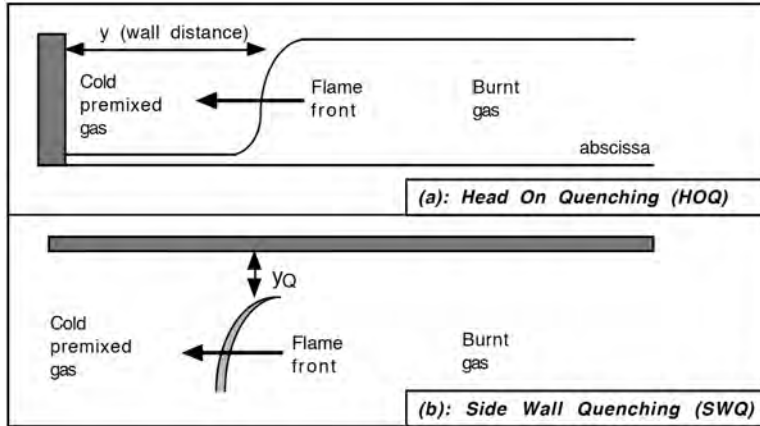


Figure 1.11: The basic configurations for flame/wall interaction in premixed flames [Delataillade et al., 2002]

and Rutland, 1998; Gruber et al., 2010]. Recently, FWI has been indicated also as a possible mechanisms for sound emission and instabilities triggering [Ihme, 2017; Ghani and Poinso, 2017].

1.3 Thesis objectives and outline

Thermal effects are a key parameter for flame dynamics and control, as well as for combustors reusability. Research has to make huge efforts to design better combustion chambers for tomorrow systems. Interactions between flames and heat can be of various nature, with effects more or less correlated to each other.

In this PhD work, we have decided to study some of this thermal effects, taking advantage of the opportunities that have arisen in this years in terms of available experimental configurations. The tool we used to perform the study is LES by means of the AVBP code [Schönfeld and Poinso, 1999; Gourdain et al., 2009]. This has been found the best compromise as our objective was to study phenomena with unsteady behaviors in "industrially oriented" configurations. The unsteadiness of the phenomena studied excludes the possibility of using Reynolds Averaged Navier-Stokes (RANS) simulation, which is the state-of-the-art in industry, and the complexity of the geometries studied, as well as their dimensions, excludes the possibility of using Direct Numerical Simulation (DNS), which cost would not be affordable.

Another decision we have taken has been to concentrate our study on combustion of a single fuel: methane. Different kinetic schemes have been used, starting from global ones and rising in complexity. The kinetic schemes behavior for various chamber conditions has been validated. Combustion of methane in premixed or diffusion flame mode has been studied, as well as its behavior with different oxidizers (air or pure oxygen).

This manuscript is divided in three parts. Part I recalls some key combustion concepts and presents the LES methodology. The AVBP code, as well as the models used in this work, are detailed. Part II and III presents the two thermal effects studied:

- Part II is dedicated to the prediction of thermal loads on the walls of rocket combustors. A single element GCH_4/GOx combustor is studied, with the aim of understanding all the parameters necessary to perform a correct prediction of the wall heat fluxes in this kind of configuration. Numerical data have been validated against experimental data available from the Technische Universität München, where we participated to the 2015 SFB/TRR 40 Summer Program.
- Part III is dedicated to plasma assisted combustion in gas turbines. A phenomenological model to describe the effect of nanosecond repetitively pulsed plasma discharges on the flame dynamics has been built thanks to a collaboration with the King Abdullah University of Science and Technology (KAUST) in Saudi Arabia. The resulting model has been applied to a methane-air swirl-stabilized premixed flame and its effects on flame stability have been studied.

Part I

**Theoretical background and
modeling of turbulent
reactive flows via Large
Eddy Simulation**

Chapter 2

Governing equations of turbulent reactive flows

Contents

2.1 Thermodynamics of a multispecies mixture	19
2.2 Navier-Stokes equations	20
2.3 Transport properties	21
2.4 Chemical kinetics	23

The aim of this chapter is to introduce the main variables describing reactive flows as well as the physical models used in the multispecies Navier-Stokes equations solved in AVBP. Derivation is not detailed and can be found for example in [Kuo \[2005 Second Edition\]](#) or [Poinot and Veynante \[2011\]](#).

2.1 Thermodynamics of a multispecies mixture

Combustion is characterized by multispecies mixtures, where each species k has its own properties:

- mass fraction: $Y_k = m_k/m$, the ratio of the mass of species k , m_k over the total mixture mass m .
- density: $\rho_k = \rho Y_k$, where ρ is the density of the mixture
- molar mass of species k : W_k
- molar fraction of species k : $X_k = \frac{W}{W_k} Y_k$, where W is the molar mass of the mixture
- molar concentration of species k : $[X_k] = \rho \frac{X_k}{W}$
- constant pressure mass heat capacity: $C_{p,k}$
- mass enthalpy: $h_k = h_{s,k} + \Delta h_{f,k}^0$, where $h_{s,k} = \int_{T_0}^T C_{p,k} dT$ is the sensible enthalpy and $\Delta h_{f,k}^0$ is the formation enthalpy at reference temperature T_0

2. GOVERNING EQUATIONS OF TURBULENT REACTIVE FLOWS

Considering a mixture composed of N species, $\sum_{k=1}^N Y_k = 1$, the mixture molar mass can be obtained by:

$$\frac{1}{W} = \sum_{k=1}^N \frac{Y_k}{W_k} \quad \text{or} \quad W = \sum_{k=1}^N X_k W_k \quad (2.1)$$

For perfect gases, the mixture total pressure P can be considered as the sum of the partial pressures p_k of each species:

$$P = \sum_{k=1}^N p_k \quad \text{where} \quad p_k = \rho_k \frac{\mathcal{R}}{W_k} T \quad (2.2)$$

where T is the mixture temperature and $\mathcal{R} = 8.314 \text{ J}\cdot\text{mol}^{-1}\cdot\text{K}^{-1}$ is the perfect gas universal constant. Using the equation of states one obtains:

$$p = \sum_{k=1}^N p_k = \sum_{k=1}^N \rho_k \frac{\mathcal{R}}{W_k} T = \rho \frac{\mathcal{R}}{W} T \quad (2.3)$$

The constant pressure mass heat capacity of the mixture C_p is given by:

$$C_p = \sum_{k=1}^N Y_k C_{p,k} \quad (2.4)$$

2.2 Navier-Stokes equations

The Navier-Stokes equations for multispecies mixtures using Einstein index notation write:

$$\frac{\partial \rho}{\partial t} + \frac{\partial}{\partial x_i} (\rho u_i) = 0 \quad (2.5)$$

$$\frac{\partial \rho u_j}{\partial t} + \frac{\partial \rho u_i u_j}{\partial x_i} + \frac{\partial P \delta_{ij}}{\partial x_i} = - \frac{\partial \tau_{ij}}{\partial x_i} \quad \text{for } j = 1, 3 \quad (2.6)$$

$$\frac{\partial \rho Y_k}{\partial t} + \frac{\partial \rho u_i Y_k}{\partial x_i} = - \frac{\partial J_{i,k}}{\partial x_i} + \dot{\omega}_k \quad \text{for } k = 1, N \quad (2.7)$$

$$\frac{\partial \rho E}{\partial t} + \frac{\partial \rho u_i E}{\partial x_i} + \frac{\partial u_j P \delta_{ij}}{\partial x_i} = - \frac{\partial q_i}{\partial x_i} + \frac{\partial u_j \tau_{ij}}{\partial x_i} + \dot{\omega}_T + \dot{Q}_{sp} \quad (2.8)$$

where u_j is the j^{th} -component of the velocity, P is the static pressure, τ_{ij} is the viscous tensor, $J_{i,k}$ is the i^{th} -component of the diffusive flux of species k , $\dot{\omega}_k$ and $\dot{\omega}_T$ are the species k and energy chemical source term, E is the total energy, q_i is the i^{th} -component of the energy flux and \dot{Q}_{sp} is the external energy source term (in this study this term will appear in part III, denoting the energy supplied by the plasma discharges). δ_{ij} is the Kronecker symbol equal to 1 if $i = j$ and 0 otherwise. Eqs. (2.5)-(2.8) are referred to as the mass, momentum, k^{th} -species and energy conservation equations respectively.

The viscous tensor is proportional to the symmetric part of the deformation tensor

(Newtonian fluid), and equality between mechanical and thermodynamic pressure (zero coefficient of bulk viscosity null, Stokes assumption) is assumed:

$$\tau_{ij} = 2\mu \left(S_{ij} - \frac{1}{3} \delta_{ij} S_{kk} \right) \quad (2.9)$$

with μ the dynamic viscosity and S_{ij} the deformation tensor:

$$S_{ij} = \frac{1}{2} \left(\frac{\partial u_j}{\partial x_i} + \frac{\partial u_i}{\partial x_j} \right) \quad (2.10)$$

The diffusive flux of species k in the mixture is calculated using the Hirschfelder and Curtiss approximation [Hirschfelder et al., 1969], yielding:

$$J_{i,k} = \rho Y_k V_{k,i} = -\rho \left(D_k \frac{W_k}{W} \frac{\partial X_k}{\partial x_i} - Y_k V_i^c \right) \quad (2.11)$$

with D_k the equivalent diffusion coefficient of species k in the rest of the mixture:

$$D_k = \frac{1 - Y_k}{\sum_{j \neq k} X_j / D_{jk}} \quad (2.12)$$

where D_{jk} is the binary diffusion coefficient of species j in species k . V_i^c in Eq. (2.11) is the correction velocity ensuring global mass conservation:

$$V_i^c = \sum_{k=1}^N D_k \frac{W_k}{W} \frac{\partial X_k}{\partial x_i} \quad (2.13)$$

The chemical source term $\dot{\omega}_k$ in the species conservation equation is described in Sec. 2.4. The energy flux is the combination of the Fourier flux and the enthalpy flux induced by species diffusion:

$$q_i = -\lambda \frac{\partial T}{\partial x_i} + \sum_{k=1}^N J_{i,k} h_{s,k} \quad (2.14)$$

where λ is the heat conduction coefficient of the mixture. Finally the reaction energy source term is linked to the species source terms by:

$$\dot{\omega}_T = - \sum_{k=1}^N \Delta h_{f,k}^0 \dot{\omega}_k \quad (2.15)$$

2.3 Transport properties

For combustion simulations simple transport models are used. The dynamic viscosity μ of the mixture is modeled through a standard power law. It is supposed independent

2. GOVERNING EQUATIONS OF TURBULENT REACTIVE FLOWS

of the species composition and only depending on the temperature:

$$\mu = \mu_0 \left(\frac{T}{T_0} \right)^b \quad (2.16)$$

where the exponent b depends on the mixture and typically lies between 0.6 and 1.0. A constant Schmidt number Sc_k for each species k is assumed to evaluate the species diffusion coefficient:

$$D_k = \frac{\mu}{\rho Sc_k} \quad (2.17)$$

The Schmidt number is a dimensionless number that compares the viscous and species diffusion rates. The thermal conductivity λ is computed similarly, assuming a constant Prandtl number Pr of the mixture:

$$\lambda = \frac{\mu C_p}{Pr} = \rho C_p D_{th} \quad \text{with} \quad D_{th} = \frac{\nu}{Pr} \quad (2.18)$$

The Prandtl number compares the viscous and thermal diffusion rates of the mixture. Finally, the Lewis number Le_k that compares the thermal and species diffusion rates is introduced as:

$$Le_k = \frac{D_{th}}{D_k} = \frac{Sc_k}{Pr} \quad (2.19)$$

For high temperature simulations (more than 5000 K), like the one performed for the modelization of plasma states of the mixture (part III), the classical laws for viscosity and thermal conductivity are not valid anymore. In this case the viscosity and thermal conductivity of the mixture are modeled according to [D'Angola et al. \[2008\]](#). An example of the differences in values with different viscosity and thermal conductivity laws can be found in Fig. 2.1. It can be seen how a classical power law is accurate up to mixture temperatures of around 2000 K, which are typical of combustion. For higher temperatures, the use of classical laws can introduce large errors. Laws like the [D'Angola et al. \[2008\]](#) one are necessary in order to have the correct transport properties.

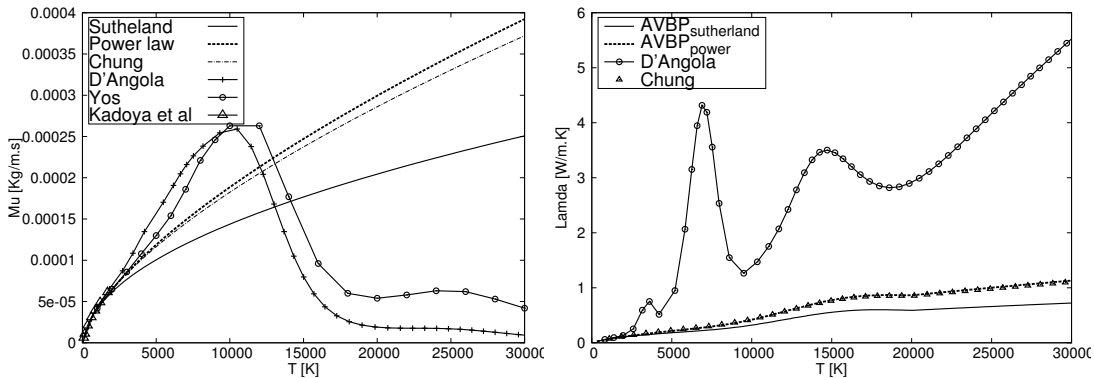


Figure 2.1: Left: viscosity as a function of mixture temperature. Right: thermal conductivity as a function of temperature. Mixture of methane and air at $\phi = 0.8$ and $P = 1$ atm

2.4 Chemical kinetics

Considering N species reacting through M reactions:

$$\sum_{k=1}^N \nu'_{kj} \mathcal{M}_k \rightleftharpoons \sum_{k=1}^N \nu''_{kj} \mathcal{M}_k \quad \text{for } j = 1, M \quad (2.20)$$

where \mathcal{M}_k is the symbol for species k , ν'_{kj} and ν''_{kj} are the molar stoichiometric coefficients of species k in reaction j . The reaction rate $\dot{\omega}_k$ of species k is the sum of all reaction rates $\dot{\omega}_{k,j}$ in reaction j :

$$\dot{\omega}_k = \sum_{j=1}^M \dot{\omega}_{k,j} = W_k \sum_{j=1}^M \nu_{kj} \mathcal{Q}_j \quad (2.21)$$

where $\nu_{kj} = \nu''_{kj} - \nu'_{kj}$ and \mathcal{Q}_j is the progress rate of reaction j . Thanks to total mass conservation:

$$\sum_{k=1}^N \dot{\omega}_k = 0 \quad (2.22)$$

The progress rate of reaction j is given by:

$$\mathcal{Q}_j = K_{fj} \prod_{k=1}^N \left(\frac{\rho Y_k}{W_k} \right)^{\nu'_{kj}} - K_{rj} \prod_{k=1}^N \left(\frac{\rho Y_k}{W_k} \right)^{\nu''_{kj}} \quad (2.23)$$

K_{fj} and K_{rj} are the forward and reverse reaction rates of reaction j respectively. The forward reaction rate is described with an Arrhenius law:

$$K_{fj} = \mathcal{A}_j \exp\left(-\frac{E_{aj}}{\mathcal{R}T}\right) \quad (2.24)$$

where \mathcal{A}_j and E_{aj} are the pre-exponential factor and the activation energy of reaction j respectively. The reverse reaction rate is given by:

$$K_{rj} = \frac{K_{fj}}{K_{eq,j}} \quad (2.25)$$

with $K_{eq,j}$ the equilibrium constant, defined following [Kuo \[2005 Second Edition\]](#). It writes:

$$K_{eq,j} = \left(\frac{P_0}{\mathcal{R}T} \right)^{\sum_{k=1}^N \nu_{kj}} \exp\left(\frac{\Delta S_j^0}{\mathcal{R}} - \frac{\Delta H_j^0}{\mathcal{R}T} \right) \quad (2.26)$$

where $P_0 = 1$ bar, ΔH_j^0 and ΔS_j^0 are the enthalpy and entropy changes for reaction j respectively:

$$\Delta H_j^0 = h(T) - h(0) = \sum_{k=1}^N \nu_{kj} W_k (h_{s,k} + \Delta h_{f,k}^0) \quad (2.27)$$

$$\Delta S_j^0 = \sum_{k=1}^N \nu_{kj} W_k s_k(T) \quad (2.28)$$

2. GOVERNING EQUATIONS OF TURBULENT REACTIVE FLOWS

s_k is the entropy of species k .

Theoretical concepts of turbulence and combustion

Contents

3.1 Basics of turbulence	25
3.2 Premixed combustion	28
3.2.1 Laminar premixed flames	28
3.2.2 Turbulent premixed flames	31
3.3 Non-premixed combustion	33
3.3.1 Laminar diffusion flames	33
3.3.2 Turbulent diffusion flames	37

Flames are usually classified in four different categories, as shown in Tab. 3.1, adapted from Poinso and Veynante [2011]. The first classification criterion is whether or not the reactants are mixed together before combustion: in the first case we talk about premixed flames and in the second case about non-premixed (also called diffusion) flames. The second classification criterion is turbulence. When velocities are high, the flows become turbulent and so the flames. The flame front is not flat anymore but wrinkling and unsteady phenomena appear. Flames are turbulent in the great majority of industrial combustion systems.

In this work, turbulent diffusion flames are studied in part II, while turbulent premixed flames are studied in part III.

3.1 Basics of turbulence

The Reynolds number, which compares inertia to viscous forces, characterizes transition from a laminar to a turbulent flow:

$$Re = \frac{|\mathbf{u}|l}{\nu} \tag{3.1}$$

where \mathbf{u} and l are the characteristic velocity and dimension of the flow and ν is the kinematic viscosity. For large Reynolds numbers inertia forces dominate and the flow is

3. THEORETICAL CONCEPTS OF TURBULENCE AND COMBUSTION




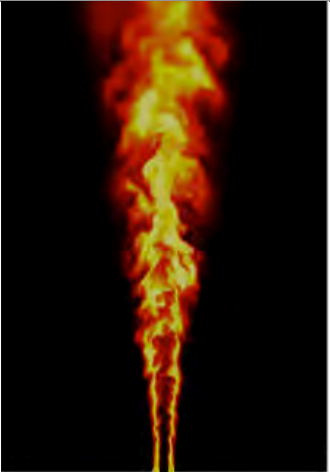
	LAMINAR	TURBULENT
PREMIXED	 <p>Bunsen Flame [Wei et al., 2015]</p>	 <p>Cambridge Flame [Sweeney et al., 2012]</p>
NON-PREMIXED	 <p>Lighter</p>	 <p>Sandia D Flame [Shum-Kivan, 2017]</p>

Table 3.1: Classification of flame regimes.

characterized by significant variations of the velocity field in space and time. In this case a multitude of vortices of varying sizes, called eddies, are convected by the mean flow. The interaction of these eddies with each other happens through a cascade process where large eddies decay into smaller ones, transmitting energy from large to small scales. In a homogeneous isotropic turbulence, the energy is spectrally distributed as presented in 3.1 where the energy density $E(k)$ is plotted versus the eddy wave number k (inverse of the eddy length scale). Three zones can be identified, going from from the largest to the smallest length scales [Pope, 2000]:

- The **integral zone** is the one in which eddies have the lowest frequencies and is characterized by the wave number k_t , which corresponds to the integral length scale l_t . In this zone the turbulent energy is produced and contains the biggest and most energetic eddies. Their size is of the order of the characteristic length

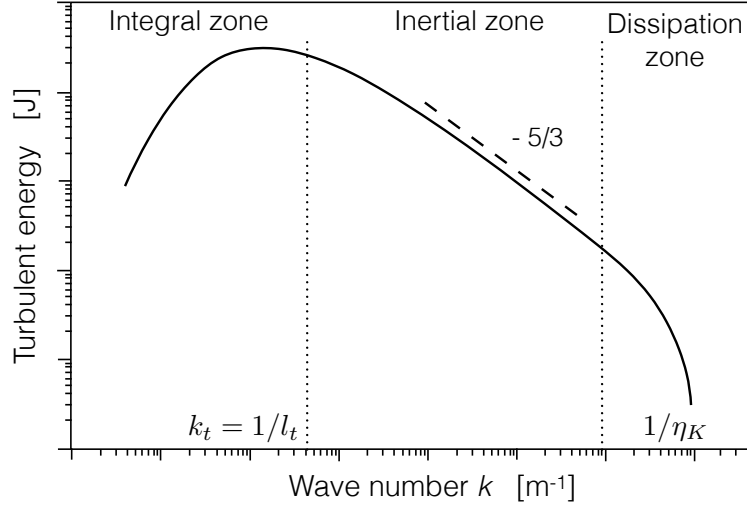


Figure 3.1: Energy density spectrum $E(k)$ in an homogeneous isotropic turbulence [Richardson, 1922].

of the geometry. The largest scales in a turbulent flow are mainly controlled by inertia and are not affected by viscous effects.

- The large eddies break down into smaller ones in the **inertial zone** via the "cascade" process. In this zone there is no eddy dissipation and the rate of energy transfer from the biggest to the smallest structures follows a constant slope $k^{-5/3}$ for isotropic statistically steady turbulence [Kolmogorov, 1941].
- In the **dissipation zone** viscous forces dominate and the turbulent energy is dissipated into heat due to the kinematic viscosity ν . This zone is characterized by the highest wave numbers and its characteristic wave number is the Kolmogorov one k_{η_K} , corresponding to the Kolmogorov length scale η_K . The Kolmogorov length scale and speed can be estimated (in isotropic homogeneous turbulence) by:

$$\eta_K = \left(\frac{\nu^3}{\varepsilon} \right)^{1/4} \quad \text{and} \quad u'_K = (\nu\varepsilon)^{1/4} \quad (3.2)$$

where the subscript K denotes the Kolmogorov scale and ε is the dissipation rate given by:

$$\varepsilon = 2\nu S_{ij} S_{ij} \quad (3.3)$$

In this chapter basic concepts of combustion are reminded. This chapter is not intended as a complete review of the theory of combustion, but only to sum up some concepts which will be mentioned in the following of this work. For a complete review one can refer to the classical textbooks of Poinso and Veynante [2011], Kuo [2005 Second Edition] or Peters [2000].

3.2 Premixed combustion

3.2.1 Laminar premixed flames

Combustion, which in general involves various intermediate species and reactions to convert reactants into products, can be seen from a macroscopical point of view as a unique reaction:



where ν'_F and ν'_O are the stoichiometric coefficients of fuel and oxidizer respectively. The mixture is said stoichiometric when the fuel and oxidizer mass fractions of the fresh gases Y_F and Y_O follow:

$$\left(\frac{Y_O}{Y_F}\right)_{st} = \frac{\nu'_O W_O}{\nu'_F W_F} = s \quad (3.5)$$

where W_F and W_O are the molar mass of fuel and oxidizer respectively, s is the mass stoichiometric ratio and the subscript st denotes stoichiometric conditions. The equivalence ratio ϕ is given by:

$$\phi = s \frac{Y_F}{Y_O} = \left(\frac{Y_F}{Y_O}\right) / \left(\frac{Y_F}{Y_O}\right)_{st} \quad (3.6)$$

A mixture having $\phi > 1$ is called rich (excess of fuel) while a lean mixture corresponds to $\phi < 1$ (excess of oxidizer).

The thermal structure of a premixed laminar flame (in a one-dimensional formalism) is now introduced (Fig. 3.2). Several characteristic zones can be identified from left (fresh gases) to right (burnt gases):

- the **preheat zone**, chemically inert, where heat diffuses progressively from the reaction zone and increases the gas temperature.
- the **reaction layer** where the fuel is decomposed in smaller hydrocarbons which react with radicals to create secondary species. The reaction layer has a thickness δ_r .
- the **post-flame region** where secondary species are transformed in final products of the reaction.

The great majority of heat is released in the reaction layer, where a strong temperature gradient is present. In this zone the chain branching reactions occur. The post-flame region is, on the contrary, where recombination reactions occur. In this zone reactions are much slower than in the reaction layer and the zone is much thicker.

This description of the flame structure can be re-conducted to the thermal theory proposed by [Zeldowitsch and Frank-Kamenetzki \[1938\]](#), which simplified the Navier-Stokes equations under the assumptions of one-dimensional stationary flow. The ZFK analysis assumes a single-step global reaction with an Arrhenius type reaction rate and a high activation energy, unity Lewis number for all species and first order dependence of the reaction rate to fuel and oxidizer. The flame front is so described by a single

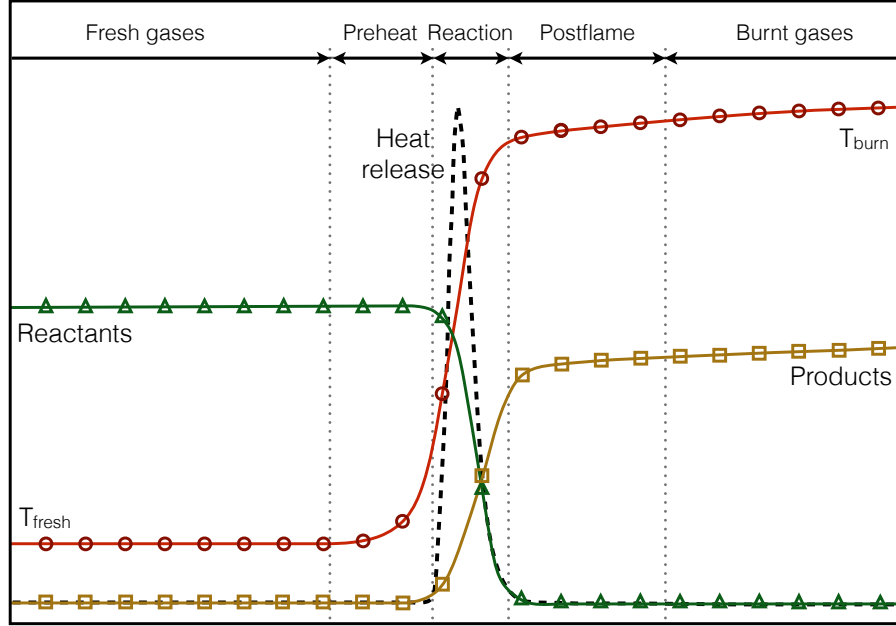


Figure 3.2: Schematic description of the laminar premixed flame structure.

differential equation and can be viewed as a wave propagating from the burnt gases toward the fresh gases at a constant velocity S_L^0 [Zeldowitsch and Frank-Kamenetzki, 1938]:

$$\rho_u S_L^0 \frac{dT}{dx} = \frac{d}{dx} \left(\frac{\lambda}{C_p} \frac{dT}{dx} \right) - \frac{Q}{C_p} \omega \quad (3.7)$$

Assuming a null reaction rate in the preheat zone and a negligible convection term in the reaction layer, the temperature balance can be written in both regions and an expression for S_L^0 is obtained by equating the temperature gradient at the frontier between these two regions:

$$S_L^0 \propto \sqrt{D_{th} \mathcal{A}} \quad (3.8)$$

where D_{th} is the thermal diffusivity and \mathcal{A} is the Arrhenius pre-exponential factor.

An important parameter for numerical simulations is the flame thickness, which has a great impact of mesh resolution needs to solve the flame structure. Several definitions of the laminar flame thickness are reported in the literature, among which:

- The diffusion thickness δ is based on the thermal diffusion of fresh gases [Poinsot and Veynante, 2011]:

$$\delta = \frac{\lambda(T_f)}{\rho(T_f) C_p(T_f) S_L^0} = \frac{D_{th}}{S_L^0} \propto \sqrt{\frac{D_{th}}{\mathcal{A}}} \quad (3.9)$$

where the subscript f denotes the fresh gases. This definition, which directly derives from the ZFK asymptotic theory, provides an estimation of the flame

3. THEORETICAL CONCEPTS OF TURBULENCE AND COMBUSTION

thickness. In practice the result is too approximate to determine the required mesh resolution.

- The thermal thickness δ_L^0 is based on the temperature gradient and is generally used to estimate the grid resolution required in LES or DNS computations:

$$\delta_L^0 = \frac{T_b - T_f}{\max(|\nabla T|)} \quad (3.10)$$

where the subscript b denotes the burnt gases. The computation of a 1D laminar flame allows to estimate the flame thermal thickness.

- The reaction layer thickness δ_r can also be used to estimate the flame thickness with $\delta_r = \delta_L^0/\beta$, where β is given by:

$$\beta = \alpha \frac{E_a}{\mathcal{R}T_b} \quad \text{and} \quad \alpha = \frac{T_b - T_f}{T_b} \quad (3.11)$$

The parameters α and β measure the heat release by the flame and the activation energy respectively. Since typical values of β range between 10 and 20, $\delta_r < \delta_L^0$ and using this definition leads to stronger mesh resolution constraint.

Other relevant speeds

We introduce here some other relevant speeds which might be of interest for kinematic interpretation of the propagation of premixed flames. The absolute velocity of the flame in the reference frame \mathbf{w} can be decomposed following Fig 3.3:

- The **absolute speed** $S_a = \mathbf{w} \cdot \mathbf{n}$, which is the flame front speed in the absolute reference frame.
- The **displacement speed** $S_d = (\mathbf{w} - \mathbf{u}) \cdot \mathbf{n} = S_a - \mathbf{u} \cdot \mathbf{n}$, which is the flame front speed relative to the local flow velocity \mathbf{u} . S_d is useful for a kinematic interpretation of the flame as an interface.
- The **consumption speed** S_c is the speed at which reactants are consumed, and is equal to the integral of fuel consumption in the direction normal to the flame. The expression of S_c reads

$$S_c = -\frac{1}{\rho_f (Y_F^f - Y_F^b)} \int_{-\infty}^{\infty} \dot{\omega}_F \mathbf{dn}. \quad (3.12)$$

Contrarily to the displacement speed, the consumption speed is a global quantity. Its interpretation is simpler than the displacement speed, but this quantity can only be evaluated globally.

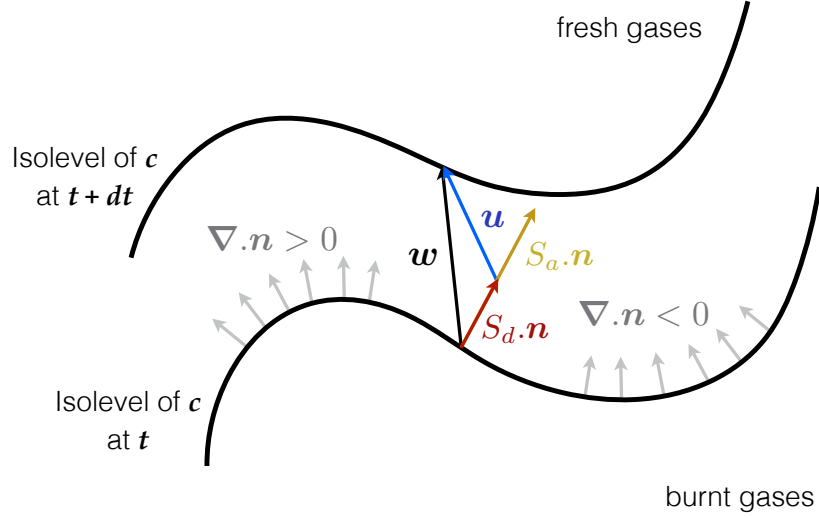


Figure 3.3: Flame speed definitions, following Poinso and Veynante [2011].

For a laminar steady premixed flame, the following relations can be obtained

$$S_a = 0 \quad (3.13)$$

$$S_L^0 = S_c = S_d^* = \frac{\rho}{\rho_f} S_d \quad (3.14)$$

where S_d^* is the density weighted displacement speed [Hong et al., 1999], introduced to take into account flow dilatation. For more complex cases, these quantities might strongly differ under the effect of turbulence, unsteadiness and stretch (curvature and strain).

3.2.2 Turbulent premixed flames

Turbulent premixed combustion is the result of the interaction between the flame front and the flow eddies. The turbulent eddies have a size which ranges from the Kolmogorov to the integral scales and have characteristic speeds ranging from the Kolmogorov velocity u'_K to the integral Root Mean Square (RMS) velocity u' .

Chemistry can be characterized by a chemical time scale $\tau_c = \delta_L^0 / S_L^0$, where δ_L^0 and S_L^0 are respectively the thermal thickness and flame speed of an unstrained laminar premixed flame. This chemical time τ_c corresponds to the time required for the flame to propagate over a distance equal to its own thickness.

Turbulence is characterized simultaneously by the turbulence time scale of the most energetic structures $\tau_t = l_t / u'_t$, and by the time scale of the smallest turbulent scales (the Kolmogorov time scale) $\tau_K = \eta_K / u'_K$.

The turbulent/flame interactions are so generally described by means of two reduced numbers which compare this different time scales:

- The **Damköhler number** Da is defined as the ratio of the integral time scale τ_t

3. THEORETICAL CONCEPTS OF TURBULENCE AND COMBUSTION

to the chemical time scale τ_c :

$$Da = \frac{\tau_t}{\tau_c} = \frac{l_t S_L^0}{\delta_L^0 u_t'} \quad (3.15)$$

Two cases may be distinguished:

- for high Da number ($Da \gg 1$), the turbulent time scale is much larger than the chemical time scale and the structure of the flame front is not affected by turbulence. This regime is usually referred as **flamelet regime** or **thin wrinkled flame regime** and has the characteristics that the turbulent flame front can be assimilated to a collection of laminar flame elements called "flamelets".
 - for small Da number ($Da \ll 1$), the turbulent time scale is much smaller than the chemical time scale: the reactants and products are mixed by turbulent motion before reacting via a slow chemical process. This corresponds to the **well stirred reactor** limit.
- The **Karlovitz number** Ka identifies the interactions between the turbulent small scales and the flame:

$$Ka = \frac{\tau_c}{\tau_K} = \frac{\delta_L^0 u_K'}{\eta_K S_L^0} \quad (3.16)$$

Various expressions of the Karlovitz number can be found in the literature. Using the relation $S_L^0 \sim \nu/\delta_L^0$, a unity flame Reynolds number is obtained:

$$Re_{fl} = \frac{\delta_L^0 S_L^0}{\nu} = 1 \quad (3.17)$$

yielding:

$$Ka = \left(\frac{u'}{S_L^0} \right)^{3/2} \left(\frac{l_t}{\delta_L^0} \right)^{-1/2} = \left(\frac{\delta_L^0}{\eta_K} \right)^2 \quad (3.18)$$

using Eq. (3.2). This shows how the Karlovitz number compares the laminar flame length scale to the smallest turbulent scale.

Since the Reynolds, Damköhler and Karlovitz numbers are related through $Re = Da^2 Ka^2$, the transition between the different combustion regimes can be defined using only two of this non-dimensional numbers. Following Peters [2000], a diagram of the various combustion regimes can be constructed (Fig. 3.4) based on characteristic lengths and speeds of flame and turbulence. This permits to describe the possible combustion regimes via the Reynolds, Damköhler and Karlovitz numbers.

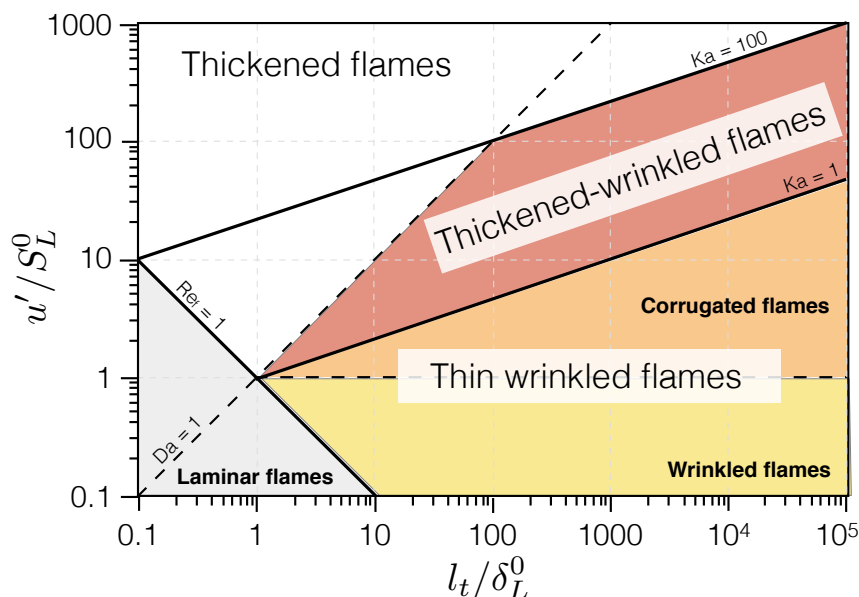


Figure 3.4: Combustion regime diagram for premixed turbulent combustion from Peters [2000].

3.3 Non-premixed combustion

3.3.1 Laminar diffusion flames

In the case of diffusion flames, fuel and oxidizer are not mixed before combustion. This happens in many applications, i.e. rocket engines, mainly to ensure a safe fuel storage. Diffusion flames are largely controlled by mixing, which must bring the reactants into the reaction zone localized around stoichiometry, which is the region where fuel and oxidizer are mixed adequately to burn.

A schematic view of this type of flame structure is given in Fig. 3.5. The temperature peak is located in the reaction zone and diffuses towards the fresh fuel and oxidizer streams. Contrarily to premixed flames, diffusion flames do not propagate and have no intrinsic thickness. The inner structure of a diffusion flame is imposed by the external conditions, which depend on the local stretch.

Diffusion flames are characterized by two main length scales [Bilger, 1989]:

- **the diffusion layer thickness** l_d , which is the zone where the mixture fraction z goes from 0 to 1 and where fuel and oxidizer may coexist, diluted by combustion products.
- **the reaction zone thickness** l_r , which corresponds to the zone where reaction occurs. This zone typically lies around the stoichiometric mixture fraction z_{st} .

These length scales are not equivalent to the premixed flame thermal and reactive thicknesses previously defined since they can evolve separately and are strongly dependent

3. THEORETICAL CONCEPTS OF TURBULENCE AND COMBUSTION

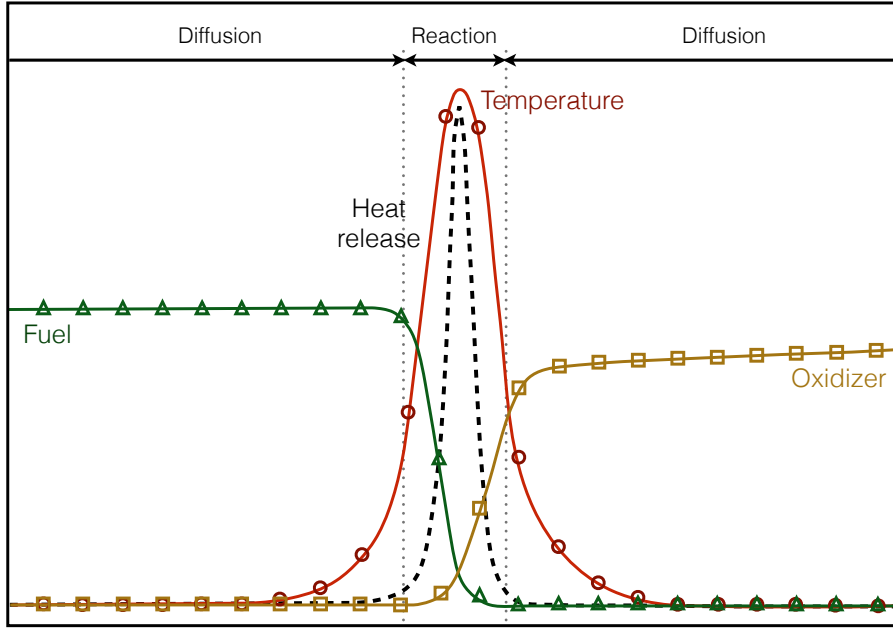


Figure 3.5: Schematic description of the laminar diffusion flame structure.

on the flow conditions.

Similarly to the premixed flames, a laminar diffusion flame can be characterized by the flame Damköhler number:

$$Da^{fl} = \frac{\tau_f}{\tau_c} \quad (3.19)$$

The flow time scale can be estimated from the scalar dissipation rate at stoichiometric conditions $\tau_f = \chi_{st}^{-1}$ [Libby and Williams, 1994], with $\chi = 2D(\nabla z)^2$ and z the mixture fraction.

Since χ_{st} measures the mixture fraction gradient, it can be used to estimate the diffusion layer thickness $l_d \simeq \sqrt{D/\chi_{st}}$. Asymptotic theories [Linan, 1974] relate the reaction and diffusion layer thicknesses through the flame Damköhler number Da^{fl} :

$$\frac{l_r}{l_d} \simeq (Da^{fl})^{-1/b} \quad (3.20)$$

where $b = \nu'_F + \nu'_O + 1$ is obtained from the stoichiometric coefficients of the global reaction.

The mixture fraction z is very convenient to describe non-premixed combustion. z is a chemistry-independent "conserved scalar" which satisfies the non-reactive transport equation:

$$\rho \frac{\partial z}{\partial t} + \rho \mathbf{u} \cdot \nabla z = \nabla \cdot (\rho D \nabla z) \quad (3.21)$$

where D is the diffusivity (either thermal or species depending on the definition of z). All scalar quantities of the flow (temperature, concentration or density) are then

uniquely related to the mixture fraction. In this work, the mixture fraction is defined following Bilger [1989] and based on the coupling function β [Williams, 1985]:

$$z = \frac{\beta - \beta_0}{\beta_1 - \beta_0} \quad (3.22)$$

with

$$\beta = \sum_{l=1}^{N_e} \gamma_l \sum_{k=1}^{N_s} \frac{a_{l,k} W_l Y_k}{W_k} \quad (3.23)$$

where β_0 and β_1 are the values of β evaluated in the fuel and oxidizer streams respectively, γ_l and W_l are the weighting factor and the atomic weight of the element l respectively, and $a_{l,k}$ is the number of atoms of element l in one molecule of species k . The choice of Bilger for γ_l is used in this work with $\gamma_C = 2/W_C$, $\gamma_H = 1/(2W_H)$, $\gamma_O = -1/W_O$ and $\gamma_N = 0$. z is linked to the equivalence ratio by:

$$\phi = \frac{z}{1-z} \frac{1-z_{st}}{z_{st}} \quad (3.24)$$

An important canonical case representative of practical applications is the steady strained one-dimensional diffusion flame. This combustion regime is at the basis of numerous tabulated chemistry models for non-premixed flames. A schematic of this type of flame is given in Fig. 3.6. The strain rate is not exactly constant in this situation

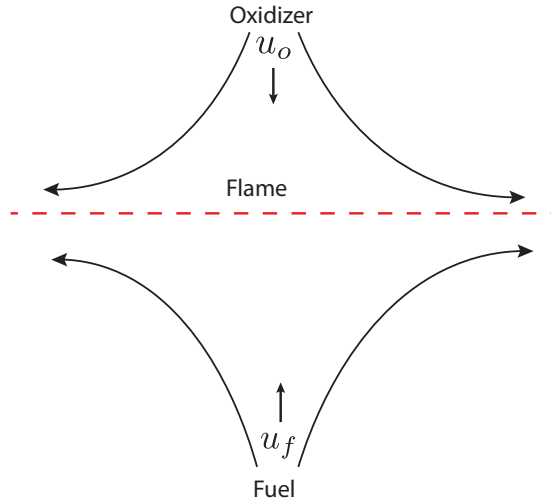


Figure 3.6: Steady strained one-dimensional diffusion flame.

along the flame normal, but it can be estimated as a global quantity:

$$a \simeq \frac{u_f + u_o}{L} \quad (3.25)$$

where u_f and u_o are respectively the fuel and oxidizer injection velocity and L is the distance between the two inlets. Under the assumption of asymptotically infinitely fast

3. THEORETICAL CONCEPTS OF TURBULENCE AND COMBUSTION

chemistry, it can be shown that the flame consumption speed (integrated fuel reaction rate along the flame normal) is linked to the strain rate a and the diffusivity D as Poinso and Veynante [2011]

$$S_c \propto \sqrt{aD} \quad (3.26)$$

$$(3.27)$$

and that the scalar dissipation rate is directly proportional to the strain rate

$$\chi \propto a. \quad (3.28)$$

Compared to premixed flame for which the stretch only introduces a small linear correction to the flame consumption speed, which remains essentially piloted by the intrinsic properties of the premixed flame, the scalar dissipation rate directly controls the diffusion flame consumption speed:

$$S_c \propto \sqrt{\chi D} \quad (3.29)$$

Diffusion flames are therefore very sensitive to local flow conditions.

All the theoretical concepts above mentioned were derived assuming infinitely fast chemistry. However, they remain valid for finite rate chemistry in the high Damköhler limit, corresponding to low strain values. As shown in Fig. 3.7, when the strain rate increases too much, the response of finite rate chemistry deviates from the ideal one. The maximum temperature of the flame decreases and beyond a certain threshold value, quenching occurs.

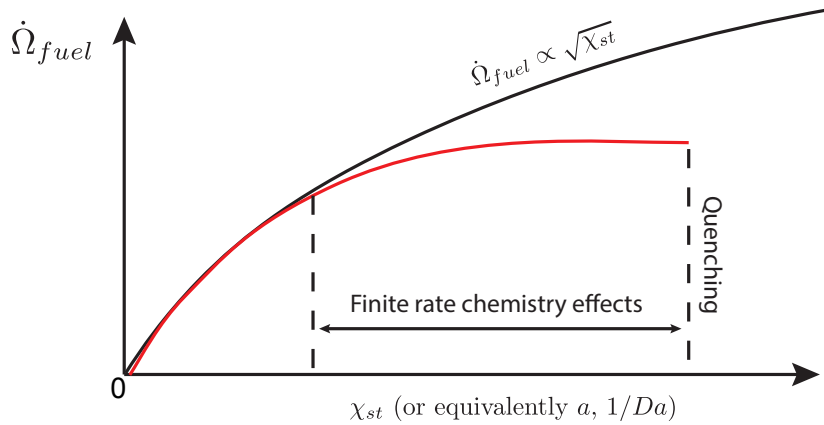


Figure 3.7: Diffusion flame consumption speed vs scalar dissipation (or equivalently strain rate a or inverse of Damköhler $1/Da$) for infinitely fast chemistry (black) and finite rate chemistry (red).

3.3.2 Turbulent diffusion flames

Differently from premixed flames, which have intrinsic properties, the structure of diffusion flames is governed by the scalar dissipation rate which is directly linked to the turbulent strain rate. Since diffusion flames do not exhibit well-defined characteristic scales, establishing a universal combustion diagram in this situation is not straightforward. Figure 3.8 (left) illustrates a comparison between the laminar flame length scale and the turbulence length scales.

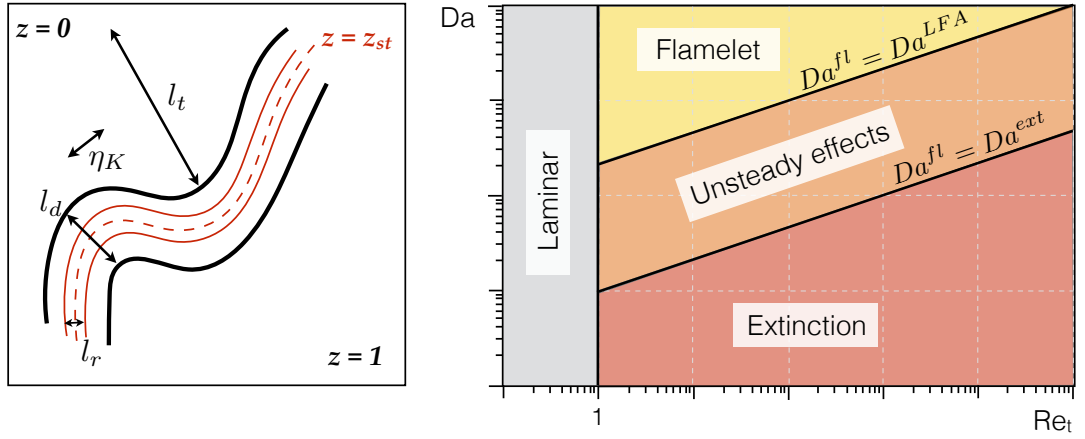


Figure 3.8: Definition of diffusion flame thickness and turbulence length scale (left). Non-premixed combustion diagram as function of the turbulent Reynolds number Re_t and Damköhler number Da [Cuenot and Poinso, 1994] (right).

Similarly to the premixed case, combustion regimes can be roughly estimated for diffusion flames by comparison of these scales. As shown in Cuenot and Poinso [1994], several regimes can be identified in a log-log diagram based on the turbulent Reynolds number Re_t and the Damköhler number $Da \simeq 2\sqrt{Re_t}Da^{fl}$ (Fig. 3.8, right). Three regimes can be identified:

- The **flamelet regime** corresponds to a Da^{fl} lower than a critical value Da^{LFA} (LFA: laminar flamelet assumption). In this regime the inner flame structure is not affected by turbulence.
- When Da^{fl} is higher than the critical value Da_{ext} (ext: extinction), **quenching** occurs because chemical times are too large compared to flow scales.
- In-between, there is an intermediate situation with strong unsteady effects.

Modeling of turbulent reactive flows via Large Eddy Simulation

Contents

4.1 Numerical simulation approaches: DNS, LES, RANS	40
4.2 Large Eddy Simulation	41
4.2.1 Filtered viscous fluxes	42
4.2.2 Subgrid fluxes closure	43
4.3 Turbulent viscosity models	44
4.4 Combustion modeling	46
4.4.1 Thickened Flame model	46
4.5 Chemistry description	48
4.5.1 Methane chemistry	49
4.6 The LES code AVBP	50
4.6.1 Numerical methods	50
4.6.2 Artificial viscosity	51
4.6.3 Boundary conditions	51

In turbulent flows, the ratio between characteristic turbulence lengths can be expressed as [Kolmogorov, 1941]:

$$\frac{l_t}{\eta_K} = Re^{3/4} \quad (4.1)$$

This ratio gives the discretization required in each direction to explicitly compute all the scales of the flow. Considering a three dimensional computation, the number of grid points N_{pt} scales as:

$$N_{pt} = \left(Re^{3/4} \right)^3 = Re^{9/4} \quad (4.2)$$

The Reynolds number in aeronautical combustor can go up to $Re \approx 1.0^6$, leading to numerical grid containing $N_{pt} \approx 3.0^{13}$. Taking into account the chemical reactions further stiffen the problem since realistic combustion chemistry involves hundreds of species through thousands of reactions, and the characteristic chemical time scales spread over a very wide range.

4. MODELING OF TURBULENT REACTIVE FLOWS VIA LARGE EDDY SIMULATION

A full resolution of all turbulent scales in complex geometries is still out of reach with current computational resources. In order to reduce the computational cost a modeling effort has to be made, leading to different numerical simulation strategies.

4.1 Numerical simulation approaches: DNS, LES, RANS

Depending on the modeling effort required, different CFD methodologies can be used to solve the compressible reactive Navier-Stokes set of equations:

- **Direct Numerical Simulation (DNS)** is the brute force approach. It consists in explicitly resolving the full instantaneous Navier-Stokes equations from the largest to the smallest turbulent scales. The number of grid points required is of the order of magnitude of $Re^{9/4}$, as mentioned. Even if DNS of full realistic configurations are not yet affordable, academic configurations (moderate Reynolds number) are now investigated by using High Performance Computing (HPC) [see for example [Chen et al., 2009](#)]. DNS is nowadays used mostly to understand physical phenomena in turbulent combustion and helps in building models for LES and RANS approaches.
- **Reynolds Averaged Navier-Stokes (RANS)** simulations solve only the time-averaged values of all Navier-Stokes quantities. The governing RANS equations are obtained by averaging the instantaneous equations. The unclosed terms which appear are solved by means of models, which represent the effect of the entire turbulence spectrum on the mean flow field. This kind of numerical simulation are largely used in industry thanks to their affordable computational cost. However, the largest scales of the turbulent motion strongly depending on the simulated configuration, the RANS closure models often lack universality.
- **Large Eddy Simulation (LES)** introduces a scale separation between the turbulent large scales and the smaller ones. The former are supposed to greatly depend on the geometry and are explicitly calculated while the latter are modeled. Modeling of the small scale is expected to be easier than RANS closure models since the small scale turbulence have a self-similar universal nature (at least far from boundary layers). In LES, a filter scale Δ is introduced to separate the resolved scales and the modeled scales. Similarly to the RANS averaging operator, the filtering operator is applied to the governing equations. Conservation equations are obtained for filtered quantities with unclosed terms that relate to the behavior of the smallest scales which are above the cut-off length scale k_Δ . Compared to RANS, LES main advantage is its intrinsic capability to capture unsteady features. LES has experienced a fast development over the last 20 years and appears to be an excellent candidate to investigate unsteady phenomena in complex configurations.

A summary of this three approaches is shown in Fig. 4.1. By construction, LES tends towards DNS when the cut-off length scale goes to η_K .

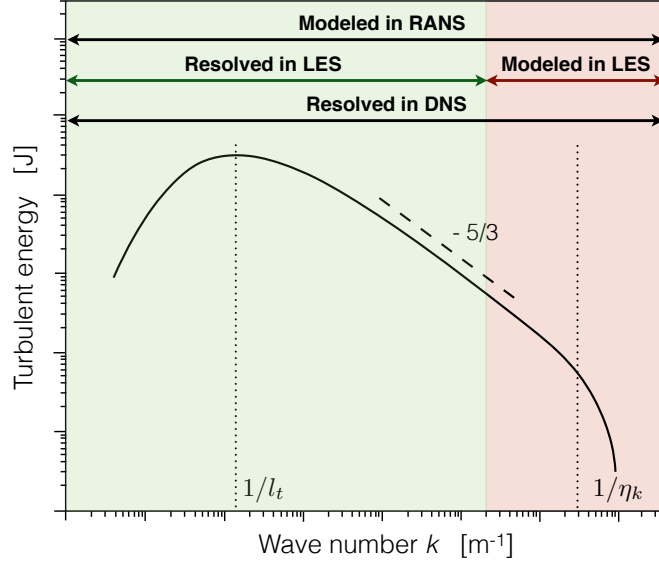


Figure 4.1: Turbulence energy spectrum plotted as function of the wave number k . RANS, LES and DNS are depicted in terms of spatial ranges explicitly resolved and modeled for each computational approach.

4.2 Large Eddy Simulation

The LES approach can be seen as a filtering operation (denoted by $\bar{\cdot}$ in the following). When applied on a general quantity Q , the resulting expression of the filtered quantity \bar{Q} reads

$$\bar{Q}(\mathbf{x}) = \int Q(\mathbf{y}) F_{\Delta}(\mathbf{x} - \mathbf{y}) \, \mathbf{d}\mathbf{y}, \quad (4.3)$$

where F_{Δ} is the filter kernel and Δ is the filter width.

The unresolved or subgrid scale (SGS) contribution is defined by:

$$Q'(\mathbf{x}, t) = Q(\mathbf{x}, t) - \bar{Q}(\mathbf{x}, t) \quad (4.4)$$

For variable density flows, a Favre-filtering operation (weighted by the density) is preferred, and the expression of the Favre-filtered quantity \bar{Q} reads

$$\bar{\rho} \tilde{Q}(\mathbf{x}) = \int \rho Q(\mathbf{y}) F_{\Delta}(\mathbf{x} - \mathbf{y}) \, \mathbf{d}\mathbf{y} = \bar{\rho} \bar{Q}, \quad (4.5)$$

Two classes of LES can be distinguished depending on whether the filtering operation is applied explicitly to the conservation equations, which are subsequently resolved numerically (referred to as "explicit LES") or results from the discretization on an under-resolved grid size (referred to as "implicit LES"). In this work, only implicit LES will be used.

4. MODELING OF TURBULENT REACTIVE FLOWS VIA LARGE EDDY SIMULATION

Applying the filtering operation to Eqs. 2.5-2.8 yields:

$$\frac{\partial \bar{\rho}}{\partial t} + \frac{\partial \bar{\rho} \tilde{u}_i}{\partial x_i} = 0 \quad (4.6)$$

$$\frac{\partial \bar{\rho} \tilde{u}_j}{\partial t} + \frac{\partial \bar{\rho} \tilde{u}_i \tilde{u}_j}{\partial x_i} + \frac{\partial \overline{P \delta_{ij}}}{\partial x_i} = \frac{\partial}{\partial x_i} [\bar{\tau}_{ij} - \bar{\rho}(\widetilde{u_i u_j} - \tilde{u}_i \tilde{u}_j)] \quad \text{for } j = 1, 3 \quad (4.7)$$

$$\frac{\partial \bar{\rho} \tilde{Y}_k}{\partial t} + \frac{\partial \bar{\rho} \tilde{u}_i \tilde{Y}_k}{\partial x_i} = \frac{\partial}{\partial x_i} [\bar{J}_{i,k} - \bar{\rho}(\widetilde{u_i Y_k} - \tilde{u}_i \tilde{Y}_k)] + \bar{\omega}_k \quad \text{for } k = 1, N \quad (4.8)$$

$$\frac{\partial \bar{\rho} \tilde{E}}{\partial t} + \frac{\partial \bar{\rho} \tilde{u}_i \tilde{E}}{\partial x_i} + \frac{\partial \overline{u_i P \delta_{ij}}}{\partial x_i} = \frac{\partial}{\partial x_i} [\bar{q}_i - \bar{\rho}(\widetilde{u_i E} - \tilde{u}_i \tilde{E})] + \tau_{ij} \frac{\partial \overline{u_i}}{\partial x_j} + \bar{\omega}_T + \dot{\bar{Q}}_{sp} \quad (4.9)$$

In Eqs. 4.6-4.9, the Left Hand Side (LHS) contains the filtered inviscid fluxes while viscous and turbulent (or SGS) fluxes as well as source terms appear in the Right Hand Side (RHS).

4.2.1 Filtered viscous fluxes

The filtered viscous fluxes appearing in the LES governing equations are given by:

- **Laminar filtered stress tensor** $\bar{\tau}_{ij}$:

$$\bar{\tau}_{ij} = \overline{2\mu \left(S_{ij} - \frac{1}{3} \delta_{ij} S_{kk} \right)} \quad (4.10)$$

$$\text{approximation: } \bar{\tau}_{ij} \simeq 2\bar{\mu} \left(\tilde{S}_{ij} - \frac{1}{3} \delta_{ij} \tilde{S}_{kk} \right) \quad (4.11)$$

$$\text{with: } \tilde{S}_{ij} = \frac{1}{2} \left(\frac{\partial \tilde{u}_j}{\partial x_i} + \frac{\partial \tilde{u}_i}{\partial x_j} \right) \quad (4.12)$$

$$\text{and: } \bar{\mu} \simeq \mu(\bar{T}) \quad (4.13)$$

- **Diffusive species flux vector** $\bar{J}_{i,k}$:

$$\bar{J}_{i,k} = \overline{-\rho \left(D_k \frac{W_k}{\bar{W}} \frac{\partial X_k}{\partial x_i} - Y_k V_i^c \right)} \quad (4.14)$$

$$\text{approximation: } \bar{J}_{i,k} \simeq -\bar{\rho} \left(\bar{D}_k \frac{W_k}{\bar{W}} \frac{\partial \tilde{X}_k}{\partial x_i} - \tilde{Y}_k \tilde{V}_i^c \right) \quad (4.15)$$

$$\text{with: } \tilde{V}_i^c = \sum_{k=1}^N \bar{D}_k \frac{\partial \tilde{X}_k}{\partial x_i} \quad (4.16)$$

$$\text{and: } \bar{D}_k \simeq \frac{\bar{\mu}}{\bar{\rho} S c_k} \quad (4.17)$$

- **Filtered heat flux \bar{q}_i** :

$$\bar{q}_i = \lambda \frac{\partial T}{\partial x_i} - \overline{\rho \sum_{k=1}^N V_{k,i} Y_k h_{s,k}} \quad (4.18)$$

$$\text{approximation: } \bar{q}_i \simeq \bar{\lambda} \frac{\partial \tilde{T}}{\partial x_i} - \sum_{k=1}^N \bar{J}_{i,k} \tilde{h}_{s,k} \quad (4.19)$$

$$\text{with: } \bar{\lambda} \simeq \frac{\bar{\mu} \overline{C_p}(\tilde{T})}{Pr} \quad (4.20)$$

The species and thermal diffusion fluxes have been approximated using a simple gradient assumption.

4.2.2 Subgrid fluxes closure

The unresolved scales effect on the filtered quantities appearing in Eqs. 4.6-4.9 must be modeled. SGS closures are given by:

- The **unresolved Reynolds tensor** $\bar{\tau}_{ij}^{sgs} = -\bar{\rho}(\widetilde{u_i u_j} - \tilde{u}_i \tilde{u}_j)$, which is generally represented by an eddy-viscosity model, as a diffusive contribution with an associated turbulent viscosity ν_t and similar in form to the laminar contribution:

$$\bar{\tau}_{ij}^{sgs} = 2\bar{\rho}\nu_t \left(\tilde{S}_{ij} - \frac{1}{3}\delta_{ij}\tilde{S}_{kk} \right) \quad (4.21)$$

Various expressions for ν_t have been established (detailed in Sec. 4.3).

- The **unresolved species fluxes** $\bar{J}_{i,k}^{sgs} = -\bar{\rho}(\widetilde{u_i Y_k} - \tilde{u}_i \tilde{Y}_k)$, which are modeled with a diffusive contribution based on a turbulent diffusivity:

$$\bar{J}_{i,k}^{sgs} = -\bar{\rho} \left(D_k^t \frac{W_k}{\bar{W}} \frac{\partial \tilde{X}_k}{\partial x_i} - \tilde{Y}_k \tilde{V}_i^{c,t} \right) \quad (4.22)$$

$$\text{with: } \tilde{V}_i^{c,t} = \sum_{k=1}^N \bar{D}_k^t \frac{\partial \tilde{X}_k}{\partial x_i} \quad (4.23)$$

$$\text{and: } D_k^t = \frac{\mu_t}{\rho S_c^t} \quad (4.24)$$

where S_c^t is the turbulent Schmidt number of species k , equal for all species $S_c^t = S_c^t$. The turbulent Schmidt numbers are imposed by the user and their value is generally $S_c^t \approx 0.7$.

- The **unresolved energy flux** $\bar{q}_i^{sgs} = -\bar{\rho}(\widetilde{u_i E} - \tilde{u}_i \tilde{E})$, which is modeled by means

4. MODELING OF TURBULENT REACTIVE FLOWS VIA LARGE EDDY SIMULATION

of a turbulent thermal conductivity:

$$\bar{q}_i^{sgs} = -\lambda_t \frac{\partial \tilde{T}}{\partial x_i} + \sum_{k=1}^N \bar{J}_{i,k} \tilde{h}_{s,k} \quad (4.25)$$

$$\text{with: } \lambda_t = \frac{\mu_t \bar{C}_p}{Pr^t} \quad (4.26)$$

where Pr^t is the turbulent Prandtl number, also imposed by the user and generally $Pr^t \approx 0.7$

4.3 Turbulent viscosity models

The turbulent viscosity model has the scope of correctly accounting for the interaction between the resolved and the unresolved scales. The subgrid scales are assumed to have a universal behavior. Following the Kolmogorov cascade theory [Kolmogorov, 1941] their contribution is generally represented as purely dissipative. Under this hypothesis the energy is transferred only from the filtered motions to the residual motions, with no backscatter [Pope, 2000]. In complex turbulent flow, energy transfer from small residual scales to the largest scale is also possible through backscatter [Leslie and Quarini, 1979]. The main subgrid models available in AVBP are described below:

- The **Smagorinsky model** was initially proposed by Smagorinsky [1963]. The expression of the turbulent viscosity, based on a mixing-length analogy, reads:

$$\nu_t = (C_S \Delta) \sqrt{2 \tilde{S}_{ij} \tilde{S}_{ij}}, \quad (4.27)$$

where Δ is the characteristic filter width (linked to the cube-root of the cell volume) and C_S is the model constant, with a typical value $C_S = 0.17$ estimated from the Kolmogorov spectrum [Lilly, 1967]. This model is able to correctly predict the decay of turbulence in homogeneous isotropic turbulence. However, the model is non-vanishing in pure shear. It is therefore generally not suitable for wall-bounded flows when using no-slip walls [Sagaut, 2002] and is generally too dissipative [Germano et al., 1991].

- An extension of the Smagorinsky model is the **dynamic Smagorinsky model**. In this approach, the constant C_S is no longer a user-defined constant. Instead, it is evaluated dynamically in the simulation on the basis of the Germano identity, as done in Lilly's procedure [Lilly, 1992] using a test-filter scale.
- The **WALE model** was initially proposed by Ducros et al. [1998]. The turbulent viscosity reads

$$\nu_t = (C_w \Delta)^2 \frac{(s_{ij}^d s_{ij}^d)^{3/2}}{(\tilde{S}_{ij} \tilde{S}_{ij})^{5/2} + (s_{ij}^d s_{ij}^d)^{5/4}}, \quad (4.28)$$

with

$$s_{ij}^d = \frac{1}{2} (\tilde{g}_{ij}^2 + \tilde{g}_{ji}^2) - \frac{1}{3} \tilde{g}_{kk}^2 \delta_{ij}, \quad (4.29)$$

where $C_w = 0.4929$ is the model constant and \tilde{g}_{ij} denotes the resolved velocity gradient. It was developed to obtain correct scaling laws in near wall regions for wall bounded flows.

- The **SIGMA model** was proposed by Nicoud et al. [2011]. The singular values $\sigma_1 \geq \sigma_2 \geq \sigma_3$ of a tensor built using resolved velocity gradients are used to build the turbulent viscosity:

$$\nu_t = (C_\sigma \Delta)^2 \frac{\sigma_3(\sigma_1 - \sigma_2)(\sigma_2 - \sigma_3)}{\sigma_1^2}, \quad (4.30)$$

where $C_\sigma = 1.35$ is the constant of the model. Note that the singular values σ_i have the following near-wall behaviors:

$$\begin{cases} \sigma_1 = O(1) \\ \sigma_2 = O(y) \\ \sigma_3 = O(y^2) \end{cases} \quad (4.31)$$

where y is the normal coordinate to the wall surface and $O(y^p)$ denotes a term of the order of p , i.e. behaving like y^p when the distance to the solid boundary decreases: $y \mapsto 0$. Thus, the SIGMA model behaves correctly in the near-walls region: $\nu_t = O(y^3)$. The SIGMA model has moreover an improved behavior for rotating flows, as detailed below.

A summary of the properties of the different models is presented in Tab. 4.2. In this work, the SIGMA model is preferred in most cases: it has the correct asymptotic behavior for wall-bounded flows, and induces no subgrid viscosity for solid rotation. This last property is important for swirling flows which tend to exhibit large rotational structures. The correct treatment of axi-symmetric expansion might also be important when considering jet flames.

	Smagorinsky	WALE	SIGMA
Correct asymptotic behavior at walls	No	Yes	Yes
No subgrid viscosity for solid rotation	Yes	No	Yes
No subgrid viscosity for pure shear	No	Yes	Yes
No subgrid viscosity for axi-symmetric expansion	No	No	Yes
No subgrid viscosity for isotropic expansion	No	Yes	Yes

Figure 4.2: Comparison of the properties of the different subgrid scale models. Adapted from Nicoud et al. [2011].

4.4 Combustion modeling

The flame front, i.e. the region in which chemical reactions take place, is generally very thin. Considering actual computational resources, the standard mesh size Δ_x which can be used in the flame zone for a LES simulation is generally bigger than the flame thickness δ_L^0 . Considering also that, depending on the configuration and the operating conditions, 5 to 50 points are needed in order to correctly solve the flame structure, subgrid combustion models are clearly necessary. In LES, combustion models have been developed to approximate the filtered species reaction rates $\bar{\omega}_k$ (see Eq. (4.8)) from the resolved quantities. Reviews proposed by [Veynante and Vervisch \[2002\]](#), [Pitsch \[2006\]](#) or the textbook of [Poinsot and Veynante \[2011\]](#) give an overview of the combustion models available, which will not be detailed here.

In this work, for premixed flames, the artificially Thickened Flame (TF) model [[Colin et al., 2000](#); [Légier et al., 2000](#)] has been used and will be presented in subsection 4.4.1. For non-premixed flames, a model based on the work of [Shum-Kivan \[2017\]](#) has been developed and will be detailed in chapter 5.

4.4.1 Thickened Flame model

The fundamental idea behind the Thickened Flame model (TF) is to artificially broaden the flame front to allow its correct resolution on the LES grid. Recalling the asymptotic analysis of chapter. 3.2.1 it can be shown that the laminar flame speed and thickness scale as

$$S_L^0 \propto \sqrt{\dot{\omega} D}, \quad (4.32)$$

$$\delta_L^0 \propto \sqrt{D/\dot{\omega}}. \quad (4.33)$$

where D is the diffusivity and $\dot{\omega}$ the source term. Therefore, if the following transformations are applied to the thermal and species diffusivity and to the species source terms

$$D \rightarrow \mathcal{F}D, \quad (4.34)$$

$$\dot{\omega} \rightarrow \frac{\dot{\omega}}{\mathcal{F}}, \quad (4.35)$$

one obtains

$$S_L^0 \rightarrow S_L^0, \quad (4.36)$$

$$\delta_L^0 \rightarrow \mathcal{F}\delta_L^0 \quad (4.37)$$

The laminar flame speed is conserved and the flame front is thickened. The thickening factor \mathcal{F} is adjusted in order to obtain the grid resolution needed to correctly resolve the flame front. However, thickening the flames alters their interaction with turbulence. In particular, the flame wrinkling is reduced and the time scale ratio between turbulence and chemistry is modified. To compensate these effects, an efficiency function \mathcal{E} is also

introduced

$$D \rightarrow \mathcal{E}FD, \quad (4.38)$$

$$\dot{\omega} \rightarrow \mathcal{E} \frac{\dot{\omega}}{\mathcal{F}}, \quad (4.39)$$

which increases the flame speed without impacting the flame thickness:

$$S_L^0 \rightarrow \mathcal{E}S_L^0 \quad (4.40)$$

$$\delta_L^0 \rightarrow \mathcal{F}\delta_L^0. \quad (4.41)$$

This function, which must compensate the reduction of the flame surface wrinkling, is generally defined as the ratio between the un-thickened flame of thickness δ_L^0 and the thickened flame

$$\mathcal{E} = \frac{\Xi(\delta_L^0)}{\Xi(\mathcal{F}\delta_L^0)}. \quad (4.42)$$

The wrinkling factors involved in this expression are described by an efficiency function [see for example [Colin et al., 2000](#); [Charlette et al., 2002](#)]. In this work, the efficiency function derived by [Charlette et al. \[2002\]](#) is used.

The efficiency function relies on the assumption of equilibrium between turbulence and sub-grid scale flame surface. The evaluation of velocity fluctuations at the filter scale u'_Δ is estimated by an operator based on the rotational of the velocity to remove the dilation contribution [[Colin et al., 2000](#)]. Ξ is then evaluated as follows:

$$\Xi(\delta_L^0) = \left(1 + \min \left[\frac{\Delta_e}{\delta_L^0}, \Gamma \left(\frac{\Delta_e}{\delta_L^0}, \frac{u'_\Delta}{S_L^0}, Re_{\Delta_e} \right) \frac{u'_\Delta}{S_L^0} \right] \right)^\beta \quad (4.43)$$

where $\beta = 0.5$ is the model parameter, Δ_e is the filter size and Re_{Δ_e} is the turbulent Reynolds number at the effective filter size,

$$Re_{\Delta_e} = 4 \frac{\Delta_e}{\delta_L^0} \frac{u'_\Delta}{S_L^0}. \quad (4.44)$$

The artificial thickening is applied in a zone near the flame front which is detected by means of flame sensors [[Légier et al., 2000](#); [Jaravel et al., 2016](#)]. This is done to avoid a modification of diffusivity in all the domain, which will affect mixing. The efficiency function is applied in the same zone as the thickening. As a result the final equations solved using the dynamic thickening approach are:

$$\begin{aligned} \frac{\partial \tilde{\rho} \tilde{Y}_k}{\partial t} + \frac{\partial \tilde{\rho} \tilde{u}_i \tilde{Y}_k}{\partial x_i} &= \frac{\partial}{\partial x_i} \left[\left(\mathcal{E} \mathcal{F} \frac{\bar{\mu}}{Sc_k} + (1 - \mathcal{S}) \frac{\mu_t}{Sc_k^t} \right) \frac{W_k}{\bar{W}} \frac{\partial \tilde{X}_k}{\partial x_i} - \tilde{\rho} \tilde{Y}_k \left(\tilde{V}_i^c + \tilde{V}_i^{c,t} \right) \right] \\ &+ \frac{\mathcal{E} \tilde{\omega}_k}{\mathcal{F}} \quad \text{for } k = 1, N \end{aligned} \quad (4.45)$$

4. MODELING OF TURBULENT REACTIVE FLOWS VIA LARGE EDDY SIMULATION

and

$$\begin{aligned}
 \frac{\partial \rho \tilde{E}}{\partial t} + \frac{\partial \rho \tilde{u}_i \tilde{E}}{\partial x_i} &= - \frac{\overline{\partial u_i P \delta_{ij}}}{\partial x_i} \\
 &+ \frac{\partial}{\partial x_i} \left[\overline{C_p} \left(\mathcal{E} \mathcal{F} \frac{\bar{\mu}}{Pr} + (1 - \mathcal{S}) \frac{\mu_t}{Pr^t} \right) \frac{\partial \tilde{T}}{\partial x_i} \right] \\
 &+ \frac{\partial}{\partial x_i} \left[\sum_{k=1}^N \left(\left(\mathcal{E} \mathcal{F} \frac{\bar{\mu}}{Sc_k} + (1 - \mathcal{S}) \frac{\mu_t}{Sc_k^t} \right) \frac{W_k}{\bar{W}} \frac{\partial \tilde{X}_k}{\partial x_i} - \rho \tilde{Y}_k (\tilde{V}_i^c + \tilde{V}_i^{c,t}) \right) \tilde{h}_{s,k} \right] \\
 &+ \frac{\mathcal{E} \bar{\omega}_T}{\mathcal{F}} + \dot{Q}_{sp}
 \end{aligned} \tag{4.46}$$

with:

$$\tilde{V}_i^c + \tilde{V}_i^{c,t} = \sum_{k=1}^N \left(\mathcal{E} \mathcal{F} \frac{\bar{\mu}}{\rho Sc_k} + (1 - \mathcal{S}) \frac{\mu_t}{\rho Sc_k^t} \right) \frac{W_k}{\bar{W}} \frac{\partial \tilde{X}_k}{\partial x_i} \tag{4.47}$$

The sensor \mathcal{S} is zero outside the flame zones and goes to unity in the flame zone. Equations 4.45 and 4.46 replace Eqs. 4.8 and 4.9 respectively.

4.5 Chemistry description

Due to computational resources, a direct inclusion of detailed chemical mechanisms in LES is not possible. Each species needs an additional transport equations and radicals are usually associated with source terms at high stiffness. This will impose to reduce the time step. To overcome this problem, two different approaches have been developed. **Tabulated chemistry** is the easier approach and lies on the fact that the kinetic scheme variables are linked. The flame structure is tabulated in a look-up table as a function of a limited number of variables, notably temperature and mixture fraction. This approach can be convenient in some cases but it can bring with it two main problems: 1) the size of the table can rapidly increase when the number of parameters increases and 2) the choice of the prototype flame used to create the table is not obvious in complex configurations where the combustion regime is unknown.

Reduced schemes are the result of a simplification of detailed schemes. The aim is to reproduce the chemical behavior of the detailed scheme using as few species and reactions as possible. In this work, reduced schemes are used. Reduced schemes can be classified in two classes:

- Global schemes [Jones and Lindstedt, 1988; Franzelli, 2011] are built to reproduce macroscopic quantities such as the premixed flame speed and the burnt gas state. These mechanisms use optimization techniques to determine the rate coefficients for a given range of operating conditions. Since the number of reaction is low (≤ 4), their implementation in LES codes is easy. All information about intermediate species and flame structure are not available anymore.
- Analytical mechanisms use a quasi-steady-state (QSS) approximation for some species and a partial equilibrium formulation for some reactions. The quasi-steady-state approach can be used when the creation rate of a species is slow

compared to its consumption rate, which means that the species is very quickly consumed after being produced so that its mass can not significantly change. In this case the net rate of the species is considered equal to zero and its concentration is calculated from an analytical formulation instead of its conservation equation, which is not solved. Partial equilibrium hypothesis is valid when both the forward and backward reaction rates of a species are fast compared to all other reactions. Analytical mechanisms have been proposed to include more physical insight in the chemical description. The reduction of a detailed mechanism can be achieved through a two-step procedure, performing first a skeletal reduction to obtain a skeletal mechanism and then a second reduction to reduce the stiffness of the obtained mechanism. The construction of a skeletal mechanism aims at removing redundant species/reactions from the detailed mechanism using for instance Sensitivity Analysis [Tomlin et al., 1992] or Directed Relation Graph (DRG) Analysis [Lu and Law, 2005]. The resulting skeletal scheme is generally still too large and too stiff for LES in complex geometries so that techniques such as the Computational Singular Perturbation (CSP) [Lam and Goussis, 1994] or Intrinsic Low-dimensional Manifold (ILDM) [Maas and Pope, 1992] are used to further reduce the number of species based on their lifetime.

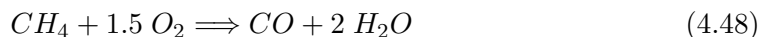
In this work, combustion of methane is studied. The reduced schemes used are detailed below.

4.5.1 Methane chemistry

Two methane mechanisms are used in this work to investigate the premixed methane-air combustion of the PACCI configuration (part III): a global two-step chemistry and an analytically 13 species reduced scheme. The same analytically reduced scheme is used to study high pressure oxi-combustion of methane of the TUM configuration (chapter 5). Global features of this two kinetic scheme are presented here. A comparison between them and with the detailed mechanism GRI 3.0 (Smith et al. [1999], called GRI30 in the following) will be presented for each configuration separately.

4.5.1.a Global scheme: 2S_CH4_BFER

The simplest mechanism used in this study is the the 2S_CH4_BFER (called BFER in the following) two-step mechanism of Franzelli et al. [2012] where the Pre-Exponential Adjustment (PEA) [Légier, 2001] method allows to reproduce the laminar flame speed over a wide range of equivalence ratio. This global scheme involves six species and two reactions given by:



where the oxidation reaction (Eq. (4.48)) is irreversible and the recombination of CO into CO₂ is reversible (Eq. (4.49)). When using a global scheme, the structure of the flame front is completely lost and only the global thermal balance between reaction and diffusion processes is reproduced to recover the flame speed.

4. MODELING OF TURBULENT REACTIVE FLOWS VIA LARGE EDDY SIMULATION

4.5.1.b Analytical scheme: LU13

The analytically reduced mechanism developed by Sankaran et al. [2007] (called LU13 in the following) is used in this study. This analytical mechanism has been derived for air/methane lean premixed combustion through the sequential application of directed relation graph (DRG) [Lu and Law, 2005], sensitivity analysis and computational singular perturbation (CSP) [Lu et al., 2001] over the GRI-1.2 detailed mechanism [Frenklach et al., 1995]. The final skeletal mechanism contains 73 elementary reactions with 17 species, among which CH_2 , $\text{CH}_2(\text{S})$, HCO and CH_2OH are identified as QSS species through CSP. The remaining 13 species are fully resolved, namely, H_2 , H , O , O_2 , OH , H_2O , HO_2 , CH_3 , CH_4 , CO , CO_2 , CH_2O and N_2 . The QSS algebraic relations are solved analytically. Using Analytically Reduced Chemistry (ARC) permits to reproduce in a sufficient accurate way the structure of the flame and to take into account intermediate chemical reactions. This could be important in cases in which for example dissociations or low temperature chemistry occur.

4.6 The LES code AVBP

The AVBP solver is a massively-parallel code for the simulation of compressible reacting flows [Schönfeld and Rudgyard, 1999], developed by CERFACS and IFPEN, that solves the Navier-Stokes equations explicitly on unstructured and hybrid grids. AVBP is based on a "Cell-Vertex" finite volume formulation [Rudgyard, 1993] where the solution variables are stored at the nodes but the flux integration is computed on the cells. The cell residuals (or variations) are then distributed to the nodes in order to obtain the updated solution. Finite element numerical schemes are available [Colin and Rudgyard, 2000]. Over the last decade, AVBP has been optimized to have a good scalability on thousands of processors on various machine architectures, allowing to have a reasonable return time even with large grid sizes.

4.6.1 Numerical methods

A complete review of the numerical schemes implemented in AVBP is presented in the Ph.D. of Lamarque [2007]. The two numerical schemes used in this work are:

- The **Lax-Wendroff (LW) scheme** developed by Lax and Wendroff [1960] is a finite volume centered scheme using an explicit time integration with a single Runge-Kutta step. Its accuracy is of second order in both space and time. Its main advantage stems from the fact that its formulation includes a streamwise stabilization term making it quite robust and a mass lumping operation resulting in a low computational cost. This numerical scheme is used in chapter 5 and 8 and for the initialization of the simulations of chapter 7.
- The **Two step Taylor-Galerkin 'C' (TTGC) scheme** developed by Colin and Rudgyard [2000] is a finite element scheme of the continuous Taylor-Galerkin family [Donea and Huerta, 2003]. Its accuracy is of third order in both space and time. Specifically built for LES, TTGC has good properties regarding dissipation and dispersion. However, these advantages make it less robust than LW and

the explicit mass matrix inversion increases the computational cost (about 2.5 time more expensive than LW). TTGC is used in this work for the numerical simulations of chapter 7, 8 and 9.

4.6.2 Artificial viscosity

The numerical schemes employed in AVBP are spatially centered, and are therefore prone to point-to-point oscillations (also named wiggles) close to regions of steep gradients. A localized artificial viscosity (AV) term is added to the discrete equations in order to limit these spurious oscillations. This is done in practice by the introduction of two artificial viscosity terms:

- A background dissipation term (4^{th} order hyper-viscosity) limits the amplitude of wiggles.
- A 2^{nd} order viscosity term smooths local gradients, and introduces artificial dissipation. To preserve global dissipation properties of the scheme, it is applied only in regions where a sensor is triggered. The sensor employed is similar to shock capturing sensors, it is linear preserving and detects strong deviations of variables from linear behavior.

4.6.3 Boundary conditions

Boundary conditions are a key point in CFD codes and especially in AVBP which aims at simulating compressible reactive flows in confined domains. In particular, two kind of boundary conditions have to be treated with care:

- **Inlets and Outlets**, which influence the acoustic behavior of the computational domain. They are handled in AVBP by means of the Navier-Stokes Characteristic Boundary Condition (NSCBC) developed by Poinso [1991] and extended to multi-species flows by Moureau et al. [2005]. NSCBC boundary conditions are used for every inlet and outlet in the present study.
- **Walls**, in which the boundary layer is in general not solved due to the very high number of grid points this would require. Wall laws are available in AVBP, both with adiabatic or isothermal formalisms. Wall laws have been used in the present study and, in particular, the advanced formulation developed by Cabrit [2009] has been used in chapter 5, where an insight on its characteristics will be presented.

Part II

**Wall heat flux prediction in
rocket combustors**

Chapter 5

LES of a single element GO_x/GCH₄ combustor

Contents

5.1	Combustion and heat transfer in rocket engines	56
5.2	Wall modeling	57
5.2.1	Standard wall law	58
5.2.2	Coupled wall law	59
5.3	Combustion modeling	60
5.4	Paper <i>Int. J. Heat Mass Transfer</i>	61
5.5	Additional material	80
5.5.1	Effect of the mesh	80
5.5.2	Possible causes for the heat flux underestimation	82
5.6	Few words about CPU time	86

In this chapter wall heat flux prediction in rocket combustors is studied.

Large Eddy Simulation is used to investigate flow and combustion in a single element GO_x/GCH₄ sub-scale combustor. The aim is to predict wall heat fluxes and establish a simulation methodology, as well as needs to correctly simulate this kind of configuration. The experimental facility has been provided by the Technische Universität München in the context of the Transregio SFB TRR40 about "Technological Foundations for the Design of Thermally and Mechanically Highly Loaded Components of Future Space Transportation Systems".

A brief introduction about heat transfer in rocket engines is presented in section 5.1, then an insight in wall and combustion models used in the LES is shown in sections 5.2 and 5.3. The entire study is presented in section 5.4. Additional material is provided in section 5.5. It has been written in the form of a journal paper for publication.

5.1 Combustion and heat transfer in rocket engines

Combustion in rocket engines takes place at very high temperature and pressure in order to provide the conditions necessary to generate the desired thrust. High pressure combustion leads to very thin flames in an highly turbulent environment. The flames strongly interact with the flow, which wrinkles and stretches them leading also sometimes to local extinction. Moreover, the very high temperature reached (≈ 3500 K) produce high thermal loads on the combustor walls, which have to be correctly designed from a thermal point of view.

The combustion conditions just mentioned are very complicate to reproduce in experimental facilities. It is thus difficult to study the basic physical phenomena behind them with the aim of increasing the system performances and ensuring their mechanical integrity. In Europe, very few experimental facilities are able to reproduce the rocket engines combustion environment. The MASCOTTE bench operated by ONERA in France is dedicated to cryogenic rocket combustion, both at super-critical and sub-critical conditions. Many studies have been performed, mainly using H₂/O₂ as propellant [Brummund et al., 1996; Snyder et al., 1997; Herding et al., 1998; Candel et al., 1998; Tripathi et al., 1999; Juniper et al., 2000; Candel et al., 2006; Singla et al., 2006; Habiballah et al., 2006, among others]. The bench has been then adapted to the study of CH₄/O₂ combustion [Singla et al., 2005, 2007]. In Germany, an experimental facility at DLR Lampoldshausen permits experimental studies on cryogenic propulsion, both using hydrogen or methane as a fuel [Brummund et al., 1996; Mayer and Tamura, 1996; Oschwald et al., 1997; Haidn et al., 1998; Mayer et al., 2001; Gurliat et al., 2003; Cuoco et al., 2004; De Rosa et al., 2006; Yang et al., 2007; Arnold et al., 2009; Lux and Haidn, 2009; Hardi et al., 2014a,b; Gröning et al., 2016, 2017, among others]. Recently the Technische Universität München has made a huge effort in studying CH₄/O₂ combustion for space propulsion application, providing several test cases [Celano et al., 2013, 2014, 2015; Silvestri et al., 2014, 2015, 2016a,b, 2017; Winter et al., 2017; Perakis et al., 2017].

Running experimental facilities, especially at these extreme conditions, is very expensive. For this reason, numerical simulation has appeared as a promising approach for the understanding of the rocket combustion physics and has the aim of becoming a key design tool in industry.

Most numerical studies have been realized using RANS, thanks to its low computational cost. RANS is already massively used in industry for the dimensioning of rocket combustors but it has major limitations. Being indeed the whole turbulence spectrum modeled in this kind of approach, the prediction capability can be limited, especially in application strongly turbulent and with complex unsteadinesses at various scales. For this reason, and thanks to the increase in computational resources, LES has arisen in the last period. LES has already been successfully applied to rocket combustion [Oefelein, 2005; Matsuyama et al., 2006; Schmitt, 2009; Masquelet et al., 2009; Schmitt et al., 2011; Ruiz, 2012; Rocchi, 2014; Mari, 2015; Müller et al., 2015; Hakim et al., 2015; Urbano et al., 2016; Tudisco et al., 2016; Zips et al., 2017; Schmitt et al., 2017; Potier, 2018].

Regarding heat transfer at walls, this requires good accuracy in predicting energy transfers. The life of the engine is indeed really sensitive to the maximum temperature reached in the walls and the cooling system has to be correctly designed. Wall resolved RANS simulation has already proven its capability to retrieve measured heat fluxes (for example in one of the MASCOTTE experimental operating points [Dorey et al., 2014]). When using LES, performing a wall resolved simulation is not possible because of the high CPU cost it brings [Chapman, 1979; Piomelli, 2008]. Wall modeling is necessary in this case to reduce the computational cost. Classical wall laws can however be not fully satisfactory [Masquelet et al., 2009; Potier, 2018] and improved approaches [Cabrit, 2009] have to be used (section 5.2).

The wall flow is very important in rocket engines and the right behavior of the wall law in predicting the wall shear stress τ_w and the wall heat flux q_w is mandatory in order to retrieve the right chamber pressure and engine performances. Moreover, the wall heat transfer is a key point in designing the chamber walls cooling. When talking about wall-modeled approaches, two different categories can be distinguished. The first approach consists in running hybrid RANS/LES simulations, in which the boundary flow is solved using a RANS approach and the main flow using a LES one. This approach will not be detailed here and the reader is referred to, for example, Piomelli [2008]; Mockett et al. [2012]. The second approach is the so-called wall-modeled LES approach, in which LES is used everywhere and adapted boundary conditions are implemented in order to compensate the unresolved boundary layer [Larsson et al., 2016; Bose and Park, 2018]. In wall-modeled LES the wrong gradients predicted due to the unresolved boundary layers are reconstructed by means of a model, which permits to retrieve the correct wall shear stress and wall fluxes. This is generally done by separating the boundary layer in two sub-layers: an inertial turbulent layer and a viscous layer where molecular diffusion dominates over turbulent diffusion [Pope, 2000]. The wall shear stress is in this way algebraically linked to the flow velocity at some distance of the wall. The law-of-the-wall approach has been adopted in this work and will be described in section 5.2

5.2 Wall modeling

The classical approach in modeling turbulent boundary layers is to use so-called wall laws, in order to have a correct estimation of the gradients at walls (Fig. 5.1, right). The turbulent boundary layer is generally divided into the fully turbulent external zone and the internal zone (Fig. 5.1, left).

The internal zone is the one in which molecular and turbulent diffusion phenomena compete. In this zone we can define characteristic flow scales: the friction velocity $u_\tau = \sqrt{\tau_w/\rho_w}$ and the friction distance $y_\tau = \nu_w/u_\tau$, where τ_w is the wall shear stress and ρ_w and ν_w are respectively the density and the kinematic viscosity evaluated at the wall. Wall units are generally introduced: $u^+ = u/u_\tau$ and $y^+ = y/y_\tau$. The thermal boundary layer can be treated in a similar way, introducing the friction temperature $T_\tau = q_w/(\rho_w C_{p,w} u_\tau)$ and obtaining $T^+ = (T_w - T)/T_\tau$. Here q_w denotes the wall heat flux and $C_{p,w}$ the heat capacity evaluated at the wall.

5. LES OF A SINGLE ELEMENT GOX/GCH₄ COMBUSTOR

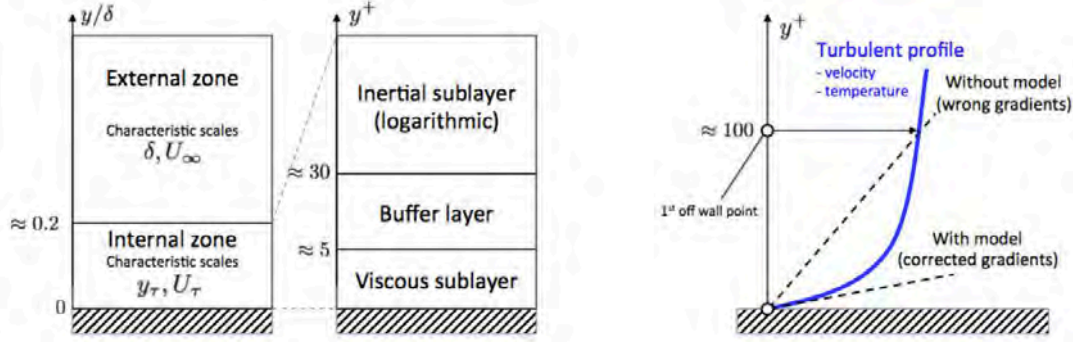


Figure 5.1: Left: schematic of the turbulent boundary layer in different zones [Cabrit, 2009]. Right: schematic of the wall gradient estimation [Potier, 2018]

The internal zone can be further divided into three sub-layers (Fig. 5.1, left):

- The viscous sublayer ($y^+ < 5$), where diffusion phenomena are essentially laminar and dominated by molecular diffusion.
- The inertial (or logarithmic) sublayer ($y^+ > 30$), where turbulent diffusion dominates over molecular diffusion.
- The buffer sublayer ($5 < y^+ < 30$), which is the intermediate zone between inertial and viscous sub-layers. Here the molecular and turbulent diffusion are of the same order.

5.2.1 Standard wall law

The standard wall law derivation [see for example Kays et al., 2004] can be done considering a fully developed turbulent boundary layer over an infinite flat plate. The problem is considered as statistically steady and one-dimensional. The derivation is detailed in Cabrit [2009] and will not be presented here.

Integrating separately for the viscous and the inertial sub-layers, the standard wall law equation can be written. For the viscous sublayer, it writes:

$$u^+ = y^+ \quad (5.1)$$

for velocity and

$$T^+ = Pr y^+ \quad (5.2)$$

for temperature. Both laws are linear laws.

For the inertial sublayer it writes:

$$u^+ = \frac{1}{\kappa} \ln(y^+) + C \quad (5.3)$$

for velocity and

$$T^+ = \frac{Pr_t}{\kappa} \ln(y^+) + C_T(Pr) \quad (5.4)$$

for temperature. Both laws are logarithmic laws, where $\kappa = 0.41$ is the Von Karman constant, $C = 0.55$ and the integration constant C_T depends on the Prandtl number. Based on an experimental database going from $Pr = 6.0 \times 10^{-3}$ to $Pr = 40 \times 10^3$ the correlation reads:

$$C_T(Pr) = (3.85Pr^{1/3} - 1.3)^2 + 2.12\ln(Pr) \quad (5.5)$$

where the value 2.12 has been obtained considering $Pr_t = 0.85$.

In AVBP the switch between the linear and logarithmic laws is done at a critical value $y_c^+ = 11.445$.

5.2.2 Coupled wall law

[Cabrit \[2009\]](#) has demonstrated by means of wall-resolved LES how rocket engine boundary flows do not respect the assumption made to derive standard wall laws. In particular, when the ratio between the gas temperature and the wall temperature is high ($T_g/T_w > 3$), it is mandatory to account for the temperature and density gradients in the boundary layer. He derived during his work a so-called "coupled" wall-law. The wall law used during this work is the one developed by [Cabrit \[2009\]](#) when not accounting for chemistry in the boundary layer. In the coupled wall law the velocity and temperature write:

$$y^+ < y_c^+ : u^+ = y^+ ; \quad (5.6)$$

$$T^+ = y^+ \quad (5.7)$$

$$y^+ > y_c^+ : \frac{2}{Pr_t B_q} \left(\sqrt{1 - KB_q} - \sqrt{T^+} \right) = \frac{1}{\kappa} \ln y^+ + C_{vd} ; \quad (5.8)$$

$$T^+ = (Pr y^+) e^\Gamma + (Pr_t u^+ + K) e^{1/\Gamma} \quad (5.9)$$

with

$$\Gamma = \frac{10^{-2}(Pr y^+)^4}{1 + 5Pr^3 y^+} \quad (5.10)$$

$B_q = T_\tau/T_w$ is the isothermal parameter, $C_{vd} = 5.5$ is the Van Driest constant and K writes:

$$K = \beta(Pr) - Pr_t C_{vd} \left(\frac{Pr_t}{\kappa} - 2.12 \right) (1 - 2\ln(20)) \quad (5.11)$$

with

$$\beta(Pr) = (3.85Pr^{1/3} - 1.3)^2 + 2.12\ln Pr \quad (5.12)$$

Using a Van Wijngaarden-Dekker-Brent [[Press et al., 1986](#)] resolution algorithm, the quantities of interest τ_w and q_w are retrieved. The coupled wall law tends to the standard one when the ratio T_g/T_w tends to 1.

The work of [Cabrit \[2009\]](#), which took as the highest ratio $T_g/T_w = 3$, has been extended by [Potier \[2018\]](#). He added a case at temperature ratio of $T_g/T_w = 5$, showing how the error when using a classical wall law is even higher in this case.

5. LES OF A SINGLE ELEMENT GOX/GCH₄ COMBUSTOR

It will be shown in section 5.4 how the temperature ratio in the configuration studied can reach $T_g/T_w > 5$: the use of the coupled model of the wall law is mandatory in order to have a good estimation of the wall quantities. Tests performed with the standard law-of-the-wall confirmed that the error committed would be unacceptable.

5.3 Combustion modeling

Similarly to the premixed flames, the principal effect of turbulence on the diffusion flames is of wrinkling them. Wrinkling increases the fame surface and consequently the total heat release rate. Moreover, turbulence has additional effects on the flame structure by acting on the strain rate. In LES, where turbulence is not resolved in its whole spectrum, it is necessary to use a turbulent combustion model in order to determine the correct heat release rate. Different models exist in literature, mostly based on the flamelet hypothesis, which is valid for high Damköhler numbers. This hypothesis permits to decouple the inner flame structure, which can be considered as the one of a laminar diffusion flame at a fixed strain rate, and the transport of the turbulence-deformed flame. Turbulent combustion models have the aim of coupling these two problems. The most used methodologies are based on Probability Density Function (PDF) models or flame surface models. A review of turbulent combustion models for diffusion flames can be found for example in Peters [2000].

Another approach, which aims to define for diffusion flames an *a priori* model similar to the one used for premixed flames (section 4.4.1), has been recently proposed by Shum-Kivan [2017]. It is based on the fact that, similarly to the premixed flames where the aim is to retrieve the correct turbulent flame speed, the model has to retrieve the correct heat release rate of the diffusion flame. It is indeed the heat release rate which controls the turbulent diffusion flame position and length.

The thickness of the diffusion flame is proportional to the inverse of the mixing fraction gradient, itself proportional to the square root of the velocity gradient. This means that, in the case of an LES simulation, this thickness will depend on the value of the velocity gradients solved on the mesh. The simulated flame fits thus to the resolved flow, which is a significant difference with the premixed flame which has its own thickness. For this reason, it is not necessary to thicken artificially the diffusion flame for issues of numerical stability. However, if the calculation of the flame is numerically possible, the heat release rate is not necessarily estimated correctly. The goal of the model is therefore to recover the exact heat release rate, which could be obtained for example from a DNS of the flame. Shum-Kivan [2017] found that the difference between the heat release rate obtained in LES and DNS comes on one hand from the resolved scalar dissipation rate, usually lower than the exact scalar dissipation rate and secondly from the wrinkling defect associated with the modification of the Damköhler number of the resolved flame, induced by the coarser mesh. Both effects lead to an underestimation of the heat release rate. On the contrary, the mesh under-resolution acts like a numerical diffusion, causing an increase of the thermal thickness of the flame and an over-estimation of the global heat release. Finally, the loss in sub-grid scale strain rate and wrinkling have an opposite effect on the numerical diffusion. All these effects can be reflected in a

modified diffusivity D_{TCI} in the flame zone :

$$D_{TCI} = F_{num} \cdot F_{\Pi} \cdot F_{\Lambda} \cdot D \quad (5.13)$$

where $F_{num} < 1$ represents the effect of numerical diffusion, $F_{\Pi} > 1$ represents the loss in flame wrinkling and $F_{\Lambda} > 1$ represents the loss in strain rate. Contrarily to a premixed flame, where the factor F is strictly > 1 (using a thickened flame model for example [Légier et al., 2000]), $F_{tot} = F_{num} \cdot F_{\Pi} \cdot F_{\Lambda}$ can be greater or lower than one for a diffusion flame.

In a turbulent diffusion flame, as in premixed flames, a modification of D in the whole domain would modify the mixing of reactants and products and must be avoided. The modification of D is therefore applied locally in the flame zone by means of a flame sensor. The flame sensor used in this work is the one developed by Shum-Kivan [2017]. It is based on the stoichiometric mixture fraction z_{st} and reads:

$$\theta = \min(A \times \exp(-B \times (z - z_{st})^2), 1) \quad (5.14)$$

where A and B are constants which control the steepness and width of the sensor and have been arbitrarily fixed to 4 and 2000, respectively. Finally the diffusivity is modified as follows:

$$D^* = \theta D_{TCI} + (1 - \theta)(D + D_t) \quad (5.15)$$

with D_t the turbulent diffusivity introduced by the sub-grid scale model. Note that, as for premixed flames, the diffusivity introduced by the sub-grid scale model is deactivated in the flame zone. Note that, contrarily to premixed flames, the chemical source term is not modified by F_{tot} . This is the consequence of high Da combustion, leading to a diffusion-controlled flame.

In the work of Shum-Kivan [2017], the thickening factor setting from an LES has not been done. The setting was always done by comparison with DNS.

During this work, the model developed by Shum-Kivan [2017] is used. A first approach to determine the thickening factor when DNS are not available is proposed.

5.4 Paper *Int. J. Heat Mass Transfer*

In this section the paper prepared for publication in the *International Journal of Heat and Mass Transfer* is reported. It presents a LES of a single element GOx/GCH₄ sub-scale combustor. The aim of this work is of reproducing the flow and flame which develop and quantitatively evaluate the pressure and wall heat flux evolution along the combustion chamber. Key parameters for LES of this kind of configuration are highlighted.

The test case, as well as the experimental results have been provided by the team of Prof. Haidn at the Technische Universität München, where we participated to the 2015 SFB/TRR 40 Summer Program. A "blind test" was performed by different groups, showing a significant spread in results, compared to the test data [Roth et al., 2015; Maestro et al., 2015]. Updated results have been presented by Roth et al. [2016], Maestro et al. [2016] and Müller et al. [2016]. Recent results by Maestro et al. [2017] showed also early results in terms of LES needs to compute this kind of configuration.

Large Eddy Simulation of combustion and heat transfer in a single element GCH₄/GOx rocket combustor

Dario Maestro^a, Bénédicte Cuenot^a, Laurent Selle^b

^aCERFACS, CFD Team, 42 Av. Gaspard Coriolis, 31057 Toulouse, France

^bIMFT, 2 Allée du Professeur Camille Soula, 31400 Toulouse, France

Abstract

The single element GCH₄/GOx rocket combustion chamber developed at the Technische Universität München has been computed using Large Eddy Simulation. The aim of this work is to analyze the flow and combustion features at high pressure, with a particular focus on the prediction of wall heat flux, a key point for the development of reusable engines. The impact of the flow and flame, as well as of the model used, on thermal loads is investigated. Longitudinal distribution of wall heat flux, as well as chamber pressure, have been plotted against experimental data, showing a good agreement. The link between the heat released by the flame, the heat losses and the chamber pressure has been explained by performing an energetic balance of the combustion chamber. A thermally chained numerical simulation of the combustor structure has been used to validate the hypothesis used in the LES.

Keywords: Large-eddy simulation, GCH₄/GOx combustion, Wall heat transfer, Rocket propulsion

1. Introduction

Cost effectiveness has become nowadays a major design constraint for rocket engines. This is due to a shift in the market of access to space from government agencies to private companies, which claim to reduce the cost per kilogram in orbit by at least one order of magnitude. Such an ambitious goal requires a technological breakthrough of the propulsion system, which has to be operated at low cost and be reusable. A major path of evolution for rocket engines has been found to be the substitution of liquid hydrogen by hydrocarbons as fuel. The propellant combination liquid oxygen-liquid hydrogen (LOx/LH₂) has been used for a long time and is commonly used today to propel among others the European launcher Ariane 5. This is thanks to the very high specific impulse of hydrogen, which has however drawbacks in terms of cost of production and handling. Its low density requires large storage tanks, which have moreover to be kept at a very low temperature to maintain the propellant in a liquid state (around 20 K). In addition, hydrogen requires the use of Helium, an expensive and scarce fossil gas, to drain and pressurize.

Among others hydrocarbons, methane characteristics are particularly promising. It offers high specific impulse (compared to kerosene for instance [1]), high density at common tank pressures (around 6 times the density of hydrogen), low pollution and low cost both for production and handling [2]. With the objective of reusable engines, the fuel cooling properties have also become one of the key parameters for the selection of hydrocarbon fuels. Thanks to its high thermal conductivity, specific heat and low viscosity, the heat transfer performance of methane is higher

compared to other hydrocarbon fuels. Moreover, in cooling systems, the maximum temperature allowed for coolant-side wall is commonly limited by the cocking temperature of the fuel: the typical value for methane is 970 K, higher than propane (700 K) and kerosene (590 K) [3].

Compared to H₂/O₂ combustion, which has been extensively studied, there is a lack of knowledge of CH₄/O₂ combustion at high pressure. Flame and flow behavior, including flame stabilization, temperature stratification as well as gas composition near walls are however key phenomena for a best engine operation. In particular, controlling the wall temperature during operation is a mandatory step to reach the objective of reusable engines. Indeed, life cycle of rocket engines strongly depends on the wall temperature: a difference of 40 K may lead to a life reduction of 50 % of a cryogenic propellant rocket chamber [4]. Thermal loads on the walls, including their unsteady behavior, are consequently required for the design of combustion chambers. In view of the complexity and cost of experiments, numerical simulations are essential to understand the physical phenomena and predict thermal stresses on the chamber walls.

Although different groups performed experimental investigations [5, 6], few data are available for combustion of gaseous oxygen and gaseous methane at relevant chamber conditions. In order to provide experimental data specifically suited for numerical simulations, a test campaign has been conducted at the Technische Universität München. In the context of the national research program Transregio SFB/TR-40 on "Technological Foundation for the design of thermally and mechanically high loaded components of

Future Space Transportation System” a new combustor rig has been developed and tested. Experimental data has been provided by Celano et al. [7]. The test case has been firstly simulated during the 2015 SFB/TRR 40 Summer Program. A ”blind test” was performed by different groups, showing a significant spread in results, compared to the test data [8, 9]. Updated results have been presented by Roth et al. [10], Maestro et al. [11] and Müller et al. [12].

Recent results by Maestro et al. [13] showed how the prediction of wall heat flux in a rocket chamber type configuration requires both correct modeling of the flow and flame, including the chemical flame structure, the gas composition and the temperature gradient at walls.

In this paper a full 3D Large Eddy Simulation (LES) of the experimental setup is presented. The objective is twofold: (i) investigate the capability of LES to retrieve correct estimations of wall heat flux and chamber pressure evolution and (ii) analyze the flow and flame and their impact on thermal loads. To assess the robustness and reliability of the LES, the impact of the chosen models and parameters is carefully analyzed.

The paper is structured as follows: first, the experimental setup is presented in section 2, then simulation strategy and numerical setup are described in section 3. Flow and flame structures are analyzed in section 4, where quantitative comparisons with measurements are shown. A chained heat conduction simulation of the solid structure is performed in section 5, in order to cross-validate the heat flux estimations. Finally, conclusions and future works are summarized in section 6.

2. Experimental configuration

The configuration (Fig. 1) consists of a 290 mm-long

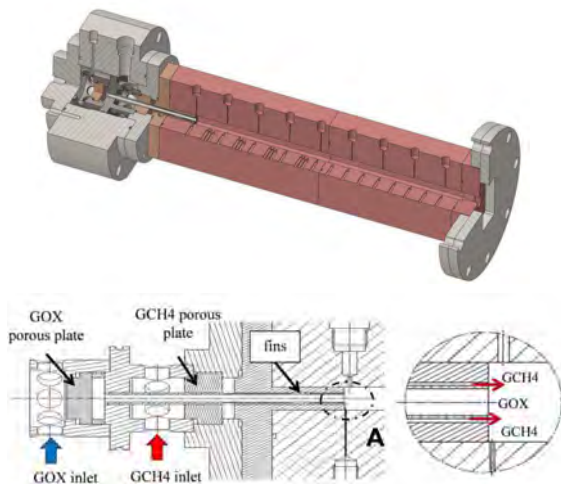


Figure 1: Single-injector combustion chamber and detail of the injector [14].

combustion chamber fed by a single shear coaxial injector, operating at a nominal pressure of 20 bar. The injector is mounted on an oxygen-free copper combustion chamber with a square cross section (12×12 mm) and a nozzle at the exit. The nozzle features a contraction ratio of 2.5, leading to a Mach number in the chamber of 0.24. Combustion chamber and injector characteristics are summarized in Tab. 1.

Table 1: Characteristic combustion chamber and injector dimensions.

Combustion chamber		
Chamber length	[mm]	290
Chamber width	[mm]	12
Chamber height	[mm]	12
Throat height	[mm]	4.8
Contraction ratio A_{cc}/A_{th}	[-]	2.5
Injector		
GOx diameter	[mm]	4
GOx post wall thickness	[mm]	0.5
GOx post recess	[mm]	0
GCH ₄ outer diameter	[mm]	6
Injector area ratio A_{GCH_4}/A_{GO_x}	[-]	0.7

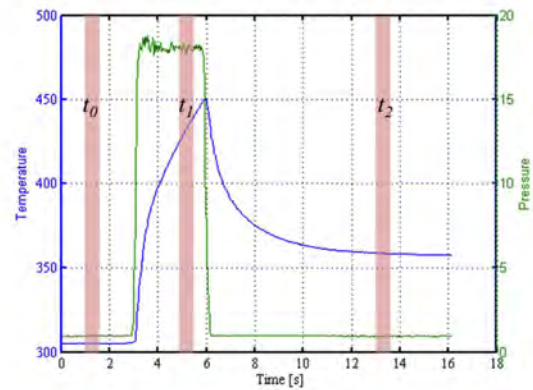


Figure 2: Typical chamber pressure and thermocouple temperature evolution during a hot run. Reproduced from [14] with permission from M. Celano.

The injector is mounted with no recess on the faceplate providing, thanks to the coaxial configuration, a central core of gaseous oxygen surrounded by high speed gaseous methane. Two porous plates are placed in the oxidizer and fuel manifolds to ensure homogeneous injection conditions in terms of temperature and pressure. The inlet mass flow rates of $\dot{m}_{CH_4} = 0.0017$ kg/s and $\dot{m}_{O_2} = 0.0045$ kg/s, are imposed using sonic orifices. This leads to a global oxidizer/fuel ratio $O/F = 2.6$. The injection temperatures of oxygen and methane are of 278 K and 269 K respectively.

The combustion chamber is equipped with pressure transducers, equally spaced on the side wall in order to extract the static pressure distribution $P(x)$ along the cham-

5. LES OF A SINGLE ELEMENT GOX/GCH₄ COMBUSTOR

ber axis. This permits a better understanding of the heat release rate distribution and of the complex heat transport processes. Thermocouples have been used in order to quantify the temperature field in the chamber structure. The recorded data have been post-processed in order to reconstruct the wall heat flux evolution along the chamber walls solving the inverse heat conduction problem [15]. Detailed information about the experimental measurement setup can be found in Celano et al. [14, 7, 15]. The chamber is capacitively cooled and therefore the wall chamber temperature increases during the burning experimental time, which is of 3 s. The measured wall temperature in the chamber is averaged over an evaluation time of 0.5 s, centered at 2/3 of the burning time (t_1 in Fig. 2).

3. Simulation setup

3.1. Geometry - Computational domain and mesh characteristics

The computational domain is the full three-dimensional chamber. It starts 1 mm before the faceplate, so that only a small part of the injector is calculated, and extends to the nozzle exit, so that the full nozzle is simulated. The domain is discretized with a hybrid tetrahedral-prisms unstructured mesh of about 200×10^6 cells. The flame zone refinement has been treated with a particular attention, especially in the post-tip zone, which has been discretized with 20 cells (characteristic mesh size $\Delta_0 = 25 \mu\text{m}$). Ten prisms layers have been used to discretize the chamber walls region, leading to an average y^+ value of about 40. A schematic view of the mesh in the near injector region is presented in Fig. 3.

3.2. Chemical kinetics

The LES is run with the analytically reduced mechanism developed by Sankaran et al [16] and called here the LU13 mechanism. Analytical mechanisms use a partial equilibrium formulation for some reactions and a quasi-steady-state (QSS) approximation for some species. The QSS approach can be used when the consumption rate of a species is fast compared to its creation rate. This means that the species is very quickly consumed after being produced so that its mass can not significantly change. In this case the net rate of the species is considered equal to zero, its conservation equation is not solved and its concentration is calculated from an analytical formulation instead. The LU13 mechanism has been derived by Sankaran et al. [16] for air/methane lean premixed combustion using directed relation graph (DRG) [17], sensitivity analysis and computational singular perturbation (CSP) [18] over the GRI-1.2 detailed mechanism [19]. The final skeletal mechanism contains 73 elementary reactions with 17 species. CH₂, CH₂(S), HCO and CH₂OH are identified as QSS species through CSP and their algebraic relations are solved analytically. The remaining 13 species are fully resolved, namely, H₂, H, O, O₂, OH, H₂O, HO₂, CH₃, CH₄, CO, CO₂, CH₂O and N₂.

Mari et al. [20] pointed out that oxy-combustion of methane is very sensitive to the number of species used in the reduced mechanism and that, if they are not sufficient, the equilibrium state of the burnt gases is not correctly retrieved. The kinetic scheme has therefore been validated first on equilibrium calculations and then on 1D premixed and strained counterflow diffusion flames, using representative strain rate values. This has been done using the CANTERA [21] software and a detailed analysis can be found in Maestro et al. [11].

Under experimental conditions, the equilibrium temperature is 3290 K and the burnt gases composition (Tab. 2) is dominated by H₂O and CO, which prevails over CO₂. It is also visible that a small quantity of O₂ is still present in the reaction products, while CH₄ is completely consumed. The LU13 analytically reduced mechanism recovers very well the correct burnt gases state. The relative error is lower than 0.01% for the temperature and species mass fractions (Tab. 2). For a further validation of the ki-

Table 2: Equilibrium values: comparison between detailed (GRI30) and reduced (LU13) mechanisms.

	GRI30	LU13 [16]
Temperature [K]	3289.11	3289.14
O ₂ mass fraction [-]	5.242e-3	5.243e-3
CH ₄ mass fraction [-]	4.328e-10	4.328e-10
CO ₂ mass fraction [-]	1.663e-1	1.663e-1
CO mass fraction [-]	3.713e-1	3.713e-1
HO ₂ mass fraction [-]	2.196e-5	2.196e-5
H ₂ O mass fraction [-]	4.037e-1	4.037e-1

netic scheme, 1D premixed flames have been computed to check the value of flame speed and flame thickness. From detailed chemistry calculations, using the experimental temperature and pressure and considering a stoichiometric mixture, these have been found to be 1.4 m/s and 1.7×10^{-5} m, respectively. The flame speed is slightly under-predicted by the reduced mechanism, with a relative error of 15 %. The agreement on the flame thickness is excellent, with a relative error of 3 % for the reduced mechanism.

The behavior of the reduced scheme is also evaluated in the configuration of a strained counter-flow diffusion flame, in order to represent the environment in which the flame develops in the combustion chamber. To vary the strain rate applied to the flame, a series of calculations have been made with different values for the fuel and oxidizer streams velocity. Starting from a very low value, the strain rate is increased up to the value at which extinction occurs. Evolutions of the maximum temperature and maximum heat release rate versus strain rate are plotted in Fig. 4 for the detailed and reduced mechanisms. As expected from theory, an increase in strain rate causes a decrease in maximum temperature, as the result of faster diffusion. Conversely, the maximum heat release rate increases with increasing strain rate, until extinction sud-

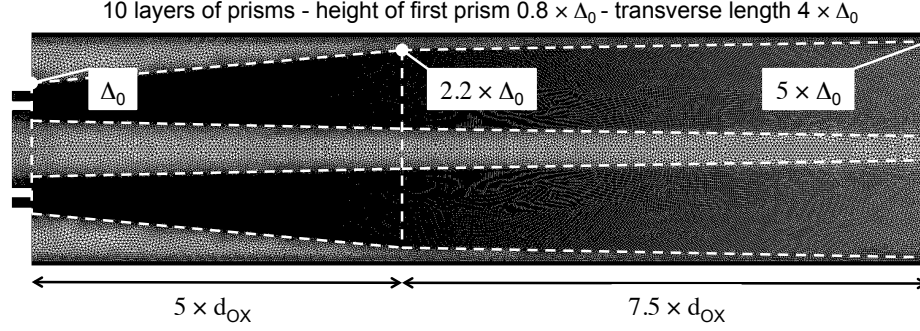


Figure 3: Longitudinal cut through the mesh near the injector.

denly occurs. For both quantities, the LU13 mechanism gives results very close to the detailed mechanism. The extinction strain rate value is slightly different, with the LU13 mechanism which underestimates it; however, as it will be detailed in the following, the maximum values of resolved strain rate found in the numerical simulations are always lower than $1.2 \times 10^5 \text{ s}^{-1}$, values for which the error of the LU13 mechanism stays very low.

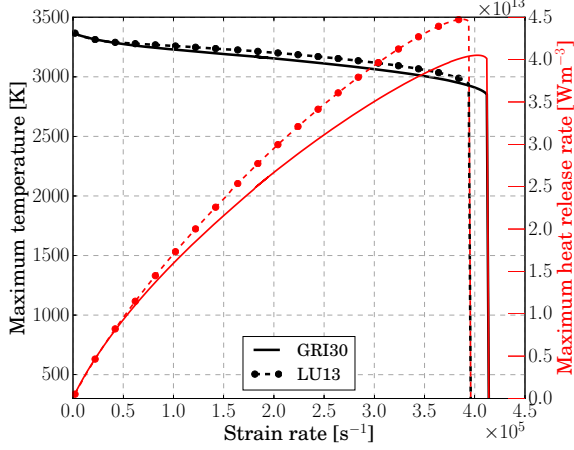
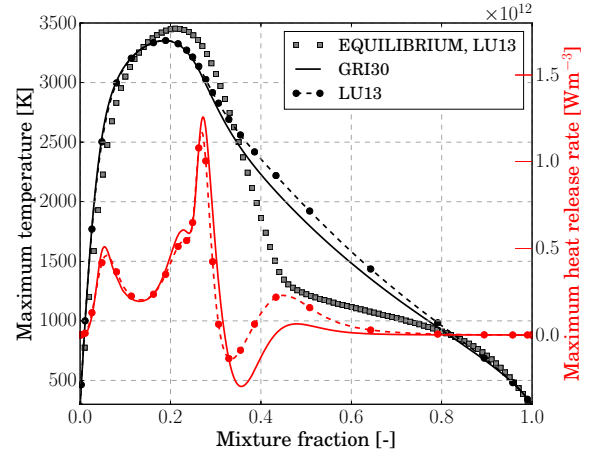


Figure 4: Strained diffusion flames: evolution with strain rate of maximum temperature (black) and maximum heat release rate (red). Comparison between detailed (GRI30) and reduced (LU13) mechanisms.

The diffusion flame structures obtained with the two chemical schemes are then compared in the mixture fraction space at a representative strain rate value, $a = 5000 \text{ s}^{-1}$, in Fig. 5. To evaluate this value, scalar dissipation rate along the stoichiometric surface $\chi_{st} = 2D(\partial z/\partial x_i)_{st}^2$, with z the mixture fraction calculated according to Bilger's [22] definition and D the diffusion coefficient, has been extracted from the simulation in a representative area of the flow (see Sec. 4.2). Reminding that:

$$\chi_{st} = \frac{a}{\pi} \exp(-2[\text{erf}^{-1}(1 - 2z_{st})]^2) \quad (1)$$


 Figure 5: Strained diffusion flame at $a = 5000 \text{ s}^{-1}$: profile of temperature (black) and heat release rate (red). Comparison between detailed (GRI30) and reduced (LU13) mechanisms.

where a is the strain rate, and erf is the error function defined as:

$$\text{erf}(\eta) = \frac{2}{\sqrt{\pi}} \int_0^\eta e^{-x^2} dx \quad (2)$$

one can retrieve the strain rate values in the numerical simulations. A probability distribution function has been extracted in this area and results are presented in Fig. 6: the peak of probability is at a strain rate value of about 5000 s^{-1} , while the maximum value encountered is of about $1.2 \times 10^5 \text{ s}^{-1}$.

The temperature and heat release rate profiles shown in Fig. 5 are well reproduced by the LU13 mechanism in comparison to GRI30. The temperature profile peaks near the stoichiometric value $z_{st} = 0.2$, where it exhibits a low curvature, linked to the complex, multiple-peaks profile of the heat release rate, which extends over a relatively large range of z . The reduced scheme describes well the complexity of this profile, associated to different reactions located at different values of the mixture fraction. Note that

5. LES OF A SINGLE ELEMENT GOX/GCH₄ COMBUSTOR

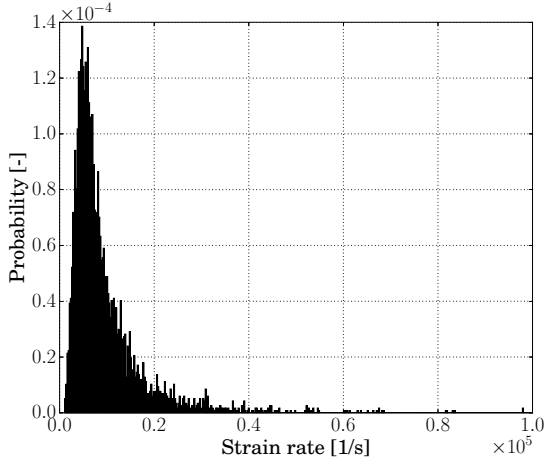


Figure 6: Probability density function of strain rate in a representative area for the flame (white box in Fig. 9)

on the rich side the temperature is slightly over-predicted by the LU13 mechanism, due to the lack of some radicals.

The gray line in Fig. 5 represents the equilibrium temperature for the whole range of mixture fraction. If equilibrium is almost reached around stoichiometry and on the lean side, denoting fast chemistry, it is far to be the case on the rich side, due to slow recombination reactions in this zone. This justifies the importance of including a direct integration of chemistry rather than using an "infinitely fast" chemistry formulation, which would always stay on the equilibrium line.

3.3. Boundary conditions

The inlet mass flow rates of gaseous oxygen (GOx) and methane (GCH₄), as well as the experimentally measured temperature, have been prescribed at inlet using the NSCBC formulation [23]. At the outlet there is no need to specify any boundary condition, since the flow is expected to be supersonic. The velocity profile prescribed at inlet corresponds to a turbulent flow, coherent with a previous RANS simulation [24]. The injector walls, as well as the faceplate, post-tip and nozzle walls are treated as adiabatic walls, with a law-of-the-wall formalism. Chamber walls are treated as isothermal, with an imposed temperature profile reconstructed from experimental data (Fig. 7). Wall flow in the chamber is modeled with an isothermal wall law, using an improved formulation that couples the velocity and temperature profiles to take into account the interaction between the strong temperature and velocity gradients in the boundary layer. A detailed description of this coupled wall law can be found in the work of Cabrit [25], who demonstrated that for wall bounded flows in which the gases temperature is much higher than the wall temperature ($T_g/T_w > 3$), standard wall laws [26] are not valid

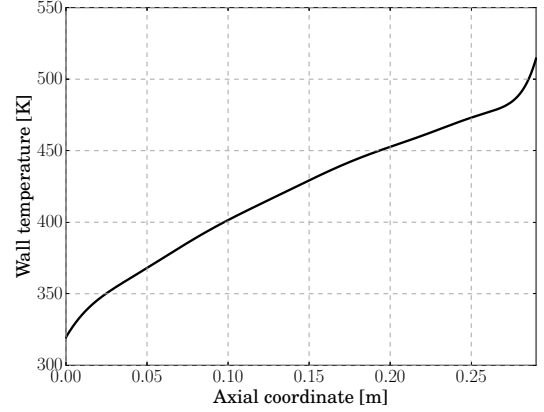


Figure 7: Imposed temperature along the axial coordinate of the combustion chamber.

anymore. In the coupled wall law the velocity and temperature write:

$$y^+ < y_c^+ : u^+ = y^+ ; \quad (3)$$

$$T^+ = y^+ \quad (4)$$

$$y^+ > y_c^+ : \frac{2}{\text{Pr}_t B_q} \left(\sqrt{1 - K B_q} - \sqrt{T^+} \right) = \frac{1}{\kappa} \ln y^+ + C_{vd} ; \quad (5)$$

$$T^+ = (\text{Pr} y^+) e^\Gamma + (\text{Pr}_t u^+ + K) e^{1/\Gamma} \quad (6)$$

with

$$\Gamma = \frac{10^{-2} (\text{Pr} y^+)^4}{1 + 5 \text{Pr}^3 y^+} \quad (7)$$

$B_q = T_\tau/T_w$ is the isothermal parameter, $C_{vd} = 5.5$ is the Van Driest constant and K writes:

$$K = \beta(\text{Pr}) - \text{Pr}_t C_{vd} \left(\frac{\text{Pr}_t}{\kappa} - 2.12 \right) (1 - 2 \ln(20)) \quad (8)$$

with

$$\beta(\text{Pr}) = (3.85 \text{Pr}^{1/3} - 1.3)^2 + 2.12 \ln \text{Pr} \quad (9)$$

Using a Van Wijngaarden-Dekker-Brent [27] resolution algorithm, the quantities of interest τ_w (wall shear stress) and q_w (wall heat flux) are retrieved. Reminding wall temperature of Fig. 7 and the equilibrium temperature of 3290 K, one can calculate values of $T_g/T_w > 5$ in the present case: the use of the coupled model of the wall law is mandatory in order to have a good estimation of the wall quantities. Tests performed with the standard law-of-the-wall confirmed that the resulting error would be unacceptable.

3.4. Numerical setup

The LES is carried using the AVBP solver, developed by CERFACS and IFPEN. It is an unstructured, explicit, compressible code [28, 29]. The numerical scheme used is the Lax-Wendroff [30] one, second order in time and

space. The sub-grid stress tensor is closed using the Sigma model [31]. Constant turbulent Prandtl number and turbulent Schmidt number (value fixed at 0.7 for both) are used to deduce the thermal and species diffusion terms at the sub-grid level, assuming an eddy-diffusivity approach. A power-law function is used to model the molecular viscosity and a constant Prandtl number is used for the thermal conductivity.

$$\mu = \mu_{ref} \left(\frac{T}{T_{ref}} \right)^n, \quad \lambda = \frac{\mu c_p}{Pr} \quad (10)$$

The coefficients in the model have been fitted to the results of the Chapman-Enskog theory [32] with Wilke mixing rules [33], $\mu_{ref} = 1.282 \times 10^{-5} \text{ Pa} \cdot \text{s}$, $n = 0.703$ and $Pr = 0.895$. The reference temperature is $T_{ref} = 278 \text{ K}$ and c_p denotes the heat capacity at constant pressure. The parameters have been fitted at a composition corresponding to a mixture fraction $z = 0.7$. This has been evaluated to be the better compromise for wall heat flux evaluations as previous numerical simulations showed that the mixture close to chamber walls is fuel rich. Away from the walls the turbulent transport is assumed to be dominating and thus the error committed is expected to be smaller.

Turbulence/combustion interaction (TCI) is accounted for with the thickened flame concept [34]. Originally derived for premixed flames, it was recently extended by Shum-Kivan [35] to non premixed combustion. In the case of LES and for high Da number, the diffusion flame thickness is controlled by the mixture fraction gradient solved on the mesh. The simulated flame fits thus to the resolved flow and the LES mesh, whatever its resolution. This is a significant difference with premixed flames which have their own thickness. For this reason, it is not necessary to further artificially thicken a diffusion flame for issues of numerical stability. However, if the calculation of the flame is numerically stable, the heat release rate is not necessarily estimated correctly. Shum-Kivan [35] demonstrated that the difference between the heat release rate obtained from LES and the exact reference (from DNS in his work) comes from three different effects: the mesh under-resolution, the missing sub-grid scale strain rate and the missing sub-grid scale flame wrinkling. The mesh under-resolution acts like numerical diffusion, causing an increase of the thermal thickness of the flame and an overestimation of the global heat release; the loss in sub-grid scale strain rate and wrinkling cause on the contrary an underestimation of the heat release rate. Following the thickened flame concept, Shum-Kivan [35] proposed to recover the exact heat release rate by a modification of the diffusivity D_{TCI} in the flame zone :

$$D_{TCI} = F_{num} \cdot F_{\Pi} \cdot F_{\Lambda} \cdot D \quad (11)$$

where $F_{num} < 1$ represents the effect of the mesh under-resolution, $F_{\Pi} > 1$ represents the loss in flame wrinkling and $F_{\Lambda} > 1$ represents the loss in strain rate. Contrarily to a premixed flame, where the factor F is strictly > 1 [34],

$F_{tot} = F_{num} \cdot F_{\Pi} \cdot F_{\Lambda}$ can be greater or lower than one for a diffusion flame. In addition, as in premixed flames, a modification of D in the whole domain would modify the mixing of reactants and products outside the reaction zone, which must be avoided. The modification of D is then applied locally in the flame zone by means of a flame sensor. For diffusion flames, it is based on the stoichiometric mixture fraction z_{st} and it reads:

$$\theta = \min(A \times \exp(-B \times (z - z_{st})^2), 1) \quad (12)$$

where A and B are constants which control the steepness and width of the sensor and have been fixed to 4 and 2000, respectively. Tests on laminar flames and also turbulent flames have been performed in order to make sure that the reaction zone is adequately detected while keeping the non-reacting zone unaffected. Finally the diffusivity is modified as follows:

$$D^* = \theta D_{TCI} + (1 - \theta)(D + D_t) \quad (13)$$

with D_t the turbulent diffusivity introduced by the sub-grid scale model. The determination of F_{tot} is a key element in this approach and, in this work, as a first step, simple rules were applied. The correction coefficient was estimated as $F_{num} = \Delta_0 / \Delta_{cell}$, where Δ_0 is the mesh size required to resolve the flame in the whole range of strain rate at the resolved scale and Δ_{cell} is the local characteristic size of the single cell. Figure 6 shows a strain rate with a non-negligible occurrence of $a = 5000 \text{ s}^{-1}$: at these conditions the flame thickness is found to be of $154 \mu\text{m}$ and a mesh size of $\Delta_0 = 25 \mu\text{m}$ provides 6 points in the flame thickness, which are in general sufficient. Figure 6 also shows that the strain rate may reach up to $a = 1.2 \times 10^5 \text{ s}^{-1}$, which occurs very rarely. At this strain rate, the diffusion flame thickness is found to be of $34 \mu\text{m}$ which is close to Δ_0 , meaning that this flamelet will be present but not accurately described. However, the low occurrence of this strain rate makes this error acceptable. With $\Delta_0 = 25 \mu\text{m}$, F_{num} is found in the range $0.025 < F_{num} < 1$.

Then, in order to account for sub-grid scale effects the coefficient $F_{sgs} = F_{\Lambda} \cdot F_{\Pi} > 1$ has also been applied. The development of a model to directly evaluate this coefficient for a diffusion flame is beyond the scope of this work and will be the subject of further studies. The sub-grid scale strain rate has been here evaluated by calculating the turbulence dissipation

$$\epsilon = 2\nu S_{ij} S_{ij} \quad (14)$$

from the resolved field, with $\nu = \mu/\rho$ the kinematic viscosity and

$$S_{ij} = \frac{1}{2} \left(\frac{\partial u_j}{\partial x_i} + \frac{\partial u_i}{\partial x_j} \right) \quad (15)$$

the deformation tensor. The turbulence dissipation is evaluated in the flame zone, giving $\epsilon \approx 10^6 \text{ m}^2/\text{s}^3$. The sub-

5. LES OF A SINGLE ELEMENT GOX/GCH₄ COMBUSTOR

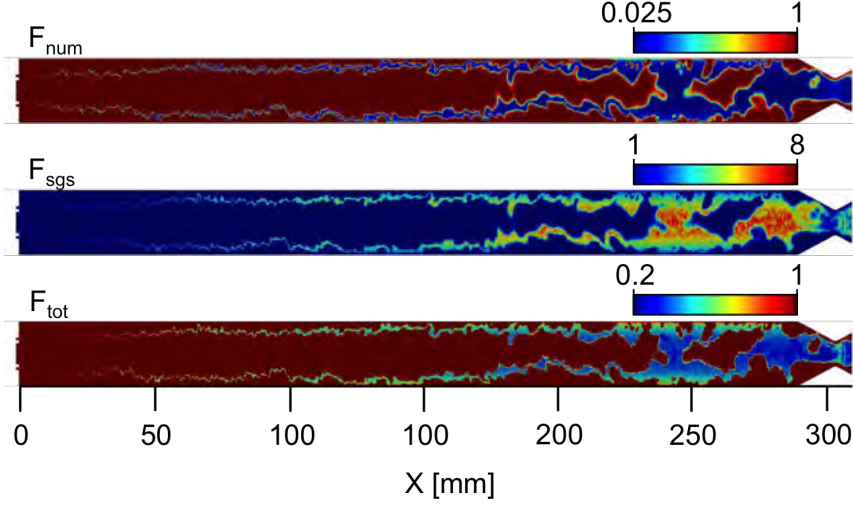


Figure 8: Fields of F_{num} (top), F_{sgs} (middle) and F_{tot} (bottom). View is stretched by a factor 2 in transverse direction for visualization reasons.

grid scale strain rate can be evaluated, under the hypothesis of homogeneous isotropic turbulence:

$$a_{sgs} = \sqrt{\epsilon/\nu} \approx 10^5 \text{ s}^{-1} \quad (16)$$

being $\nu \approx 5 \times 10^{-5} \text{ m}^2/\text{s}$ in the flame zone. This value is higher than the value of the resolved strain rate calculated in section 3.2, i.e. $\approx 10^3 - 10^4 \text{ s}^{-1}$ and could lead to an increase in the total heat release rate. It is however known [36] that, in order to increase the flame heat release rate, turbulent structures have to perturb the flame for a sufficient amount of time. The highest sub-scale strain rates are generally associated to the smallest vortical structures and small vortices are rapidly dissipated. Considering this, together with the fact that an increase of one order of magnitude in strain rate leads to an increase in heat release rate lower by far from one order of magnitude (see Fig. 4), we make the assumption that $F_\Lambda \approx 1$ as a first step.

Regarding F_Π , it has been calculated as an efficiency function following the model of Charlette et al. [37]. This model evaluates the loss in wrinkling caused by the artificial thickening of the flame by the mesh. To do that, it compares the flame wrinkling Ξ of the unthickened and mesh-thickened flames. It writes:

$$F_\Pi = \frac{\Xi(\delta_L^0)}{\Xi(\Delta_{cell})} \quad (17)$$

where δ_L^0 is the unthickened flame thickness.

The efficiency function relies on the assumption of equilibrium between turbulence and sub-grid scale flame surface. The evaluation of velocity fluctuations at the LES filter scale u'_Δ is estimated by an operator based on the rotational of the velocity to remove the dilatation contribution [38]. $\Xi(\Delta_{cell})$ is directly known from the LES solution. In premixed flames, $\Xi(\delta_L^0)$ is evaluated as follows:

$$\Xi(\delta_L^0) = \left(1 + \min \left[\frac{\Delta_e}{\delta_L^0}, \Gamma \left(\frac{\Delta_e}{\delta_L^0}, \frac{u'_\Delta}{S_L^0}, \text{Re}_{\Delta_e} \right), \frac{u'_\Delta}{S_L^0} \right] \right)^\beta \quad (18)$$

where $\beta = 0.5$ is a model parameter, S_L^0 and δ_L^0 are the laminar premixed speed and thickness, Δ_e is the LES filter size and Re_{Δ_e} is the flame Reynolds number evaluated at the filter size,

$$\text{Re}_{\Delta_e} = 4 \frac{\Delta_e u'_\Delta}{\delta_L^0 S_L^0}. \quad (19)$$

This expression for the flame wrinkling can be adapted to diffusion flames, interpreting S_L^0 and δ_L^0 as the flame speed and thickness of a diffusion flame under the effect of the sub-grid scale strain rate a_{sgs} . The efficiency function becomes:

$$\Xi(\delta_L^d) = \left(1 + \min \left[\frac{\Delta_e}{\delta_L^d}, \Gamma \left(\frac{\Delta_e}{\delta_L^d}, \frac{u'_\Delta}{\delta_L^d a_{sgs}}, \text{Re}_{\Delta_e} \right), \frac{u'_\Delta}{\delta_L^d a_{sgs}} \right] \right)^\beta \quad (20)$$

detoting with δ_L^d the sub-scale diffusion flame thickness. The characteristic time associated to the diffusion flame is $\tau_d = 1/a_{sgs} \approx 10^{-5} \text{ s}$. It is noticeable how this is close to the characteristic time of a stoichiometric premixed flame at the experimental pressure and temperature, i.e. $\tau_p = \delta_L^0/S_L^0 \approx 10^{-5} \text{ s}$, where $S_L^0 = 1.4 \text{ m/s}$ and $\delta_L^0 = 1.7 \times 10^{-5} \text{ m}$ (see section 3.2).

The values of F_{sgs} predicted by this model are in the range $1 < F_{sgs} < 8$. This leads to an overall $0.2 < F_{tot} = F_{num} \cdot F_{sgs} < 1$. This is coherent with the results of Shum-Kivan [35].

Fields of F_{num} , F_{sgs} and F_{tot} can be seen in Fig. 8. It can be noticed how F_{num} is equal to one in the zone

close to the injector lip and then decreases as the mesh is coarsened.

4. Results and discussion

Results of the LES are presented in this section, which begins with an overview of the near-injector flow. An analysis of the flame features follows, with a qualitative and quantitative description of the GCH_4/GOx flame structure and dynamics. A comparison with OH^* chemiluminescence from the experiment is shown. Finally, the axial pressure evolution and the wall heat flux are compared to the experimental data and an energy balance is detailed to explain these results.

4.1. Near injector flow field

Figure 9 shows instantaneous and averaged fields of temperature. The flame anchors in the wake of the split-

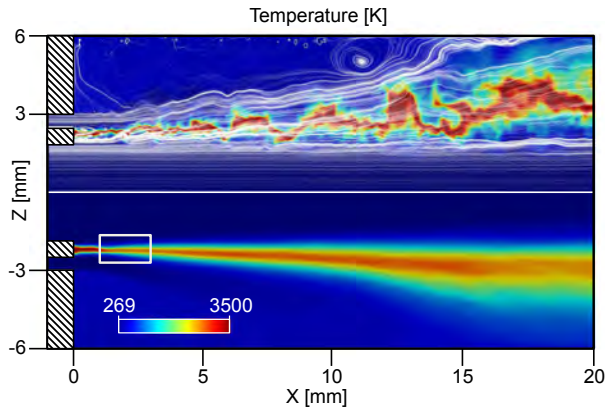


Figure 9: Temperature field on a longitudinal cut in the near-injector zone. Top: instantaneous field, streamlines. Bottom: temporally averaged field.

ter, where a stable recirculation zone is observed between the cold fuel and oxidizer inflows. The flame then progressively thickens under the effect of turbulence which destabilizes, stretches and wrinkles it. The instantaneous field, along with an analysis of streamlines, shows how the flame is strongly stretched and tends to stay thin in the zone close to the injector. Further downstream, where the strain rate is lower, the thermal expansion of the burnt gases starts to act in the radial direction. This thickens the reaction zone and pushes the cold flow of methane towards the wall, closing the recirculation zone at nearly 14 mm. The recirculation zone is filled by a mixture of fresh methane and burnt gases pockets which detach from the flame and move backward. This is shown in Fig. 10, where an instantaneous field of CH_4 and CO mixture fraction is presented.

A time averaged flow field of OH mass fraction, integrated on the sight-line is shown in Fig. 11 and compared to a visualization of the OH^* chemiluminescence from the

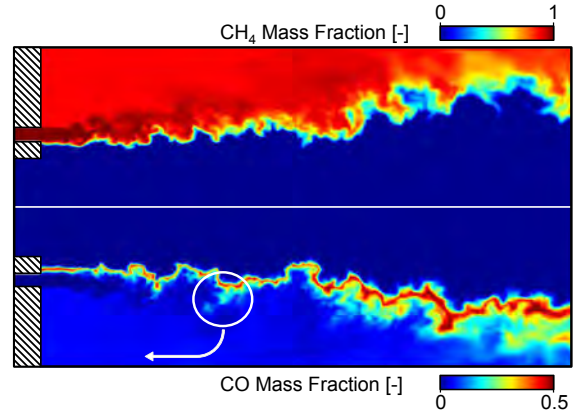


Figure 10: Top: instantaneous field of CH_4 mass fraction. Bottom: instantaneous field of CO mass fraction.

experiment [39], in the same area near the injector. As quantitative data are not available, fields have been normalized by their maximum value. The contours have been taken between 10% and 90% of the maximum value.

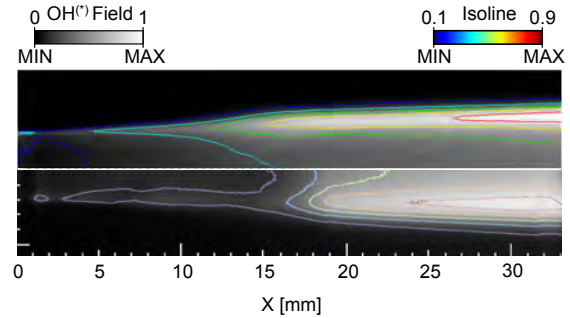


Figure 11: Top: time averaged field of OH mass fraction from the LES. Bottom: OH^* field from experiment [39].

Results show a very good agreement in flame shape and stabilization. Experimental visualization shows that the flame is weak up to a distance of 4 to 5 GOx injector diameters, then becomes suddenly brighter. The same behavior is retrieved by the numerical simulation, only slightly earlier. This sudden increase of OH coincides with the flame thickening at an axial coordinate of 15 to 20 mm, corresponding to the end of the recirculation zone.

Note that the species OH^* is not present in the numerical simulation and that OH distribution may differ from OH^* .

4.2. Flame structure

Figure 12 shows an instantaneous field of mixture fraction in the whole chamber. The mixture fraction is calculated following Bilger's definition [22]. The isoline of stoichiometric mixture fraction (white line) is taken as an indicator of the flame position since the flame

5. LES OF A SINGLE ELEMENT GOX/GCH₄ COMBUSTOR

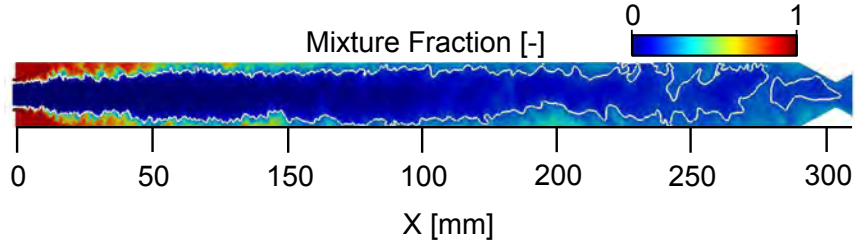


Figure 12: Field of mixture fraction in a plane perpendicular to injection. White line: isoline of stoichiometric mixture fraction. View is stretched by a factor of 2 in the transverse direction for better visualization.

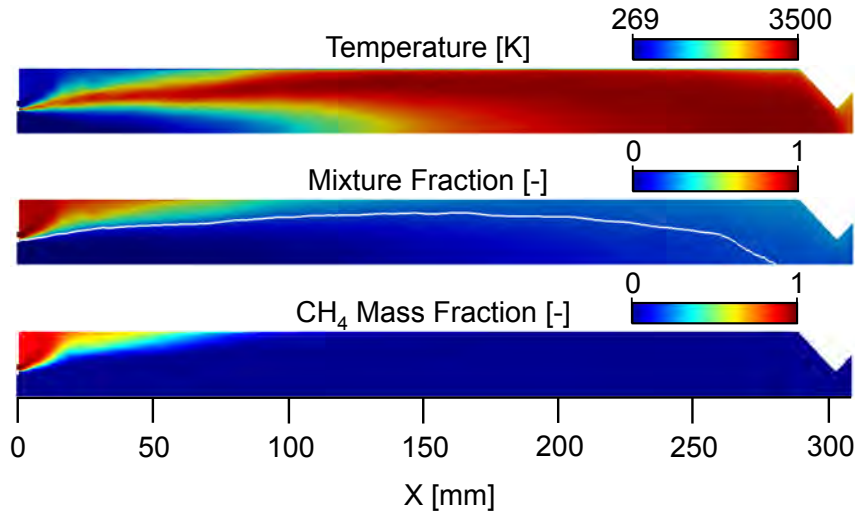


Figure 13: Longitudinal cut of mean flow fields, stretched by a factor of 4 in transverse direction for better visualization. Top: temperature. Middle: mixture fraction (white line: stoichiometric mixture fraction). Bottom: methane mass fraction.

burns in a diffusion regime. The flame closes between $x = 250$ mm and $x = 290$ mm, where pockets start to detach and exit the combustion chamber, denoting an intermittent incomplete combustion. The flame mostly stays away from the walls, and flame-wall interaction occurs rarely.

The mean flame shape is presented in Fig. 13, top and middle, where time averaged fields of temperature and mixture fraction on a longitudinal cut are shown. The isoline of stoichiometric mixture fraction marks the average position of the flame. The mean flame is attached to the injector lip, expanding radially with a maximum radial position located at about $x = 150$ mm and closing around $x = 280$ mm, just upstream the chamber end.

Figure 13, bottom, shows an averaged field of methane mass fraction. It is visible that fuel accumulates along the walls.

It is also visible that a thermal boundary layer is formed due to the joint effects of heat losses, induced by the constant-temperature boundary condition, and the presence of a layer of cold methane near the walls. The thermal boundary layer is less and less visible downstream due

to the preferential concentration of methane at the edges, as it will be shown later. A thin layer is still present but is not easily visible with the color scale used here.

In order to confirm that the combustion regime is indeed diffusion, the flame structure in the 3D simulation has been compared to 1D counterflow diffusion flames. Values for the 3D simulation have been collected in the vicinity of the injector, between 1 and 3 mm downstream the injector tip, in a cylinder around the flame (white box in Fig. 9). The 1D flame computation has been performed with the Cantera software [21] at the most probable and maximum values of strain rate found in this zone, i.e. $a = 5000$ 1/s and $a = 120000$ 1/s. Results are reported in Fig. 14. A classical diffusion flame structure at strain rate far from extinction can be identified. The LES simulation exhibits some dispersion, due to the range of resolved strain rates. Note that the maximum flame temperature is reached and that there is no evidence of heat losses on the flame structure.

To illustrate the 3D shape of the flame, Figs. 15 and 16 show transverse cuts of the instantaneous and averaged fields of temperature and methane mass fraction. In the

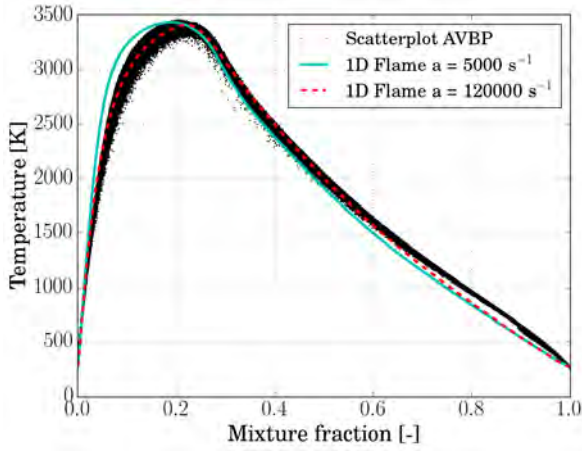


Figure 14: Scatterplots of temperature vs mixture fraction in the near injection zone, with superimposed curve for a 1D counterflow diffusion flame at a characteristic scalar dissipation rate value.

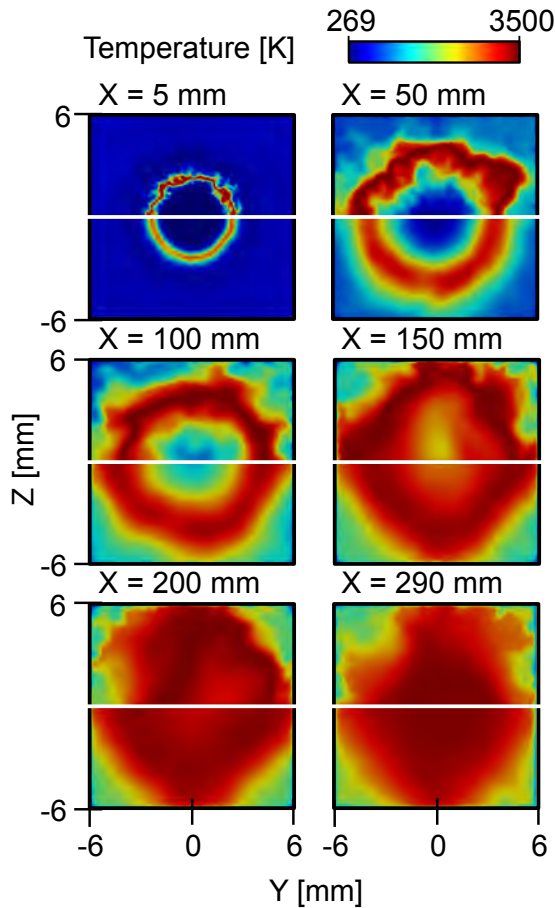


Figure 15: Transverse cuts of instantaneous (top) and time averaged (bottom) temperature fields.

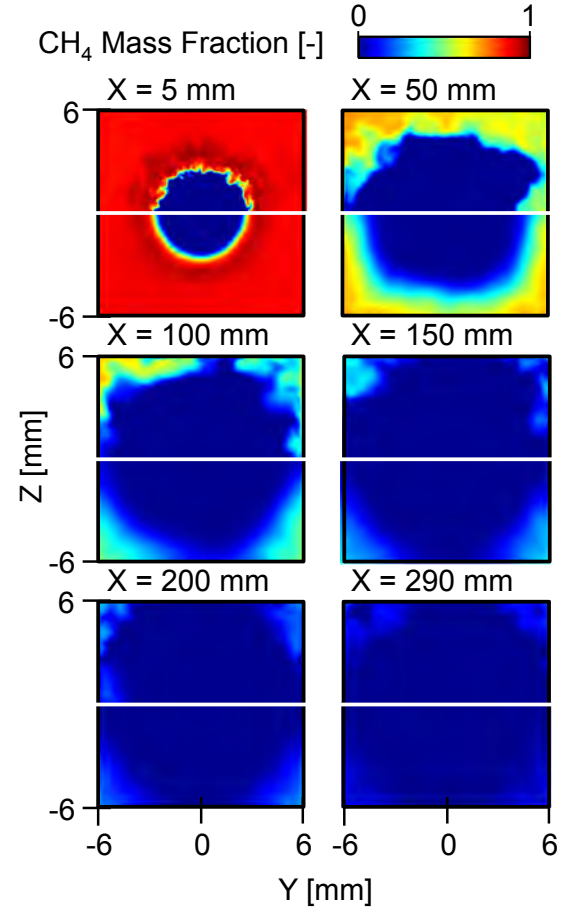


Figure 16: Transverse cuts of instantaneous (top) and time averaged (bottom) methane mass fraction fields.

near injection region, the flame shape is imposed by the injector geometry, leading to a cylindrical flame. Further downstream, the flow field is dominated by the turbulent mixing and the flame shape tends to adapt to the square section of the chamber, resembling to an octagram.

Fields of methane mass fraction on transverse cuts show that the edges of the chamber are filled with CH_4 , and remain significantly colder than the central region of the chamber walls. This has a noticeable impact on the circumferential distribution of the heat flux at walls, as shown in Sec. 4.3.

4.3. Quantitative comparison with experimental data

Available experimental data are the axial pressure distribution, indicating the burning intensity, and the heat flux at the chamber walls. The time-averaged pressure distribution along the chamber axis shown in Fig. 17. In order to better compare the profile shapes, the pressure is also plotted in a non-dimensional form, taking the reference value at the last pressure transducer (i.e., at $x =$

5. LES OF A SINGLE ELEMENT GOX/GCH₄ COMBUSTOR

272.5 mm). The LES curve is normalized by the value

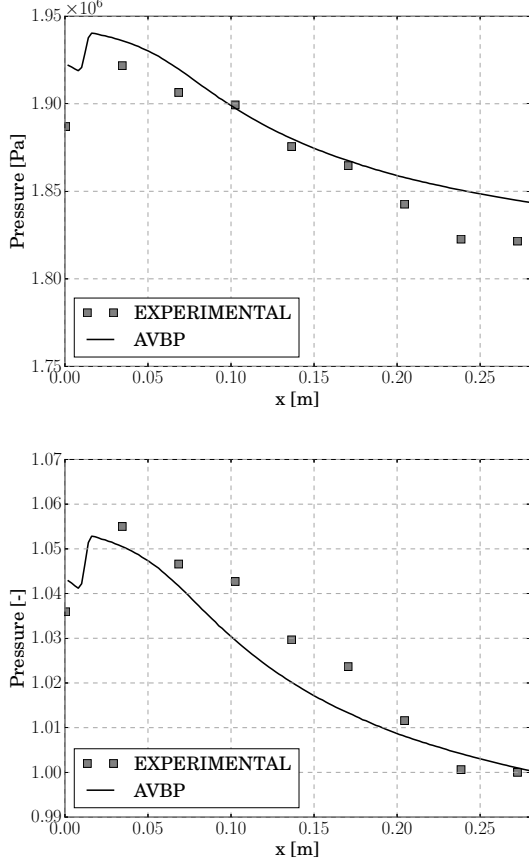


Figure 17: Top: time averaged axial pressure evolution. Bottom: time averaged normalized pressure evolution

recorded in the numerical simulation at the same axial position ($x = 272.5$ mm). The profile extracted from measurements shows a fast pressure increase close to the injector, followed by a constant and relatively slow pressure decrease. The pressure difference between the two measurement positions at the end of the chamber is nearly zero, indicating the end of the combustion process. The comparison with LES shows that the overall pressure level is quite well predicted, with a slight overestimation. The normalized profiles (top of Fig. 17) show that, in the first half of the chamber, the decrease in pressure is slightly too fast in the LES, denoting a higher heat release rate than in the experiment. However, close to the end of the chamber, the pressure slope decreases, indicating a reduction in heat release and the end of combustion, consistently with the experiment. This is also in agreement with the flame closure at nearly two thirds of the chamber observed in Fig. 12. The pressure level reached at the exit of the combustion chamber is higher than in the experiment. This is the result of lower heat losses at walls in this zone which

are now analyzed.

The evolution of the heat flux at walls has been experimentally obtained using the thermocouples temperatures recorded during the hot fire tests. Celano et al. [7] reconstructed the wall heat flux by solving an inverse heat conduction problem. The main assumption of these calculations is that the heat flux is constant in the circumferential direction of the chamber. In order to compare the LES data with the experimental heat flux profile, the numerical data have been therefore circumferentially averaged.

Results are presented in Fig 18 (top). Experimental data show a local maximum of heat flux in the near injection region, as a result of the recirculation zone. Downstream the heat flux increases with a fairly constant rate, reaching the highest heat load of 5.33 MW/m² at the end of the chamber. The numerical simulation predicts fairly well the axial evolution of the wall heat flux, denoting a correct prediction of the flow and flame dynamics. However the values are slightly underestimated for axial positions greater than 120 mm. Possible causes leading to these differences will be discussed in the following. In order to

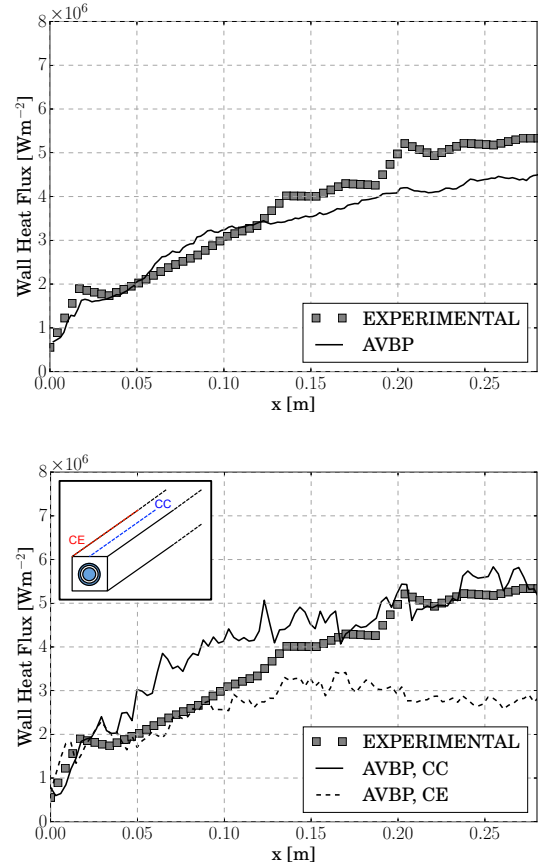


Figure 18: Top: circumferentially and time averaged axial profiles of heat flux at walls. Bottom: circumferentially and time averaged axial profile of wall heat flux at the chamber center and edge.

verify the assumption of constant heat flux in the circumferential direction, Fig. 18 (bottom) compares the heat flux along the center of the chamber wall (CC in the following) and along the chamber edge (CE in the following). Results show significant differences due to geometrical effects of a cylindrical flame in a square section chamber, highlighted in Figs. 15 and 16. The preferential convection of fresh methane towards the CE leads to a thicker thermal layer in this zone and therefore to a lower heat flux. On the contrary, at the CC, the hot gases are closer to the walls, leading to a higher heat flux. Only very close to the injection plane, the heat flux is higher at CE than at CC. This is also due to the chamber shape, combined to the presence of the corner recirculation zone. Fig. 19 represents the wall flow in the near injection region: a wall temperature field is shown and the mean flow motion is schematized. The

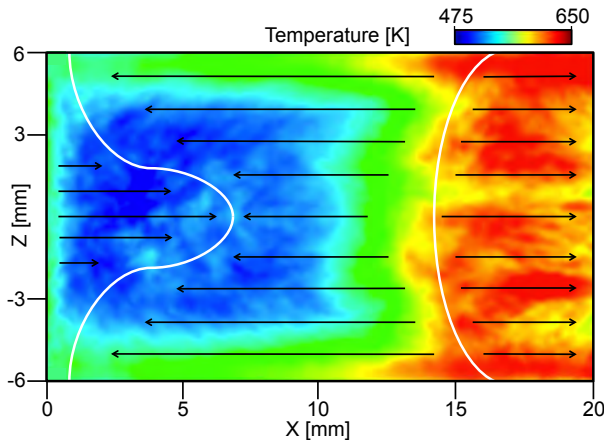


Figure 19: Schematics of the wall flow in the near injection region. White lines: representation of the zero axial velocity isolines. Black arrows: mean flow direction.

CE are further away than the CC from the methane injector, leading to corner recirculation zones which extend further upstream. This results in a larger area in which hot gases are brought back from the flame to the CE in comparison to the CC in which the fresh methane rapidly touches the walls and is convected downstream. In order to further investigate the impact of this non-uniformity, a chained thermal conduction simulation is presented in section 5.

Three possible reasons for the under-estimation of the wall heat flux in the second half of the combustion chamber have been identified. First, the combustion model coefficients have been set by using simple rules. This can lead to a slight different flame shape (different length and/or radial expansion) and to an inaccurate prediction of the heat flux at walls. This should not have a leading order impact in the second half of the chamber, but can have an impact in the first half, changing the overall heat release distribution in the combustion chamber. Second, the power-law function used for the molecular viscosity and

the Prandtl number used for the thermal conductivity have been fitted for a fuel rich mixture ($z = 0.7$). This value is acceptable in the first half of the chamber, while in the second half a local mixture fraction of $z = 0.2-0.4$ is often found at walls. This could generate an error in the evaluation of the wall heat flux, which can be underestimated of around 5 – 10 %. Third, an influence of the sub-grid scale model on the heat fluxes is found. The Sigma model [31] is used here because of its very good properties for shear flows, which permit to avoid a large amount of turbulent viscosity and dissipation in the flame. However, it has naturally an asymptotic behavior at solid boundaries: for this reason the turbulent viscosity in zones really close to the walls is very small. This is correct in a case where the boundary layers are resolved, but could lead to errors using wall laws, where the first node off walls is still in the turbulent region. With wall laws it could be better to use models like Smagorinsky [40], in which no damping for walls is present. On the contrary, this kind of model is known to be too dissipative [41] in the flame zone. In order to check the influence of the sub-grid scale model, an additional LES with the Smagorinsky model has been performed. A leading order effect of the sub-grid scale model on the wall heat flux has been found, confirming what already observed by Potier [42]. The wall heat flux estimated using the Smagorinsky model is up to 50 % higher than the one estimated using the Sigma one, as shown in Fig. 20.

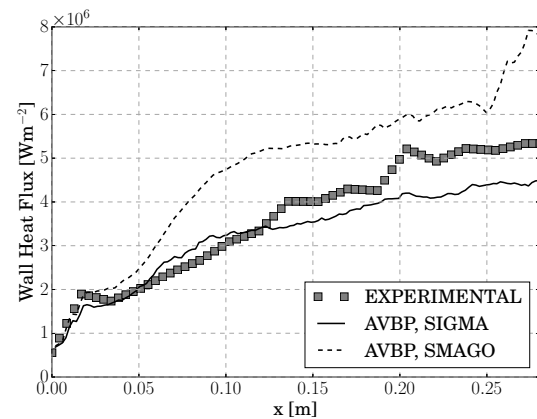


Figure 20: Circumferentially and time averaged axial profiles of heat flux at walls. Comparison between the Sigma [31] and Smagorinsky [40] sub-grid-scale models.

4.4. Energy balance

In order to highlight in a precise way the strong coupling between the heat released by the flame, the heat losses at walls and the pressure evolution in the chamber, an energy balance has been performed. An equation for the conservation of pressure can be obtained from the

5. LES OF A SINGLE ELEMENT GOX/GCH₄ COMBUSTOR

conservation of sensible energy e_s . The equation for local conservation of pressure writes [43]:

$$\begin{aligned} \frac{\partial}{\partial t} \left[\frac{1}{\gamma-1} P - \rho C_p T_0 \right] + \frac{\partial}{\partial x_i} \left[\frac{1}{\gamma-1} P u_i - \rho C_p u_i T_0 \right] = \\ = \dot{\omega}_T + \frac{\partial}{\partial x_i} \left(\lambda \frac{\partial T}{\partial x_i} \right) + \sigma_{ij} \frac{\partial u_i}{\partial x_j} + \dot{Q} + f_{vol} \end{aligned} \quad (21)$$

We make now the following assumptions:

- negligible contribution of viscous stresses:

$$\sigma_{i,j} \frac{\partial u_i}{\partial x_j} \approx 0 \quad (22)$$

- no heat source term other than the flame:

$$\dot{Q} = 0 \quad (23)$$

- no external volumetric forces:

$$f_{vol} = 0 \quad (24)$$

- the energy balance is applied to a time averaged field which is considered to correspond to a steady state solution of the flow:

$$\frac{\partial}{\partial t} \left[\frac{1}{\gamma-1} P - \rho C_p T_0 \right] = 0 \quad (25)$$

- reference temperature $T_0 = 0$ K (as in AVBP):

$$\rho C_p u_i T_0 = 0 \quad (26)$$

- constant γ . The value chosen ($\gamma = 1.2026$) is the one which allows to retrieve the correct pressure at the exit of the chamber, so that the pressure evolution can be correctly evaluated.

The equation for the local conservation of pressure then becomes:

$$\frac{1}{\gamma-1} \frac{\partial}{\partial x_i} (P u_i) = \dot{\omega}_T + \frac{\partial}{\partial x_i} \left(\lambda \frac{\partial T}{\partial x_i} \right) \quad (27)$$

Considering the mean values on a transverse cut of the combustion chamber, we can define a reference state at $x = 0$ mm where $u = u_0$ and $P = P_0$. Starting from this point, by means of successive integration on a control volume of fluid enclosed between the chamber walls, the reference cut plane and successive planes at growing axial positions $x = x'$, a 1-D axial evolution of the quantity of interest can be written. Integrating on a control volume $\mathcal{V} = \mathcal{S} \cdot (x' - x_0)$, with \mathcal{S} the cross section of the combustion chamber, it writes:

$$\begin{aligned} \frac{1}{\gamma-1} \iiint_{\mathcal{V}} \frac{\partial}{\partial x} (P u) d\mathcal{V} = \\ = \frac{1}{\gamma-1} \iint_{\mathcal{S}} \left(\int_{x_0}^{x'} \frac{\partial}{\partial x} (P u) dx' \right) d\mathcal{S} \quad (28) \\ = \frac{\mathcal{S}}{\gamma-1} [u_{x'} P_{x'} - u_0 P_0] \end{aligned}$$

$$\iiint_{\mathcal{V}} \dot{\omega}_T d\mathcal{V} = [HRR]_{\mathcal{V}} \quad (29)$$

$$\iiint_{\mathcal{V}} \frac{\partial}{\partial x} \left(\lambda \frac{\partial T}{\partial x} \right) = \iint_{\delta\mathcal{V}} \lambda \overrightarrow{\text{grad}}(T) \overrightarrow{d\mathcal{S}} = [Q_{walls}]_{\delta\mathcal{V}} \quad (30)$$

Finally, the theoretical evolution of the chamber pressure is obtained:

$$\bar{P}(x) = \frac{1}{\bar{u}(x)} \left[u_0 P_0 + \frac{\mathcal{S}}{\gamma-1} (HRR(x) + Q_{walls}(x)) \right] \quad (31)$$

Equation 31 shows that the static pressure evolution along the axial distance is controlled by three terms: the heat release rate, the heat losses and the mean velocity. The axial evolution of the quantities of interest is shown in Fig. 21. The black curve represents the evolution of the integrated

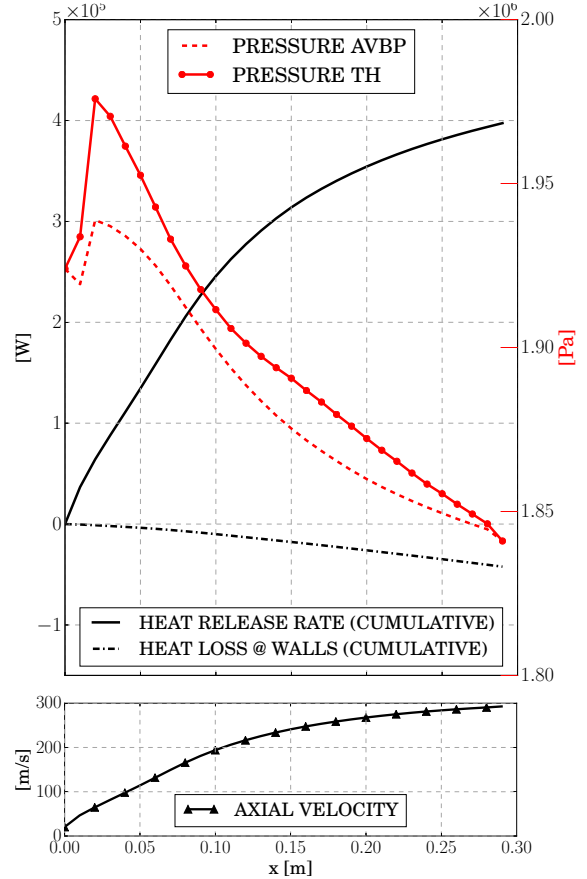


Figure 21: Energetic balance of the combustion chamber. Top: axial evolution of integrated heat release rate (black), heat fluxes at walls (dot-dashed), chamber pressure (dashed, red) and theoretical chamber pressure from Eq. 31 (red, dots). Bottom: evolution of the axial velocity in the combustion chamber.

heat release rate, which increases linearly in the first third

of the chamber. Combustion slows then down and the curve slope decreases, with an asymptotic behavior to becoming constant at the end of the chamber. At the exit of the chamber the slope is not zero, denoting incomplete combustion. This is coherent with the presence of pockets of burning gases which exit the combustion chamber, as shown in Fig. 12. The axial evolution of the heat losses at walls is plotted by a dot-dash line. After a first zone in which the increase is really slow (up to $x = 70$ mm), the losses grow in a quasi-linear way.

The total amount of power released by the flame is of 397 kW. The heat power lost at wall is of 42 kW, i.e. 10.6 % of the flame power.

Using Eq. 31, the theoretical evolution of pressure can be plotted as a function of the evolution of the above-mentioned quantities and of the axial velocity (Fig. 21, bottom): the result is in quite good agreement with the actual pressure evolution in the combustion chamber. After a first peak caused by the end of the recirculation zone, the pressure decreases as we move downstream due to the acceleration of the gases.

Quantitatively the pressure curve obtained using the energy equation is slightly different from the one effectively extracted from the numerical simulation. This is due to the strong assumptions made during its derivation. Particularly, the assumption of constant γ and the value chosen has been found to strongly influence the results.

The effects of heat losses on the chamber pressure evolution can now be quantified. Especially, it can be analyzed if the difference found between the LES and the experiment in heat fluxes and pressure curves can be linked. The cumulative heat losses at walls from the experiment have been calculated, resulting in a total heat power lost at walls of around 51 kW, i.e., 21.5% higher than than in LES. Using the LES heat release rate and axial velocity profiles, Eq. 31 can be used to compute the theoretical pressure evolution associated to the experimental heat losses at walls. Results are plotted in Fig. 22.

The heat losses at walls have a clear effect on the pressure evolution: starting from an axial coordinate of $x=120$ mm, the theoretical chamber pressure takes lower values when calculated using the experimental heat losses curve rather than the LES one. It is so clear how the over-estimation of the chamber pressure found in the LES is linked to the under-estimation of heat fluxes. It is however visible how this effect is not the only responsible of the differences found, since the theoretical pressure evolution calculated using the experimental heat losses does not have the same behavior as the experimental pressure evolution. The heat release rate (as well as the axial velocity) distribution are responsible for the resting differences.

5. Thermally chained numerical simulation

As mentioned before, the hypothesis of circumferentially constant heat flux at walls is not perfectly valid.

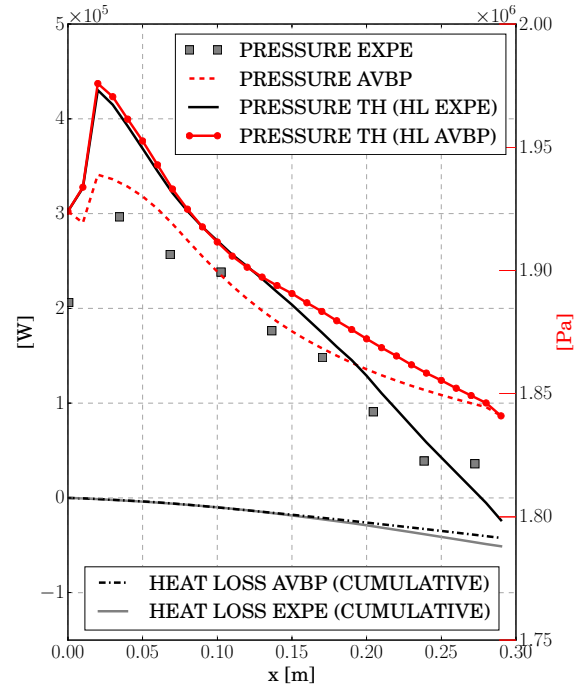


Figure 22: Energetic balance of the combustion chamber. Axial evolution of experimental pressure (square symbols), LES chamber pressure (dashed, red), theoretical chamber pressure from Eq. 31 using the LES heat fluxes (red, dots), theoretical chamber pressure from Eq. 31 using the experimental heat fluxes (black).

To investigate the associated errors, the calculation of the heat conduction in the combustion chamber walls is performed, starting from the wall heat fluxes provided by the LES. This will provide the temperature field inside the combustion chamber walls, to be compared directly to values recorded by thermocouples during the test campaign.

The thermal simulation has been performed by means of the AVTP solver, dedicated to conduction in solids. AVTP solves the time-dependent temperature diffusion equation, where the heat diffusion follows Fourier's law. The solid solver takes into account local changes of heat capacity and conductivity with temperature. The second-order Galerkin diffusion scheme [44] for spatial discretization is derived from the AVBP solver. Time integration is achieved either with an explicit or an implicit first order forward Euler scheme. The implicit system, which has been used in the present study, is solved with a parallel matrix free conjugate gradient method [45].

The whole chamber structure has been simulated, starting from 29 mm before the faceplate until the end of the nozzle, and has been discretized by means of a fully tetrahedral unstructured mesh of about 50×10^6 cells. An illustration of the mesh characteristics can be seen in Fig. 23. The mesh is very well refined at chamber walls, where cells slightly smaller than the respective ones on the fluid side have been used in order to avoid interpolation problems.

5. LES OF A SINGLE ELEMENT GOX/GCH₄ COMBUSTOR

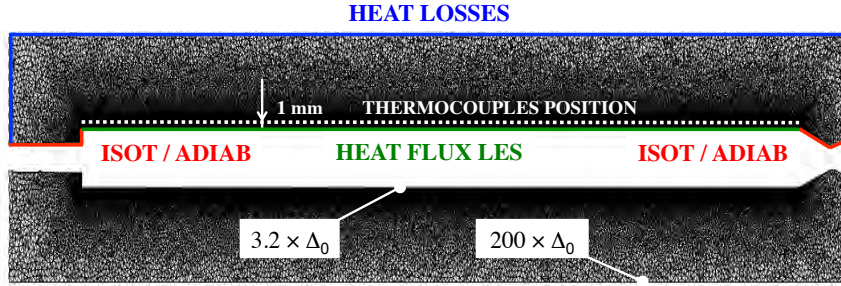


Figure 23: Longitudinal cut through the mesh (view stretched by a factor 4 in transverse direction) and boundary conditions for the AVTP simulation.

The cells are then coarsened until the external walls of the chamber.

The structure material is oxygen-free copper (Cu-HCP). The material constants used are in accordance with [46] and have been set as: density $\rho = 8940 \text{ kg/m}^3$, heat capacity $c_p = 393 \text{ J/(kg} \cdot \text{K)}$ and thermal conductivity $\lambda = 385 \text{ W/(m} \cdot \text{K)}$. The computational domain has been initialized with a constant temperature of 290 K and the following boundary conditions have been used:

- Inner chamber walls: imposed heat fluxes (constant in time and variable in space) from the LES with the Sigma sub-grid-scale model. As an example, the flux on one chamber wall at an axial coordinate $x = 120 \text{ mm}$ is presented in Fig. 24. It is assumed that

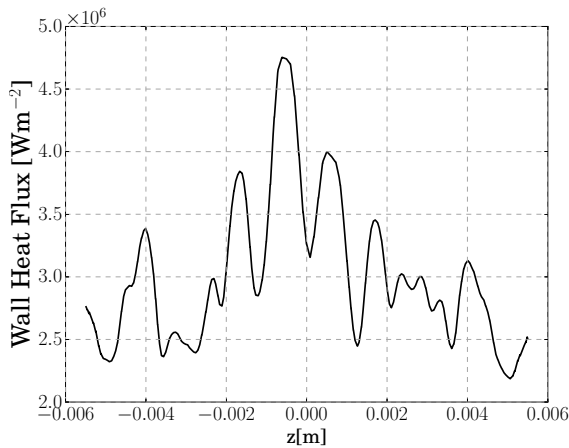


Figure 24: Circumferential distribution of the wall heat flux on a cut at an axial coordinate $x = 120 \text{ mm}$.

steady heat fluxes are quickly reached after ignition and so the heating of the structure during the start-up is neglected. Consider also that as soon as the pressure in the chamber reaches its operating value, the combustion process does not change anymore, this is coherent with the experimental conditions described in Fig. 2. The major assumption is here the constant wall temperatures used in LES (correspond-

ing to the ones measured at 2/3 of the burning time). This could be avoided by performing a fully AVBP-AVTP coupled simulation and may be the subject of further studies. This kind of simulation would be however very CPU expensive.

- Faceplate and external GCH₄ injector wall: conditions on these walls are unknown so that two extreme cases have been performed. In the first case the walls have been both fixed to the experimental chamber wall temperature at the faceplate axial coordinate (ISOT). In the second case an adiabatic condition has been assumed (ADIAB).
- Nozzle walls: here too, two cases have been studied. In the first case the walls have been fixed at the experimental chamber wall temperature at the last chamber wall axial coordinate (ISOT). In the second case an adiabatic condition has been assumed (ADIAB).
- Chamber outer walls: imposed heat losses considering an air temperature of 290 K (the same as the initial temperature of the solid) and an arbitrary convective heat transfer coefficient of $10 \text{ W/(m}^2 \cdot \text{K)}$ (in accordance with [46]).

A summary of the boundary conditions is given in Fig. 23. The whole three seconds of the experiment have been simulated.

In order to compare the temperature field in the solid with the data recorded in the experiment, the axial evolution of temperature at the position of the first row of thermocouples has been extracted. The thermocouples are installed along the chamber axis at a distance of 1 mm from the chamber walls (see Fig. 23). The temperature field extracted from the numerical simulation has been averaged during 0.5 s , starting 2 s after the beginning of the run, exactly as in the experiment. Results are shown in Fig. 25. The agreement is excellent up to an axial coordinate $x = 120 \text{ mm}$, corresponding to the good prediction of wall heat flux by the LES. At higher axial coordinates the temperature is underestimated, as was the heat flux. Results also reveal the influence of the boundary condition on

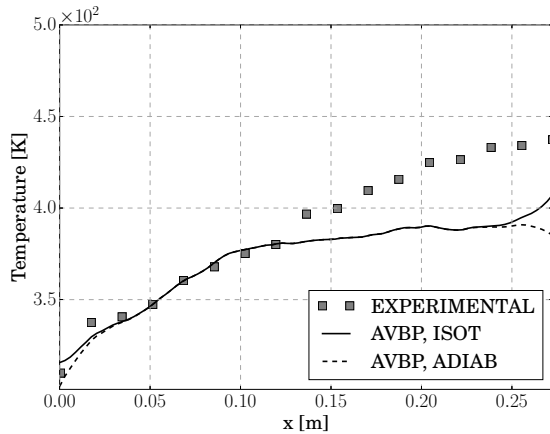


Figure 25: Solid structure temperature evolution at 1 mm from the chamber walls

the nozzle walls. An influence of the boundary condition is visible also at the injector side, even if it is of smaller amount.

The good results on the temperature in the first half of the chamber permit to cross-validate the LES methodology and give confidence with regards to the results obtained.

In order to illustrate the three-dimensional character of the temperature field in the solid a longitudinal and transverse cut (at $x = 120$ mm) of the chamber wall are presented in Fig. 26. The fields correspond to a simulation time of 2.5 s, i.e., the end of the averaging time for the temperature axial evolution of Fig. 25.

Focusing specifically on the transverse cut (top of Fig. 26), one can notice how the temperature field in the combustion chamber wall assumes a quasi-round shape, coherent with the heat flux distribution of Fig. 24. A slight sign of preferential heat diffusion in the directions where the external walls are closer is visible.

Analyzing the circumferential distribution of solid temperature on the inner chamber walls, one can quantify the impact of imposing a circumferentially constant value of temperature in the LES. Figure 27 shows the temperature profile on one side of the inner chamber wall, from edge to edge. The wall temperature varies between 370 K at chamber edges and 390 K at the chamber center. Considering a circumferentially constant temperature, the error introduced is not of leading order.

Moreover, it can be here quantified the difference between the wall temperature calculated with AVTP and the one evaluated at TUM using the thermocouples data and the in-house tool *Thermtest* [47], based on numerical correlations. The difference is evaluated at $x = 120$ mm, the position at which the experiment and numerical simulation provide the same wall heat flux and thermocouple temperature. Here, the temperature predicted by *Thermtest* at the chamber center is of about 410 K, i.e., 20 K higher than the one predicted using AVTP.

6. Conclusions and future work

A single element GCH_4/GO_x rocket combustion chamber has been computed using Large Eddy Simulation.

The flow and flame structures in the near injector flow field have been studied and a comparison with experimental visualizations of the flame has been provided, showing a good agreement in terms of flame shape and evolution. The overall flame structure has also been analyzed. The analysis showed a purely strained diffusion flame which closes at nearly two thirds of the chamber length. The flame rarely touches the walls and pockets of burning gases intermittently cross the nozzle. In the transverse direction the flame shape and the reactants preferential distribution have been highlighted, denoting an octagonal flame shape and a concentration of methane at the chamber edges.

Numerical simulation data in terms of axial pressure and axial wall heat flux evolution have been compared to experimental data, showing a good agreement. It has been found an influence of leading order of the interaction between the wall law and the sub-grid scale model used for turbulent viscosity. An energy balance to explain the contribution of heat release rate and heat losses at walls to the pressure evolution has been developed.

Finally, a thermally chained numerical simulation of the heat conduction in the chamber structure has been performed in order to cross-validate the heat flux evaluation with regards to the temperature measured in the solid structure during the hot firing tests. Results showed an excellent agreement in the zones in which the wall heat flux was well predicted. This gives strength to the LES results and permits to label the methodology used as reliable for wall heat flux evaluations.

Differences in terms of wall heat flux evaluation and chamber structure temperature have been found in the second half of the combustion chamber and further work is necessary in order to improve the prediction in this zones.

Further work will have to focus on an improvement of the TCI combustion model, which is here very preliminary. Moreover, the influence of the sub-grid scale turbulent viscosity model has to be further analyzed, in order to develop a model with overall good characteristics in the flame and in wall flows with law-of-the-wall models.

From a thermal point of view it would be interesting to perform coupled simulations with the chamber structure, in order to avoid hypothesis on the temperatures and fluxes steady behavior and on the circumferential distribution of wall temperature and heat fluxes. Moreover, a thermal coupling with the injector lip would provide information on the anchoring mechanism which is here "forced" by the adiabatic condition on the lip wall.

7. Acknowledgments

The authors acknowledge CINES of GENCI for giving access to HPC resources under the allocations A0032B10157 and A0012B07036. The authors extend special thanks to

5. LES OF A SINGLE ELEMENT GOX/GCH₄ COMBUSTOR

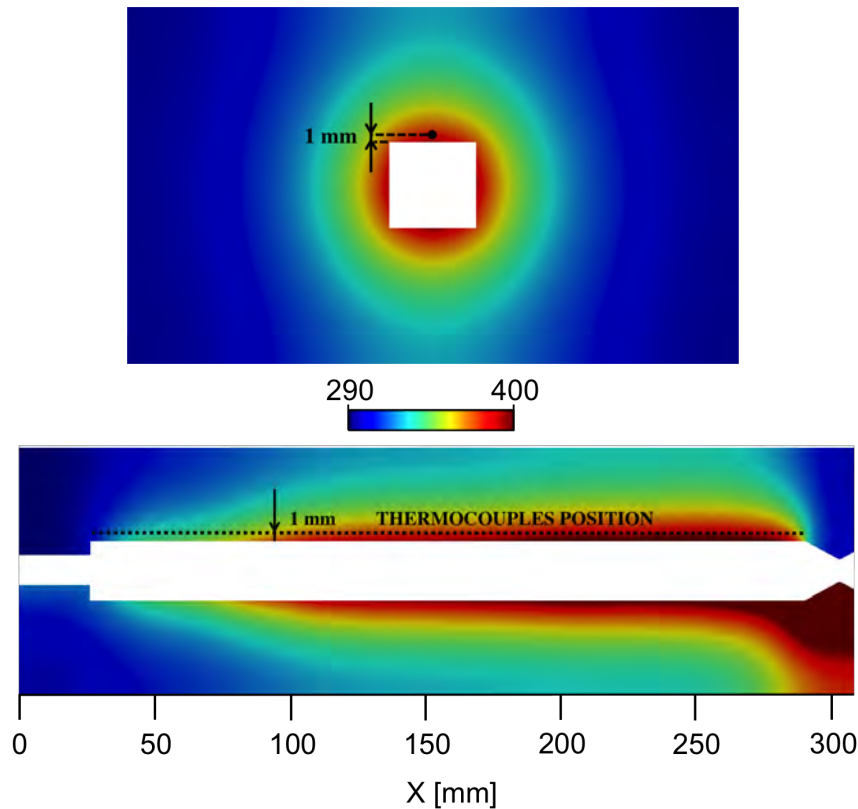


Figure 26: Temperature field in the chamber wall. Top row: transverse cut at $x = 120$ mm. Bottom row, top half: longitudinal cut with adiabatic injector, faceplate and nozzle walls (ADIAB case). Bottom row, bottom half: longitudinal cut with isothermal injector, faceplate and nozzle walls (ISOT case).

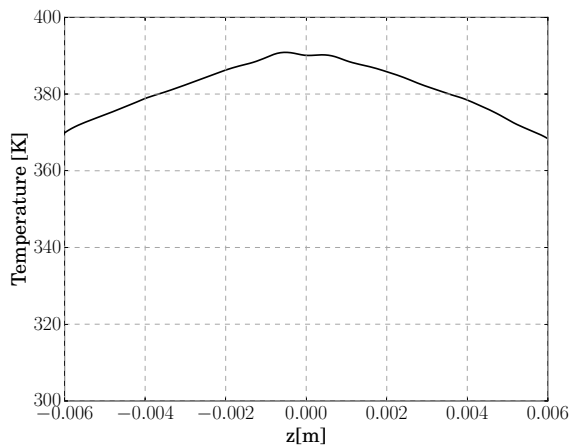


Figure 27: Solid structure temperature evolution on one side of the inner chamber walls.

Mariella Celano, Simona Silvestri, Christoph Kirchberger, Gregor Schlieben and Oskar Haidn for providing the test case and insightful discussions.

- [1] H. Burkhardt, M. Sippel, A. Herberitz, and J. Klevanski.

- Kerosene vs methane: a propellant tradeoff for reusable liquid booster stages. *Journal of Spacecraft and Rockets*, 41(5):762–769, 2004.
- [2] D. Preclik, G. Hagemann, O. Knab, C. Mading, D. Haeseler, O.J. Haidn, A. Woschnak, and M. DeRosa. Lox-hydrocarbon preparatory thrust chamber technology activities in germany. In *41st AIAA/ASME/SAE/ASEE Joint Propulsion Conference & Exhibit*, 2005.
- [3] K. Liang, B. Yang, and Z. Zhang. Investigation of heat transfer and coking characteristics of hydrocarbon fuels. *Journal of Propulsion and Power*, 14(5), 1998.
- [4] A. Fröhlich, M. Popp, G. Schmidt, and D. Thelemann. Heat transfer characteristics of h₂/o₂-combustion chambers. In *Joint Propulsion Conference and Exhibit*, 1993.
- [5] L. Vingert, M. Habiballah, and P. Vuillermoz. Upgrading of the mascotte cryogenic test bench to the lox/methane combustion studies. In *4th International Conference on Launcher Technology "Space Launcher Liquid Propulsion"*, Liège, Belgium, page 77, 2002.
- [6] F. Cuoco, B. Yang, and M. Oswald. Experimental investigation of lox/h₂ and lox/ch₄ sprays and flames. In *24th International Symposium on Space Technology and Science*, 2004.
- [7] M. P. Celano, S. Silvestri, G. Schlieben, C. Kirchberger, O. J. Haidn, T. Dawson, R. Ranjan, and S. Menon. Experimental and numerical investigation of GOX-GCH₄ shear-coaxial injector element. In *SP-2014-2969417*, 2014.
- [8] C. Roth, O. Haidn, H. Riedmann, B. Ivancic, D. Maestro, B. Cuenot, L. Selle, Y. Daimon, A. Chemnitz, R. Keller, et al. Comparison of different modeling approaches for CFD simula-

- tions of a single-element GCH₄/GOX rocket combustor. *Proceedings of the 2015 Summer Program*, 2015.
- [9] D. Maestro, L. Selle, and B. Cuenot. Thermally chained LES of a GCH₄/GOX single element combustion chamber. *Proceedings of the 2015 Summer Program*, 2015.
 - [10] C. Roth, O. Haidn, A. Chemnitz, T. Sattelmayer, G. Frank, H. Müller, J. Zips, R. Keller, P. Gerlinger, D. Maestro, L. Selle, B. Cuenot, and H. Riedmann. Numerical investigation of flow and combustion in a single element gch₄/gox rocket combustor. In *52nd AIAA/SAE/ASME Joint Propulsion Conference*, 2016.
 - [11] D. Maestro, B. Cuenot, A. Chemnitz, T. Sattelmayer, C. Roth, O. Haidn, Y. Daimon, R. Keller, P. M. Gerlinger, G. Frank, et al. Numerical investigation of flow and combustion in a single-element gch₄/gox rocket combustor: Chemistry modeling and turbulence-combustion interaction. In *52nd AIAA/SAE/ASME Joint Propulsion Conference*, 2016.
 - [12] H. Müller, J. Zips, M. Pfitzner, D. Maestro, B. Cuenot, S. Menon, R. Ranjan, P. Tudisco, and L. Selle. Numerical investigation of flow and combustion in a single-element gch₄/gox rocket combustor: A comparative les study. In *52nd AIAA/SAE/ASME Joint Propulsion Conference*, 2016.
 - [13] D. Maestro B. Cuenot, L.Selle. Large eddy simulation of flow and combustion in a single-element gch₄/gox rocket combustor. In *7th European Conference for Aeronautics and Space Sciences (EUCASS)*, 2017.
 - [14] M. P. Celano, S. Silvestri, G. Schlieben, C. Kirchberger, and O. J. Haidn. Injector characterization for a gox-gch₄ single element combustion chamber. In *5th European Conference For Aeronautics And Space Sciences (EUCASS)*, 2013.
 - [15] M.P. Celano, S. Silvestri, J. Pauw, N. Perakis, F. Schily, D. Suslov, and O. J. Haidn. Heat flux evaluation methods for a single element heat-sink chamber. In *6th European Conference of Aeronautics and Space Science, Krakow, Poland*, 2015.
 - [16] R. Sankaran, E. Hawkes, J. Chen, T. Lu, and C. Law. Structure of a spatially developing turbulent lean methane-air bunsen flame. *Proceedings of the combustion institute*, 31(1):1291–1298, 2007.
 - [17] T. Lu and C. Law. A directed relation graph method for mechanism reduction. *Proceedings of the Combustion Institute*, 30(1):1333–1341, 2005.
 - [18] T. Lu, Y. Ju, and C. Law. Complex csp for chemistry reduction and analysis. *Combustion and Flame*, 126(1):1445–1455, 2001.
 - [19] M. Frenklach, H. Wang, M. Goldenberg, G.P. Smith, and D.M. Golden. Gri-mech: An optimized detailed chemical reaction mechanism for methane combustion. topical report, september 1992-august 1995. Technical report, SRI International, Menlo Park, CA (United States), 1995.
 - [20] R. Mari. *Influence of heat transfer on high pressure flame structure and stabilization in liquid rocket engines*. PhD thesis, 2015.
 - [21] D. Goodwin, H. K Moffat, and R. Speth. Cantera: An object-oriented software toolkit for chemical kinetics, thermodynamics, and transport processes. *Caltech, Pasadena, CA*, 2009.
 - [22] R.W. Bilger, S.H. Staarner, and R.J. Kee. On reduced mechanisms for methane-air combustion in nonpremixed flames. *Combustion and Flame*, 80(2):135–149, 1990.
 - [23] T. Poinsoot and S. Lele. Boundary conditions for direct simulations of compressible viscous flows. *J. Comput. Phys.*, 101(1):104–129, 1992.
 - [24] Y. Daimon, H. Terashimay, Negishi H., and O. Haidn. Combustion Modeling Study for a GCH₄/GOX single element combustion chamber: Steady State Simulation and Validations. *Proceedings of the 2015 Summer Program*, 2015.
 - [25] O. Cabrit. *Modelisation des flux parietaux sur les tuyeres des moteurs a propergol solide*. PhD thesis, 2009.
 - [26] W.M. Kays, M.E. Crawford, and B. Weigand. *Convective heat and mass transfer*. McGraw-Hill Inc., New York, 2004.
 - [27] W. H. Press, B. P. Flannery, S. A. Teukolsky, and W. T. Vetterling. *Numerical recipes: The art of scientific computing*. Cambridge U. Press, Cambridge, MA, 1986.
 - [28] T. Schönfeld and M. Rudgyard. Steady and unsteady flows simulations using the hybrid flow solver avbp. *AIAA Journal*, 37(11):1378–1385, 1999.
 - [29] N. Gourdain, L. Gicquel, G. Staffelbach, O. Vermorel, F. Duchaine, J-F. Boussuge, and T. Poinsoot. High performance parallel computing of flows in complex geometries - part 2: applications. *Comput. Sci. Disc.*, 2(1):28pp, 2009.
 - [30] P. D. Lax and B. Wendroff. Systems of conservation laws. *Commun. Pure Appl. Math.*, 13:217–237, 1960.
 - [31] F. Nicoud, H. Baya Toda, O. Cabrit, S. Bose, and J. Lee. Using singular values to build a subgrid-scale model for large eddy simulations. *Phys. Fluids*, 23(8):085106, 2011.
 - [32] S. Chapman and T. G. Cowling. *The mathematical theory of non-uniform gases: an account of the kinetic theory of viscosity, thermal conduction and diffusion in gases*. Cambridge university press, 1970.
 - [33] C. R. Wilke. A viscosity equation for gas mixtures. *The journal of chemical physics*, 18(4):517–519, 1950.
 - [34] J.-P. Legier, T. Poinsoot, and D. Veynante. Dynamically thickened flame les model for premixed and non-premixed turbulent combustion. In *Proc. of the summer program*, pages 157–168, 2000.
 - [35] Francis Shum-Kivan. *Simulation des Grandes Echelles de flammes de spray et modélisation de la combustion non-prémélangée*. PhD thesis, Institut National Polytechnique de Toulouse, 2017.
 - [36] B. Cuenot and T. Poinsoot. Effects of curvature and unsteadiness in diffusion flames. implications for turbulent diffusion combustion. *Direct Numerical Simulation for Turbulent Reacting Flows*, page 225, 1996.
 - [37] F. Charlette, C. Meneveau, and D. Veynante. A power-law flame wrinkling model for les of premixed turbulent combustion part i: non-dynamic formulation and initial tests. *Combustion and Flame*, 131(1):159–180, 2002.
 - [38] O. Colin, F. Ducros, D. Veynante, and T. Poinsoot. A thickened flame model for large eddy simulations of turbulent premixed combustion. *Physics of Fluids*, 12(7):1843–1863, 2000.
 - [39] F. Winter, S. Silvestri, M. P. Celano, G. Schlieben, and O. Haidn. High-speed and emission imaging of a coaxial single element gox/gch₄ rocket combustion chamber. In *European Conference for Aeronautics and Space Sciences*, 2017.
 - [40] J. Smagorinsky. General circulation experiments with the primitive equations: I. the basic experiment. *Monthly weather review*, 91(3):99–164, 1963.
 - [41] M. Rudgyard, T. Schönfeld, and I. D’Ast. A parallel library for cfd and other grid-based applications. In *International Conference on High-Performance Computing and Networking*, pages 358–364. Springer, 1996.
 - [42] L. Potier. *Large Eddy Simulation of the combustion and heat transfer in sub-critical rocket engines*. PhD thesis, Institut National Polytechnique de Toulouse, 2018.
 - [43] Thierry Poinsoot and Denis Veynante. *Theoretical and numerical combustion*. RT Edwards, Inc., 2012.
 - [44] J. Donea and A. Huerta. *Finite element methods for flow problems*. John Wiley & Sons, 2003.
 - [45] V. Frayssé, L. Giraud, S. Gratton, and J. Langou. A set of gmres routines for real and complex arithmetics. *CERFACS, Toulouse Cedex, France, Tech. Rep. TR/PA/97/49, [Online]. Available: www.cerfacs.fr*, 1997.
 - [46] N. Perakis, M. P. Celano, and O. J. Haidn. Heat flux and temperature evaluation in a rectangular multi-element gox/gch₄ combustion chamber using an inverse heat conduction method. In *7th European Conference for Aerospace Sciences*, 2017.
 - [47] C. Kirchberger, G. Schlieben, and O. J. Haidn. Assessment of film cooling characteristics in a gox/kerosene rocket combustion chamber. In *49th AIAA/ASME/SAE/ASME Joint Propulsion Conference*, page 4144. 2013.

5.5 Additional material

5.5.1 Effect of the mesh

The flow and flame dynamics of the present test case have been found to be influenced at leading order by the physical mechanisms at play close to the injection plane (in the post-tip zone). To analyze the importance of the mesh used to describe these phenomena, results of the present numerical setup (which will be called "FINE" in the following) are compared with solutions obtained on a coarser mesh (which will be called "COARSE" in the following). The COARSE case is characterized by a cell size multiplied by a factor of two; in particular the post tip zone is discretized with 20 points in the case FINE and with only 10 in the case COARSE. The comparison is shown in Fig. 5.2. In order to evaluate the mesh effect on the flame, no TCI model is used for this comparison.

This change by a factor of two in the resolution, drastically changes the flow and flame structure downstream of the post-tip. On the top of Fig. 5.2, instantaneous fields of axial velocity are presented. Recirculation zones can be identified with the white zero axial velocity iso-line. In the FINE case a "tip recirculation zone" appears in the post-tip zone. Conversely, a "central recirculation zone" develops a little further downstream in the COARSE case, but not in the FINE case. Finally, "corner recirculation zones" lie in the chamber corners for both meshes. It appears that the tip recirculation zone, filled with hot burnt gases, is crucial for the flow structure just downstream: the reactant jets are pushed one against the other by this vortical structure counteracting the dilatation effect of the flame that deviate the methane jet in the COARSE case, leaving room to a central recirculation zone. The jet breakdown position coincides in the FINE case with a slowdown zone, but no back flow is observed. The corner recirculation zone length is also modified, changing from 6 mm for the COARSE case to 14 mm for the FINE case.

As a consequence of this difference in flow structure, the flame structure is also modified. Differences can be seen in the middle of Fig. 5.2, where instantaneous temperature fields are presented. With the coarse mesh, the flame is less strained and burnt gases expand radially. Using a fine mesh induces higher strain on the flame which remains very thin and straight.

The flame stabilization is also strongly affected by the flow structure downstream the post-tip, as can be seen on the bottom row of Fig. 5.2, where fields of instantaneous heat release rate are shown. In the COARSE case the reactants quickly diffuse at the post-tip creating favorable conditions for combustion and leading to a large local heat release rate. On the contrary, in the FINE case, the recirculation zone confines the flame on the oxygen side and dilutes the CH₄ flux with burnt gases, limiting the heat release rate, which reaches its maximum further downstream. One can already notice from this early comparison the effect of a coarse mesh on the diffusion flame, leading to values of the heat release rate which increase as the mesh is coarsened. This leads to a thicker, faster and thus shorter flame.

Figure 5.3 shows a comparison of the instantaneous temperature fields in a region extending further downstream, between the domain inlet and two third of the chamber length. This shows a sooner impact of hot gases at walls for the COARSE case, which would lead to wrong heat fluxes. This is due to two main causes that have to be

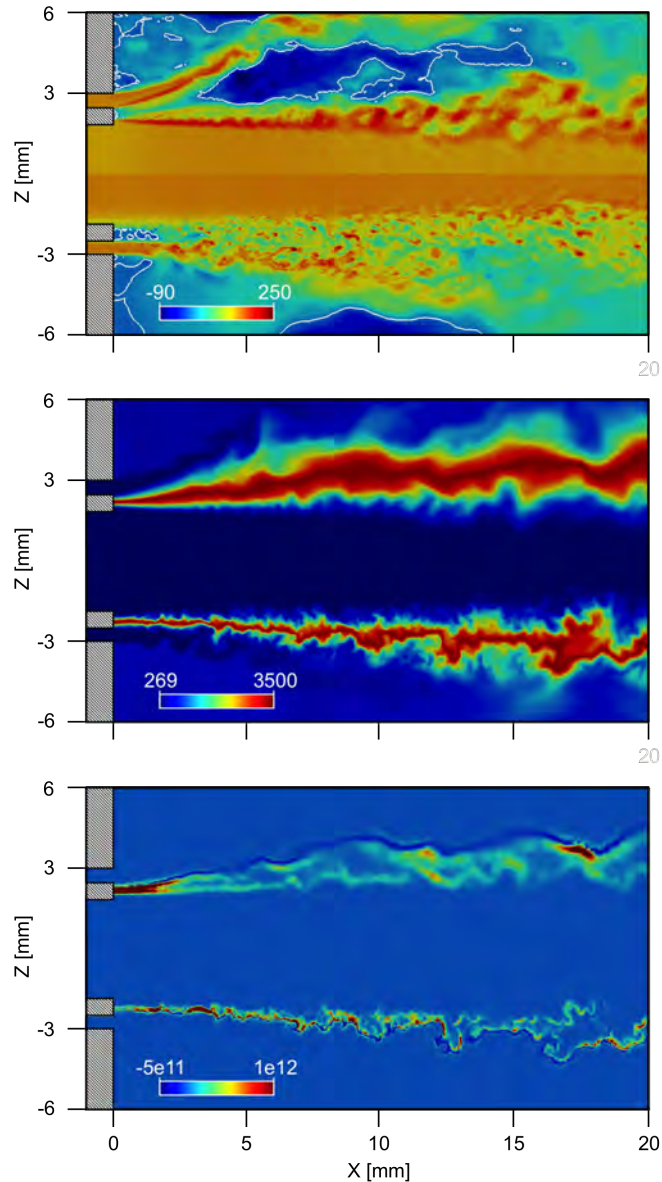


Figure 5.2: Longitudinal cuts of instantaneous fields in the near-injection region. Upper half: COARSE case; lower half: FINE case. Top: axial velocity. Middle: temperature. Bottom: heat release rate.

taken into account, especially if the aim is to evaluate heat fluxes at walls. The first observation is that the flow and flame dynamics in the near injection region strongly affects the overall flame shape. On the coarse mesh the flame, which immediately thickens in the post-tip region (as seen in Fig. 5.2), remains thick downstream since the resolved flow is not capable to strain it highly, causing an early convection of hot gases towards the wall. This phenomenon is not visible for the FINE case, where a thin flame is obtained and hot gases reach the wall zone much further downstream. The second cause of the early convection of hot gases towards the walls is the numerical

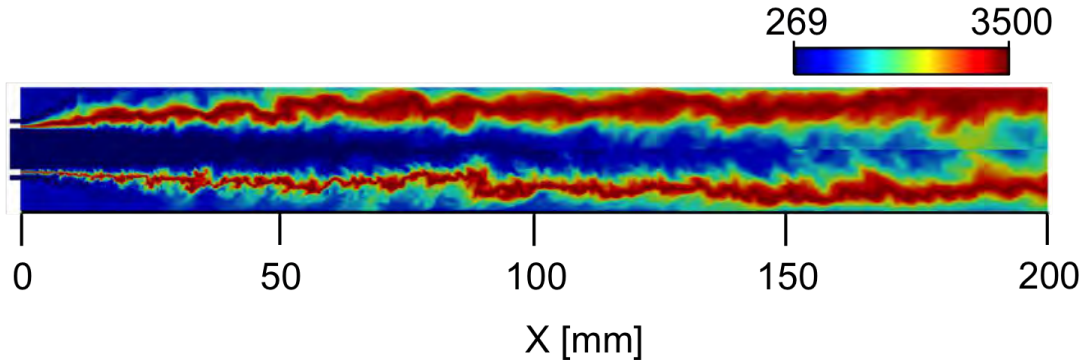


Figure 5.3: Longitudinal cut of instantaneous temperature field over one third of the chamber length. Top: coarse mesh; bottom: fine mesh.

diffusion of the COARSE mesh: it is visible from Fig. 5.3 how important it is to keep a good flame resolution also far away from the injection plane. In such a strongly confined configuration the walls are very close to the flame zone; knowing that in the diffusion regime the flame adapts its thickness to the mesh size, a coarse mesh can lead to a flame which touches the walls, leading therefore to a wrong estimation of the flame shape and wall heat flux.

5.5.2 Possible causes for the heat flux underestimation

The first thing one has to remind is that the combustion model used in this work is a preliminary one and the estimation of the coefficient used to correct the diffusivity has to be better evaluated in future work. For this reason the axial evolution of the integrated heat release rate could not be perfectly captured, leading to a slight different flame shape (different length and/or radial expansion) and to an inaccurate prediction of the heat flux at walls.

The second reason could be linked to the choice of the power-law function used to model the molecular viscosity and to the Prandtl number used for the thermal conductivity. This coefficient has been fixed assuming a mixture fraction at walls of 0.7. Fig. 5.4 shows the axial evolution of the mixture fraction at walls in the LES; the value has been circumferentially averaged. Locally the mixture fraction value takes even lower values, up to 0.2. The value of 0.7 is acceptable up to an axial coordinate $x < 120$ mm, where $0.5 < z < 0.9$. Moving downstream the assumed value really differs from the actual value found at walls and can introduce an error in the evaluation of the molecular viscosity. This is shown in Fig. 5.5, where the temperature dependency of the molecular viscosity is plotted using the power law and using the Chapman-Enskog theory with Wilke mixing rules. The cases $z = 0.7$ and $z = 0.2$ are compared. When using the power law, an error is committed in the areas where the mixture is not fuel rich. If we consider a wall temperature of 500 K, the power law underestimates the molecular viscosity of about 25 %. Considering flow conditions typical of the chamber end and applying the wall law formalism this has been evaluated in an underestimation of the wall heat flux of about 6.5 %.

The third possible reason has to be searched in the sub-grid scale model. The Sigma

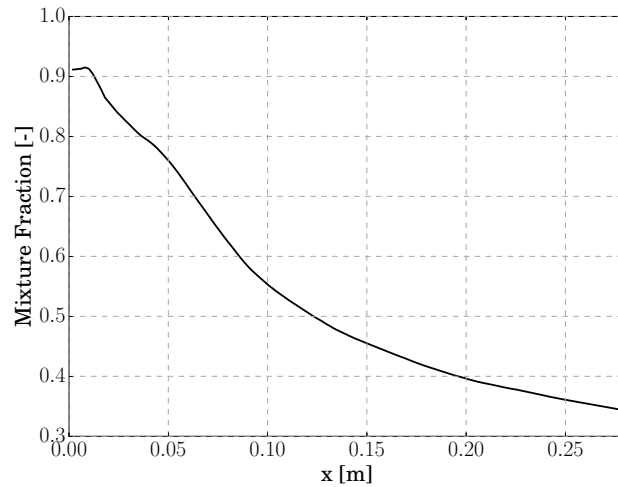


Figure 5.4: Circumferentially and time-averaged evolution of mixture fraction along the chamber walls.

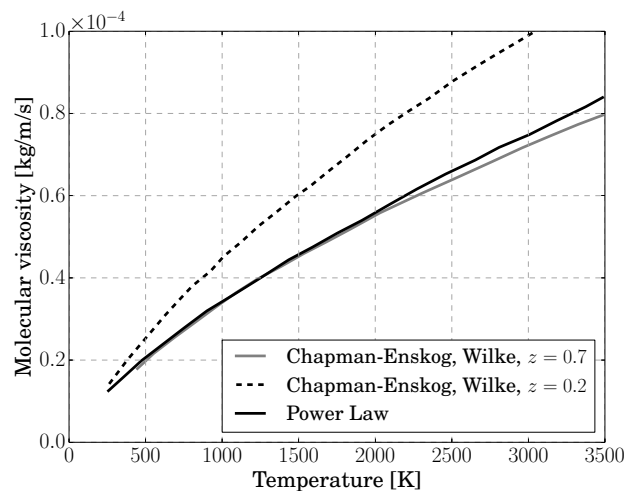


Figure 5.5: Evolution of the molecular viscosity with temperature. Comparison between the power law and the Chapman-Enskog theory with Wilke mixing rules.

model [Nicoud et al., 2011] is used here because of its very good properties for shear flows, which permit to avoid a large amount of turbulent viscosity and dissipation in the flame. However it has naturally an asymptotic behavior at solid boundaries: for this reason the turbulent viscosity in zones really close to the walls is very small. This is correct in a case where the boundary layers are resolved, but could lead to errors using wall laws, where the first node off walls is still in the turbulent region ($y^+ > 100$). With wall laws it could be better to use models like the Smagorinsky [1963] one, in which no damping for walls is present. On the contrary this kind of model is known to be too dissipative [Rudgyard et al., 1996] in the flame zone. In order to check the

5. LES OF A SINGLE ELEMENT GOX/GCH₄ COMBUSTOR

influence of the sub-grid scale model, an additional LES with the Smagorinsky model has been performed.

The evolution of pressure and heat fluxes are compared in Fig. 5.6 and 5.7 in order to verify whether or not there is an influence of the model on quantitative results.

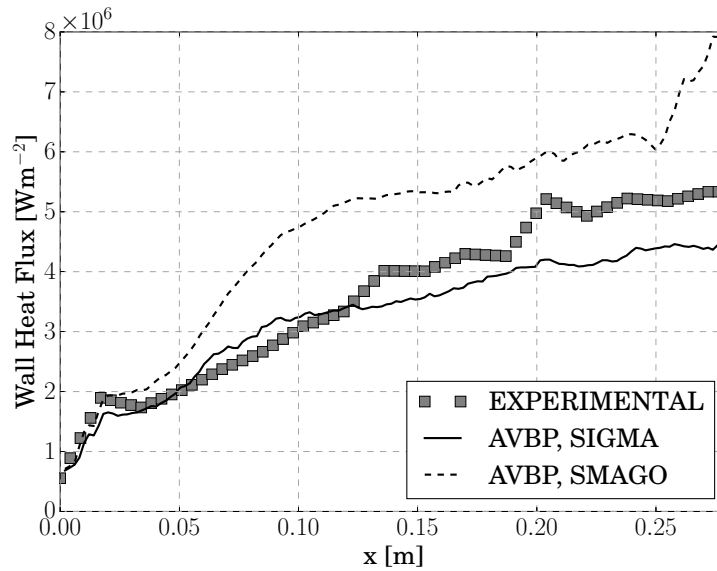


Figure 5.6: Circumferentially and time averaged axial profiles of heat flux at walls: influence of the sub-grid scale model.

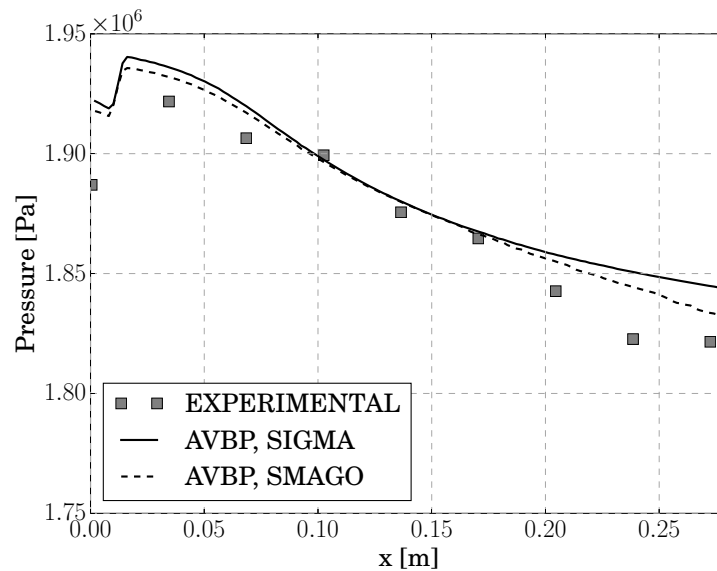


Figure 5.7: Time averaged axial profiles of pressure: influence of the sub-grid scale model.

The influence of the model is evident and of leading order on the wall heat flux. The

flux retrieved with the two models are similar in the recirculation zone, for $x < 20$ mm, then the two curves diverge. With the Smagorinsky model the flux calculated is globally 50 % higher than with the Sigma one. This has also an effect on the pressure evolution, with smaller values everywhere using the Smagorinsky model.

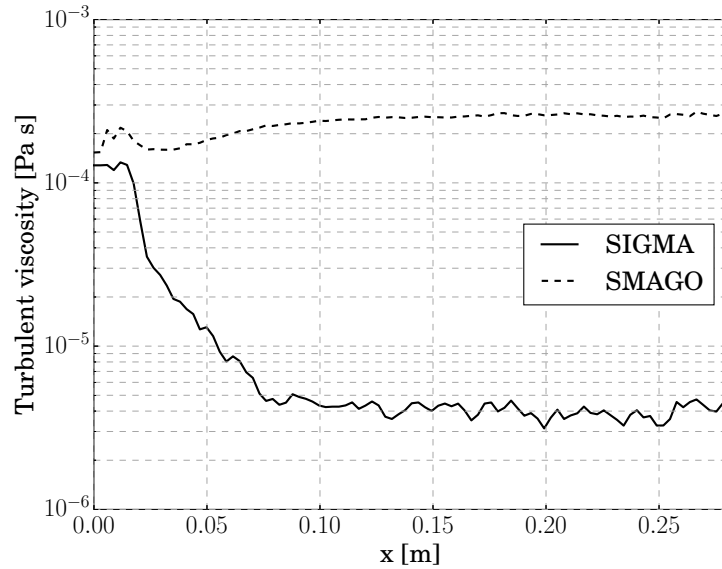


Figure 5.8: Circumferentially and time averaged axial profiles of turbulent viscosity at the first point off the wall (logarithmic scale).

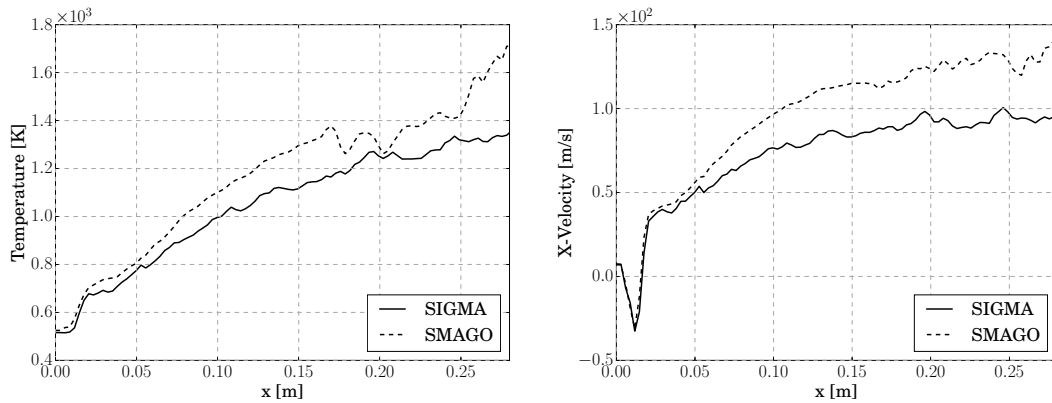


Figure 5.9: Circumferentially and time averaged axial profiles of temperature (left) and axial velocity (right) at the first point off the wall.

The reason for this behavior has to be searched in the turbulent viscosity values predicted by the model in the near wall region. The axial profile of time and circumferentially averaged values of turbulent viscosity at the first cell point off the wall are presented in Fig. 5.8: the values are similar in the recirculation zone (i.e. where the wall heat fluxes are similar) and then take very different values. The Smagorinsky model

5. LES OF A SINGLE ELEMENT GOX/GCH₄ COMBUSTOR

predicts a turbulent viscosity of around $3 \times 10^{-4} \text{ Pa} \cdot \text{s}$, while the Sigma one of around $4 \times 10^{-6} \text{ Pa} \cdot \text{s}$, which is two order of magnitude smaller.

This has an influence on the values of temperature and velocity at the first node off the wall (Fig. 5.9), which are used by the wall law to predict the wall shear stress and the wall heat flux. The difference in the heat flux evaluation by the wall law is due to both the effect of the change in velocity and temperature and the predominance of one of them is not evident.

An overall time-averaged field of turbulent viscosity is shown in Fig. 5.10. It can be seen how values are generally higher using the Smagorinsky model.

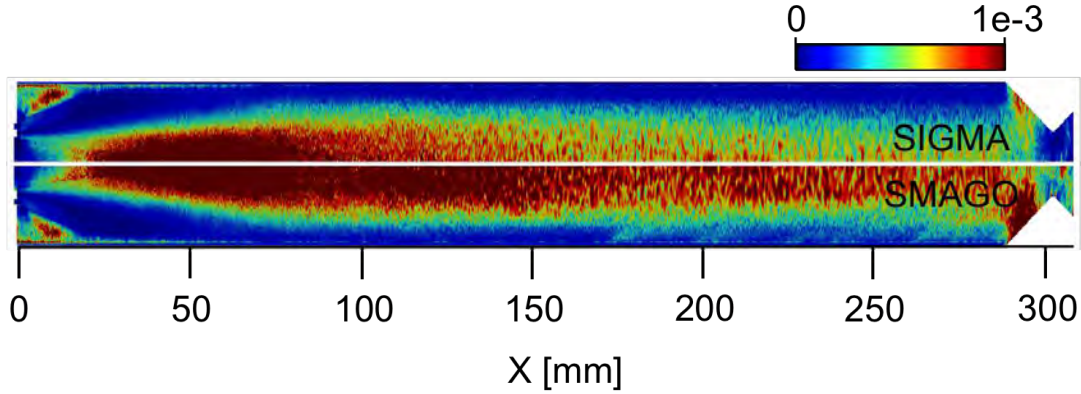


Figure 5.10: Longitudinal cut of mean turbulent viscosity field (stretched by a factor of 4 in y-direction). Top: Sigma model, bottom: Smagorinsky model.

5.6 Few words about CPU time

The convective time scale of the burner is evaluated from the mean density ρ , the total burner volume V_b and the inlet mass flow rate \dot{m} :

$$\tau_{conv} = \frac{\rho V_b}{\dot{m}} = 1.5 \text{ ms} \quad (5.16)$$

Due to the heavy mesh (200 M of cells) and to the small time step ($\approx 4 \times 10^{-9} \text{ s}$), the simulation is very CPU costly. The CPU cost associated to one convective time step on the in-house cluster NEMO (or equivalent) is about 325 kh.

The LES presented in the paper is the following of a work started earlier and the time needed to establish the flow and flame is not accounted. Since when the entire set of models described has been used, the LES has been run for a total of 2 ms. The first 0.5 ms have been discarded and data have been averaged for 1.5 ms, i.e. one convective time.

The test performed with the Smagorinsky SGS model has been run, on the contrary, for just 1/2 convective time.

Part III

**Plasma assisted combustion
in gas turbines**

Chapter 6

Bibliographical review on plasma assisted combustion

Contents

6.1	Combustion instabilities	89
6.1.1	Driving and damping of instabilities	93
6.2	Combustion instabilities control	95
6.2.1	Passive methods	95
6.2.2	Active methods	96
6.3	Plasma assisted combustion	97
6.3.1	Effects of an NRP discharge on the mixture	99
6.3.2	Enhancing combustion by means of NRP discharges	100
6.4	Modeling of NRP discharges	106

6.1 Combustion instabilities

Combustion instabilities have been known for a long time. The first one to observe an interaction between acoustics and combustion was John LeConte who, in 1858 wrote:

I happened to be one of a party of eight persons assembled after tea for the purpose of enjoying a private musical entertainment. Three instruments were employed in the performance of several of the grand trios of Beethoven, namely, the piano, violin and violoncello. Two 'fish-tail' gas burners projected from the brick wall near the piano. (...) Soon after the music commenced, I observed that the flame of the last-mentioned burner exhibited pulsations in height which were exactly synchronous with the audible beats. This phenomenon especially striking when the strong notes of the violoncello came in. It was exceedingly interesting to observe how perfectly even the trills of this instrument were reflected on the sheet of flame. A deaf man might have seen the harmony.

Flame sensibility to acoustics was clear. Twenty years more had to be waited before Rayleigh [1878] discovered that this was valid in the other way too: a moving flame

6. BIBLIOGRAPHICAL REVIEW ON PLASMA ASSISTED COMBUSTION

also excites acoustics. Since then, the thermoacoustics field exists, and has become one of the major research interests only recently with the development of high-intensity combustion systems, where unforeseen and undesired instabilities occurred.

Combustion instabilities are a major problem of several power generation and propulsion systems, such as gas turbines, liquid and solid propelled rockets and even boilers and furnaces. Such systems operate generally in stable regimes but, under certain conditions, pressure and heat release oscillations can appear. These oscillations can be of large-amplitude and are usually found at a well-defined frequency, which corresponds to an acoustic mode of the combustion chamber. This causes fluctuations in thrust and heat transfer (which can be multiplied ten-fold or more compared to the nominal value, according to [Culick and Kuentzmann \[2006\]](#)). These oscillations can also lead to structural damages or mechanical failure (see for example Fig. 6.1, from [Goy et al. \[2005\]](#)), but also to flame flashback or blow-off [[Thibaut and Candel, 1997](#); [Wolf et al., 2009](#)].



Figure 6.1: Burner assembly damaged by combustion instability (left) and new burner assembly (right) [[Goy et al., 2005](#)].

A classical historical example of how such phenomenon can be a problem in the conception of propulsion systems is the F-1 liquid rocket engine, for which 3200 full scale tests were necessary to find a stable configuration. This has been achieved with the use of baffles to control the instabilities. A full review of the design and physical processes encountered in such a system can be found in [Oefelein and Yang \[1993\]](#). The trial and error procedure performed to mitigate thermoacoustic instabilities of this F-1 engine, called for a better understanding of the mechanisms leading to instabilities, as well as the development of new methods to study and control them.

Such instabilities often appear in combustion systems because of two fundamental causes [[Culick and Kuentzmann, 2006](#)]:

- combustion chambers are acoustically closed and the internal processes that tend to damp the oscillations, which will be detailed in subsection 6.1.1, are usually weak;
- the energy sufficient to drive such instabilities is just a small part of the total

energy released during the combustion process. For example, according to [Candel \[2002\]](#), in a liquid rocket engine the mean pressure is typically $\bar{p} = 10$ MPa and the mean power density around $E_c = 50$ GWm⁻³. If an instability develops, the pressure perturbation may typically reach 1% - 10% of the mean pressure. For a 10% fluctuation, the power density associated with the unsteady motion is $E_a = 0.1$ MWm⁻³, which is clearly a minute fraction of the density of energy in the system: $E_a/E_c = 10^{-6}$.

As mentioned by [Lieuwen and Yang \[2005\]](#) and reproduced in Fig. 6.2 (adapted from [Karimi et al. \[2009\]](#)), combustion instabilities are the result of a resonant loop between the acoustics of the chamber and the heat release due to the combustion. The loop consists in the following sequence of events:

- fluctuations in velocity and/or another thermodynamic property are convected to the flame zone and cause a fluctuation in heat release rate,
- the heat release rate fluctuation generates acoustic waves [[Strahle, 1972](#)] and
- the generated acoustic oscillations excite the fluctuations in velocity or thermodynamic variables, closing the loop.

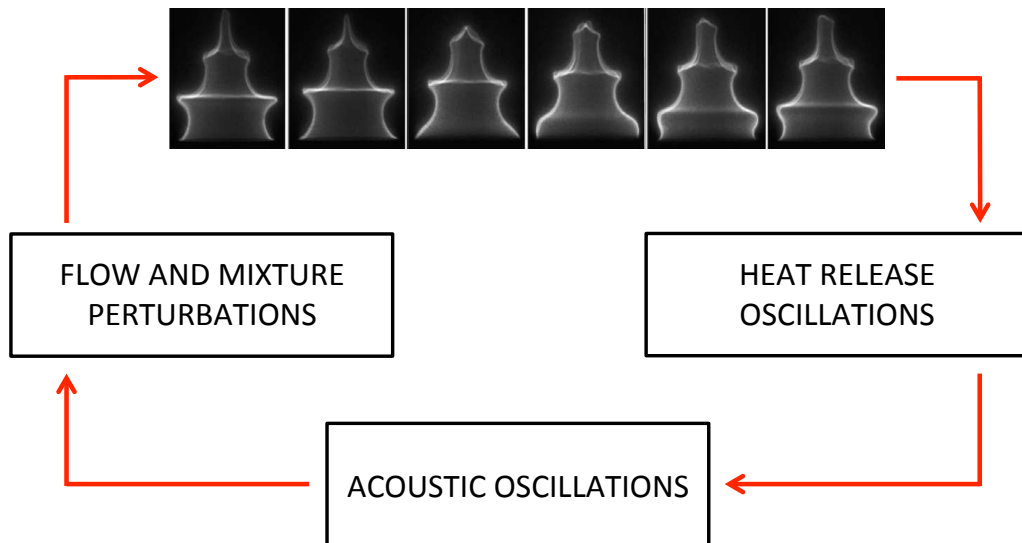


Figure 6.2: Feedback loop responsible for combustion instabilities

Then, depending on the amount of energy that is added to the acoustic perturbation by the flame and to the amount of energy that is subtracted by means of damping, the amplitude of the oscillation can increase, decrease or remain constant. A common criteria to determine the conditions under which a periodic heat transfer adds or not energy to the acoustic oscillation is the so called Rayleigh criterion [[Rayleigh, 1894](#)]. The criterion states that energy is added to the acoustic field by the periodic heat release if the heat is added to (resp. removed from) the gas when his pressure is above (resp. below) its mean value. The criterion is mathematically stated by Eq. (6.1); it indicates

6. BIBLIOGRAPHICAL REVIEW ON PLASMA ASSISTED COMBUSTION

that the heat transfer process adds energy to the acoustic field if the magnitude of the phase between heat release and the pressure oscillations is less than 90 degrees. On the other side, when these oscillations are out of phase, the acoustic field is damped by the heat addition.

$$\int_t p'(t)q'(t) dt \geq 0 \quad (6.1)$$

However, the fact that energy is added to the acoustic field does not necessarily imply that the combustor is unstable: the acoustic oscillations are spontaneously excited in the combustor only if the rate of energy supplied is greater than the rate at which acoustic energy is dissipated within the combustor or transmitted through its boundaries, as summarized by Eq. (6.2).

$$\int_T \int_V p'(x,t)q'(x,t) dt \geq \int_T \int_V \sum_i L_i(x,t) dt dV \quad (6.2)$$

where $p'(x,t), q'(x,t), V, T, L_i$ are the combustor pressure oscillation, heat addition oscillation, volume, period of the oscillation and the i th acoustic loss process respectively.

In Eq. (6.2), the equal sign identifies the condition in which limit cycle oscillations are reached: in this particular case the time derivatives of energy supplied to and removed from the system are equal. Fig. 6.3 from Poinso and Veynante [2011] shows the typical evolution of pressure in a combustor when an instability is triggered at time $t = 0$ [Poinso et al., 1988]. First, an oscillation appears. Then, if the energy

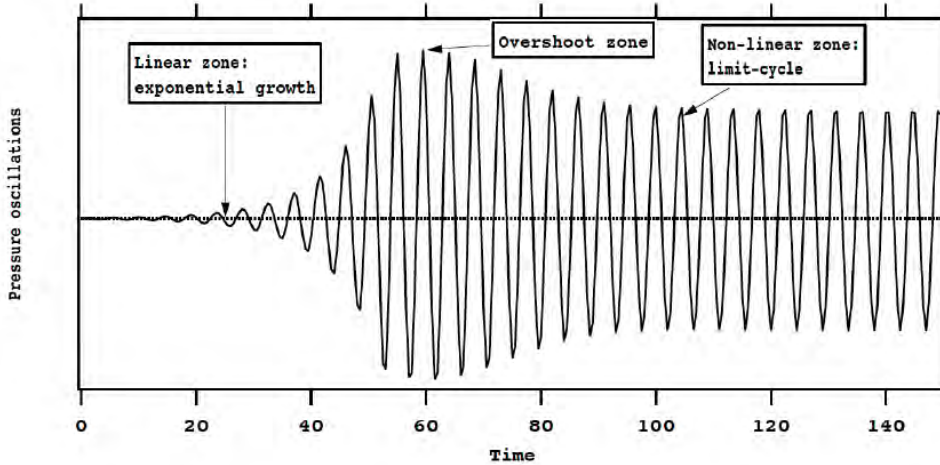


Figure 6.3: Growth of a combustion instability to limit cycle

supplied to the acoustic field by heat release is greater than the energy subtracted by the damping effects, the oscillation grows exponentially until it reaches a "second phase" when non-linear effects appear leading to an equivalence between the energy addition and damping to acoustic field: the so called limit cycle. This can be due to an increase in damping phenomena or to a change of phase between pressure and heat release oscillations. It is generally preceded by a short zone called the "overshoot zone" in which non linear phenomena lead to oscillation amplitudes greater than limit cycle

ones. When the limit cycle is reached, the Rayleigh criterion can give non sufficient information [Samaniego et al., 1993] and it is necessary to investigate and understand the physical mechanisms that create the instabilities and not only their manifestation through Rayleigh-type criteria.

6.1.1 Driving and damping of instabilities

Combustion instabilities can be triggered by various mechanisms. As illustrated by Fig. 6.4 from Lieuwen and Yang [2005] for a gas turbine configuration, the phenomena which were considered relevant are:

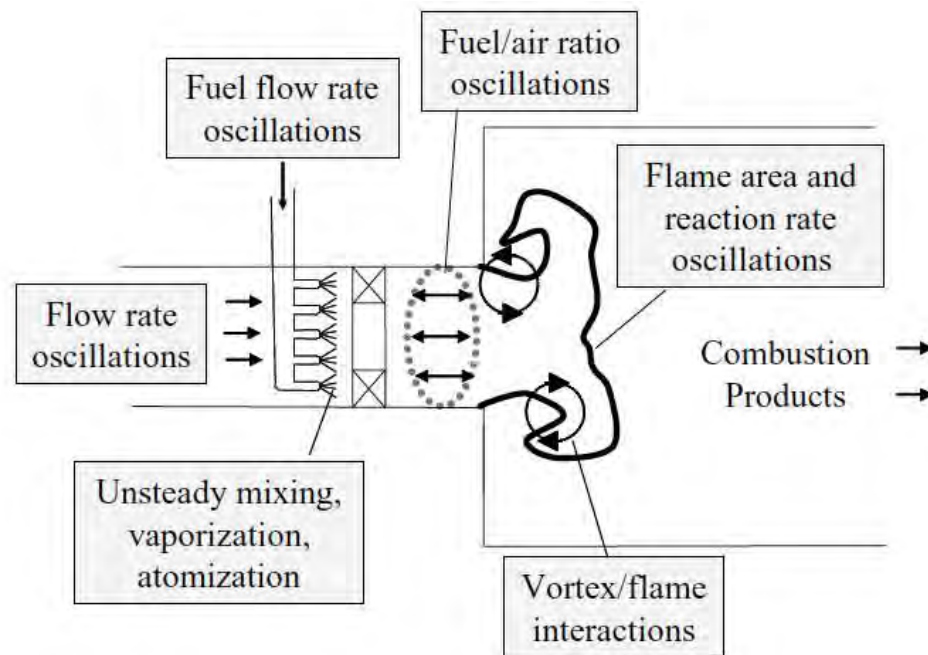


Figure 6.4: Processes that cause an instability in a gas turbine

- **Coupling between the acoustics of the combustion chamber and the feed line:** if fuel nozzles are not choked, as in real combustors, a pressure oscillation in the chamber can modulate the pressure drop across the nozzle, generating fluctuations in the fuel-injection rate. This will generate in turn fluctuations in heat release that will drive the acoustic oscillations, as shown for example by Kendrick et al. [1998].
- **Oscillations in equivalence ratio:** as investigated by Lieuwen et al. [2001], the pressure oscillation can propagate into the premixer section and influence mixing mechanisms, generating a mixture with equivalence ratio varying in time. As known from Zukoski [1978], the characteristic chemical time, which is inversely proportional to reaction rate, can vary significantly, especially in the lean regime.
- **Oscillations in atomization, vaporization and mixing:** in the case of a liquid spray, the pressure field can influence the droplet size and spacial distri-

6. BIBLIOGRAPHICAL REVIEW ON PLASMA ASSISTED COMBUSTION

bution, as well as the evaporation and mixing rates [see for example [Pera and Reveillon, 2007](#)]. This will again produce a mixture convected to the flame with equivalence ratio varying in time and space, which drives the instability. Some theoretical studies on this phenomenon have been performed by various authors: [DiCicco and Buckmaster \[1996\]](#) analyzed the role of the response time of a droplet to fluid mechanics oscillations for various fuels, droplet sizes, inlet temperatures and flow velocities. They found that instabilities are stronger in the case of low frequencies, high velocities and high liquid volatility. [Duvvur et al. \[1996\]](#) also investigated the influence of vaporization on instabilities, finding that in some cases it can directly drive the oscillations.

- **Periodically flame-area variations:** interactions between the acoustic field and the flame surface cause the latter to vary periodically in time: the flame can indeed be described as an acoustic monopole [[Hurle et al., 1968](#); [Strahle, 1971, 1972, 1978, 1985](#)]. It can be compared to an inflating and deflating balloon which radiates sound in all directions. The sound is in turn reflected back by the boundaries and drives the instabilities. Effects of the influence of flame variation on instabilities have been investigated, among others, by [Venkataraman et al. \[1999\]](#) on a coaxial dump combustor and by [Reuter et al. \[1990\]](#) on a ramjet burner.
- **Vortex shedding:** in combustors stabilized with a bluff body, as well as in those with sudden expansions or swirled flows, the presence of large scale coherent structures are often encountered. These vortices can distort the flame surface or trap volumes of fresh gases, which then burn rapidly; both mechanisms produce fluctuations in heat release that drive the instability. Evidence of this mechanism can be found in the work of [Hegde et al. \[1987\]](#) and [Schadow and Gutmark \[1992\]](#), showing that burning vortical structures can drive the instability. The fact that a number of modes are vortex driven was also investigated experimentally by [Poinsot et al. \[1987\]](#) or by [Paschereit et al. \[1998\]](#) in industrial type combustors.

Moreover, it is worth noting that heat release rate oscillations add energy to the acoustic field only if their characteristic time scale is of the order of some integer multiple of the acoustic oscillation period. Estimations of these characteristic time scales and of the way in which an instability is triggered or not can be found in [Huang and Yang \[2009\]](#), [Candel \[2002\]](#) and [Lieuwen and Yang \[2005\]](#). Each one of the mechanisms described above has a proper time scale, that also varies depending on the operating parameters: at different regimes different instabilities can appear, with different characteristic frequencies, amplitudes and behaviors.

In this process, the damping mechanisms play a crucial fundamental role that subtracts energy from the oscillation and determines whether an instability appears or not. Energy can be dissipated or removed from an unstable mode via three different processes:

- **Viscous and heat-transfer damping mechanisms:** the energy contained in an acoustic wave is converted into vortical or entropical fluctuations due to no-slip and temperature boundary conditions or flow separation at sharp edges. This effect is fully explained in [Temkin \[1981\]](#).

- **Convection and radiation of acoustic energy:** mean flow can have a significant impact on acoustic losses: acoustic energy can leave the system by propagation or convection through its boundaries. Some energy can also be lost at zero mean flow because of acoustic radiation. The effect of mean flow Mach number has been studied by [Ingard and Singhal \[1975\]](#), where a decrease of the outlet reflection coefficient is found when increasing the Mach number.
- **Transfer of energy from an unstable acoustic mode to noise or to other modes:** acoustic energy can be transmitted from coherent (narrow-band) to incoherent (spectrally distributed) oscillation by random modulation processes as reflection and scattering from turbulent eddies [[Kim, 1995](#)] or randomly flapping flame fronts [[Lieuwen et al., 2002](#)]. In this case, even if the total acoustic energy does not decrease, the specific oscillation is attenuated with an effective damping of its amplitude. Acoustic energy can also go from an unstable mode to a damped one through non linear phenomena [[Culick and Kuentzmann, 2006](#)].

6.2 Combustion instabilities control

Thermo-acoustic instabilities should be avoided in a combustor, however sometimes this is not possible. This is due to the complexity of the phenomena and to a lack of understanding, which leads to a difficult prediction of whether an instability will or will not appear. Therefore constructors have put an increasing attention on control techniques to limit or suppress them. Obviously, this must be done with attention to pollution, otherwise fuel-rich flames, more stable but more polluting could be used. Control techniques are generally classified in two categories: **passive methods**, which do not use external mechanisms and consist simply in geometrical modifications or addition of structural elements and **active methods** which use sensors and/or actuators in order to diminish or suppress the coupling between the acoustics and the flame. In this section a brief overview of the available control techniques is provided. For a detailed analysis one can refer to the book of [Culick and Kuentzmann \[2006\]](#) as well as to the reviews of [McManus et al. \[1993\]](#); [Candel \[2002\]](#); [Docquier and Candel \[2002\]](#) and [Huang and Yang \[2009\]](#).

6.2.1 Passive methods

- **Acoustic dampers:** elimination of acoustic oscillation by damping them has commonly been used in gas turbines, rocket engines and other combustion systems. The simple acoustic damper is a hole, as pointed out hilariously by [Putnam \[1971\]](#): *"To solve an oscillating combustion problem, drill a hole. If that doesn't work, drill two holes"*. This is what multi-perforated plates in the liner walls of gas turbines do, acting as an acoustic damper. It is however obvious how holes can not be drilled everywhere in a combustor and so other techniques are preferred. Two types of acoustic dampers with closed resonators have been employed in premixed gas turbine combustors: Helmholtz resonators and quarter-wave tubes. When pressure oscillations occur, flow enters and exits the resonator mouth. The energy may dissipate at the entrance, providing damping to the system. The in-

6. BIBLIOGRAPHICAL REVIEW ON PLASMA ASSISTED COMBUSTION

stallation of an acoustic damper also provides a jump in the acoustic impedance of the combustor liner and subsequently modifies the boundary conditions in such a way that certain discrete oscillations are attenuated and therefore become less destructive to the combustor. Helmholtz resonators can be found in various industrial combustors and a detailed analysis can be found in [Huang and Yang \[2009\]](#). The greater inconvenient of this kind of system is that a particular resonator works well for a specific oscillation frequency: if another frequency appears, another resonator has to be designed and inserted in the system, and so on.

Another way to damp oscillation is to use the so called "baffles". A typical baffle configuration consists of flat plates extending into a chamber perpendicularly from walls. Three mechanisms [[Huang and Yang, 2009](#)] have been proposed for explaining successful elimination of instability by baffles: (1) modification of acoustic resonance properties (i.e., frequency and waveform); (2) restriction of unsteady motion between baffle blades, and subsequent shielding of the sensitive mechanisms for instabilities; and (3) damping of oscillations by vortex shedding, flow separation, and viscous dissipation. Baffles have been largely used especially in rocket combustors (the F-1 engine is the most famous example). However, they have two major drawbacks: a priori design is difficult and multiple tests are needed to identify the best configuration.

- **Fuel staging and pilot flames:** combustion dynamics is controlled by manipulating the way in which the reactive mixtures are inserted in the combustion chamber. Fuel staging can help to suppress instabilities as the amount of heat release provided by each one of the stages can be controlled. In the same way the use of pilot flames can limit or suppress instabilities, as found for example by [Steele et al. \[1999\]](#). The main inconvenient of this kind of systems is that combustion can easily go out the range of flame temperature in which pollutant formation is low.
- **Fuel injector and burner geometries:** a modification of the geometry can change the acoustic modes shape and the time lag between flame and acoustics. It is clear how geometrical modification will work only for a defined instability but can not be adapted at each new acoustic frequency which may appear.

6.2.2 Active methods

Active control techniques use external excitations to limit combustion oscillations. The most used technique is feedback control by modulation of inlet air or fuel in order to reduce as much as possible the difference between the instantaneous desired and actual behavior of the dynamic system. The idea is to use sensors and actuators to adapt the incoming flow, as shown in Fig. 6.5 (left) from [[Huang and Yang, 2009](#)]. The adaptation of incoming flow can also serve for example to limit equivalence ratio fluctuations and limit one of the phenomena which lead to unsteady heat release (Fig. 6.5, right, from [Cohen and Banaszuk \[2003\]](#)). Note that active control of combustion by means of feedback techniques is not a matter of destructive interference in a sound field. In contrast to active noise control, the process produces successful results by favorable disruption of the sources generating the sound. When the combustion instability is

controlled, no noise exists at all. A detailed review of active techniques can be found in the already cited book of [Culick and Kuentzmann \[2006\]](#). This kind of systems have

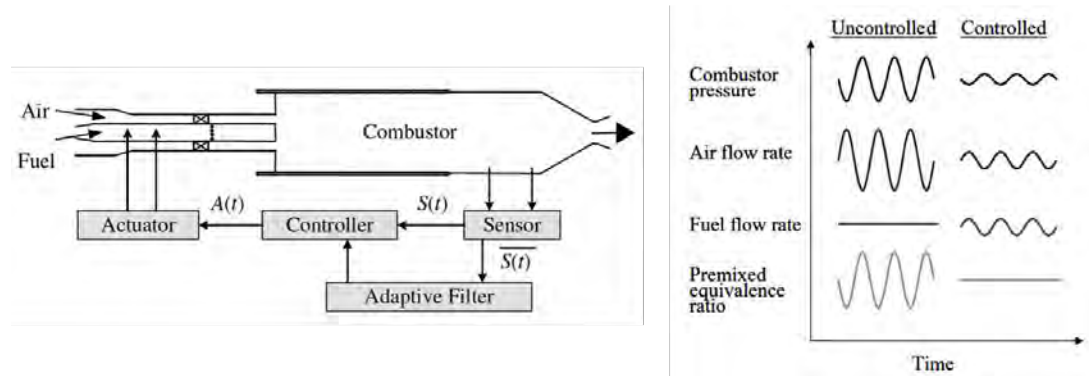


Figure 6.5: Left: schematic of an active combustion control system. Right: equivalence ratio fluctuations control by means of fuel pulsing

already been used in gas turbines, see for example [Hermann and Hoffmann \[2004\]](#). Apart from feedback control techniques, another class of active control techniques (the term "active" indicates the use of an external power supply) is arising in this recent years: electromagnetic actuators (DC electrical fields, plasma discharges) and radiofrequency. A review of DC actuators and radiofrequency will not be detailed here and can be found in the Ph.D. thesis of [Di Vita \[2016\]](#). A review of plasma assisted combustion is now presented.

6.3 Plasma assisted combustion

According to the reviews of [Starikovskiy and Aleksandrov \[2013\]](#) and [Ju and Sun \[2015\]](#) plasma, which is the fourth state of matter, provides an unprecedented opportunity for combustion and emission control thanks to its capability in producing heat, active radical species and modifying the transport properties of the mixture (see Fig. 6.6). An increase in reactants temperature can indeed enhance combustion, as well as the production of radicals (atomic O for example) which create new reaction pathways for the fuel oxidation.

Two different kinds of plasma exist. The equilibrium plasmas are characterized by electrons temperature, as well as rotational and vibrational temperature of particles, equal to the neutral gas temperature and in which the electrons number density is very high. On the contrary we talk about non-equilibrium plasmas if the temperature is not the same anywhere: electronic, vibrational, and rotational temperatures are very different from the neutral gas temperature. In this case the electrons number density is relatively low. Compared to equilibrium plasma, non-equilibrium plasma is more kinetically active due to the rapid production of active radicals and excited species via electron impact dissociation, excitation, and subsequent energy relaxation [[Raizer and Allen, 1997](#)].

The effect that plasma can have on combustion is highly dependent of this kind of

6. BIBLIOGRAPHICAL REVIEW ON PLASMA ASSISTED COMBUSTION

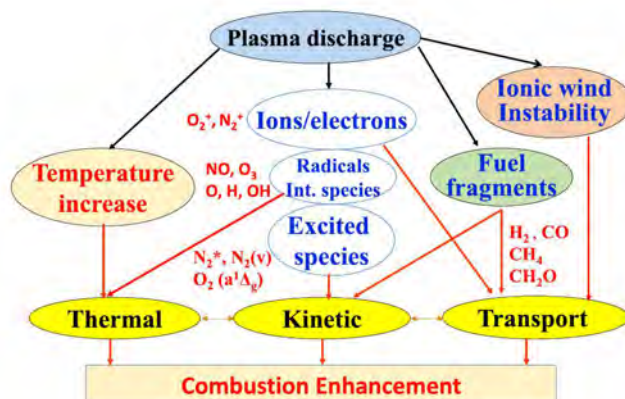


Figure 6.6: Schematic of the combustion enhancement pathways of plasma assisted combustion [Ju and Sun, 2015]

impact processes and so on plasma properties. Specifically the parameters which characterize a plasma are the electrons temperature and the electrons number density, as shown in Fig. 6.7. Among others, sparks and arcs are equilibrium plasmas, with low

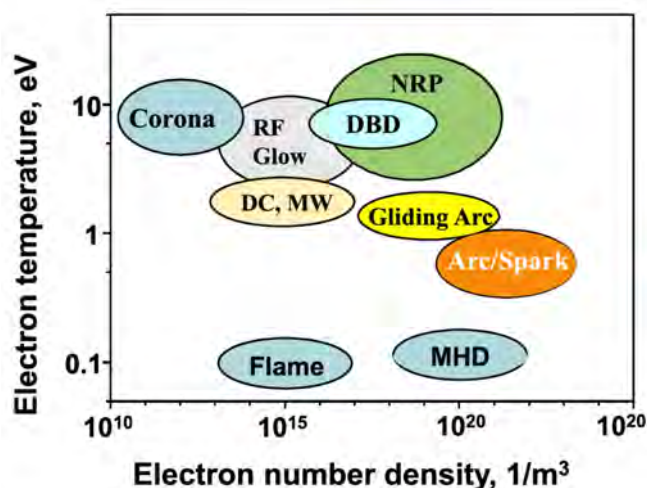


Figure 6.7: Schematic of electron temperature and number density for different discharges: Corona, direct current (DC) discharge, microwave (MW) discharge, dielectric barrier discharge (DBD), radio-frequency discharge (RF), glow discharge, gliding arc, nanosecond repetitively pulsed discharges (NRP), arc, magneto-hydrodynamic discharge (MHD) and flame. Adapted from Ju and Sun [2015]

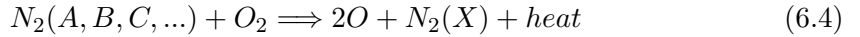
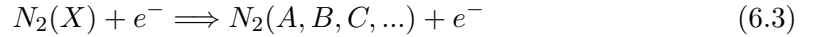
electrons temperature. On the contrary, corona, DC, glow, RF, DBD, NRP, gliding arc, and MW have higher electrons temperature and are classified as non-equilibrium plasmas. Among them, according to Starikovskaia [2006], NRP can produce a very strong reduced electric field and allow energy transfer mainly for electronic excitation and dissociation. As such, a nanosecond discharge is a highly non-equilibrium process and has high electrons temperature to enable fast electron impact dissociation in a large volume. The capability of NRPs to sustain a non-equilibrium plasma state of the

gas has been demonstrated by Kruger et al. [2002].

6.3.1 Effects of an NRP discharge on the mixture

An NRP discharge has multiple effects on the mixture in which is applied. These effects are of thermal, chemical and mechanical nature.

During an NRP discharge, a strong electric field is formed increasing the kinetic energy of free electrons. For electric field conditions typical of NRPs in air, the electrons accelerated by the electric field produce mainly electronically and vibrationally excited molecular nitrogen [Nighan, 1970; Aleksandrov et al., 1981]. This is true also in hydrocarbons-air mixtures, as shown by Starikovskiy and Aleksandrov [2013] and Bak et al. [2012]. The relaxation of the electronically N_2 excited states happens by means of collisional quenching with O_2 atoms and results in an ultrafast (time scale of nanoseconds) heating and an ultrafast dissociation of O_2 , with production of O atoms. Denoting with $N_2(A, B, C, \dots)$ the electronically excited states and with $N_2(X)$ the ground state of nitrogen, the above-mentioned mechanism can be represented by [Popov, 2001, 2011; Rusterholtz et al., 2012]:



The ultrafast heating is of the order of magnitude of 1000 K [Pai et al., 2010; Rusterholtz et al., 2012]. The vibrationally excited state will relax slowly, resulting in a slow heat release. Denoting with $N_2(v)$ the vibrationally excited state of nitrogen, the reactions involved can be summarized by:



with reaction 6.5 occurring in the time scale of the discharge, and reaction 6.6 in a much slower one. This provides a fast and slow **thermal effect** of the NRP discharge on the reactive mixture.

Regarding radical production, they are produced by direct electronic collision or by collision with excited molecules. Focusing on methane chemistry, it has been found by Sun et al. [2012] that O is the species which has the highest impact in combustion enhancing by means of a modification of the pathways for methane oxidation. Fig. 6.8 shows a path flux analysis of the fuel oxidation for a diffusion flame using a mixture of $O_2/Ar/He/CH_4$ as oxidizer and CH_4 diluted by Ar as fuel. H and OH, which are important for the chain branching reactions leading to fuel oxidation (Fig. 6.8-a), are produced by the interaction between the O molecules and fuel or its intermediate oxidized and dissociated products (Fig. 6.8-b/c). O is produced in a large amount by O_2 molecules collision with electrons or excited species (Fig. 6.8-c). Ju and Sun [2015] showed how, considering ignition, the great contribution of plasma is of bypassing the slow chain branching reactions which are at the base of the oxidation path. These

6. BIBLIOGRAPHICAL REVIEW ON PLASMA ASSISTED COMBUSTION

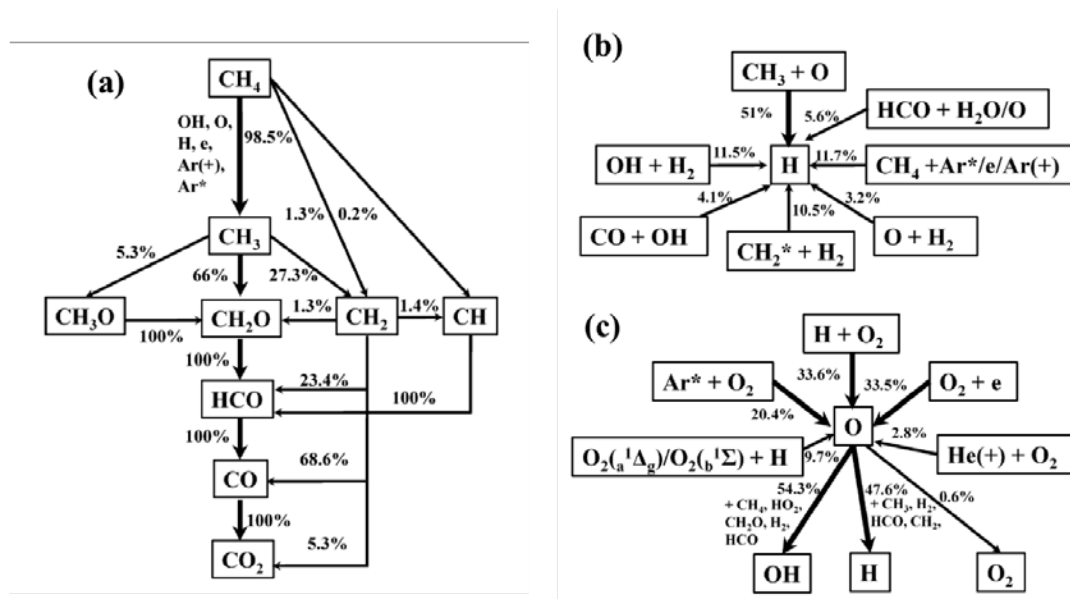


Figure 6.8: Oxidation paths for a diffusion methane flame. (a): CH₄, (b): H, (c): O
Adapted from Sun et al. [2012]

reactions produce the radicals needed to speed up the fuel oxidation but have generally an high activation energy and they are slow. If radicals are produced instead by plasma discharges, the process can be quite faster. This **chemical effect** is particularly strong at low temperatures. At high temperatures (higher than 1000 K for example for H₂/O₂ combustion according to Ju and Sun [2015]) the conventional chain branching reactions are generally dominating for radical production and the NRP discharges effect is mostly thermal. Ignition enhancing by NRP discharges has been confirmed by the experimental work of Pancheshnyi et al. [2006].

Beside thermal and chemical effects, an **hydrodynamic (mechanical) effect** is induced by NRP discharges. According to Xu et al. [2011, 2014, 2016], during each pulse temperature and pressure increase, leading to the creation and propagation of a shock wave. This can lead to wrinkling of the flame front, thus enhancing ignition particularly at high pressures.

6.3.2 Enhancing combustion by means of NRP discharges

Plasma assisted combustion has demonstrated capability of enhance combustion in a large number of combustion devices and, among them, supersonic propulsion and scramjet engines, internal combustion engines, pulse detonation engines, gas turbine engines. Plasma has been used also for fuel reforming and pollutant emission reduction. A full review of these applications can be found in Starikovskiy and Aleksandrov [2013] and Ju and Sun [2015]; we provide here only a review of plasma used to enhance or stabilize combustion in gas turbine like systems.

As discussed in chapter 1, lean blowout limit, flame stabilization and instability are the key issues of modern gas turbine engines. Several experimental facilities have proven how plasma can increase the flame stability and achieve ultra-lean combustion. Systems using nanosecond repetitively pulsed discharges are presented here since, according to Laux et al. [2013], they present the advantage of producing strong synergistic effects from pulse to pulse and of being usable in continuous operation.

6.3.2.a Increase of the stability limit

Starting with the most simple systems, a bluff body stabilized lean premixed propane-air flame at atmospheric pressure has been studied by Pilla et al. [2006]. The turbulent

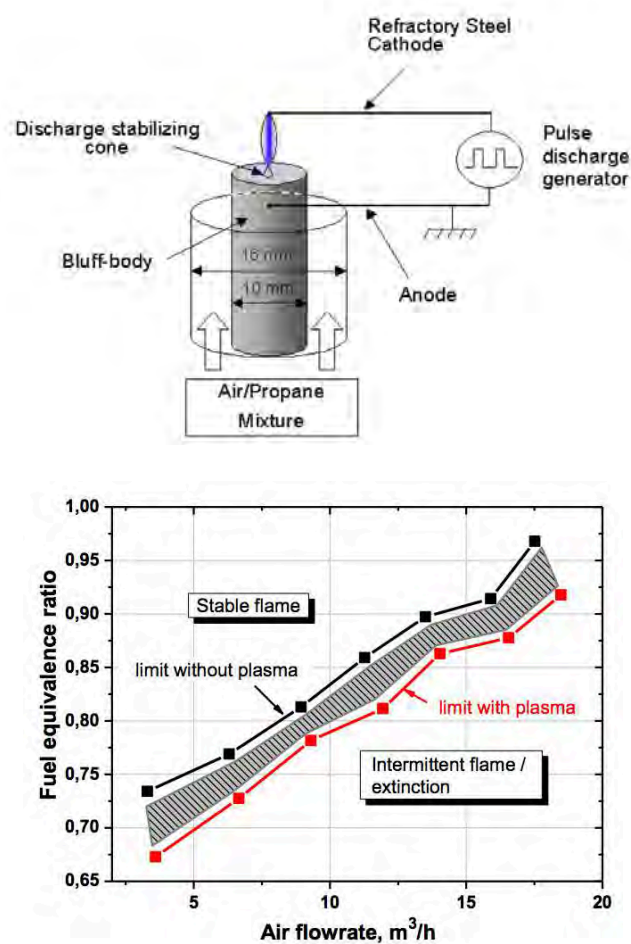


Figure 6.9: Top: experimental setup of Pilla et al. [2006]. Bottom: domain of stability, adapted by Laux et al. [2013].

flame has a power of about 25 kW. The NRP discharges, created between an aluminum bluff body and a refractory steel electrode located in the recirculation zone 5 mm downstream of the bluff body, are of 10 kV amplitude, 10 ns duration, and pulse

6. BIBLIOGRAPHICAL REVIEW ON PLASMA ASSISTED COMBUSTION

repetition frequency of 30 kHz. The energy supplied is of 2.5 mJ/pulse, corresponding to an average power of 75 W at 30 kHz. This power is less than 1 % of the power released by the stabilized flame. A schematic view of the experimental device is presented in Fig. 6.9, top. In Fig. 6.9, bottom, the effect of NRPs on the flame stabilization is shown: the plasma extends the domain of flame stability to fuel equivalence ratios about 10 % lower than without plasma.

Moving to swirl stabilized flames, more representative of gas turbine combustors, the same effect was found. Pilla et al. [2008] studied a 50 kW propane-air swirl stabilized flame. The flame is confined with quartz windows and a non-equilibrium plasma is

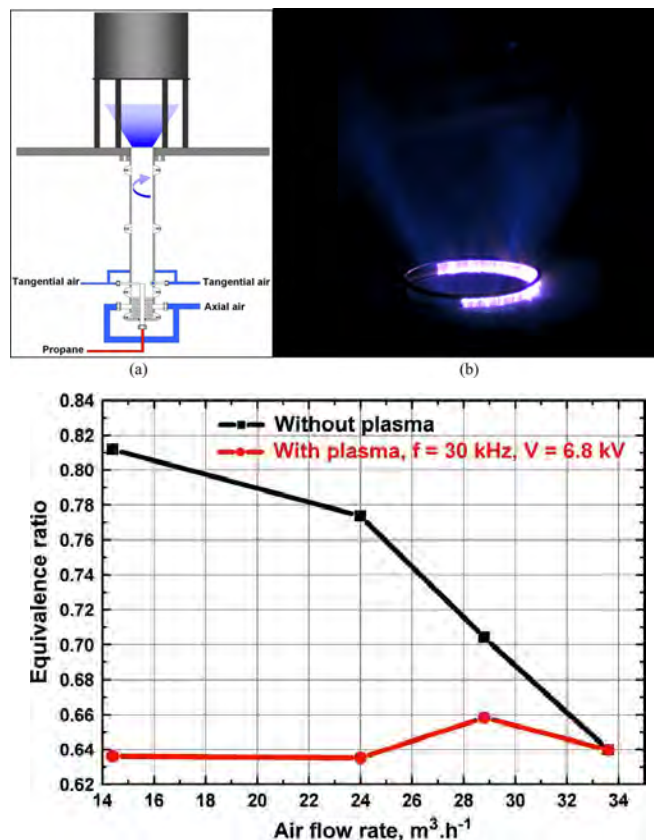


Figure 6.10: Top: experimental setup of Pilla et al. [2008]. Bottom: comparison of the equivalence ratio of the transition from the stable to the intermittent flame with and without plasma.

created between the exit of the injection tube and a ring electrode placed 5 mm above the burner (see Fig. 6.10, top). The pulses are 6.8 kV in amplitude, 15 ns in duration and at a repetition frequency of 30 kHz. Different flame regimes were obtained with this burner. The main regime is a very luminous stable flame, attached to the exit of the injector. Increasing the air flow rate leads to a lifted flame. At higher flow rates, the flame blows off. By applying NRP discharges, the domain of flame stability was extended and the equivalence ratio of the transition from the stable flame to the lifted flame was decreased by about 10 % (Fig. 6.10, bottom).

Barbosa et al. [2015] further studied the effects of a nanosecond pulsed discharge plasma

on the flame stability domain of a lean C_3H_8 /air premixed swirled flame operating at atmospheric pressure. The peak power of the combustor was 52 kW. NRP discharges

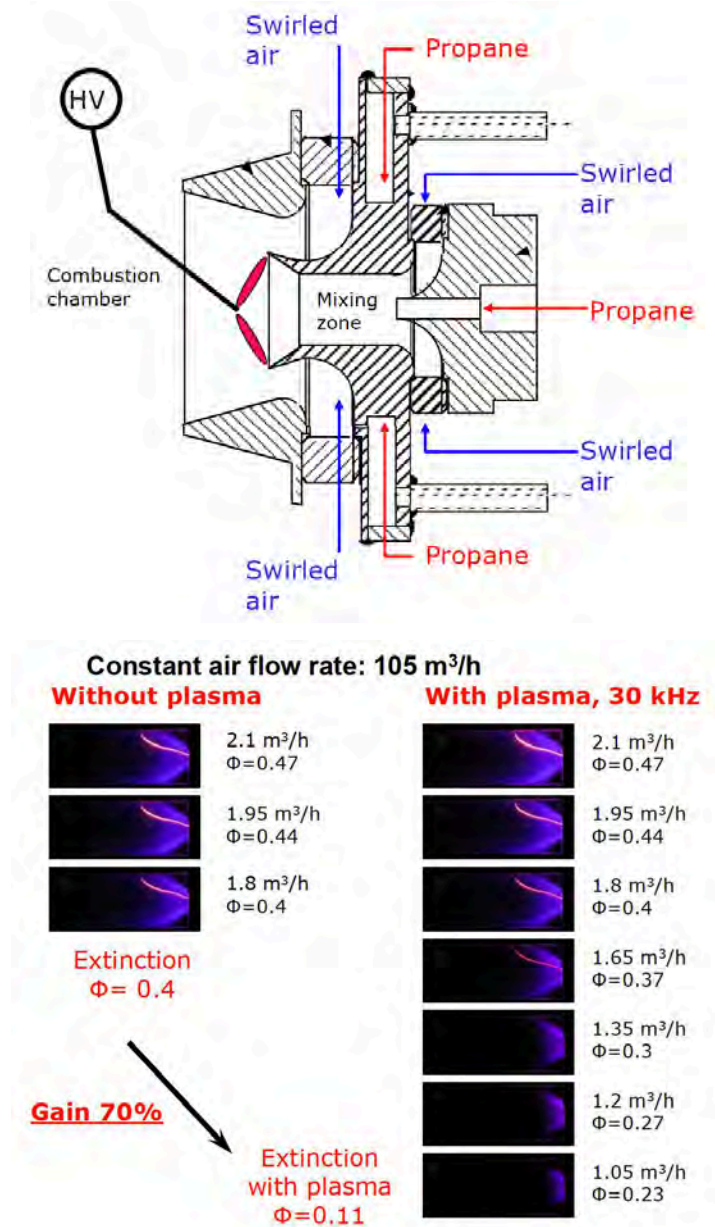


Figure 6.11: Top: experimental setup of Barbosa et al. [2015]. Bottom: CH^* chemiluminescence and evidence of the increase in stability limit, adapted by Laux et al. [2013].

was produced by a pulse generator with 10 ns pulse width, 30 kV of voltage and at a repetitive frequency of 30 kHz: the total plasma power was of approximately 350 W. A schematic of the experimental system and plasma generator position is shown in Fig. 6.11, top.

Fig. 6.11, bottom, presents images of CH^* chemiluminescence for a selected operating condition, without and with plasma discharges. It is clear how NRPs extend the stabil-

6. BIBLIOGRAPHICAL REVIEW ON PLASMA ASSISTED COMBUSTION

ity limit drastically. The blow-off equivalence ratio was diminished from 0.41 to 0.11. Similar effects were obtained for a 200 kW turbulent aerodynamic injector working with kerosene/air at 3 bar [Heid et al., 2009]. In this case, the lean extinction limit was decreased from a global equivalence ratio of 0.44 to 0.21 using NRP discharges with about 1 % of the flame power.

6.3.2.b Instabilities control

In order to perform a preliminary study to check whether or not the dynamical response of a flame can be affected by means of NRP discharges, Lacoste et al. [2013b] investigated the temporal response of a 2 kW bluff body stabilized weakly turbulent lean premixed propane/air flame. The experimental setup is the one already studied by Pilla et al. [2006], where the mass flow rates have been adapted in order to be in a stable combustion regime, with a fully developed flame. NRPs were used in order to dynamically modify the lift-off distance of the flame, which was significantly reduced. According to the authors, this showed how NRP discharges may be well suited for applications in combustion instability control: it is possible to affect the flame dynamically and this can be used to counteract the oscillations induced by acoustic perturbations. Moeck et al. [2013] studied the effect of NRP discharges on combustion instabilities in a premixed swirl stabilized combustor burning natural gas. The NRP system generates discharges with 10 ns pulse width, 12 kV in amplitude and a repetition frequency which could vary between 10 and 80 kHz. The discharge generator system was installed at the exit of the injection tube, as shown in Fig. 6.12: nanosecond pulsed discharge filaments were generated between the central pin electrode and the loop-electrode in a disk-shaped area. The effects of the discharge first on a stable flame and then on

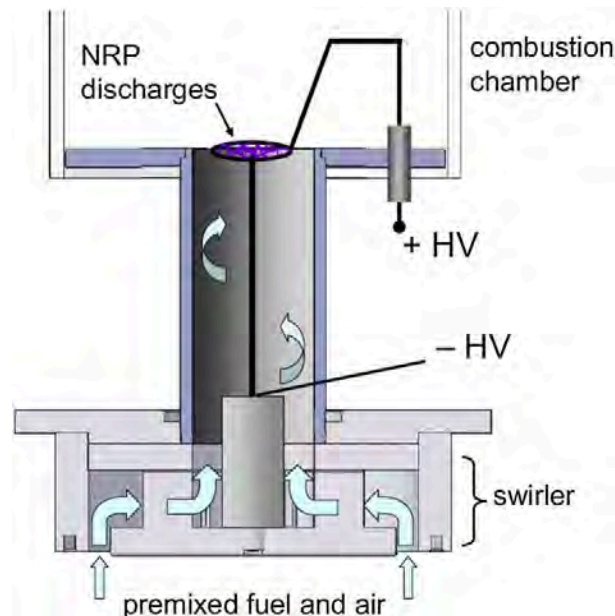


Figure 6.12: Experimental setup of Moeck et al. [2013].

instabilities were analyzed. The mean flame shape without discharges is compared to

the case with discharges at pulse repetition frequencies between 5 and 25 kHz, which corresponded to an electrical power of 30 to 150 W. The effects of the discharges for operating conditions leading to a flame of 50 kW are shown in Fig. 6.13 by means of CH^* chemiluminescence imaging. Without plasma, the flame was stabilized in the shear layers associated with the recirculation zone (Fig. 6.13-a), in a lifted position. As the discharges were activated and the pulse repetition frequency was increased, the flame moved successively further upstream and eventually stabilized in the burner passage (Fig. 6.13-b/c/d/e/f). The effect of NRP discharges on the combustion dynamics was

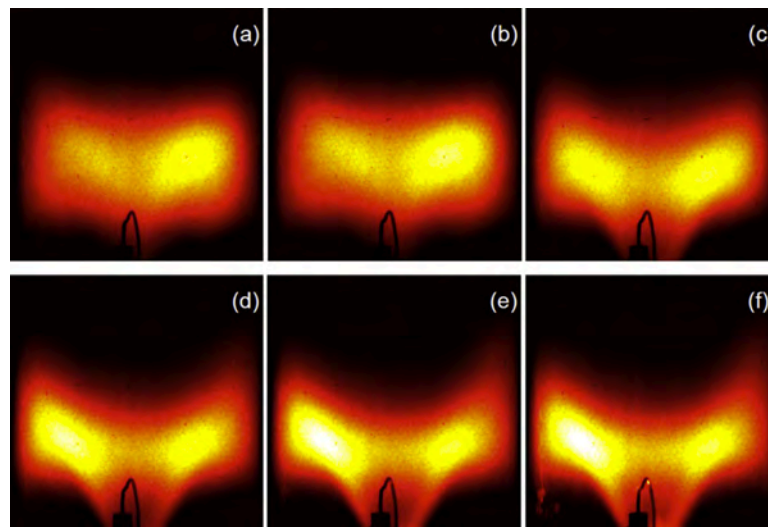


Figure 6.13: Averaged CH^* chemiluminescence intensity for the case without plasma discharges (a), and with $f = 5, 10, 15, 20,$ and 25 kHz (b-f); equivalence ratio 0.62, thermal power 50 kW [Moeck et al., 2013].

also investigated. It was found that plasma has a strong impact on the pressure oscillations associated with thermoacoustics. The use of nanosecond discharges reduced the amplitude of the pressure pulsation in nominal conditions (Fig. 6.14, top). It was also found how, at some conditions NRP discharges could trigger the instability from a stable case instead of suppressing it (Fig 6.14, bottom).

A similar experimental rig was re-designed by Lacoste et al. [2013a], who studied the dynamics of a swirl stabilized lean premixed CH_4/air flame. The burner works at atmospheric conditions and it has a thermal power of 4 kW (Fig. 6.15, left). The NRP discharges system features a pulse duration of 10 ns in duration, 8 kV in amplitude at a repetition frequency of 30 kHz; the total plasma power is 40 W. The flame transfer function was computed by means of measurement of velocity and CH^* chemiluminescence signal. The flame response was measured in a range of frequencies from 16 to 512 Hz for an equivalence ratio of 0.7. It was found how the gain of the flame transfer function was affected in almost the entire range of frequencies studied (Fig. 6.15, right, top). The gain was diminished in general. The NRP discharges were found also to mitigate by an order of magnitude the velocity fluctuations in a self-sustained combustion instability case (Fig. 6.15, right, bottom). An updated version of the experimental setup of Lacoste et al. [2013a] will be studied in chapter 7 and 9 of this work.

6. BIBLIOGRAPHICAL REVIEW ON PLASMA ASSISTED COMBUSTION

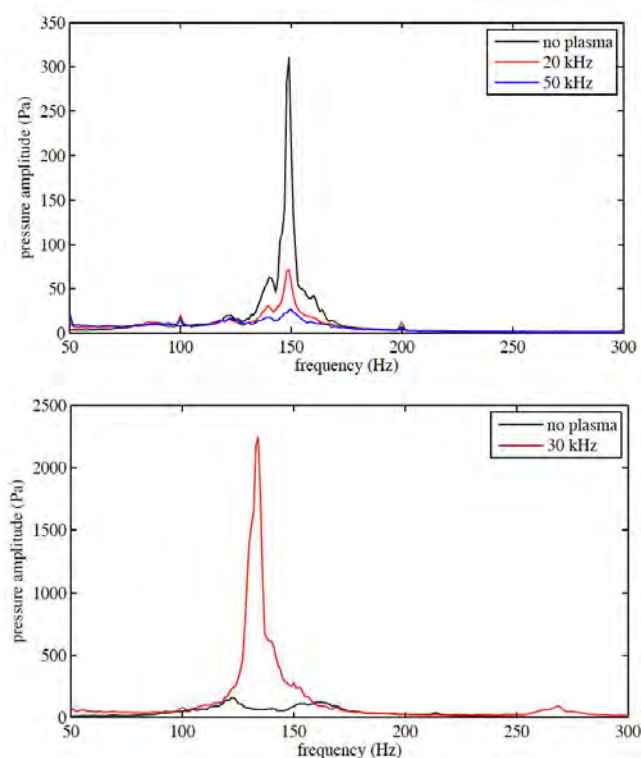


Figure 6.14: Amplitude spectra of combustion pressure without and with NRP discharges. Top: unstable case, stabilized by NRP discharges. Bottom: stable case, destabilized by NRP discharges. For details on the operating points refer to [Moeck et al. \[2013\]](#).

The experimental setup presented show how NRP discharges can be a useful tool in order to enhance and stabilize combustion. It has to be noticed most of all how the beneficial effects this kind of systems can bring will need only a very small amount of input power. The order of magnitude of the plasma power is generally of 1 % of the flame power.

Once experimentally proven the contribution NRP discharges can provide, the question of how to model them in numerical simulation rises.

6.4 Modeling of NRP discharges

Few numerical simulations are reported in literature about NRP discharges, mostly regarding ignition. Ignition of H_2 /air mixtures has been simulated by [Tholin et al. \[2014\]](#), [Kobayashi et al. \[2017\]](#) and [Yin et al. \[2013\]](#) using 2-D numerical simulation. A single pulse has been considered in the first two works, while multiple pulses are taken into account in the work of [Yin et al. \[2013\]](#). Regarding hydrocarbons, the ignition of methane/air mixtures has been studied in the work of [Breden et al. \[2013\]](#) by means of 2-D simulations of a single pulse. 0-D simulations of a single discharge have been performed by [DeFilippo and Chen \[2016\]](#) for a CH_4 /air mixture and by [Kosarev et al.](#)

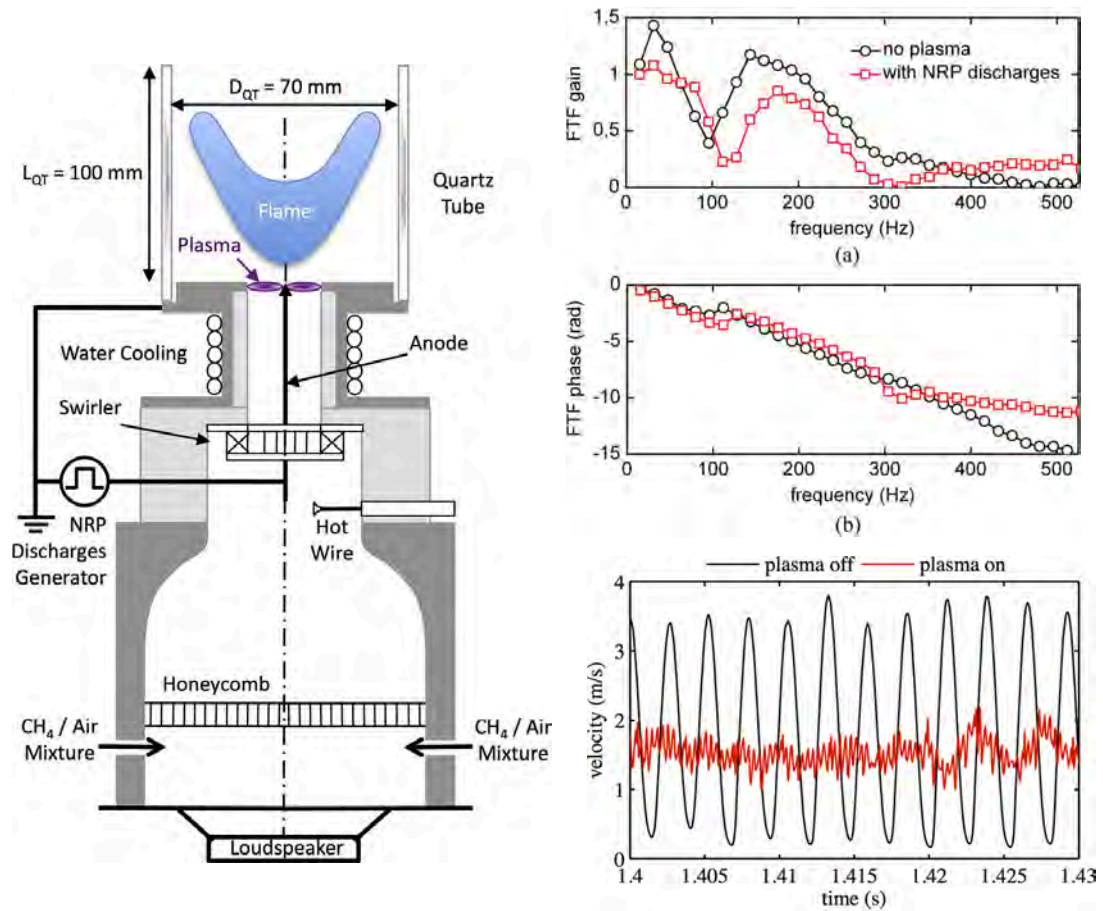


Figure 6.15: Left: experimental setup of [Lacoste et al. \[2013a\]](#). Right, top: flame transfer function measurement without and with NRP discharges; (a) gain, (b) phase. Right, bottom: velocity oscillation in a self-sustained thermoacoustic oscillation without and with NRP discharges.

[\[2008\]](#) for a $\text{CH}_4/\text{O}_2/\text{Ar}$ mixture. A mixture of n-heptane with air has been investigated by [Nagaraja et al. \[2015\]](#), which took into account multiple pulses. Regarding flame stabilization, 2-D simulations have been performed for laminar premixed methane/air flames around the lean flammability limit by [Bak et al. \[2012\]](#).

All these simulations use complex kinetic schemes, which take into account and solve the plasma phase. The plasma phase is coupled most of the time with a combustion kinetic scheme. The resulting kinetic schemes contain in general a large amount of species and reactions. As an example, [Fig. 6.16](#) presents the plasma kinetic scheme used by [Bak et al. \[2012\]](#). The scheme contains 10 excited and ionized species and electrons and 51 reactions. To simulate combustion, this scheme has been coupled to the DRM19 [[Kazakov and Frenklach](#)], containing 19 ground species and 84 reactions. Detailed kinetic schemes are well suited for 2-D simulations, in small domains, for a detailed study of the plasma phase and for understanding the physics of NRP discharges. When the aim is to integrate an NRP model into a combustion code and to perform simulations in 3-D complex geometries, with turbulent flows and flames, the

6. BIBLIOGRAPHICAL REVIEW ON PLASMA ASSISTED COMBUSTION

Reaction	Rate coefficient
$N_2 + e \rightarrow N_2(A) + e$	σ
$N_2 + e \rightarrow N_2(B) + e$	σ
$N_2 + e \rightarrow N_2(a') + e$	σ
$N_2 + e \rightarrow N_2(C) + e$	σ
$N_2 + e \rightarrow N_2^+ + 2e$	σ
$O_2 + e \rightarrow 2O + e$	σ
$O_2 + e \rightarrow O_2^+ + 2e$	σ
$CH_4 + e \rightarrow CH_3 + H + e$	σ
$CH_4 + e \rightarrow CH_4^+ + 2e$	σ
$H_2O + e \rightarrow H_2O^+ + 2e$	σ
$CO_2 + e \rightarrow CO_2^+ + 2e$	σ
$O_2^+ + e \rightarrow 2O$	$2 \times 10^{-7} (300/T_e)^{0.63} \text{ cm}^3/\text{s}$
$CH_4^+ + e \rightarrow CH_3 + H$	$2.9 \times 10^{-7} (300/T_e)^{0.53} \text{ cm}^3/\text{s}$
$H_2O^+ + e \rightarrow O + 2H$	$10^{-6} (300/T_e)^{0.5} \text{ cm}^3/\text{s}$
$CO_2^+ + e \rightarrow O + CO$	$4 \times 10^{-7} (300/T_e)^{0.5} \text{ cm}^3/\text{s}$
$e + e + N_2^+ \rightarrow e + N_2$	$10^{-19} (300/T_e)^{4.5} \text{ cm}^6/\text{s}$
$e + N_2^+ + N_2 \rightarrow N_2 + N_2$	$6 \times 10^{-27} (300/T_e)^{1.5} \text{ cm}^6/\text{s}$
$e + N_2^+ + O_2 \rightarrow N_2 + O_2$	$6 \times 10^{-27} (300/T_e)^{1.5} \text{ cm}^6/\text{s}$
$e + e + O_2^+ \rightarrow e + O_2$	$10^{-19} (300/T_e)^{4.5} \text{ cm}^6/\text{s}$
$e + O_2^+ + N_2 \rightarrow O_2 + N_2$	$6 \times 10^{-27} (300/T_e)^{1.5} \text{ cm}^6/\text{s}$
$e + O_2^+ + O_2 \rightarrow O_2 + O_2$	$6 \times 10^{-27} (300/T_e)^{1.5} \text{ cm}^6/\text{s}$
$e + e + H_2O^+ \rightarrow e + H_2O$	$10^{-19} (300/T_e)^{4.5} \text{ cm}^6/\text{s}$
$e + H_2O^+ + N_2 \rightarrow H_2O + N_2$	$6 \times 10^{-27} (300/T_e)^{1.5} \text{ cm}^6/\text{s}$
$e + H_2O^+ + O_2 \rightarrow H_2O + O_2$	$6 \times 10^{-27} (300/T_e)^{1.5} \text{ cm}^6/\text{s}$
$e + e + CO_2^+ \rightarrow e + CO_2$	$10^{-19} (300/T_e)^{4.5} \text{ cm}^6/\text{s}$
$e + CO_2^+ + N_2 \rightarrow CO_2 + N_2$	$6 \times 10^{-27} (300/T_e)^{1.5} \text{ cm}^6/\text{s}$
$e + CO_2^+ + O_2 \rightarrow CO_2 + O_2$	$6 \times 10^{-27} (300/T_e)^{1.5} \text{ cm}^6/\text{s}$
$N_2^+ + O_2 \rightarrow O_2^+ + N_2$	$6 \times 10^{-11} (300/T_g)^{0.5} \text{ cm}^3/\text{s}$
$N_2^+ + H_2O \rightarrow H_2O^+ + N_2$	$2.3 \times 10^{-9} \text{ cm}^3/\text{s}$
$H_2O^+ + O_2 \rightarrow O_2^+ + H_2O$	$4.3 \times 10^{-10} \text{ cm}^3/\text{s}$
$CO_2^+ + O_2 \rightarrow O_2^+ + CO_2$	$5.6 \times 10^{-11} \text{ cm}^3/\text{s}$
$N_2(A) + N_2 \rightarrow N_2 + N_2$	$3 \times 10^{-16} \text{ cm}^3/\text{s}$
$N_2(B) + N_2 \rightarrow N_2 + N_2$	$2 \times 10^{-12} \text{ cm}^3/\text{s}$
$N_2(B) + N_2 \rightarrow N_2(A) + N_2$	$3 \times 10^{-11} \text{ cm}^3/\text{s}$
$N_2(B) \rightarrow N_2(A) + h\nu$	$1.5 \times 10^5 \text{ 1/s}$
$N_2(a') + N_2 \rightarrow N_2(B) + N_2$	$1.9 \times 10^{-13} \text{ cm}^3/\text{s}$
$N_2(C) + N_2 \rightarrow N_2(a') + N_2$	$10^{-11} \text{ cm}^3/\text{s}$
$N_2(C) \rightarrow N_2(B) + h\nu$	$3 \times 10^7 \text{ 1/s}$
$N_2(A) + N_2(A) \rightarrow N_2(B) + N_2$	$3 \times 10^{-10} \text{ cm}^3/\text{s}$
$N_2(A) + N_2(A) \rightarrow N_2(C) + N_2$	$1.5 \times 10^{-10} \text{ cm}^3/\text{s}$
$N_2(A) + O_2 \rightarrow N_2 + 2O$	$2.3 \times 10^{-12} \text{ cm}^3/\text{s}$
$N_2(B) + O_2 \rightarrow N_2 + 2O$	$2 \times 10^{-10} \text{ cm}^3/\text{s}$
$N_2(a') + O_2 \rightarrow N_2 + 2O$	$2.8 \times 10^{-11} \text{ cm}^3/\text{s}$
$N_2(C) + O_2 \rightarrow N_2 + 2O$	$3 \times 10^{-10} \text{ cm}^3/\text{s}$
$N_2(A) + O \rightarrow N_2 + O$	$2.1 \times 10^{-11} \text{ cm}^3/\text{s}$
$O + O + N_2 \rightarrow O_2 + N_2$	$10^{-33} (300/T_g)^{0.41} \text{ cm}^6/\text{s}$
$O + O + O_2 \rightarrow O_2 + O_2$	$4 \times 10^{-33} (300/T_g)^{0.41} \text{ cm}^6/\text{s}$
$CH_4 + N_2(A) \rightarrow CH_3 + H + N_2$	$3.3 \times 10^{-15} \text{ cm}^3/\text{s}$
$CH_4 + N_2(B) \rightarrow CH_3 + H + N_2$	$3 \times 10^{-10} \text{ cm}^3/\text{s}$
$CH_4 + N_2(a') \rightarrow CH_3 + H + N_2$	$3 \times 10^{-10} \text{ cm}^3/\text{s}$
$CH_4 + N_2(C) \rightarrow CH_3 + H + N_2$	$5 \times 10^{-10} \text{ cm}^3/\text{s}$

Figure 6.16: Reaction set (except the DRM19 reduced methane/air combustion mechanism) used in 2-D kinetic simulations for methane/air plasma-induced combustion [Bak et al., 2012]

cost associated with them becomes rapidly prohibitive.

Castela [2016] estimated that, for a 3-D DNS, the cost of using a kinetic scheme with 60 species (typical order of magnitude for plasma coupled with combustion), compared to a kinetic scheme with 9 species (typical order of magnitude for classical combustion) was 20 times higher. The aim of her work was to perform 3-D simulations of multiple discharges for ignition purposes. 3-D DNS was used in order to take into account the flow patterns associated with the shock waves observed in Xu et al. [2011, 2014, 2016] and the cumulative effect of successive pulses. In order to overcome the impossibility to do so with a complex kinetic scheme, Castela et al. [2016] developed and validated a high level modeling of non-equilibrium plasmas that avoids including detailed non-equilibrium plasma kinetics. The model, based on a phenomenological description of the phenomenon, captures the main channels and their characteristic time scales through which the electric energy of the discharge is deposited into the flow. A detailed chemical kinetic model for hydrocarbons-air mixtures is considered for combustion, as well as multi-species transport model to capture the transient characteristics of NRP discharges-assisted ignition. The model has been validated in 2-D Castela et al. [2016] and 3-D configurations Castela et al. [2017].

The idea behind the model is fully based on experimental and numerical observations and stands in quantifying the repartition of the discharge energy deposition rate \dot{E}^p between chemical \dot{E}_{chem}^p , thermal \dot{E}_{heat}^p and vibrational \dot{E}_{vib}^p energies, see Fig. 6.17. This happens within the pulse (τ_{pulse}). Then, the energy stored in vibrational energy

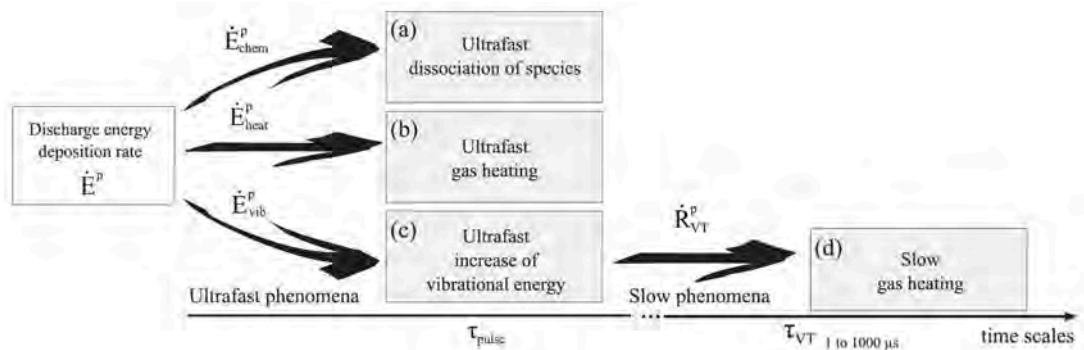


Figure 6.17: Schematic representation of the NRP discharge model assumptions. The discharge energy is assumed to be deposited into (a) chemical, (b) sensible and (c) vibrational energies within the pulse characteristic time τ_{pulse} . The vibrational energy relaxes after the pulse, leading to an increase of the (d) sensible energy within a characteristic time τ_{VT} [Castela et al., 2016].

slowly relaxes, causing a slow gas heating (time scale τ_{VT}). This simplification can be done because, in NRP discharges at atmospheric pressure, about 90 % of the discharge energy is stored into electronic and vibrational states of N_2 molecules (see section 6.3.1). Dissociative quenching reactions between ground state molecules and electronically excited N_2 molecules lead to an ultrafast increase of the gas temperature and to the dissociation of species. The most important dissociation, and the only one considered in their work, is $O_2 \implies 2O$. The relaxation of vibrationally excited N_2 molecules takes

6. BIBLIOGRAPHICAL REVIEW ON PLASMA ASSISTED COMBUSTION

longer and is associated to a much slower heat release. The fraction of energy which goes in one or another process has been fixed by means of experimental and numerical results.

The model was validated and provided very good results, together with the possibility of applying it in 3-D turbulent cases. The relative importance of the thermal and chemical effects on ignition has been studied [Castela et al., 2016], as well as the shock waves associated with the ultrafast increase in temperature [Castela et al., 2017].

In this work, the approach used by Castela et al. [2016] is retained. For LES, the use of a kinetic scheme with 60-70 species is not affordable. A phenomenological model is built instead, with the aim of reproducing the effect of NRP discharges on an experimental setup studied at KAUST (King Abdullah University of Science and Technology, Saudi Arabia). In the model developed the energy deposit is, as a first step, considered as a simple source term. No energy quota is specifically reserved for species dissociation or stored in vibrational states of molecules. Its aim is to be easily included in the AVBP code and used for a first series of LES of plasma-assisted combustion. It will also be the basis for the further developments already scheduled in the context of the French ANR program "GECCO". The phenomenological model built during this work will be presented in chapter 8.

Chapter 7

LES of a premixed swirl-stabilized burner

Contents

7.1	The PACCI experimental configuration	112
7.1.1	Available experimental data	114
7.1.2	Numerical setup	114
7.2	Non-reacting flow in the PACCI burner	118
7.2.1	Flow characteristics and flow pattern	118
7.2.2	Mean flow velocity profile	120
7.2.3	Flow instability	125
7.3	Reacting flow in the PACCI burner	126
7.3.1	Validation of the kinetic schemes	127
7.3.2	LES using the BFER 2-steps global chemistry	131
7.3.3	Impact of the kinetic scheme: LES using the LU13 ARC chemistry	140
7.4	Acoustically pulsating the PACCI burner	150
7.4.1	Forced response method for the dynamic analysis of flames	150
7.4.2	Dynamic response of the PACCI burner	151
7.5	Conclusion	161

In this chapter numerical simulations of a premixed swirl-stabilized burner are presented. The objective is to provide a series of test cases well suited to apply NRP discharges in a second phase (chapter 9). The configuration studied is the PACCI burner, experimentally investigated at KAUST by the team of Prof. Deanna Lacoste, which provided experimental data. The burner works at atmospheric pressure.

The experimental configuration is described in section 7.1. Non-reacting flow is investigated and compared to experimental results in section 7.2. Then the reacting flow is studied in section 7.3, where the flame features and dynamics are analyzed and a comparison between the 2-step BFER scheme and the ARC LU13 scheme is given. Finally the flame response to acoustic pulsation is examined in section 7.4.

7.1 The PACCI experimental configuration

The PACCI burner studied during this work is an evolution of the experimental rig already studied in [Lacoste et al. \[2013a\]](#). A schematic of the PACCI experimental configuration is shown in Fig. 7.1. The experimental setup is composed by three main

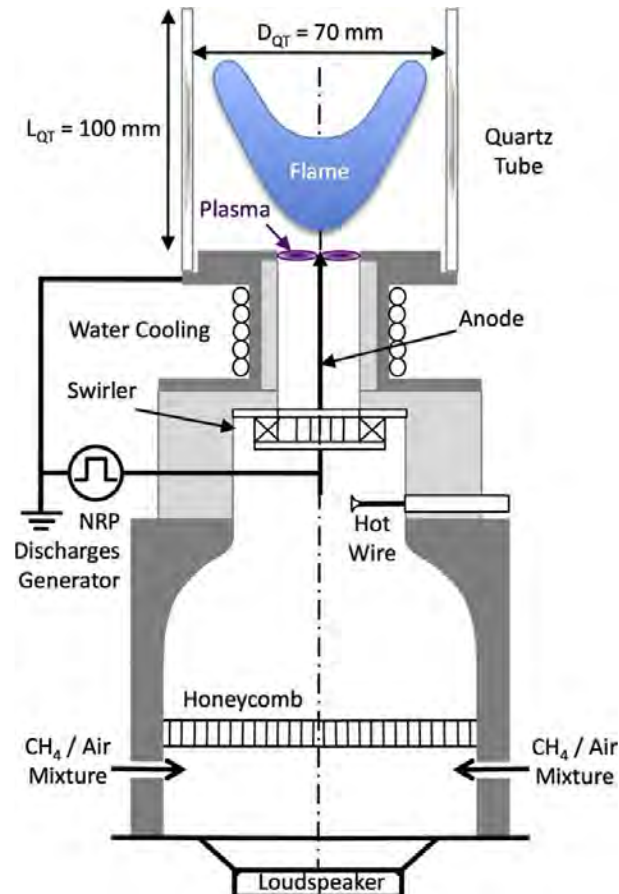


Figure 7.1: Schematic of the PACCI burner [[Lacoste et al., 2013a](#)].

elements: a swirl-stabilized burner, a NRP discharge generator system and equipments for the flame visualizations and the Flame Transfer Function (FTF) measurements.

Swirl stabilized burner. The swirl stabilized burner is axi-symmetric and composed by:

- A plenum in which a mixture of fuel and air is injected by two 8 mm diameter tubes and goes through a 20 mm long honeycomb grid to break up the largest turbulent structures. The length of the plenum is 120 cm. The mixture ratio of the mixture is fixed to 0.67 and the flow rate is chosen to obtain a thermal power of about 4 kW.
- A radial swirler, featuring 12 blades with a trailing-edge angle of 30 deg.

7.1 The PACCI experimental configuration

- An injection tube with a diameter of 18 mm.
- A quartz tube of 70 mm inlet diameter and 100 mm in length, which confines the flame.

NRP plasma discharge generator system. The NRP discharge generation system is composed by a cylindrical pin steel electrode, 2.5 mm in diameter, located at the center of the injection tube and serving as the anode, while the outlet of the injection tube is used as the cathode. In order to force the plasma discharge location at the outlet of the injection tube, a ceramic cylinder is placed for isolation, leaving only the last 1.5 mm of the injection tube available for the discharge. The electrical pulses are 8 kV in amplitude, 10 ns in duration and have a frequency of 30 kHz. The total power of the plasma is 40 W, i.e. 1 % of the flame power. To illustrate the NRP plasma discharges position one can refer to Fig. 7.2. This figure cannot be considered as a simultaneous visualization of the flame and the plasma. Since the light intensity emitted by the plasma is much brighter than that from the flame, capturing both contributions in a single photograph with the same exposure time is difficult. This reconstructed image was obtained by combining a photo from the plasma contribution with the flame with a short exposure time and a photo from the flame alone without plasma but with a much longer exposure time.



Figure 7.2: Photographic representation of the burner with a lean premixed CH_4/Air swirl-stabilized flame (blue) and NRP discharges (purple), from [Lacoste et al. \[2013a\]](#).

Diagnostics. The burner is equipped with several diagnostics in order to measure the flow and flame behavior. This includes Particle Image Velocimetry (PIV) to analyze the

7. LES OF A PREMIXED SWIRL-STABILIZED BURNER

flow field in the combustion chamber and OH^* chemiluminescence in order to track the flame. Since the aim of the experimental rig is to study FTF, the burner is equipped with a loudspeaker at the bottom end of the plenum. This is capable of providing harmonic acoustic forcing. In order to measure the flow velocity fluctuations, a hot wire is used upstream of the swirler, where the flow is axial and uniform.

7.1.1 Available experimental data

The test campaign is still currently ongoing at KAUST and the totality of experimental data is not available for comparison with the numerical simulations. For now, only the following data is available: PIV measurement of the cold flow, OH^* chemiluminescence imaging and FTF measurements for the hot flow without NRP discharges. Further data will be available for future work. Since the configuration is an evolution of the setup of [Lacoste et al. \[2013a\]](#), from which only the swirler design and the equivalence ratio are slightly different, the results can be qualitatively compared with their work.

7.1.2 Numerical setup

The computational domain used for the LES simulations is the same for the whole set of simulations performed during this work (Fig. 7.3). In order to save computational time and to handle more easily the acoustic forcing (as detailed in section 7.4), the plenum is not included in the domain. The three-dimensional burner domain starts 25 mm before the inlet of the swirler and extends up to the end of the quartz tube. Here, an atmosphere zone is added in order to simulate the exit of the chamber and to capture any influence of the outlet boundary condition on the combustion chamber flow field. The axial direction is referred as the x-axis, corresponding to the mean direction

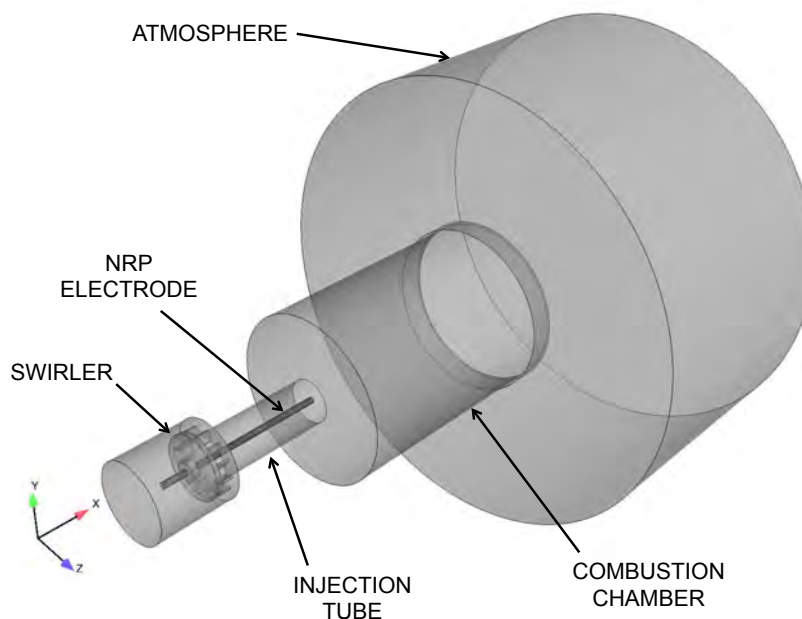


Figure 7.3: Schematic representation of the computational domain.

of the flow, while the y -axis and the z -axis denote the transverse directions.

The domain is discretized with a mesh of about 12M of cells (Fig. 7.4), which will be called M1. This is the less refined mesh used during this study and the reference one

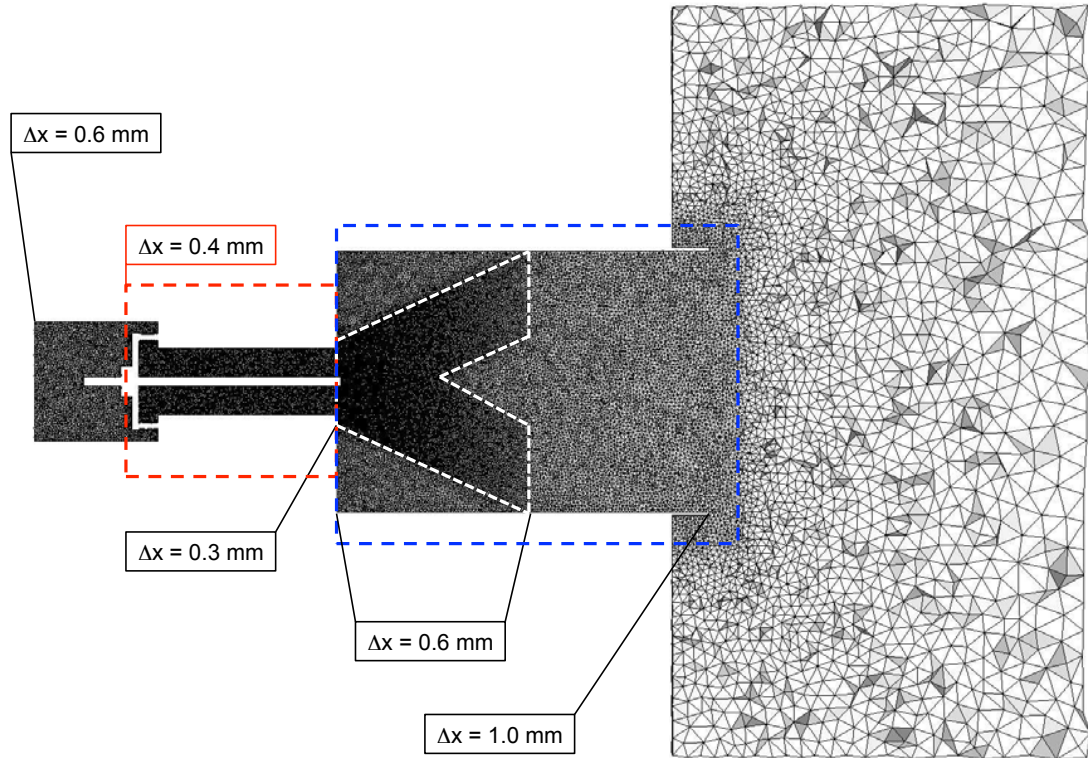


Figure 7.4: 2-D cut of the mesh M1 in the plane $z = 0$.

for the more refined meshes which will be presented in the following. The characteristic cell length Δx varies along the different zones of the chamber in order to correctly solve the physics related to each one of them. Focusing on the intake zone (red rectangle in Fig. 7.4), a particular attention has been put to the swirler discretization, where at least 10 cells per vane are used ($\Delta x = 0.4$ mm). This strategy permits to use a law-of-the-wall approach and to limit the mesh size. The same mesh discretization is kept all along the injection tube, in order to correctly capture the swirling motion and avoid larger turbulence dissipation. Regarding the combustion chamber (blue rectangle in Fig. 7.4), a mesh refinement is adopted also at the exit of the injection tube, where a cell length $\Delta x = 0.3$ mm is used, in order to correctly solve the recirculating flow due to vortex breakdown. Moreover the mesh refinement has been adapted to the presence of a flame allowing the use of the same mesh for reactive simulations. In this zone (enveloped by the white lines in Fig. 7.4), the mesh size is kept small and a very slow coarsening is adopted, with a cell length going from 0.3 mm to 0.6 mm. It is in this zone that the smallest cell sizes are encountered, to avoid large values of the thickening factor when using a combustion model, as it will be discussed in section 7.3. Around these zones, a mesh coarsening is used in order to save computational time. The mesh is coarsened from the swirler zone towards the inlet of the domain, where a cell size of 0.6 mm is used. This permits to correctly impose the mean flow, as well as to inject synthetic

7. LES OF A PREMIXED SWIRL-STABILIZED BURNER

turbulence, if wished. In the combustion chamber, outside the region enveloped by the white lines, the mesh is also coarsened. Close to the chamber faceplate, a cell size of 0.6 mm is kept in order to correctly solve the flow in the recirculation zones. Downstream of the refined zone, the coarsening is pushed a little stronger, up to a cell size of 1 mm at the chamber exit. The mesh in the "atmosphere" is strongly coarsened in order to dissipate all the possible undesired fluctuations, acting like a sponge layer.

Regarding boundary conditions, the NSCBC (Navier-Stokes Characteristic Boundary Condition, from Poinso and Lele [1992]) formalism is used for each inlet or outlet boundary condition (colored patches in Fig. 7.5). At inlet, the experimental mass flow

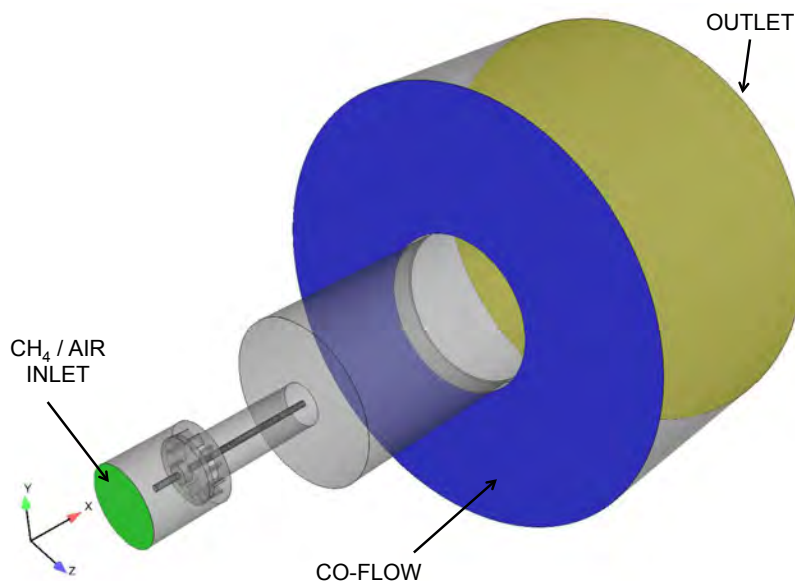


Figure 7.5: Schematic representation of the computational boundary conditions.

rate of mixture is prescribed. The mixture composition and mass flow rate are different for the non-reactive and reactive simulations; inlet conditions are listed in Tab. 7.1. A

	Mass flow rate \dot{m}	Mixture composition	Temperature
Non-reactive	1.787 g/s	Air	300 K
Reactive	1.960 g/s	CH ₄ /Air at $\phi = 0.67$	300 K

Table 7.1: Inlet conditions for non-reactive and reactive cases.

turbulence injection of 5 % of the mean inlet velocity has been tested, in order to take into account turbulence generated in the plenum and match with hot wire data. Since the flow is not very turbulent before entering the swirler, it has been found that it is the latter which generates the most of turbulence. The influence of injecting turbulence at inlet has been found indeed not to be of leading order. A co-flow is used in order to mimic the ambient air entrainment caused by the flow exiting the combustion chamber. This permits also to avoid undesired recirculation zones at the chamber exit corners. Its value is fixed in order to have a co-flow velocity between 5 and 10 % of the main flow velocity at the chamber exit. At the outlet, atmospheric pressure is imposed.

7.1 The PACCI experimental configuration

Regarding walls, different choices have been made depending on the domain zone. The entire set of walls of the intake zone, including swirler, injection tube and NRP electrode are treated with a wall-law model. In this zone the average y^+ value is about 15, i.e., between typical values for no-slip walls ($y^+ < 5$) and wall-laws ($y^+ > 30$). These two options have been simulated; the wall-law approach, which permits to have better results, is adopted. On the contrary the combustion chamber walls have been treated as non-slipping walls, since their average y^+ value is about 5. The walls confining the "atmosphere" are treated as slipping walls to restrict their influence on the surrounding flow. All the walls are treated as adiabatic.

The numerical parameters used for all the LES are listed in Tab. 7.2. Notice the

Numerical Parameters	
Convection scheme	TTGC: $\mathcal{O}(3)$ in space & time [Colin and Rudgyard, 2000]
Diffusion scheme	2Δ operator
SGS model	SIGMA [Nicoud et al., 2011]
Artif. viscosity	Colin model: $\epsilon^{(2)} = 0.05$, $\epsilon^{(4)} = 0.005$

Table 7.2: Numerical parameters for the non-reacting LES.

use of the SIGMA SGS model, which permits to avoid an over-insertion of turbulent viscosity due to "solid body rotation" of the flow, as shown for instance by Jaravel et al. [2016] when using the WALE SGS model. The LES quality is indeed very good, as shown in Fig. 7.6, where an instantaneous field of the ratio between turbulent and laminar viscosity ν_t/ν_{lam} is shown for the non-reactive case. It can be seen that $\nu_t/\nu_{lam} < 12$

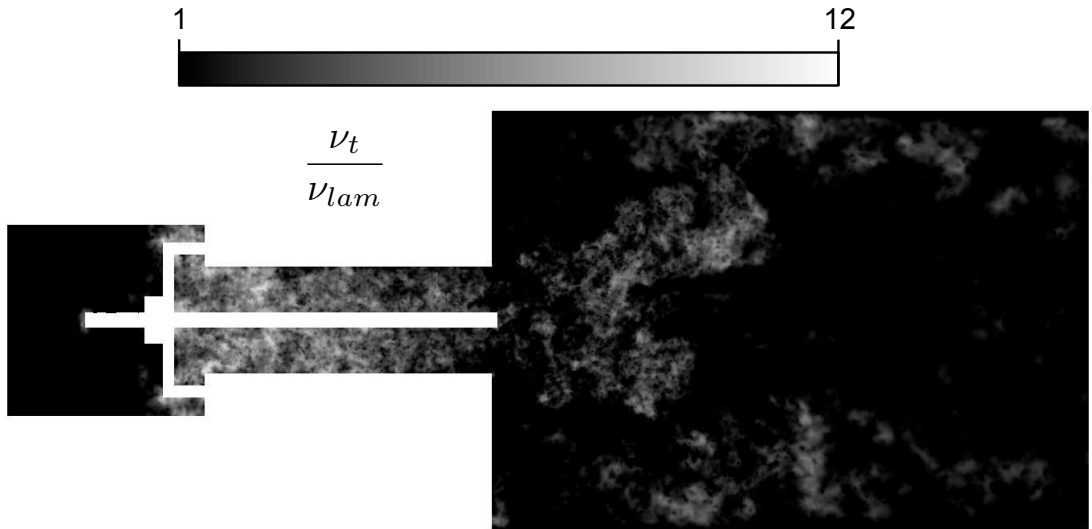


Figure 7.6: Instantaneous field of ν_t/ν_{lam} on a 2-D cut at $z = 0$. Logarithmic scale.

in the whole domain and how its mean value is much lower. It is generally considered that the value of ν_t/ν_{lam} should stay lower than 20 in the entire domain.

7.2 Non-reacting flow in the PACCI burner

7.2.1 Flow characteristics and flow pattern

The main flow characteristics for the non-reacting flow are here introduced. The geometrical parameter used to non-dimensionalize the geometrical distances and flow quantities is the outlet diameter of the injection tube D_E^{inj} , as shown in Fig. 7.7. The

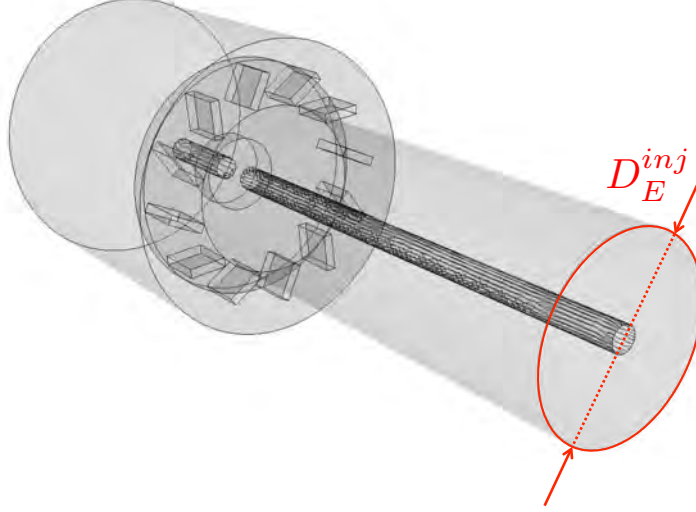


Figure 7.7: Definition of the geometrical parameter used for non-dimensionalization of variables.

main parameters are:

- the convective time scale, which is evaluated from the total burner volume V_b and the inlet flow rate \dot{m} :

$$\tau_{conv} = \frac{\rho V_b}{\dot{m}} = 275 \text{ ms} \quad (7.1)$$

- the rotation time scale, which is evaluated at the injection tube exit plane (which corresponds to the combustion chamber inlet plane):

$$\tau_{rot} = \frac{\pi R_E^{inj}}{u_\theta^{inj}} = 6 \text{ ms} \quad (7.2)$$

where R_E^{inj} is the outer radius of the injection tube and u_θ^{inj} is the mean azimuthal velocity component in the chamber inlet plane.

- the Reynolds number, which is evaluated at the combustion chamber inlet:

$$Re = \frac{|\vec{u}|^{inj} D_E^{inj}}{\nu} = 7000 \quad (7.3)$$

where $|\vec{u}|^{inj}$ is the norm of the velocity vector in the inlet plane, D_E^{inj} is the external diameter of the injection tube and ν is the kinematic viscosity.

The mean flow pattern is shown in Fig. 7.8. It can be seen how, due to the swirling

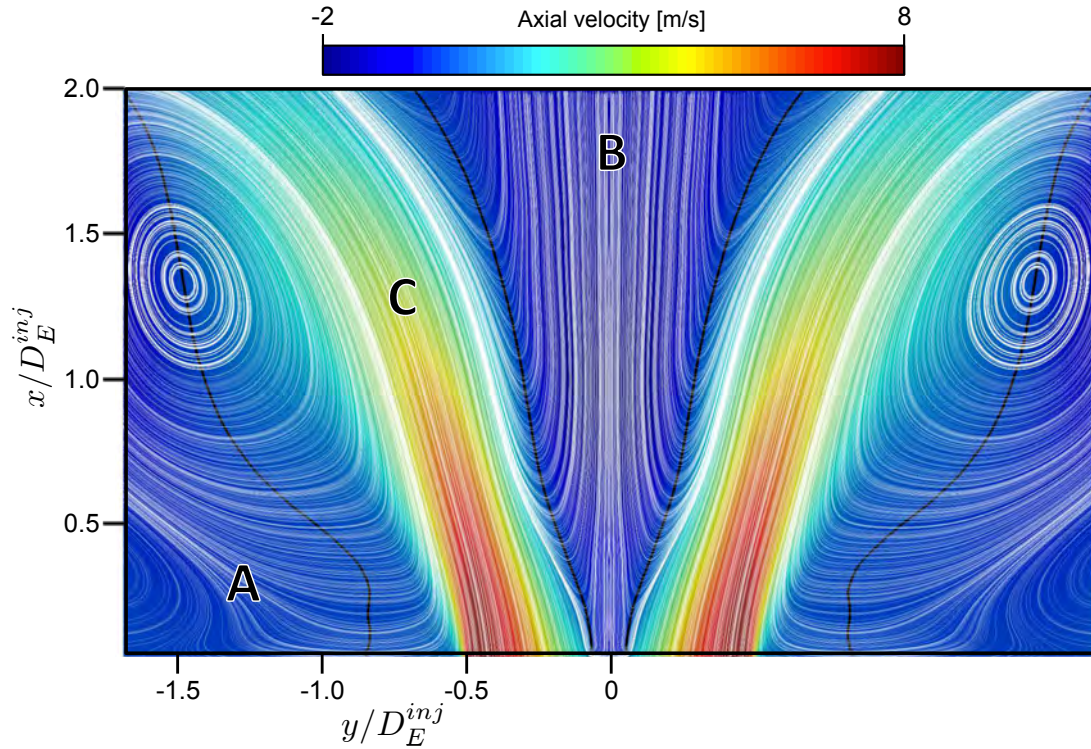


Figure 7.8: Mean flow pattern in the combustion chamber. White: time and azimuthal averaged streamlines. Black line: zero axial (x -axis) velocity iso-line. Field colored by axial velocity. A: corner recirculation zone, B: central recirculation zone, C: swirled jet.

motion of the flow, vortex breakdown appears and a central recirculation zone is formed. The presence of the central recirculation zone is due to an axial adverse pressure gradient. Indeed, the strong rotation of the incoming flow results in centrifugal forces that are compensated by a radial pressure gradient. As the swirled jet expands in the combustion chamber, the conservation of circulation implies a decay of the azimuthal velocity, hence a decay of the radial pressure gradient [Billant et al., 1998]. If the axial pressure gradient is strong enough, a bifurcation called vortex breakdown occurs [Lucca-Negro and O’Doherty, 2001], characterized by a reverse flow region. The central recirculation zone is closed near (or after) the exit of the combustion chamber. In confined environments, the swirling motion also induces recirculation on its outer part, referred to as corner recirculation zones, which close at nearly $x/D_E^{inj} = 2$. Finally, strong shear layers are located at the interfaces between the swirled jet and both the central and corner recirculation zones.

7.2.2 Mean flow velocity profile

The mean and RMS of a quantity ψ are evaluated respectively by:

$$\langle \psi(\vec{x}) \rangle = \frac{1}{T_m} \sum_{n=1}^{N_T} \psi(\vec{x}, t^n) \Delta t_m \quad (7.4)$$

$$\psi(\vec{x})_{RMS} = \sqrt{\langle \psi(\vec{x})^2 \rangle - \langle \psi(\vec{x}) \rangle^2} \quad (7.5)$$

where T_m is the recording duration, N_T is the total number of instantaneous snapshots and Δt_m is the time delay between two consecutive snapshots.

Data have been recorded during 2 convective times, in order to have statistically converged fields. Additionally, the flow fields are azimuthally averaged, in order to compare with the experimental data, as it will be shown in the following. It is convenient to introduce a cylindrical referential (x, r, θ) , whose x-axis is aligned with the x-axis of the Cartesian referential. A 2-D cut of the mean fields of axial, radial and tangential velocity are shown in Figs. 7.9, 7.10 and 7.11 respectively. The PIV fields of axial and radial velocity are added to allow a qualitative comparison. Additionally, the field of RMS axial velocity is presented in Fig. 7.12.

The red dashed line in Figs. 7.9 and 7.11, corresponding to a distance of 4 mm from the exit of the injection tube, represents the minimum x-coordinate from which PIV measurements are considered reliable. At lower x-coordinates, reflections could alter the data. It is at this axial position that a quantitative comparison of profiles of axial and tangential velocity (Fig. 7.13) has been made.

Fig. 7.9 reveals that the axial flow development is very similar between numerical simulation and experimental data. The central recirculation zone has a "bottle-neck" shape and its radial extent is comparable in the simulation and experiment. In the numerical simulation, the negative velocity zone extends up to the tip end of the electrode, while in the PIV data a zone of positive velocity is present. This is probably due to reflections on the chamber faceplate, which lead to unphysical positive velocities near it. The jet opening is also very similar in both cases. However, in the numerical simulation, the axial velocity tends to be maximum at higher radial positions in the vicinity of the chamber inlet. This will be discussed in the following. The mean axial velocity at the chamber inlet plane is of 6.15 m/s.

The similarity in jet opening is confirmed by Fig. 7.10, where fields of radial velocity are plotted. The radial velocity is here considered as positive if the flow direction is the same of the positive y -axis. The agreement is very good regarding the zones in which the higher radial velocity is found, which correspond to the early jet opening due to swirling motion and to the closing of the corner recirculation zones. The values predicted by the numerical simulation are slightly lower in magnitude than the ones recorded by PIV.

Figure 7.11 shows the field of tangential velocity extracted by the LES. No field data is available from the experiment. The tangential velocity is considered as positive when denoting a flow which turns around the x-axis according to the right-hand rule. The behavior is the one expected with a decrease in magnitude when traveling downstream as a result of the conservation of circulation. The mean tangential velocity at the

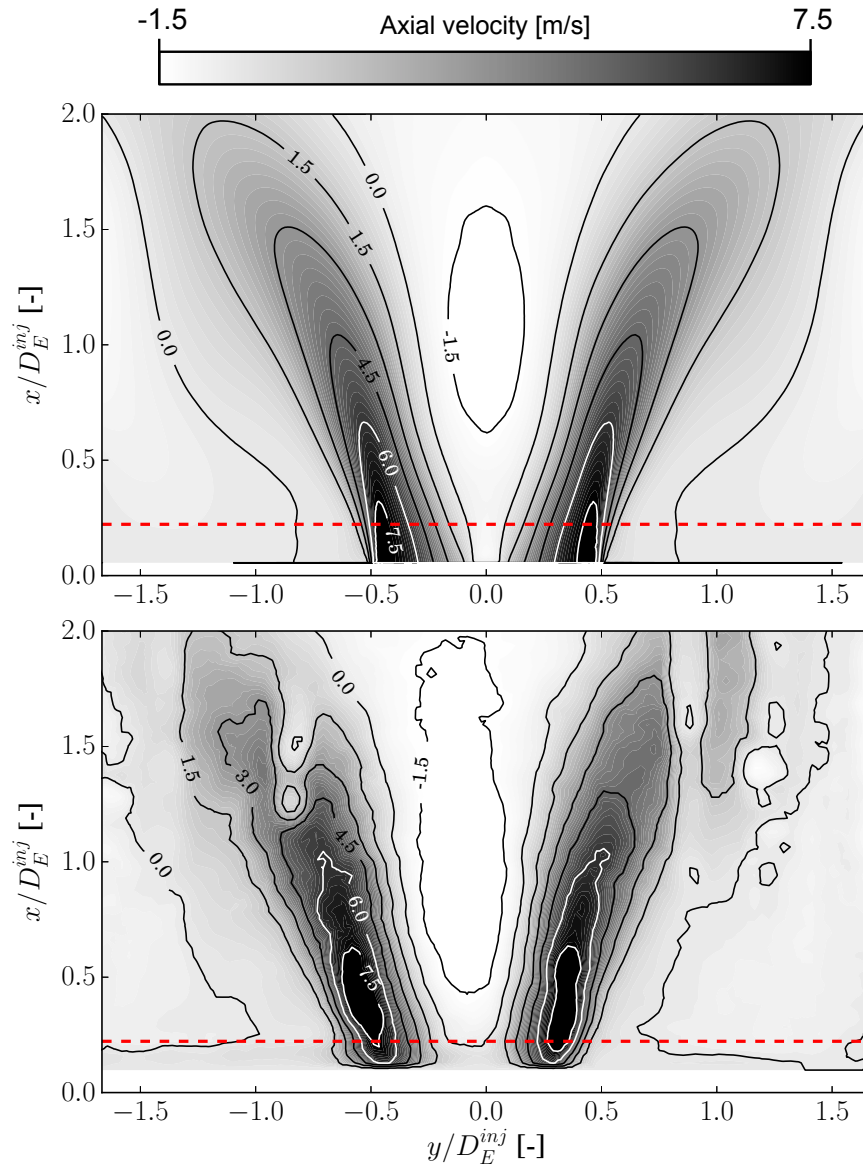


Figure 7.9: Top: time and azimuthally averaged field of axial velocity in the combustion chamber. Bottom: PIV field of axial velocity in the combustion chamber (courtesy of KAUST). Dashed line: x-position for profiles comparison.

chamber inlet plane is of 4.6 m/s.

Finally, the RMS field of axial velocity is presented in Fig. 7.12. The RMS field of the axial component shows the strong turbulence intensity at the vicinity of the stagnation point and the inner shear layer. No experimental data are available for comparison.

After this global qualitative comparison, a quantitative comparison is now introduced. Velocity profiles of axial and tangential velocity are compared between numerical

7. LES OF A PREMIXED SWIRL-STABILIZED BURNER

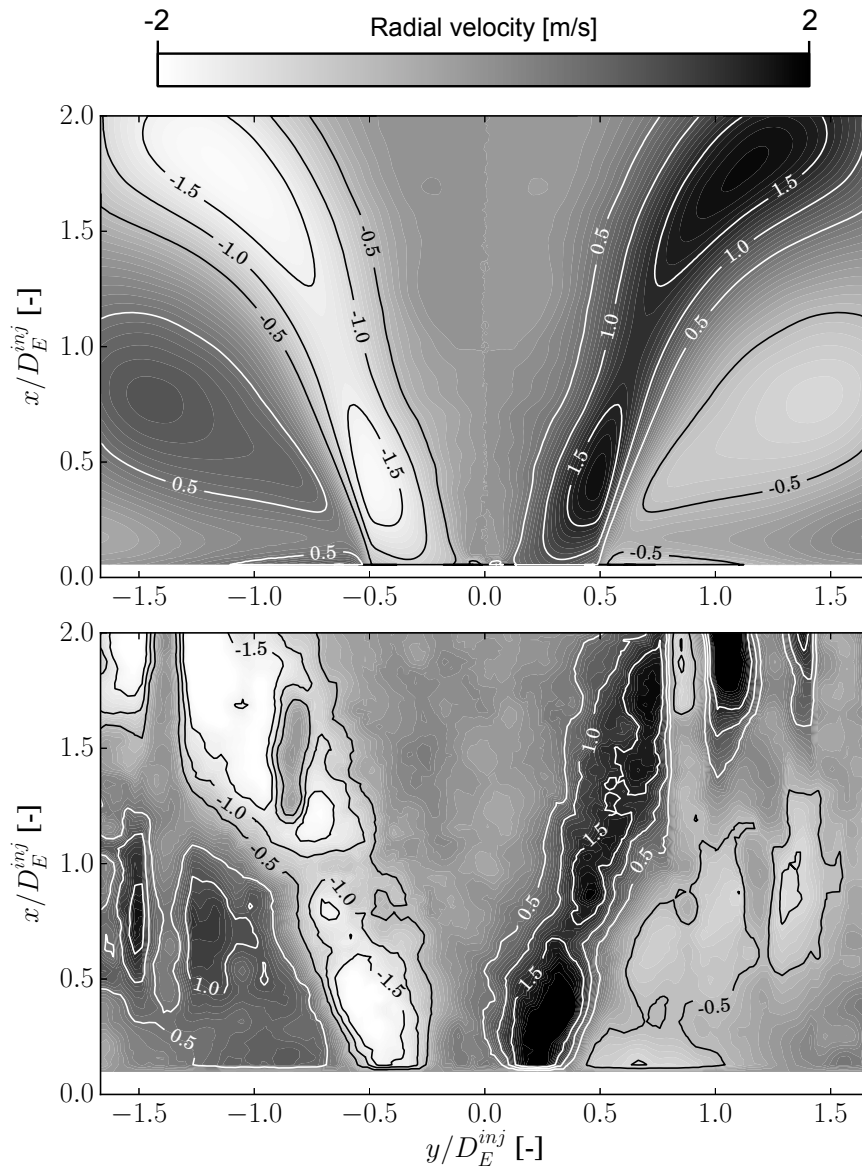


Figure 7.10: Top: time and azimuthally averaged field of radial velocity in the combustion chamber. Bottom: PIV field of radial velocity in the combustion chamber (courtesy of KAUST).

simulation and experimental data on an horizontal line 4 mm downstream of the chamber inlet. The corresponding non-dimensionalized axial position is $x/D_E^{inj} \approx 0.22$ and is denoted by a black line in Figs. 7.9 and 7.11. The results are shown in Fig 7.13. Experimental and numerical data match well overall. The axial velocity profile reproduces very well the experimental one in the recirculation zone, where the minimum of velocity is very similar. Moreover the same maximum of axial velocity is found. It can be seen however how the velocity peak is slightly shifted at an higher radial position, denoting a wider recirculation zone. This is surely linked to the tangential velocity profile, which

7.2 Non-reacting flow in the PACCI burner

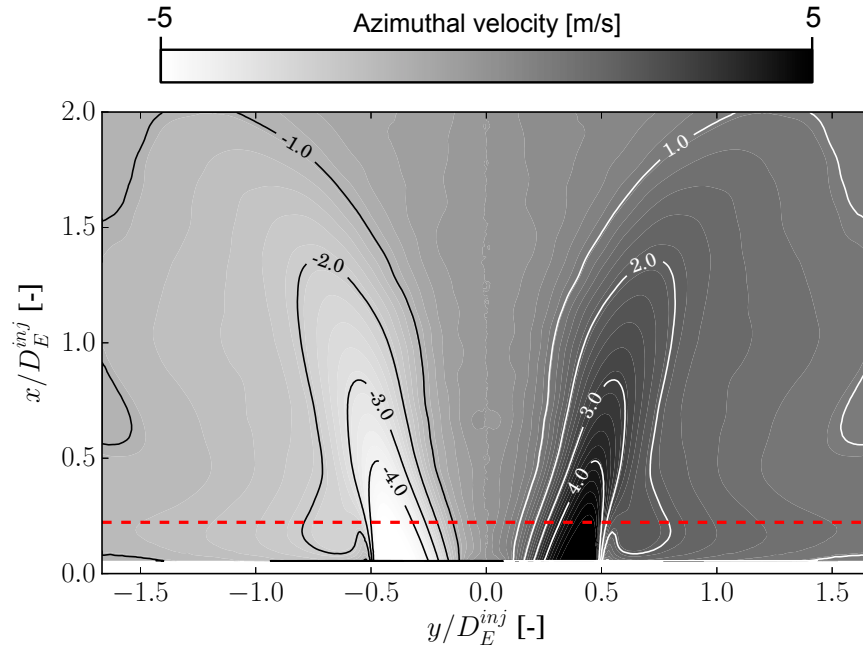


Figure 7.11: Time and azimuthally averaged field of tangential velocity in the combustion chamber. Dashed line: x-position for profiles comparison.

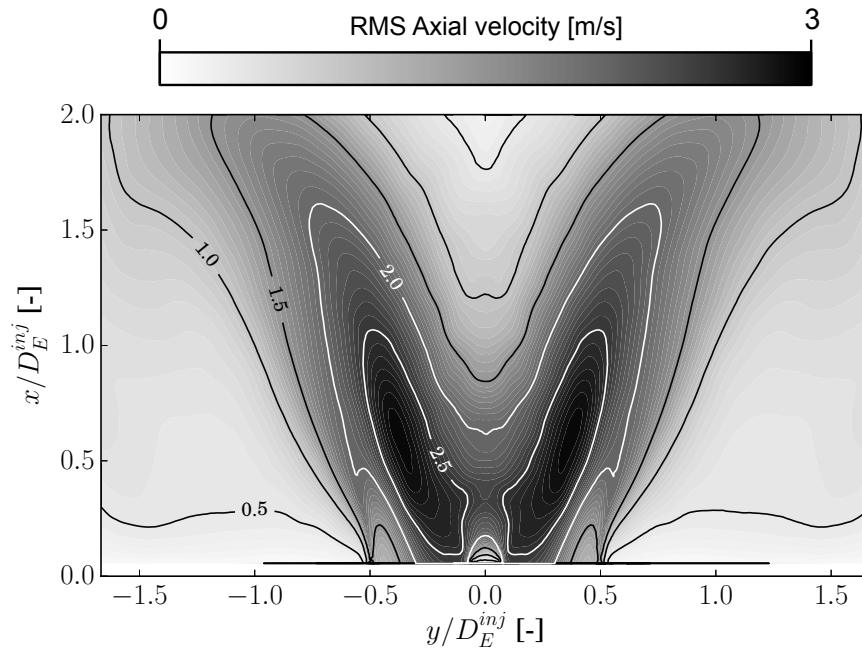


Figure 7.12: Time and azimuthally averaged RMS field of axial velocity in the combustion chamber.

exhibits slightly higher values for almost all the radial components. The reason of this

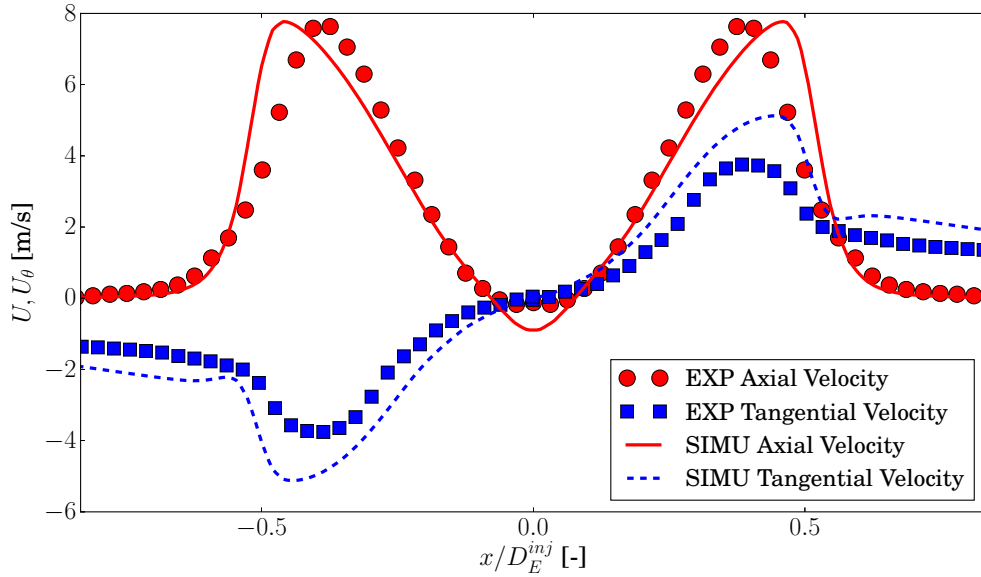


Figure 7.13: Profiles of axial (red) and tangential (blue) velocity at 4 mm from the exit of the injection tube. Solid lines: numerical simulation, symbols: experimental data.

overestimation is still unknown and has not been investigated more precisely. However, some additional test cases have been performed in order to try to understand it. The results of these test cases will not be presented into details here and just a summary is given.

First, the effect of using a wall law instead of no-slip conditions has been evaluated. Two additional LES have been performed, using no-slip boundary conditions for the entire set of walls. The first numerical simulation uses the M1 mesh, while the second one uses a modified M1 mesh with a refinement at walls, where the cell size has been divided by a factor of two. The resulting profiles were in general worst than using a wall-law model.

Second, a modified wall law to take into account a rough wall instead of a smooth one is used. For standard values of roughness, the differences on the profiles are not of leading order.

The standard wall law approach has been retained as the most reliable one.

Another parameter which could influence the profiles is the shape of the central recirculation zone. It has been found from numerical simulations that the latter closes after the exit of the combustion chamber, in the atmosphere. Any condition present in the experimental environment which is not taken into account in the LES could lead to a modification of the recirculation zone shape. This can have a feed-back effect on the opening of the swirled jet.

If one aims at a more precise estimation of the swirling flow a comparison with another LES code would be useful in order to validate the results of AVBP. If the two codes are in accordance it could be envisaged a 3D scan of the experimental swirler, in order to be sure that the CAD data used for the LES are coincident with the real geometry. A small difference in blade angle could explain the differences.

The author is still confident that the overestimation of the tangential velocity will not be a problem in order to analyze the effect of plasma discharges on the flame: since the recirculation zone is well captured, the flame root is expected to have the right axial position. Moreover, as shown in chapter 8, the NRP discharges model has been calibrated to the tangential velocity found in the numerical simulation.

7.2.3 Flow instability

Swirled flows are prone to hydrodynamic instabilities [Liang and Maxworthy, 2005]. Instabilities generally arise in the form of a precessing vortex core (PVC) [Roux et al., 2005; Syred, 2006], which interacts with the inner and outer shear layers between the swirled jet and the central and corner recirculation zones. Due to the particular geometry of this configuration, in which the swirled flow has to travel a long injection tube before entering the combustion chamber, a classical PVC structure is not found in the shear layers of the swirled jet. However, at the swirler exit, a hydrodynamical structure qualitatively similar to a PVC is present, as shown in Fig. 7.14. The structure is isolated by means of an iso-surface of low static pressure: the PVC has a helical shape, with a two branches structure. Figure 7.14 indicates the flow sign convention: the flow

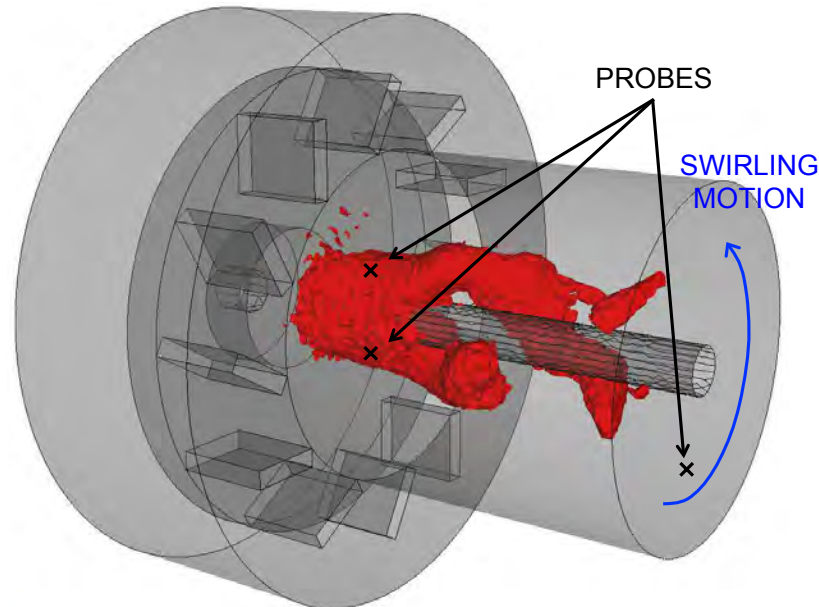


Figure 7.14: Hydrodynamical instability represented by means of an iso-surface of static pressure (red).

has a counter-clockwise rotation when looking from the outlet towards the inlet of the domain. This direction is considered as positive and so the PVC helical structure is wound in a negative direction, but is rotating in the positive direction. For example, the PVC captured in Roux et al. [2005] has similar winding and rotation orientation.

Figure 7.15, left, shows the non-dimensional power spectral density (PSD) of the axial velocity and static pressure on two diametrically opposed probes in the PVC zone. It can be seen how there is a clear indication of a periodic oscillation having a similar

7. LES OF A PREMIXED SWIRL-STABILIZED BURNER

influence on axial velocity and static pressure. The peak is located at a frequency of 660 Hz.

This instability is weak and no trace of it remains when looking a little far away downstream. The PSD of the "PROBE 1" situated in the PVC zone is compared with the corresponding one of a probe situated at the mid-length of the injection duct in Fig. 7.15, right. In this case the PSD have not been non-dimensionalized in order to show the amplitude of the oscillations: no trace of the instability is present anymore. This confirms that the PVC instability does not reach the combustion chamber.

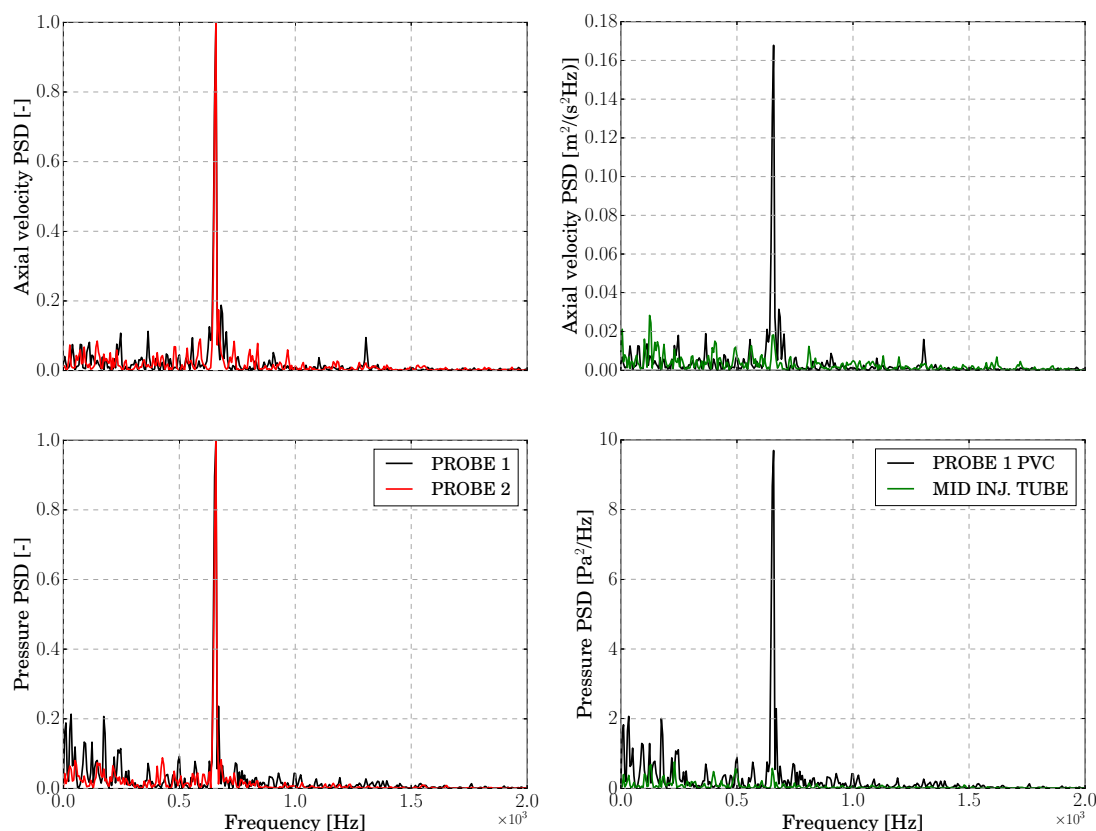


Figure 7.15: Non-dimensional power spectral density of axial velocity (top) and static pressure (bottom). Left: two probes in the PVC zone. Right: one probe in the PVC zone and one at the mid-length of the injection tube.

7.3 Reacting flow in the PACCI burner

In this section reactive simulations of the PACCI burner are presented. The ignition sequence is not investigated here since it is beyond the scope of this work. Ignition is generally obtained by replacing in an adequate zone of the converged cold field the fresh mixture by burnt gases. This is done in a zone near the chamber inlet, where the burnt gases can easily be trapped in recirculation zones and the fresh mixture can be ignited.

As already mentioned, two different kinetic schemes (BFER and LU13) are used in this study to run reacting simulations. The BFER scheme [Franzelli et al., 2012] is a global 2-step scheme which involves six species and two reactions. The Pre-Exponential Adjustment (PEA) [Légier, 2001] method is used and allows to reproduce the laminar flame speed over a wide range of equivalence ratio. The LU13 scheme is an analytically reduced mechanism [Sankaran et al., 2007] which contains 73 elementary reactions and 17 species, including 4 QSS species. The QSS algebraic relations are solved analytically.

Regarding turbulence combustion interaction, different choices have been made depending on the kinetic scheme used. When using the BFER mechanism, the classical TFLES [Légier et al., 2000] model is used, with 5 point in the flame thickness and applying the Charlette et al. [2002] efficiency function. As previously mentioned, the cell size has been set in order to avoid large values of thickening in the flame root zone. In this case, the flame thickness is about 0.6 mm; with a cell length of 0.3 mm and imposing a minimum of 5 points in the flame thickness, this leads to a thickening factor $\mathcal{F} \approx 2$. When using the LU13 mechanism, the sensor developed by Jaravel et al. [2016] is used.

The kinetic schemes validation is first presented in subsection 7.3.1. Then the LES are detailed.

7.3.1 Validation of the kinetic schemes

The reduced kinetic schemes are here validated in a canonical way for combustion mechanisms using the Cantera software. Equilibrium temperatures and species mass fractions are compared with the GRI30 kinetic scheme in Tab. 7.3. Only the species

	GRI30	LU13	BFER
Mass fraction [-]			
H ₂	1.81×10^{-6}	1.88×10^{-6}	-
O	1.57×10^{-5}	1.65×10^{-5}	-
O ₂	7.26×10^{-2}	7.39×10^{-2}	7.40×10^{-2}
OH	3.31×10^{-4}	3.42×10^{-4}	-
H ₂ O	8.44×10^{-2}	8.44×10^{-5}	8.46×10^{-5}
CO	4.74×10^{-5}	4.94×10^{-5}	5.08×10^{-5}
CO ₂	1.03×10^{-1}	1.03×10^{-1}	1.03×10^{-1}
N ₂	7.37×10^{-1}	7.38×10^{-1}	7.38×10^{-1}
Temperature [K]	1788	1793	1796

Table 7.3: Equilibrium temperatures and species mass fractions for different kinetic schemes.

mass fractions greater than 1×10^{-6} are considered. The equilibrium calculation is performed starting from a mixture at an equivalence ratio $\phi = 0.67$, a temperature of 300 K and atmospheric pressure (inlet conditions of the PACCI burner). It can be seen how the LU13 kinetic scheme provides very good results, generally slightly better

7. LES OF A PREMIXED SWIRL-STABILIZED BURNER

than the BFER one. It can be seen in particular how some species which are present at equilibrium are not considered by the BFER scheme.

Keeping the equivalence ratio equal to the one encountered in the PACCI configuration ($\phi = 0.67$), the flame structure is now compared in Fig. 7.16, where the temperature and heat release rate profiles are shown. It can be seen how the agreement is very good between the LU13 and the GRI30 schemes. When using the BFER scheme, the overall agreement is good but the heat release rate shape differs slightly. In particular, the "post-flame" zone is not correctly captured: the mixture rapidly tends to the adiabatic flame temperature and the heat release rate quickly vanishes. On the contrary its maximum value is overestimated. The crucial values of adiabatic flame temperature,

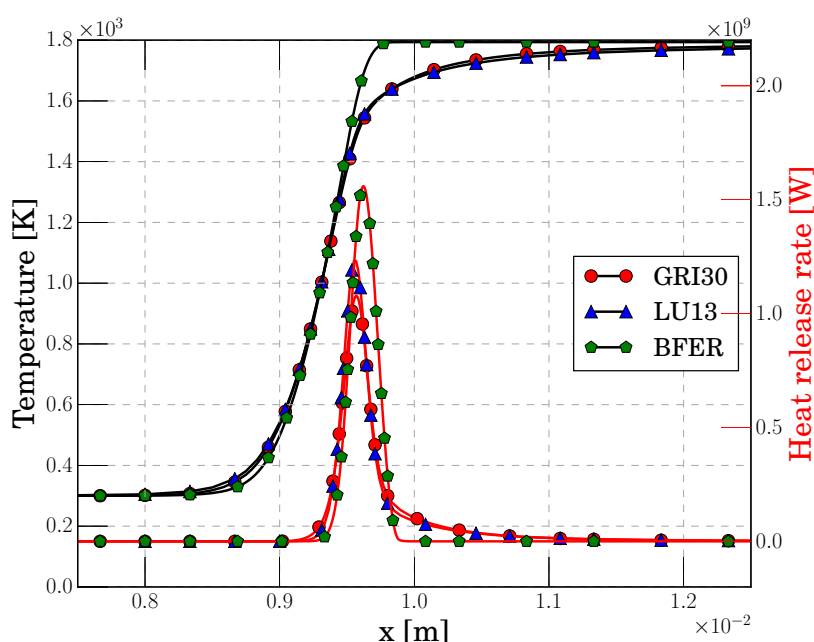


Figure 7.16: Temperature and heat release rate profiles for a 1D unstrained premixed flame using various kinetic schemes.

flame speed and flame thickness are listed in Tab. 7.4 for the three kinetic schemes. The parameters are globally well reproduced for both reduced schemes. The only noticeable thing is the underestimation of flame thickness by the BFER mechanism.

A crucial point for the NRP discharges will be the autoignition behavior, as it will be shown in chapter 8. The autoignition time is shown in Fig 7.17 for the three mechanisms. The initial mixture is set to an equivalence ratio $\phi = 0.67$ and to atmospheric pressure. The LU13 kinetic scheme has a good behavior when compared to the GRI30 one. The autoignition time is slightly overestimated for temperatures lower than 2000 K, but the agreement is excellent when the temperature is higher than this value. On the contrary, the BFER kinetic scheme strongly underestimates the autoignition time for all the range of temperature studied.

If we are in the temperature range of NRP discharges (2000 to 3000 K, as it will be

7.3 Reacting flow in the PACCI burner

	GRI30	LU13	BFER
Number of species	53	13	6
Number of reactions	325	73	2
Adiabatic Flame Temperature [K]	1787	1784	1793
Flame speed [m/s]	16.99×10^{-2}	17.57×10^{-2}	17.65×10^{-2}
Flame thickness [m]	7.29×10^{-4}	6.96×10^{-4}	6.04×10^{-4}

Table 7.4: Adiabatic flame temperature, flame speed and flame thickness for different kinetic schemes.

shown in chapter 8), the autoignition time is perfectly estimated by the LU13 scheme, while the BFER scheme underestimates it by more than one order of magnitude.

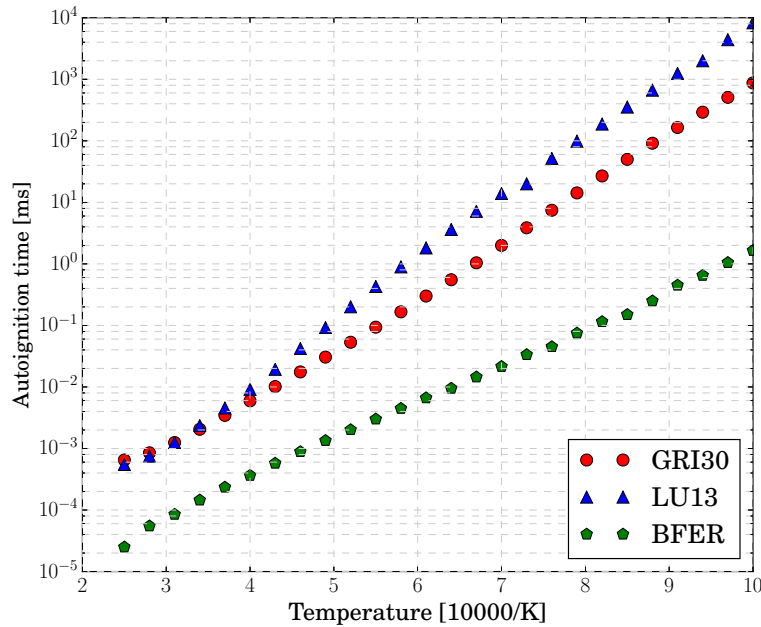


Figure 7.17: Autoignition time as a function of the mixture temperature. Logarithmic scale.

In order to check the overall mechanism behavior, the evolution of the laminar flame speed and of the adiabatic flame temperature with the equivalence ratio is also evaluated and presented in Fig. 7.18. This has been performed for an unstrained premixed flame with a mixture at initial temperature of 300 K and atmospheric pressure. It can be seen how the agreement with the detailed scheme is globally good for both reduced mechanisms. Regarding the laminar flame speed, on the lean side the agreement is very good, but an overestimation can be seen when approaching stoichiometry for both mechanisms. The LU13 mechanism stays however closer to the GRI30 mechanism than the BFER one. On the rich side both reduced kinetic schemes slightly deviate from the detailed one, with the LU13 mechanism which underestimates the flame speed and

7. LES OF A PREMIXED SWIRL-STABILIZED BURNER

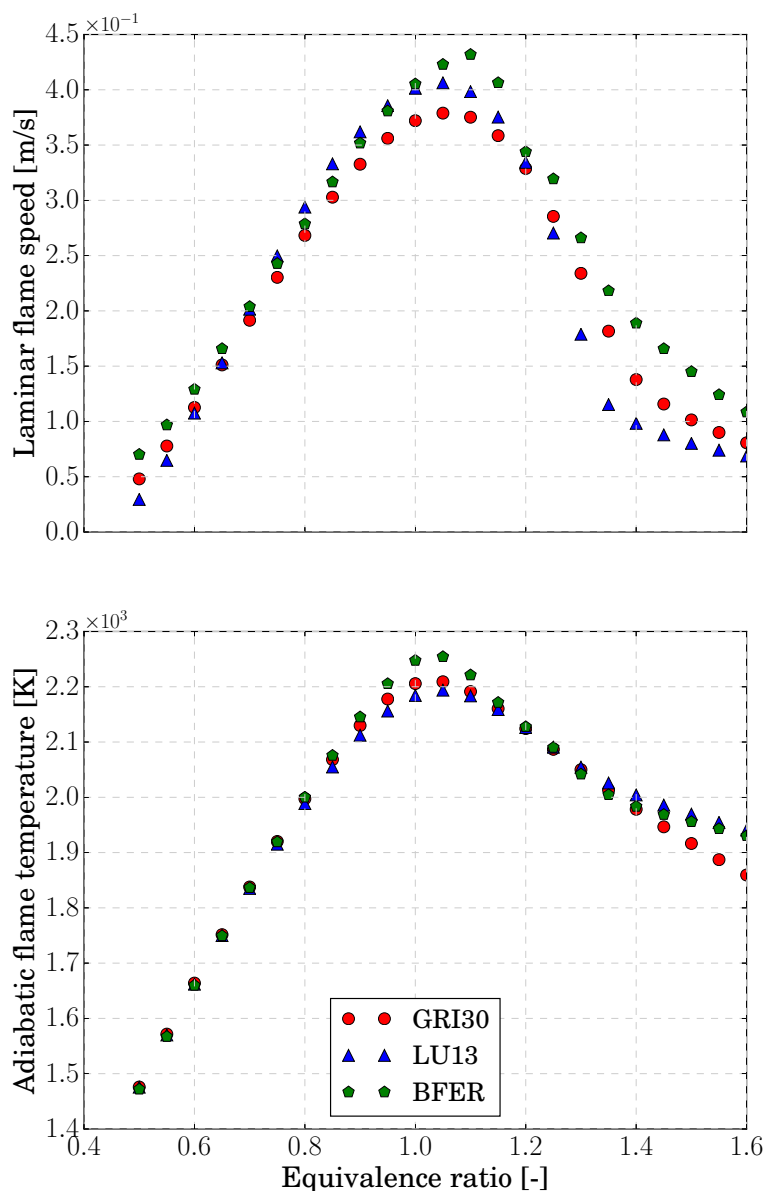


Figure 7.18: Laminar flame speed (top) and adiabatic flame temperature (bottom) as a function of the mixture equivalence ratio.

the BFER one which overestimates it. Regarding the adiabatic flame temperature, the agreement is excellent on the lean side. Some differences can be seen close to stoichiometry, with the BFER mechanism which overestimates the value of the adiabatic flame temperature. On the rich side, the agreement is excellent up to an equivalence ratio of about 1.4. For higher values, both mechanisms tend to overestimate the adiabatic flame temperature.

At the PACCI equivalence ratio ($\phi = 0.67$) the agreement is excellent both in flame speed and adiabatic flame temperature for the two mechanisms studied.

In order to save computational time, and as a first step, the BFER mechanism is used to perform the majority of the LES presented in this work. It is also the mechanism chosen to tune the NRP discharge model used in chapter 8 and 9. To evaluate the impact of the limitations of BFER, some of the simulations have also been run with the LU13 mechanism.

7.3.2 LES using the BFER 2-steps global chemistry

7.3.2.a Simulation setup

The reactive numerical simulations which use the BFER kinetic scheme are run on the mesh M1, the same one used for the non-reactive LES.

For the inlet and outlet boundary conditions, the NSCBC formalism is used, similarly to the "cold" case. The experimental mass flow rate of perfectly premixed methane and air at $\phi = 0.67$ is prescribed at inlet. Its value is fixed to 1.960 g/s. At outlet the atmospheric pressure is imposed.

Contrarily to the non-reacting case, the walls facing the flame have been treated as isothermal, instead of adiabatic. The walls treated as isothermal are the quartz walls, faceplate and pin steel electrode (red patches in Fig. 7.19). The imposed temperatures

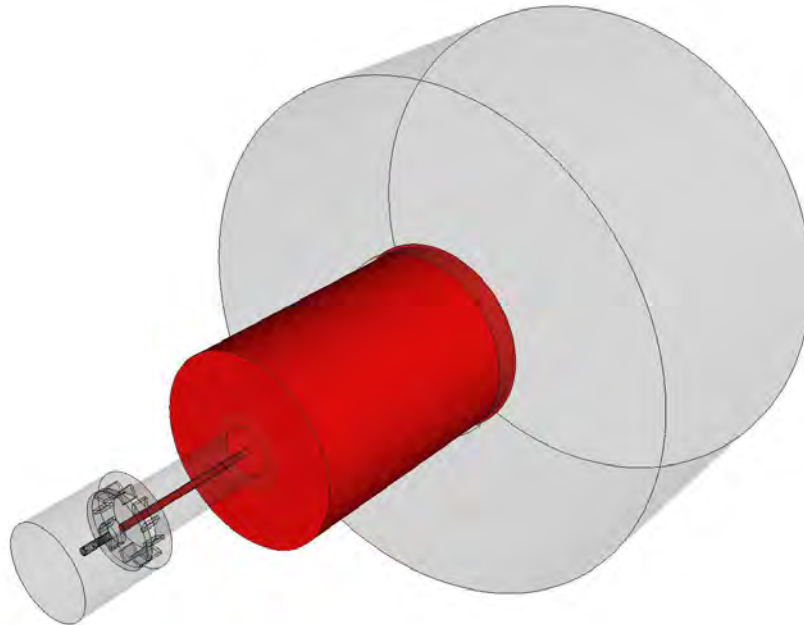


Figure 7.19: Schematic representation of the isothermal walls boundary conditions.

are the one experimentally measured, i.e. 515-610 K for the quartz tube, 515 K for the bottom part of the combustion chamber, and 494 K for the top of the central rod. It has been found indeed that this flame is strongly subject to thermal losses at walls, which can transform the flame from M-shaped to V-shaped. This has been verified by means of a LES with all adiabatic walls. An example of the difference in instantaneous

7. LES OF A PREMIXED SWIRL-STABILIZED BURNER

fields of temperature and heat release rate obtained using adiabatic or isothermal walls is shown in Fig 7.20. With adiabatic walls, due to the absence of heat losses at walls,

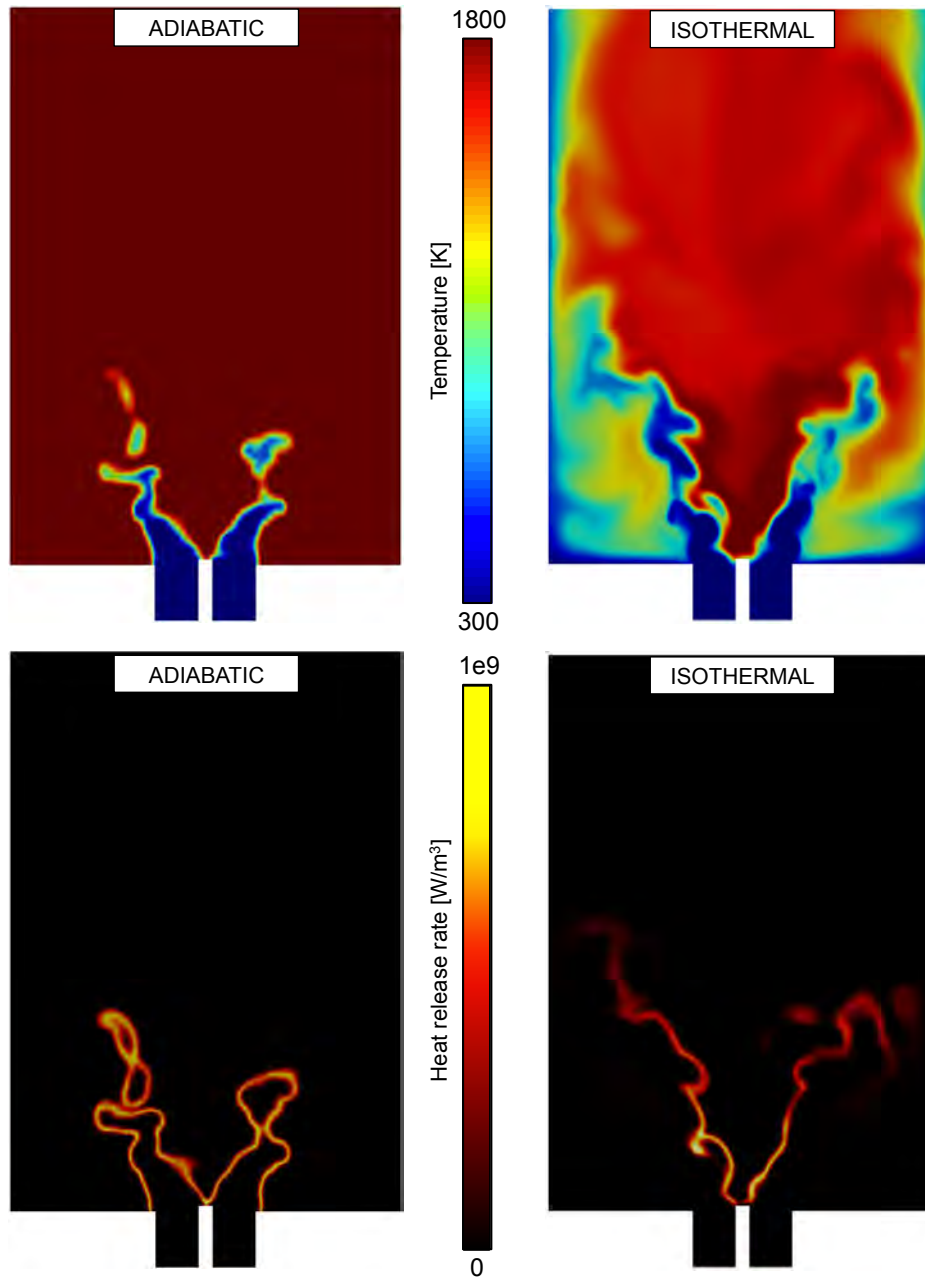


Figure 7.20: Temperature (top) and heat release rate (bottom) instantaneous fields on a 2D cut at $z = 0$. Left: adiabatic walls, right: isothermal walls.

the corner recirculation zones are filled with burnt gases at equilibrium temperature. Because of this the flame closes also in the outer shear layer and is M-shaped. Moreover, the flame is attached to the central rod. On the contrary, using isothermal walls, the gases in the corner recirculation zones are cooled down and the conditions necessary

for a flame stabilization in the outer shear layer do not exist anymore. This leads to a V-shaped, longer flame. It has also been noticed that, when using adiabatic walls, the flame root is attached to the central rod; on the contrary, when using isothermal walls, a flame quenching occurs and the flame root is slightly lifted.

During reactive simulations, a high-frequency (around 8 kHz) acoustic mode has appeared, corresponding to a radial spinning mode of the chamber. This mode is not present in the experiment, as confirmed by KAUST, where it is probably damped by means of mechanisms which can not be accounted for in the LES (i.e., structural vibrations). It has so been decided to dump the acoustic mode, in order to avoid undesired pressure fluctuations in the combustion chamber. This has been done by treating the chamber faceplate with the NSCBC formalism in order to include an "acoustically absorbing wall" in the combustion chamber. Numerically, the absorbing walls are "soft" NSCBC walls. Their mean velocity is zero but not their fluctuation. An adequate relaxation coefficient has been used on the velocity component normal to the wall in order to dump the very high frequencies of the acoustic mode but keep all the physics associated with lower frequencies. In this work the relaxation coefficient is set to $\kappa_f = 10000$ which yields a cut-off frequency of $f_{cut} = 800$ Hz. This partially reflecting boundary condition behaves like a low-pass filter [Selle et al., 2004], so that acoustic waves above f_{cut} propagate out of the domain. This kind of boundary condition has already been used and validated in the PhD thesis of Ghani [2016], where absorbing walls are used for active control.

It has been verified that the overall mass flow rate through the absorbing wall was always a very small fraction of the input mass flow rate. Fig 7.21 displays the ratio between the mass flow rate through the absorbing wall and the inlet mass flow rate as a function of physical time. The value of the latter is generally lower than 1 %, with peaks which never exceed 2 %.

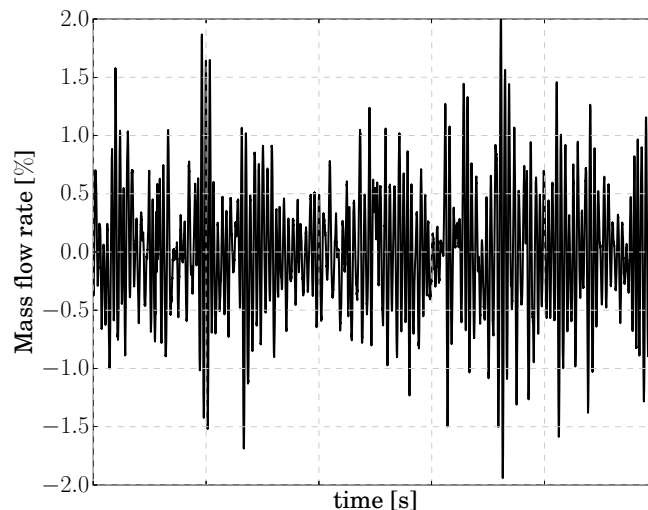


Figure 7.21: Temporal evolution of the ratio between the mass flow rate through the absorbing wall and the inlet mass flow rate.

7. LES OF A PREMIXED SWIRL-STABILIZED BURNER

7.3.2.b Results

The convective time scale of the burner is evaluated in the same way as for the "cold" LES, using the total burner volume V_b , the inlet flow rate \dot{m} and the mean density ρ :

$$\tau_{conv} = \frac{\rho V_b}{\dot{m}} = 75 \text{ ms} \quad (7.6)$$

It is lower than for the cold case. The numerical simulation has been run for a total of two convective time, additionally to the transient ignition, in order to obtain statistically converged data.

Mean fields

The flow pattern is illustrated in Fig. 7.22 where time and azimuthal averaged fields of axial velocity and temperature are shown. Streamlines are superimposed in white. It can be seen how, thanks to the swirling motion, a central recirculation zone is

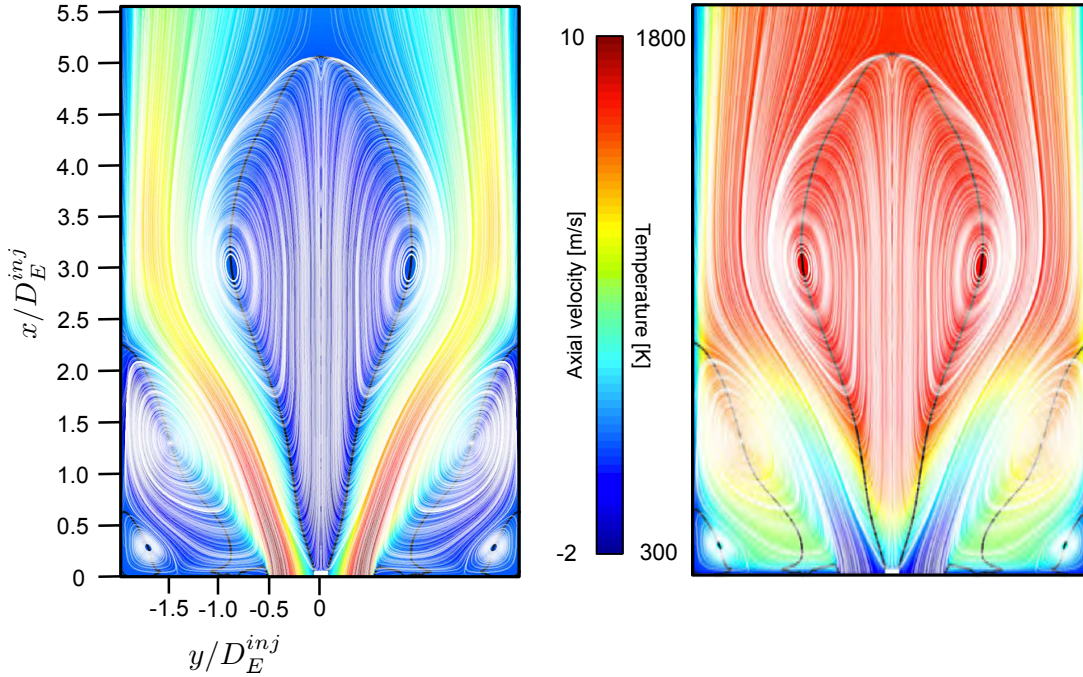


Figure 7.22: Mean flow pattern in the combustion chamber. White: time and azimuthal averaged streamlines. Black line: zero axial (x -axis) velocity iso-line. Left: field colored by axial velocity. Right: field colored by temperature.

formed. The latter extends from the tip of the NRP electrode until $x/D_E^{inj} \approx 5$, close to the exit of the combustion chamber. The recirculating flow is formed by hot burnt gases in the range $1.5 < x/D_E^{inj} < 5$. However, for $x/D_E^{inj} < 1.5$ a colder flow is present. In this zone the velocity is negative in average but a strong variation of flow characteristics is present, switching from cold fresh gases flowing downstream to hot burnt ones recirculating upstream.

Corner recirculation zones are also present, filled by burnt gases which are cooled down

by the cold walls. The corner recirculation zones close at $x/D_E^{inj} \approx 2.25$, a little downstream compared to the "cold" case.

The effect of the isothermal boundary condition on walls is visible on the temperature fields, with the presence of a thermal boundary layer near them.

The time and azimuthal averaged flow fields of main flow variables, as well as of species mass fractions are presented in Figs. 7.23, 7.24 and 7.25. Figure 7.23 illustrates

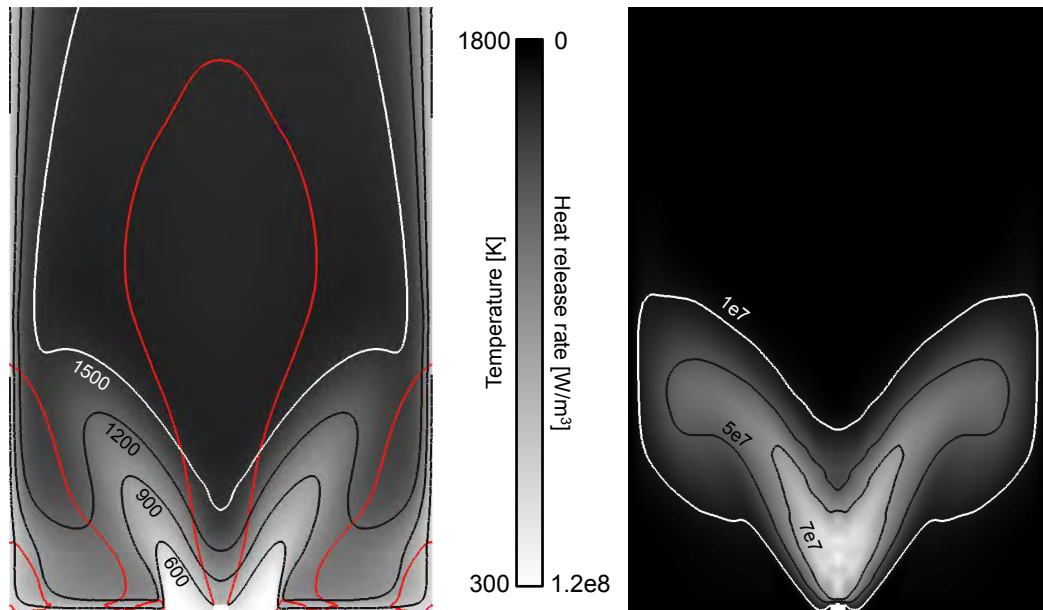


Figure 7.23: Time and azimuthal averaged flow field of temperature (left) and heat release rate (right) in the combustion chamber. Red line: iso-line of zero axial velocity

the flame shape. The flame is V-shaped and occupies around the half of the combustion chamber in height. The flame root strongly moves, as can be seen by the wide zone at high heat release rate, which denotes an unsteady reaction zone. This is also confirmed by the fields of RMS quantities presented in Fig. 7.24. The RMS axial velocity field is qualitatively similar to the cold flow one, with the higher activity in the inner shear layer. A very important field for flame stability is the RMS temperature one, which permits to check whether the flame strongly moved or not. This fields confirms the strong instability of the flame root in this configuration. Finally, Fig. 7.25 presents the mass fraction of CO and CO₂. These two species have been chosen as they are the only intermediate product present in the BFER scheme and a main combustion product. The CO is concentrated in the flame zone, as expected. Outside the flame the oxidation of CO in CO₂ operates and almost no CO is present at chamber exit. Looking at the field of CO₂ mass fraction highlights how the corner recirculation zones are completely filled with burnt gases.

In order to verify if the numerical simulation is able to retrieve the correct flame shape, the time and azimuthally-averaged field of heat release rate is compared with an image of the time-averaged Abel-inverted field of OH* emission collected in the experiment (Fig. 7.26). Both fields have been non-dimensionalized by their maximum values; note that, due to isolated points with high values, the experimental field results

7. LES OF A PREMIXED SWIRL-STABILIZED BURNER

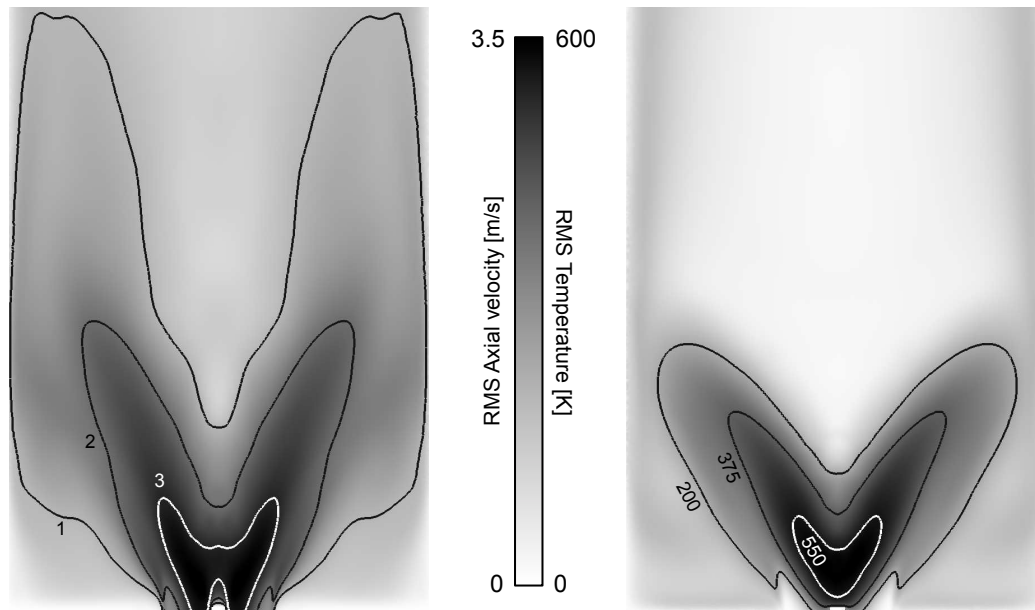


Figure 7.24: Time and azimuthal averaged flow field of RMS axial velocity (left) and RMS temperature (right) in the combustion chamber.

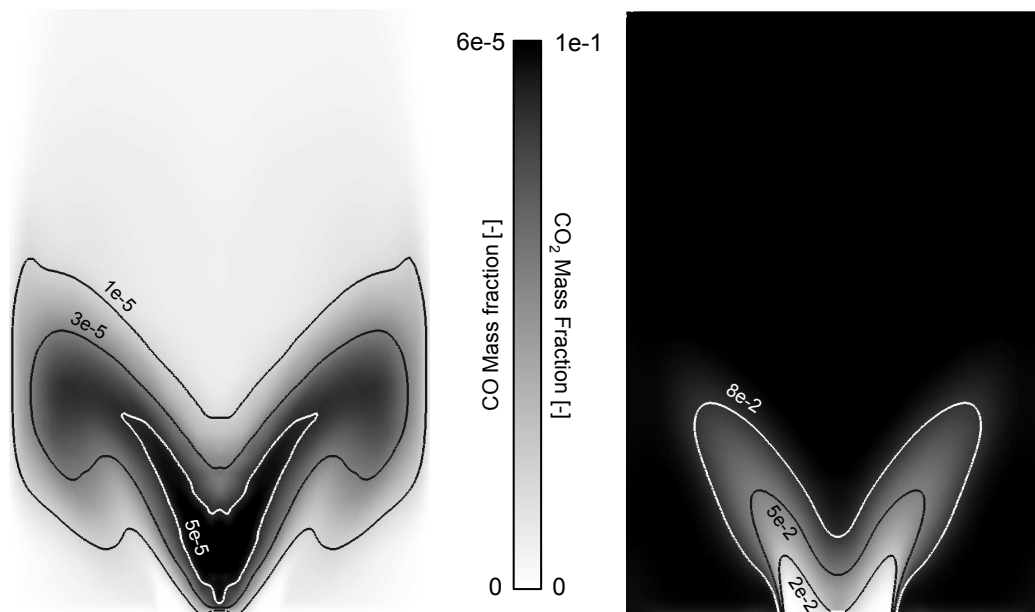


Figure 7.25: Time and azimuthal averaged flow field of CO (left) and CO₂ (right) mass fraction in the combustion chamber.

less bright than the numerical one. The flame shape is qualitatively well captured by the numerical simulation. It can be noticed how:

- both numerical simulation and experiment show large RMS temperature values near the top of the pin steel electrode, denoting an intermittent attached-lifted

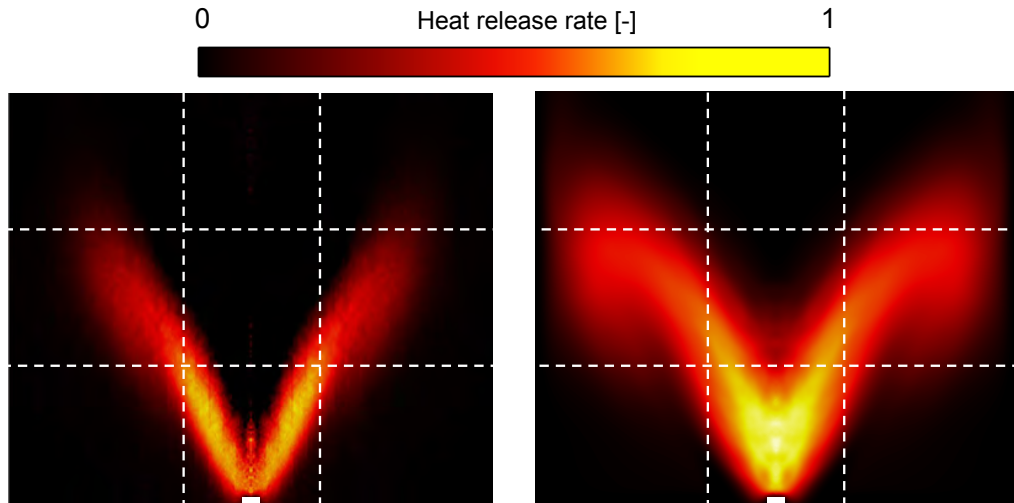


Figure 7.26: Left: time-averaged Abel-inverted image of the OH^* emission (courtesy of KAUST). Right: time and azimuthally-averaged field of the heat release rate from the numerical simulation. Both fields have been normalized by their respective maximum values.

flame and a significant movement of the flame root

- the numerical simulation predicts a flame opening and flame length almost identical to the experiment
- the numerical simulation shows a larger zone of low heat release rate values compared to the experiment, especially in the flame axis, just above the flame root zone, and in the outer recirculation zones. This can be due to a slightly larger flame motion or, more probably, to a lack of information on weak light emission in the data collection of OH^* emission.

Flame dynamics

As already shown by RMS fields, the flame alternates phases in which it is attached to the pin steel electrode to phases in which it is completely lifted. This phenomenon is shown using LES in Fig. 7.27 by means of a series of instantaneous fields of temperature in a 2-D cut at $z = 0$. An iso-line of heat release rate is added (white line), in order to track the flame front. This dynamical behavior causes fluctuations in the heat release rate of the flame, as shown in Fig. 7.28, top. Here the mean heat release rate is plotted for the entire simulation time. The red dots identify the temporal instants at which the snapshots of Fig. 7.27 have been taken. In Fig. 7.28, bottom, the temporal evolution of temperature and axial velocity on a probe situated on the burner axis, at $x = 10$ mm (one tenth of the chamber length, see probe position in Fig. 7.27) is shown. The integrated heat release rate strongly variates (Fig. 7.28, top). The maximum values recorded can reach twice the minimum ones. This flame variability is driven by the interactions with the turbulent flow in which the flame lives. The flame is stretched by the flow and its surface is modified. Pockets of unburnt gases separate and suddenly

7. LES OF A PREMIXED SWIRL-STABILIZED BURNER

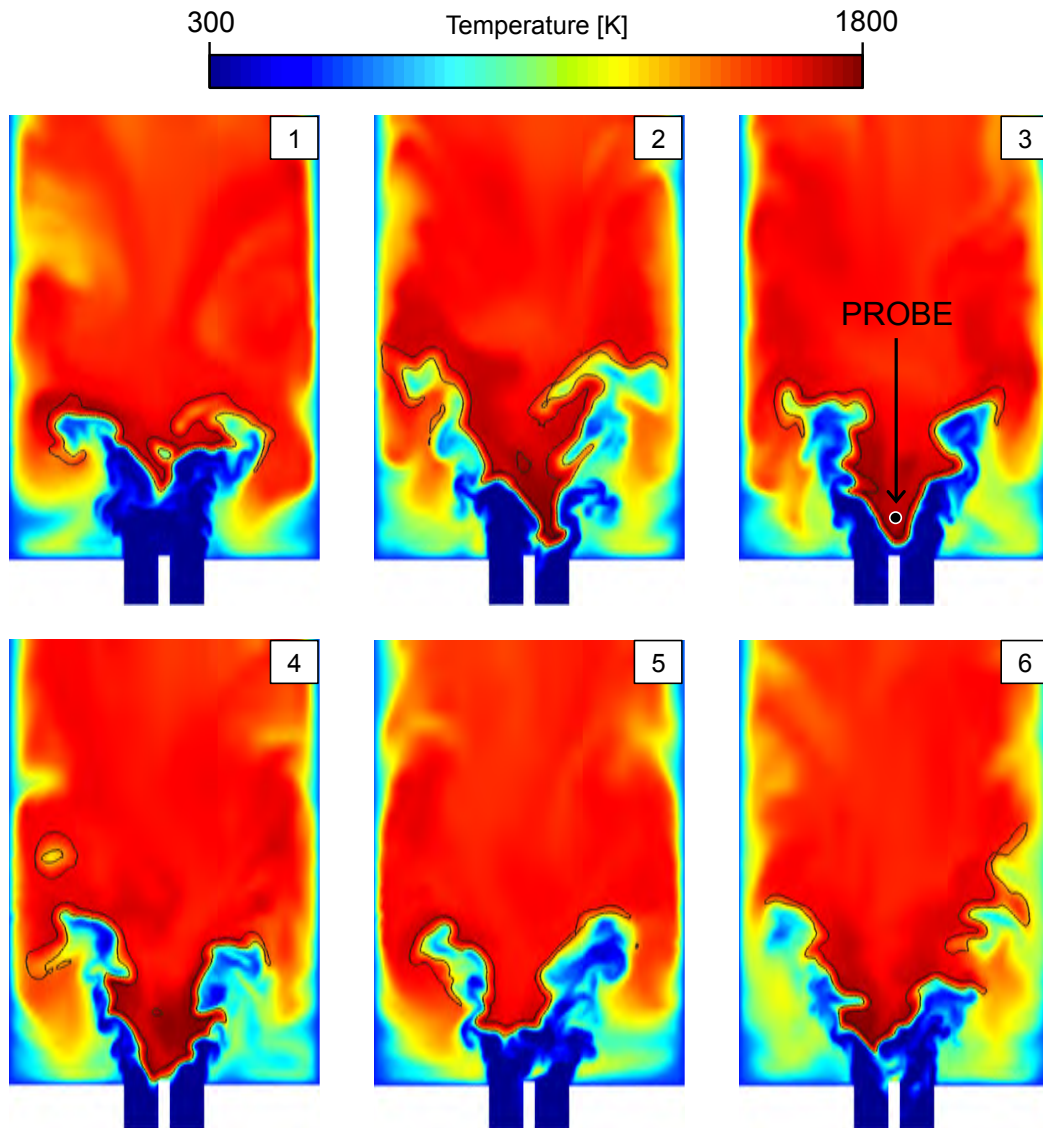


Figure 7.27: Instantaneous fields of temperature on a 2D cut at $z = 0$. Black line: iso-line of heat release rate ($1 \times 10^8 \text{ W/m}^3$).

burn. This is confirmed by the values of axial velocity and temperature recorded in the central zone of the burner. The alternation of instants in which the axial velocity is positive (meaning a flow directed towards the chamber exit) with instants in which the axial velocity is negative (meaning a recirculating flow) can be seen. In the first case, fresh gases occupy the zone and the temperature is very low. In the second case the burnt gases recirculate towards the rod downstream end, leading to high temperature. The variation of mean heat release rate follows this evolution, with maximum values when a lifted flame suddenly has favorable conditions to reattach to the rod. Moreover, it seems that the points where the mean heat release rate is maximum (points 2, 4 and 6 in Figs. 7.27 and 7.28) are the ones where the flame surface is larger.

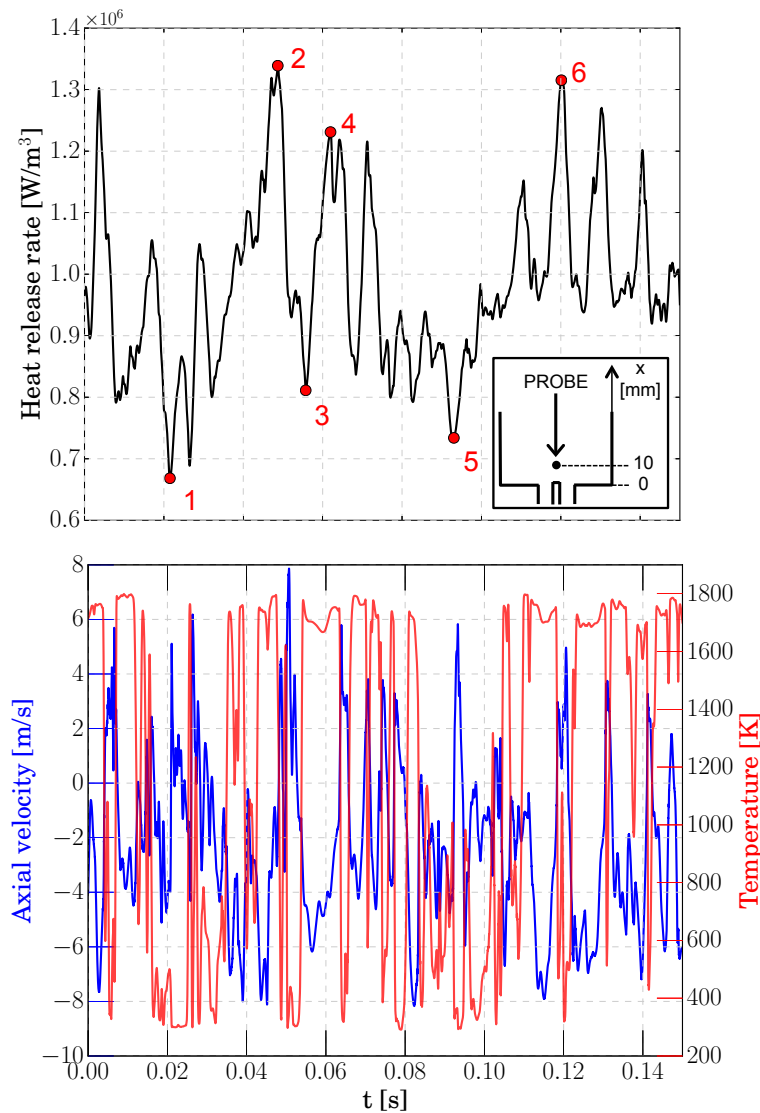


Figure 7.28: Top: temporal evolution of the mean heat release rate. Bottom: temporal evolution of temperature and axial velocity on a probe situated in the burner axis, at $x = 10$ mm.

The frequency signature of the heat release rate has been checked, in order to distinguish between natural oscillations of the flame and a forced response when acoustically pulsating the flow (as will be shown in section 7.4). Fig. 7.29 presents a power spectral density of the integrated heat release rate: the oscillations have a very low frequency, with the two main peaks situated around 10 and 80 Hz. It is not the objective here to correctly capture the very low frequency of 10 Hz, which would require a much longer simulation time. The aim is to check that no natural oscillation is present at a frequency close to the one at which the flame will be acoustically pulsed.

The flame dynamics just described has been confirmed by experimental results. OH^* chemiluminescence images show the alternating lifted-attached flame position, as

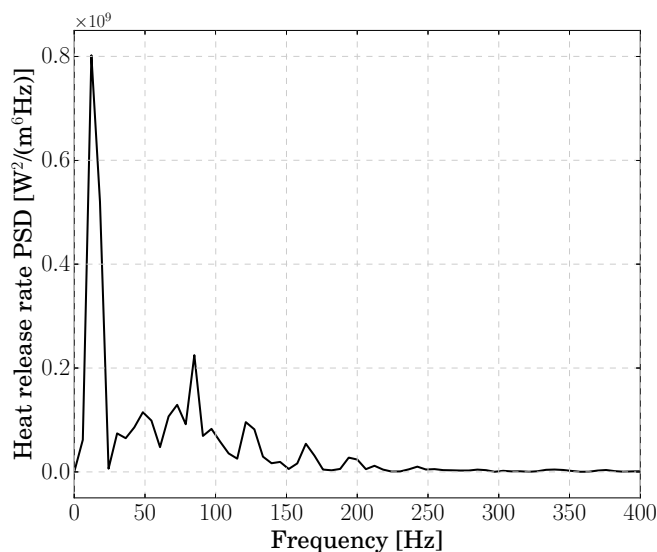


Figure 7.29: Power spectral density of mean heat release rate.

illustrated in Fig 7.30. This dynamics can be found in other studies in literature. See,

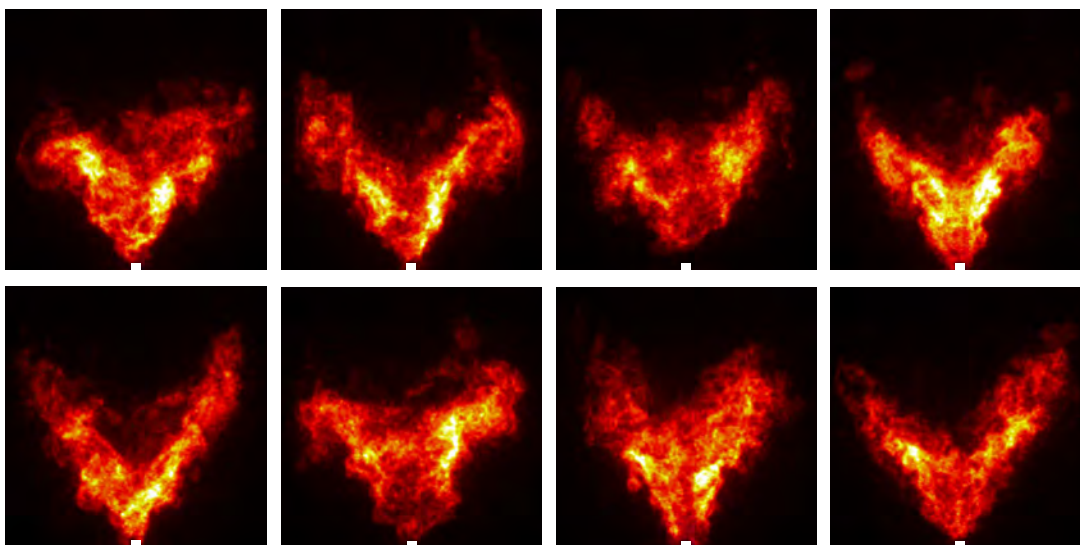


Figure 7.30: OH* chemiluminescence instantaneous fields at various temporal instants (courtesy of KAUST).

among others, [Bellows et al. \[2007a,b\]](#); [Thumuluru et al. \[2007\]](#).

7.3.3 Impact of the kinetic scheme: LES using the LU13 ARC chemistry

The impact of using kinetic schemes with different complexity is now evaluated. The LES simulation presented above has been run again using the LU13 ARC kinetic

scheme, starting from a reacting simulation run with the BFER kinetic scheme. The additional transported species are added and, after a transient phase, data are collected.

7.3.3.a Simulation setup

A new mesh is generated for this numerical simulation, which will be called mesh M2. The mesh M2 is a modified version of the mesh M1, from which all the crucial parameters are kept. The only difference is the cell size in the flame root zone, with a minimum value falling from 0.3 mm to 0.1 mm and a slower coarsening. A schematic of the cell size can be seen in Fig. 7.31. This has been necessary to overcome some

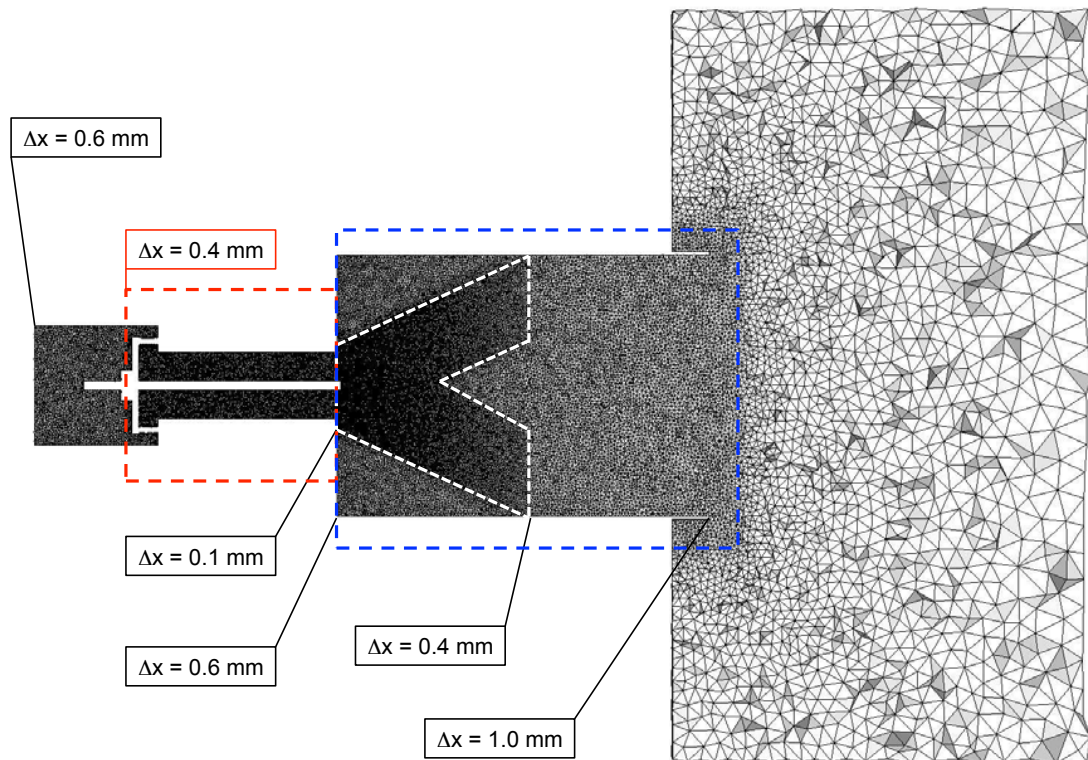


Figure 7.31: 2-D cut of the mesh M2 in the plane $z = 0$.

problems found when thickening the flame with this kinetic scheme and is expected since the LU13 ARC scheme involves much more species than the BFER. As seen in Fig. 7.16, the LU13 scheme tends slower to the adiabatic flame temperature than the BFER one. It has been found in this case that, when applying a TFLES model, the increase in diffusivity leads to a too strong diffusion and heat release rate decrease, which prevents the flame root to stabilize at the right position. As it has been shown, the flame root dynamics is crucial in this configuration and has to be well captured. The choice made here has been to refine the grid in order to have values of \mathcal{F} close to 1, but it is mandatory to investigate this problem into deeper detail in future works.

Boundary conditions and numerical parameters are the same as in the LES with the BFER mechanism.

7.3.3.b Results

Additionally to the transient phase, the numerical simulation has been run during 150 ms, i.e. two convective times, in order to collect statistically converged data.

Mean fields

The flow pattern is illustrated in Fig. 7.32 where the time and azimuthal averaged field of axial velocity is shown, compared to the one obtained with the BFER kinetic scheme. Streamlines are superimposed in white: the flow pattern is identical, with a central

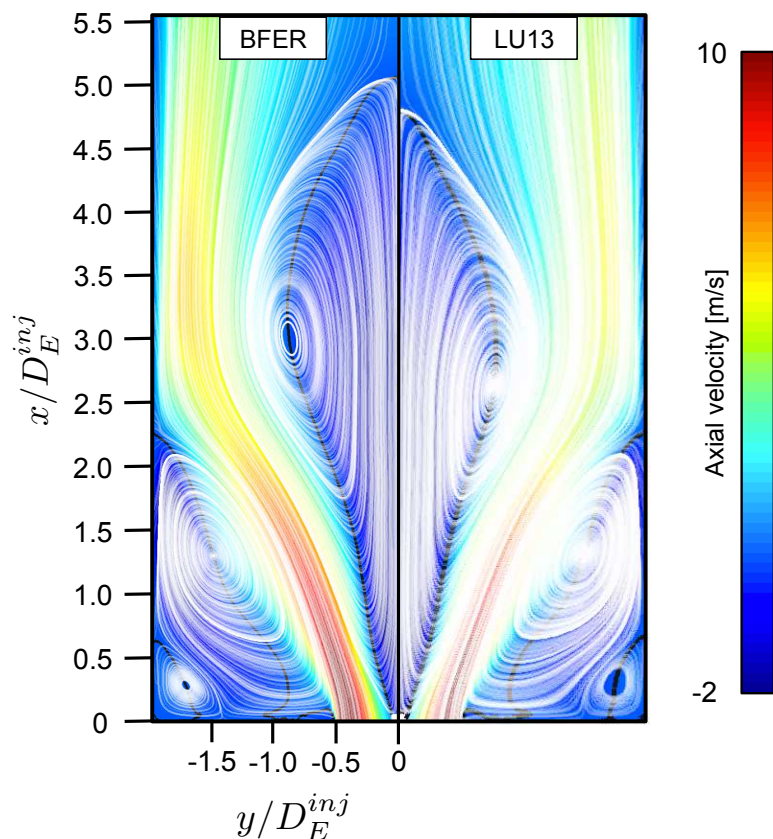


Figure 7.32: Mean flow pattern in the combustion chamber. White: time and azimuthal averaged streamlines. Black line: zero axial (x -axis) velocity iso-line.

recirculation zone and two corner recirculation zones. However, the central recirculation zones closes a little upstream when using the LU13 kinetic scheme, compared to the case in which the BFER mechanism is used. This is symptom of a less lifted flame in average, with a central recirculation zone which is, in average, less pushed downstream by the lifted flame.

This is confirmed when looking at the time and azimuthal averaged flow fields of main flow variables, as well as of species mass fractions, which are presented in Figs. 7.33, 7.35 and 7.41 and compared to the ones obtained with the BFER mechanism.

Figure 7.33, in which mean temperature and heat release rate fields are shown, shows indeed a hot zone which extends upstream when using the LU13 kinetic scheme,

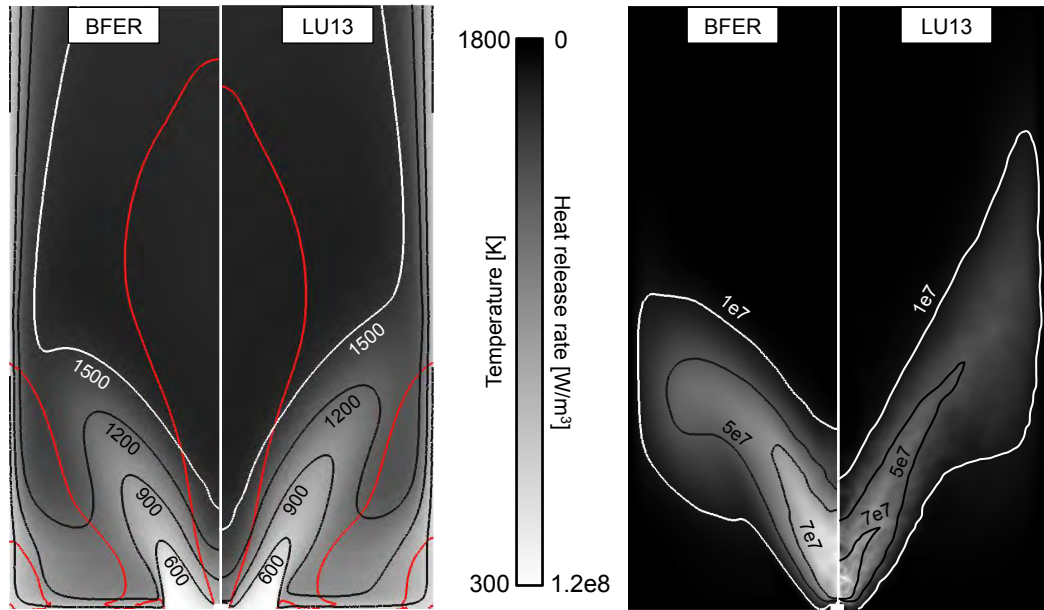


Figure 7.33: Time and azimuthal averaged flow field of temperature (left) and heat release rate (right) in the combustion chamber. Red line: iso-line of zero axial velocity. Comparison between BFER and LU13 mechanisms.

where stable burnt gases are found closer to the upper end of the central rod. This denotes a less lifted flame in average. This is also confirmed when looking at the mean field of heat release rate, where the central zone is characterized by slightly lower values. The flame shape is similar in both cases and the one predicted by the LU13 scheme seems to be a little more in agreement with the data collected experimentally in the flame root zone (Fig. 7.34). However, the flame is longer when using the ARC scheme.

Analyzing now Fig. 7.35, one can notice that the field of RMS axial velocity is substantially identical in both cases, with a slight sign of less lifted flame. This is on the contrary evident when looking at the RMS temperature field. In the flame root zone the values are globally lower, with maximum shifted towards the downstream end of the central rod. This denotes once again a less lifted flame in average. It confirms however a very unstable flame with a strong flame root motion. Moreover, higher values are found in the corner recirculation zones and the area of non-zero temperature RMS extend a little more downstream.

All the above mentioned differences are also evaluated quantitatively by means of 1D profiles at 5 different axial positions, corresponding to $x/D_E^{inj} = 0.15, 0.3, 0.6, 1.5$ and 3.0 . A scheme is provided in Fig. 7.36. Profiles of mean and root-mean-square values of axial velocity and temperature are shown respectively in Figs. 7.37, 7.38, 7.39 and 7.40.

The more pronounced differences are found when analyzing Fig. 7.41, where the mean fields of CO and CO₂ mass fractions are shown. As expected, since the kinetic scheme is strongly different, first order differences are found. Looking at the left side, the time and azimuthal averaged field of carbon monoxide mass fraction is presented. The first difference is on the order of magnitude of the maximum values, which is

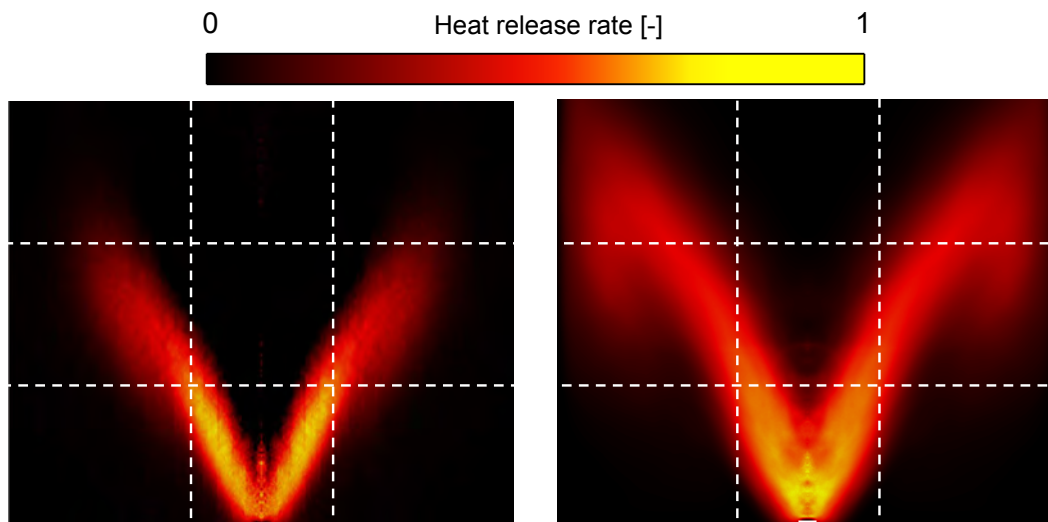


Figure 7.34: Left: time-averaged Abel-inverted image of the OH* emission (courtesy of KAUST). Right: time and azimuthally-averaged field of the heat release rate from the numerical simulation using the LU13 mechanism. Both fields have been normalized by their respective maximum values.

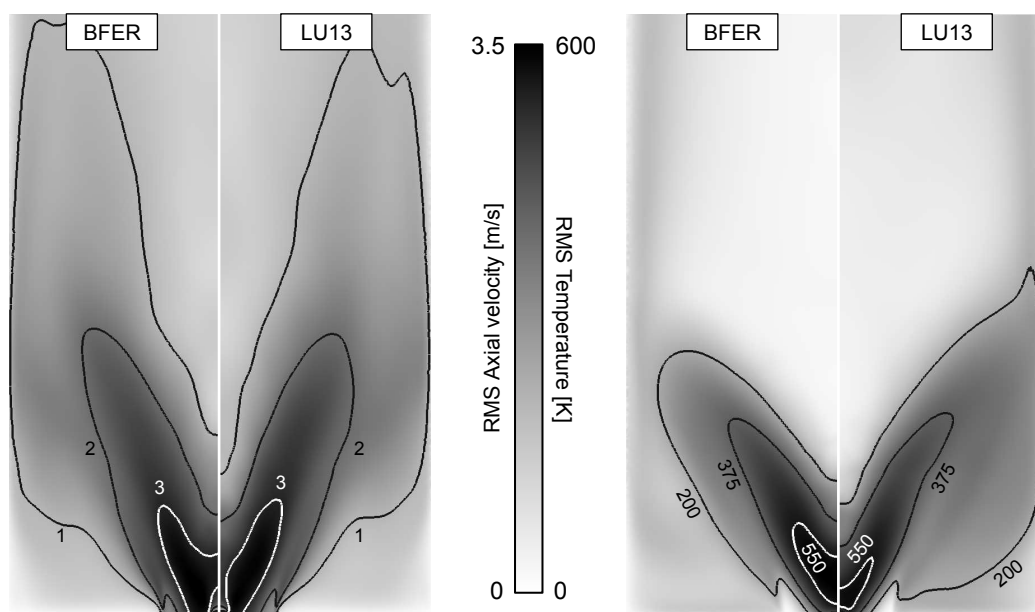


Figure 7.35: Time and azimuthal averaged flow field of RMS axial velocity (left) and RMS temperature (right) in the combustion chamber. Comparison between BFER and LU13 mechanisms.

100 time larger when using the ARC mechanism. This is clearly due to the intrinsic propriety of the BFER mechanism, in which the CO oxidation is very slow, as previously explained. This higher concentration is also visible in the corner recirculation zones and has a direct impact on the CO₂ mass fraction field. Moreover, CO is mostly oxidized

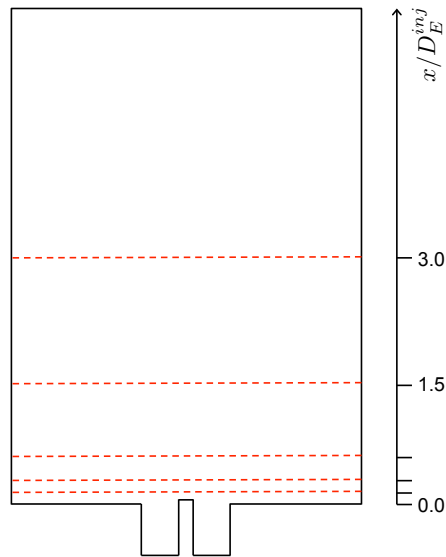


Figure 7.36: Schematic of 1D profiles position.

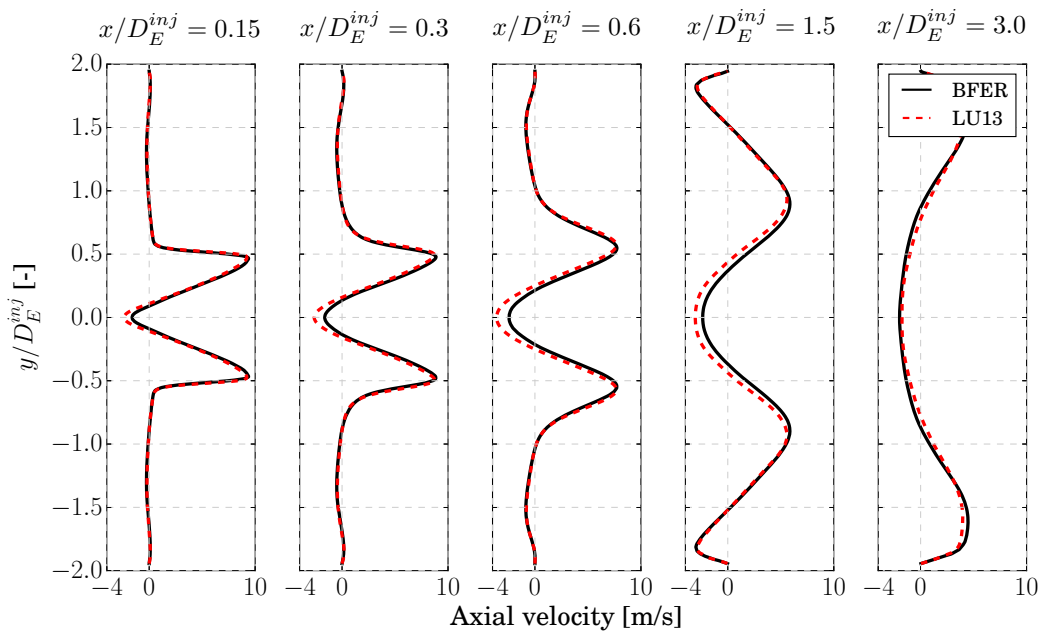


Figure 7.37: 1D axial velocity mean profiles at different axial positions. Comparison between BFER and LU13 kinetic schemes.

at the outlet of the combustion chamber, giving a similar field in both cases.

Flame dynamics

Figure 7.42 shows, in the same way as for the BFER case, the temporal evolution of the integrated heat release rate in the entire domain (top) and the temporal evolution of temperature and axial velocity on a probe situated in the chamber axis, 10 mm

7. LES OF A PREMIXED SWIRL-STABILIZED BURNER

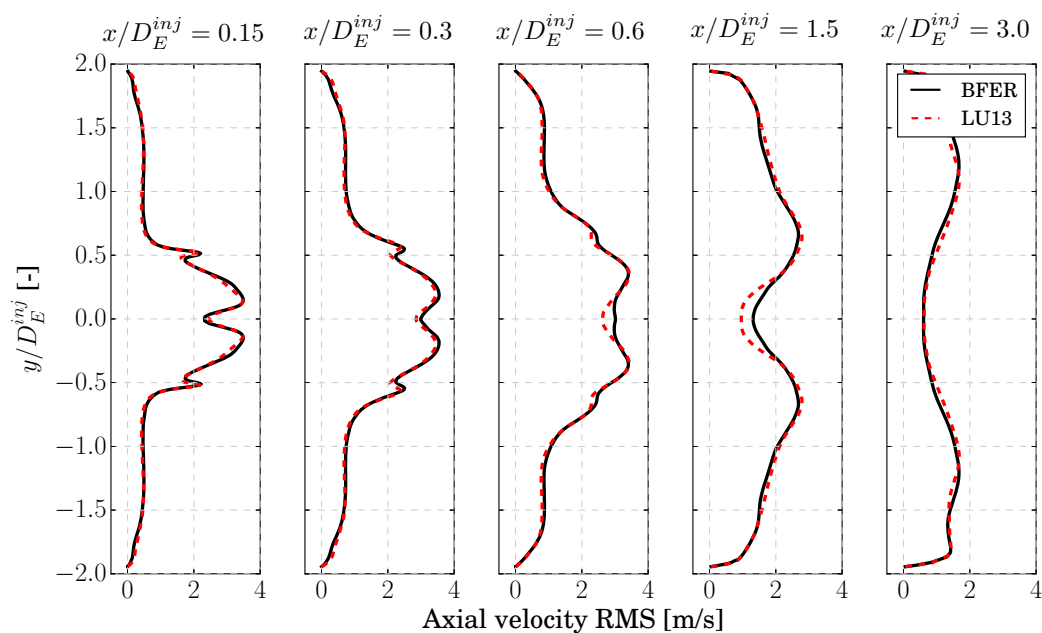


Figure 7.38: 1D axial velocity RMS profiles at different axial positions. Comparison between BFER and LU13 kinetic schemes.

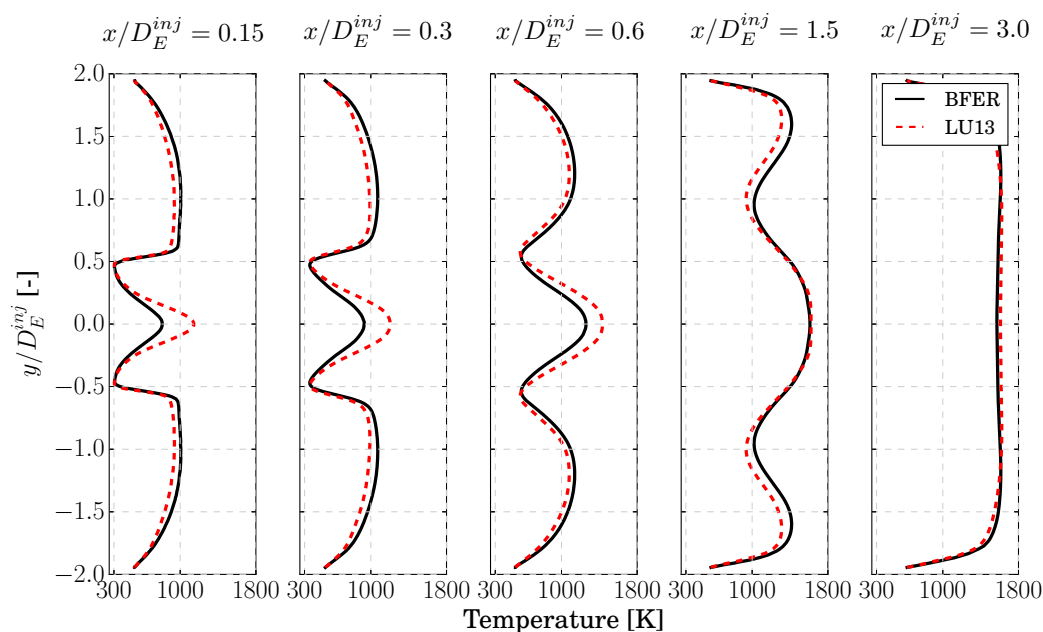


Figure 7.39: 1D temperature mean profiles at different axial positions. Comparison between BFER and LU13 kinetic schemes.

far away from the rod end (bottom). The flame behavior observed using the BFER kinetic scheme is totally retrieved (see Fig. 7.28), with a fluctuating heat release rate during the simulation time. Moreover, the already observed behavior of an alternation of states with hot burnt gases with a negative axial velocity and cold fresh gases with

7.3 Reacting flow in the PACCI burner

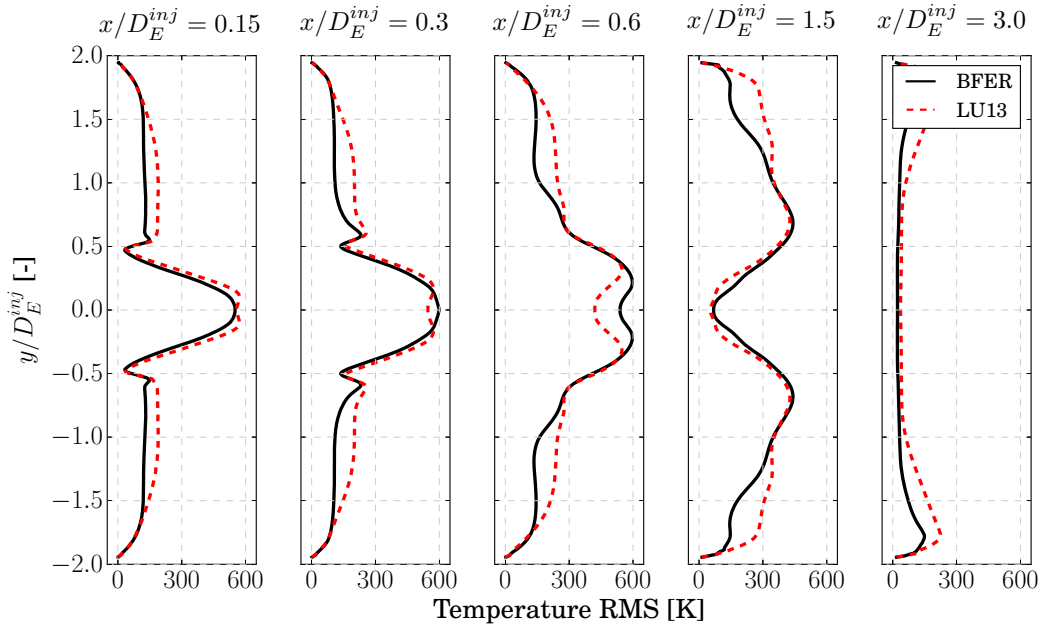


Figure 7.40: 1D temperature RMS profiles at different axial positions. Comparison between BFER and LU13 kinetic schemes.

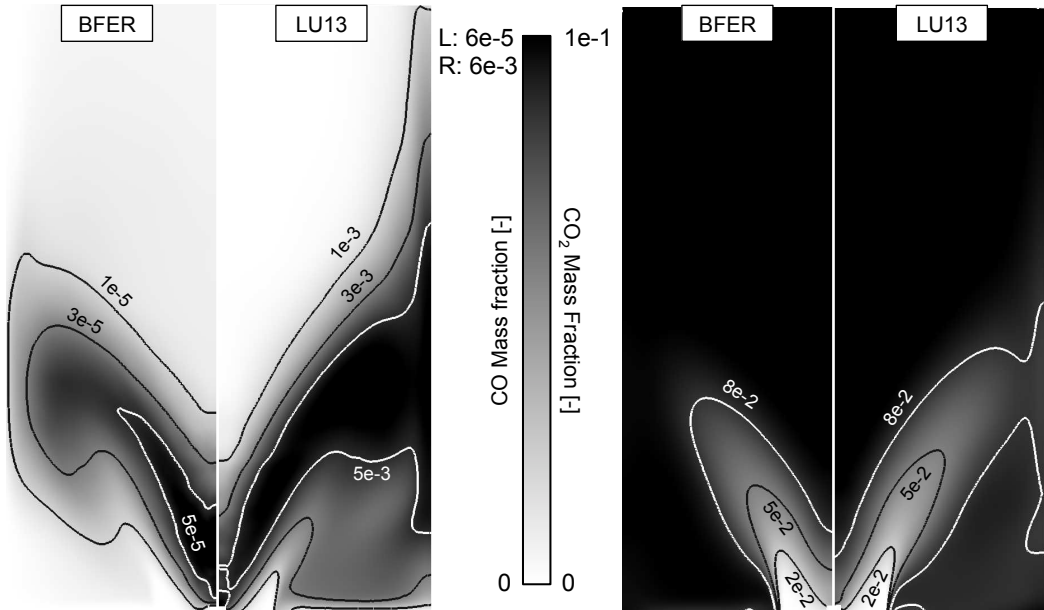


Figure 7.41: Time and azimuthal averaged flow field of CO (left) and CO₂ (right) mass fraction in the combustion chamber. Comparison between BFER and LU13 mechanisms. Note that, on the left side, the two fields have different maximum values (L: left, BFER; R: right, LU13).

a positive axial velocity is present. However, in this case, the fluctuation amplitude of the heat release rate is lower than for the BFER kinetic scheme. This is caused by

7. LES OF A PREMIXED SWIRL-STABILIZED BURNER

a less frequent oscillation between the two above-mentioned states. Using the LU13 scheme, as already seen by the mean fields, the flame moves a little less and the hot zone is generally present in a more upstream position.

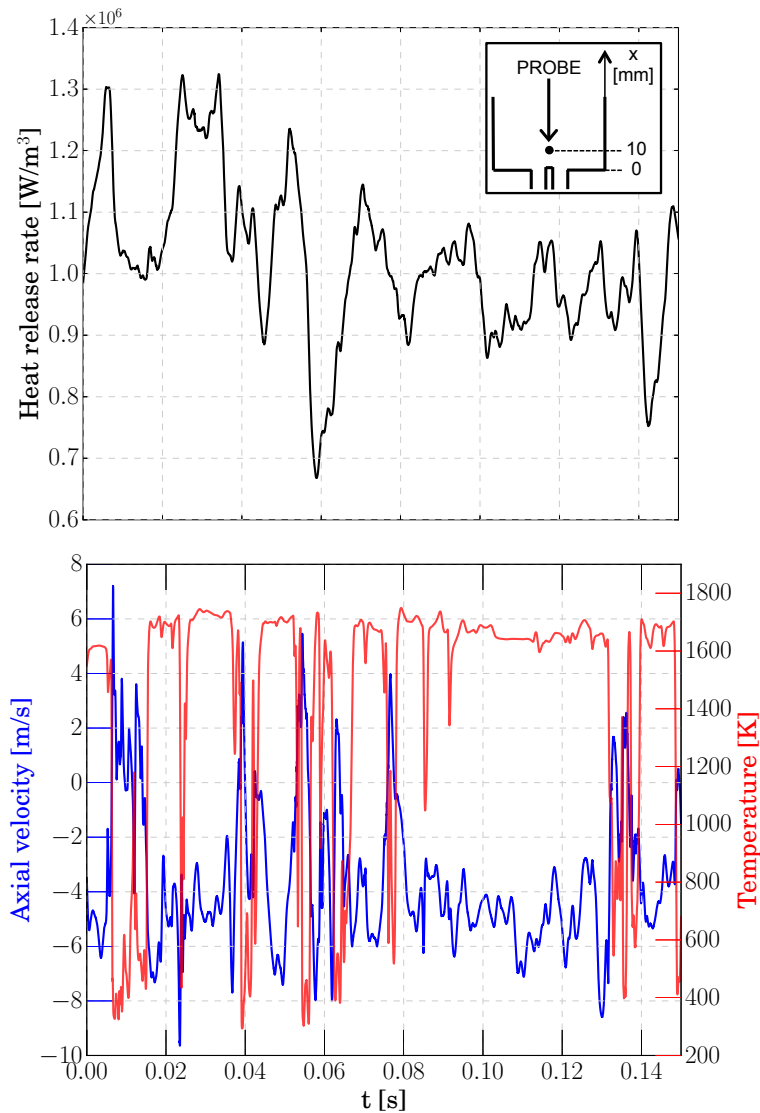


Figure 7.42: Top: temporal evolution of the mean heat release rate. Bottom: temporal evolution of temperature and axial velocity on a probe situated in the burner axis, at $x = 10$ mm.

The frequency signature of the integrated release rate has also been verified for this case. Fig. 7.43 presents a power spectral density of the integrated heat release rate: the oscillations have a very low frequency, with the two main peaks situated around 10 and 50 Hz and minor peaks around 65 Hz and 80 Hz. Once again, no natural oscillation is present at a frequency close to the one at which the flame will be acoustically pulsed, as shown in section 7.4.

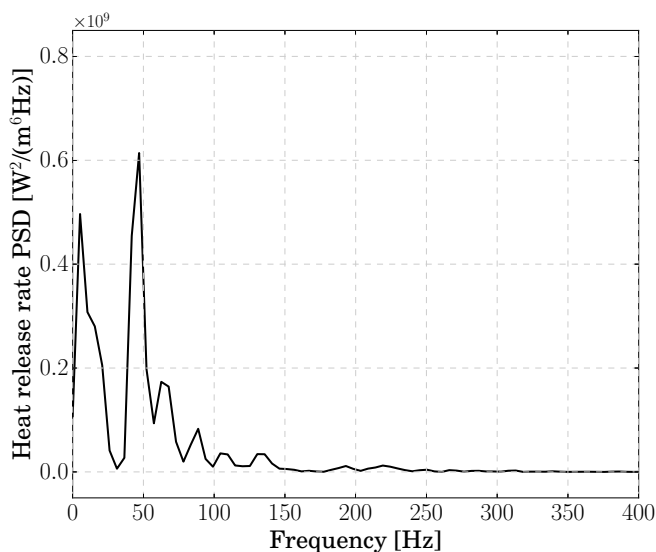


Figure 7.43: Power spectral density of mean heat release rate using the LU13 mechanism.

7.3.3.c Few words about CPU time

The higher number of species transported, as well as the heavier source terms computation, makes the ARC kinetic scheme more expensive in CPU time. Moreover, at least for this particular case, the LU13 simulation required a more refined mesh. Table 7.5 summarizes the CPU time needed to perform 150 ms of physical time on 15 nodes (360 CPUs) using the CERFACS in-house cluster NEMO (or equivalent). The LU13

Table 7.5: CPU time for different PACCI cases.

	BFER	LU13
CPU hours	~95k	~200k

kinetic scheme demands 110.5 % additional CPU time, compared to the BFER one, an additional cost which remains small considering that a scheme like LU13 is much more complex than BFER.

7.3.3.d Concluding remarks

It has been shown how the key features of the reacting flow in the PACCI burner are captured in a similar way when using the BFER or the LU13 kinetic schemes. However, using the LU13 mechanism, the flame seems to be moving less and to be less lifted. Moreover a longer flame is found using the ARC kinetic scheme. No absolute conclusion can be drawn in this case on which one of the setups is best, since no sufficient experimental data are available. The flame root motion seems to be slightly better captured when using the LU13 kinetic scheme, which on the contrary predicts a flame longer than expected. Due to the small differences in results, only the BFER scheme will be used for the more CPU expensive cases.

7.4 Acoustically pulsating the PACCI burner

In this section an LES with acoustic pulsation of the PACCI burner is performed, to check the dynamic response of the burner and provide a benchmark for the comparison between the burner response without and with the use of NRP plasma discharges.

The forced response method used in this work for the dynamic analysis of the flame is first briefly presented, then the dynamic response of the PACCI burner is analyzed.

7.4.1 Forced response method for the dynamic analysis of flames

The dynamic response of a flame is generally measured by means of the so-called Flame Transfer Function (FTF), which provides information about the stability of the system. This kind of approach is generally referred as to the "forced response method", in which a perturbation is introduced in the system and the flame response is recorded.

The FTF measures the ratio of the relative heat release rate fluctuation (\dot{Q}'/\bar{Q}) to the relative inlet velocity perturbation issued from the acoustic forcing (u'/\bar{u}). In the frequency domain it writes:

$$F(\omega) = \frac{\dot{Q}'(\omega)/\bar{Q}}{u'(\omega)/\bar{u}} \quad (7.7)$$

where ω is the angular frequency. Generally, F is expressed in terms of gain $N = |F(\omega)|$ and time delay $\tau = \text{Arg}(F(\omega))/(2\pi f)$, being f the forcing frequency. Doing so it results:

$$F(\omega) = Ne^{i\omega\tau}. \quad (7.8)$$

This approach has been first introduced for acoustically compact flames by [Crocco \[1951, 1952\]](#). Since then, it has been used for the study of the response of laminar and turbulent flames.

Experimentally, it has been shown how the OH* chemiluminescence is proportional to the heat release fluctuations in premixed flames (see for example [Haber et al. \[2000\]](#)), making possible to measure the FTF. [Kim et al. \[2010\]](#) show how higher perturbation frequencies caused a reduction of the gain and an increase of the absolute phase value. This phenomenon has been confirmed in laminar flames by several authors [[Balachandran et al., 2005](#); [Durox et al., 2009](#); [Karimi et al., 2009](#); [Kornilov et al., 2009](#), among others], which observed the saturation of the phase and the decrease of the flame amplitude above certain frequencies. This is also known as the low-pass behavior of the flame. An overshoot in gain has been observed on the contrary by [Schuller et al. \[2003\]](#) from laminar flames and [Armitage et al. \[2006\]](#) from turbulent V-flames; this has been associated to vortex roll-up at the flame base. From the global conservation laws it can be derived that, in all cases, the gain is unity in the limit of zero frequency. This has been observed by various groups and an example of the resulting transfer functions can be found in [Polifke and Lawn \[2007\]](#).

In flames stabilized by means of a swirled flow, the swirler influences the FTF behavior twofold. Axial perturbations which are traveling at the speed of sound perturb the flame in a classical way. At the same time, azimuthal disturbances originated by

the interaction of the axial perturbation with the swirler blades, which propagate at convection speed, also perturb the flame. This has been shown by Palies et al. [2010, 2011], and it is schematically represented in Fig 7.44.

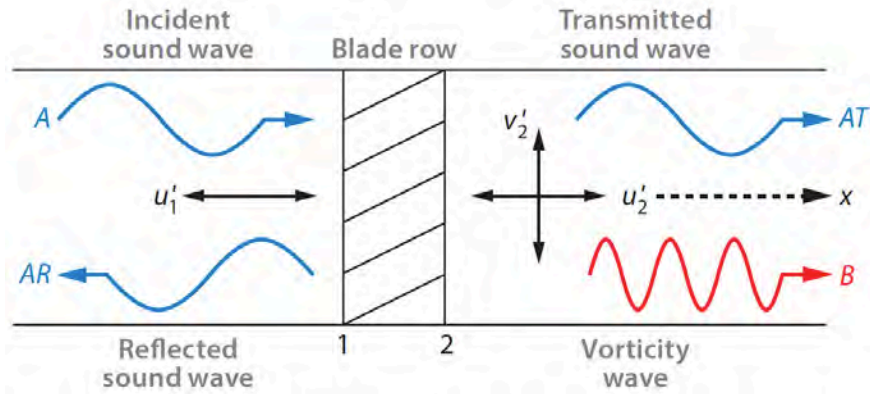


Figure 7.44: Decomposition of acoustic velocity perturbation after impinging a swirler [Candel et al., 2014].

Numerically, the FTF can be obtained by means of computational fluid dynamics simulation [Giauque et al., 2005; Kornilov et al., 2009; Tay Wo Chong et al., 2010; Duchaine et al., 2011; Hermeth et al., 2013; Ghani, 2016, among others]. In this approach an unsteady CFD calculation is performed and controlled excitations are imposed in order to generate time series of velocity and heat release rate oscillation. Then, the data is post-processed to obtain the FTF. This is the approach used in this work.

7.4.2 Dynamic response of the PACCI burner

7.4.2.a Simulation setup

The acoustically forced simulation has been run using the BFER kinetic scheme. The mesh used is the M1 one. The boundary conditions and the numerical parameters are the one used for the reacting simulation, as detailed in subsection 7.3.2.a.

In order to analyze the temporal data in a convenient way, the time step has been fixed to the value of 8.5×10^{-8} s, corresponding to a CFL ≈ 0.7 .

Acoustic forcing is introduced by generating a harmonic acoustic perturbation at the domain inlet (Fig. 7.5) using the inlet wave modulation method [Kaufmann et al., 2002]. The forcing amplitude has been chosen to be about 40 % of the mean mass flow rate, in order to have an acceptable signal-to-noise ratio. Test cases have been performed with a lower value of 10 %, equal to the one of the experimental campaign performed at KAUST, but this would have needed a too long simulation time in order to eliminate noise. This choice permits to perform a qualitative but not quantitative comparison with experimental results and a quantitative comparison between numerical simulations without and with NRP discharges. High values of the forcing amplitude

7. LES OF A PREMIXED SWIRL-STABILIZED BURNER

can also cause non-linearities in the flame response: this will have to be studied in deeper detail in further studies.

Only one excitation frequency has been simulated. The chosen frequency is of 160 Hz, corresponding to the local maximum of flame response obtained during the experimental campaign.

Hermeth et al. [2013] and Ghani [2016] have shown that, when the aim is to evaluate the FTF, the numerical simulation has to be run for about 4 forcing cycles after reaching a stabilization of the burner response. This needs generally 1 or 2 forcing cycles. Ghani [2016] showed moreover that, in some cases, using 2 or 4 forcing cycles for the evaluation of the FTF does not lead to significant differences. Taking this into account, the numerical simulation has been run for a total of 8 forcing cycles. Discarding the first cycle, needed to establish the burner response, the FTF can be estimated using 7 oscillation cycles. Doing so, we are guaranteed that the minimum number of forcing cycles is used. Moreover, averaging on a larger number of cycles will reduce the uncertainties due to cycle-to-cycle variations which can be important in this case, as it will be shown. For a forcing frequency of 160 Hz, the total simulation time is of 50 ms, corresponding to 2/3 of a burner convective time.

7.4.2.b Mean fields

Time and azimuthal averaged flow fields of main flow variables are shown in Figs. 7.45 and 7.46 and compared to the ones obtained in the simulation without acoustic forcing.

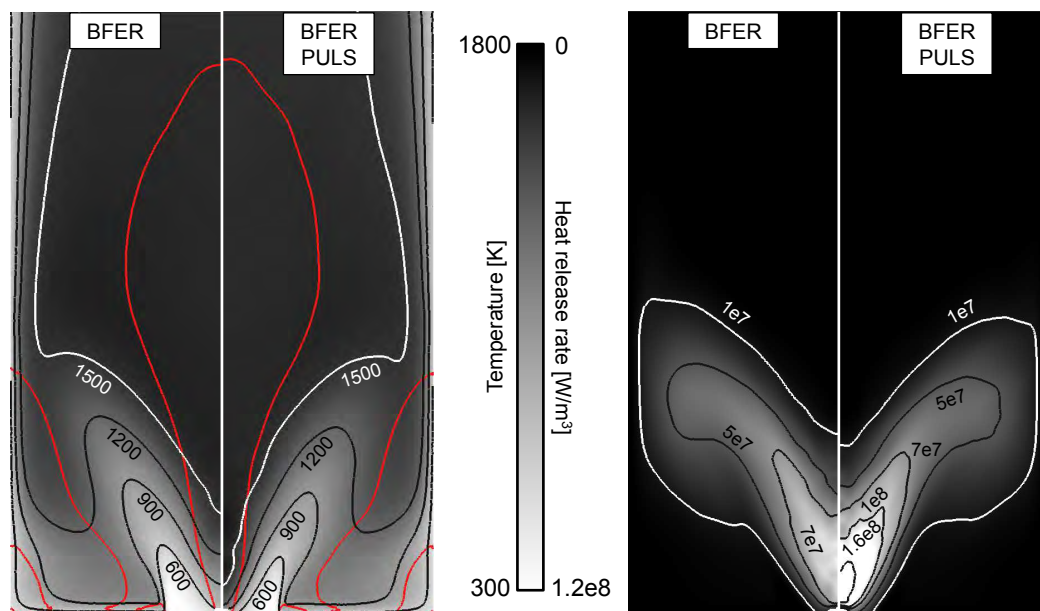


Figure 7.45: Time and azimuthal averaged flow field of temperature (left) and heat release rate (right) in the combustion chamber. Red line: iso-line of zero axial velocity. Comparison between numerical simulations without and with acoustic forcing.

Figure 7.45 displays mean temperature and heat release rate fields and shows signif-

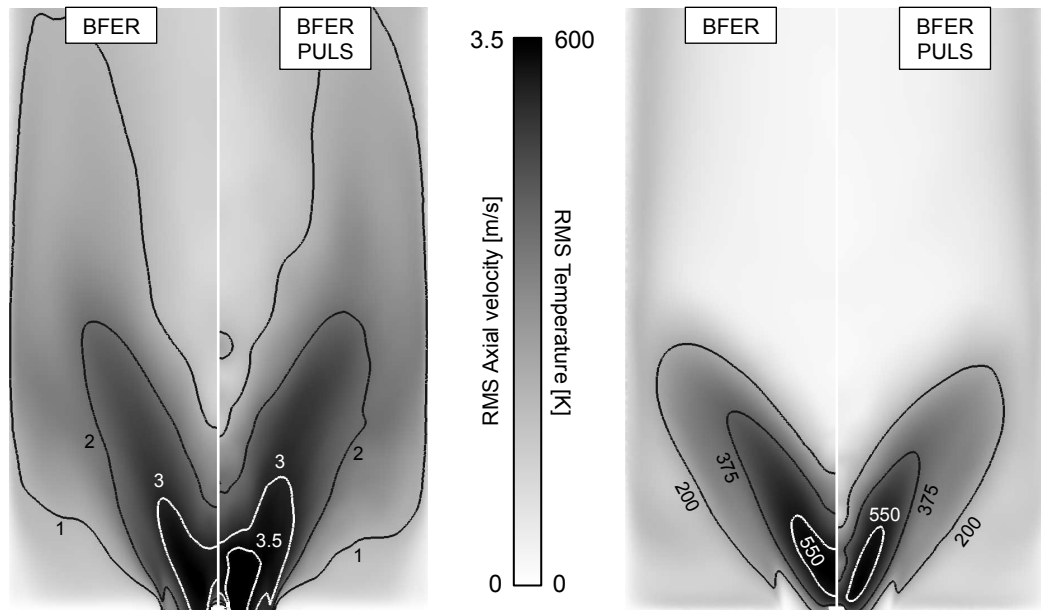


Figure 7.46: Time and azimuthal averaged flow field of RMS axial velocity (left) and RMS temperature (right) in the combustion chamber. Comparison between numerical simulations without and with acoustic forcing.

icant differences only in the central zone, where the hot zone has been found to extend upstream when applying an acoustic forcing. In this central zone, the heat release rate has been found moreover to be higher in average. This seems to be due to the effect of the acoustic forcing on the flame structure, as shown in the following: the natural alternation of lifted and attached states of the flame is suppressed and the flame follows the forcing frequency, which controls it. Higher wrinkling of the flame in the central zone is responsible for higher heat release rate. Fig. 7.46 shows that the field of RMS axial velocity is similar in shape, but quite different in absolute values. As one can expect, when applying a forcing the RMS value increases in magnitude and the interested area is larger. One can see for example the zone at the exit of the injection tube where, in the case of acoustic forcing, all the area is subject to higher values of axial velocity RMS. The field of RMS temperature reveals a central zone characterized by lower values, denoting a flame root which crosses the burner axis less often. This is coherent with the mean temperature field, which shows a central zone filled by hotter gases. In the shear zone the values are similar to the one obtained for the unforced simulation.

All these differences can be evaluated quantitatively by means of 1D profiles at the 5 different axial positions of Fig. 7.36. Profiles of mean and root-mean-square values of axial velocity and temperature are shown respectively in Figs. 7.47, 7.48, 7.49 and 7.50. The mean fields of CO and CO₂ mass fractions are not shown for this case, since no main differences are found.

7. LES OF A PREMIXED SWIRL-STABILIZED BURNER

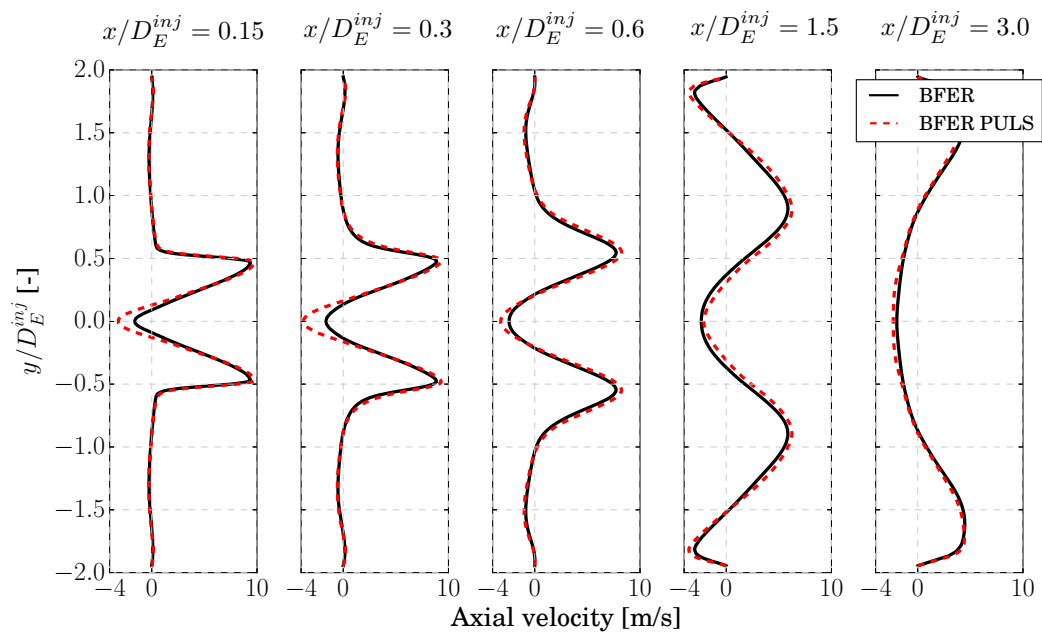


Figure 7.47: 1D axial velocity mean profiles at different axial positions. Comparison between unforced and forced simulation.

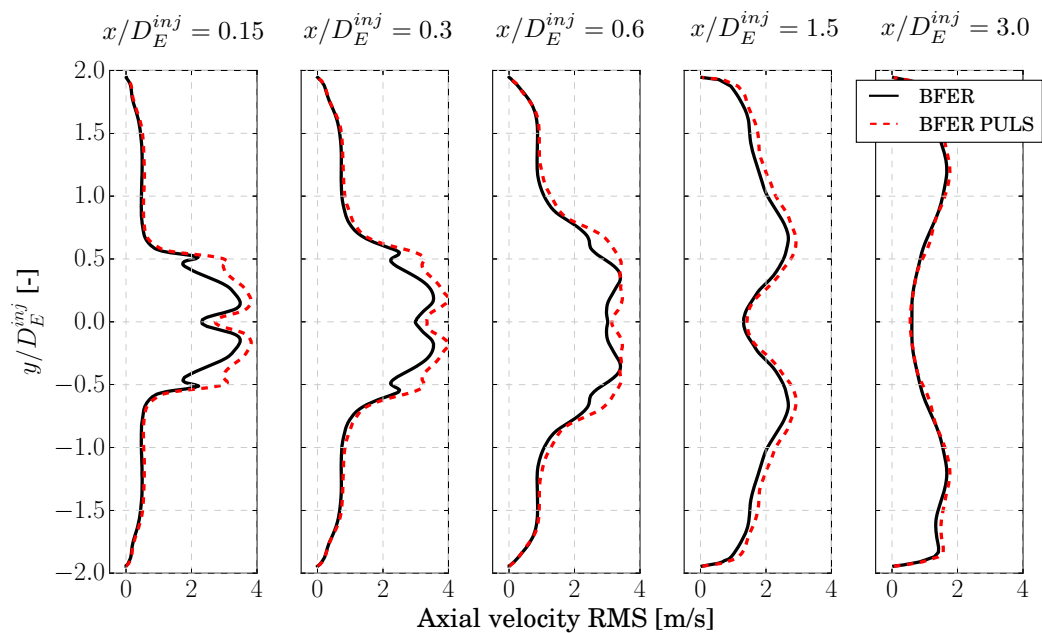


Figure 7.48: 1D axial velocity RMS profiles at different axial positions. Comparison between unforced and forced simulation.

7.4.2.c Flame dynamics

The flame dynamics is here analyzed looking at Fig. 7.51, where the evolution of the mean heat release rate is plotted as a function of the forcing cycle. The physical time

7.4 Acoustically pulsating the PACCI burner

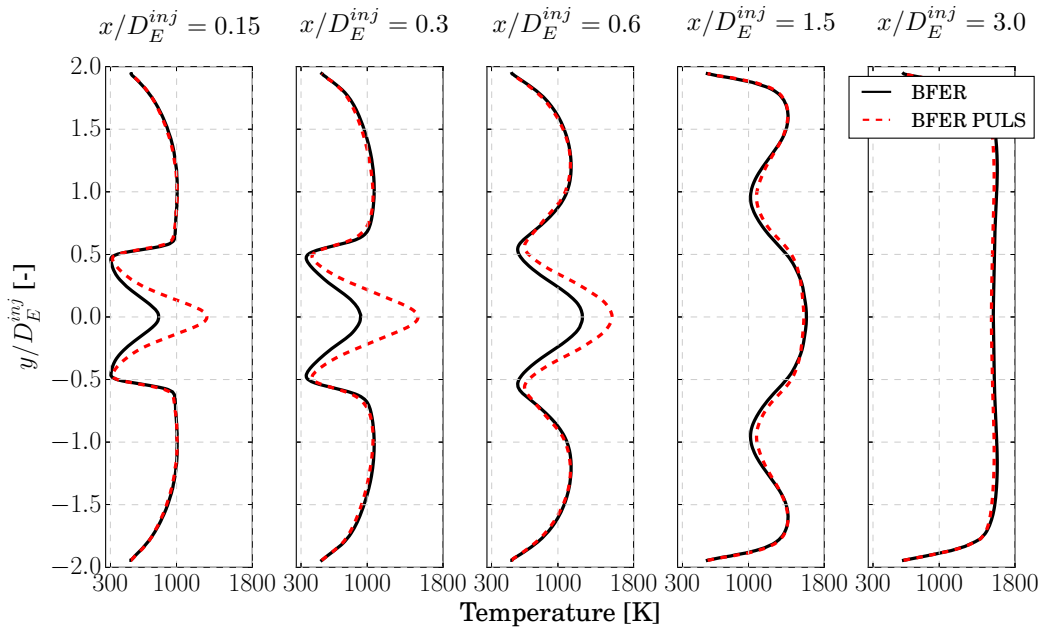


Figure 7.49: 1D temperature mean profiles at different axial positions. Comparison between unforced and forced simulation.

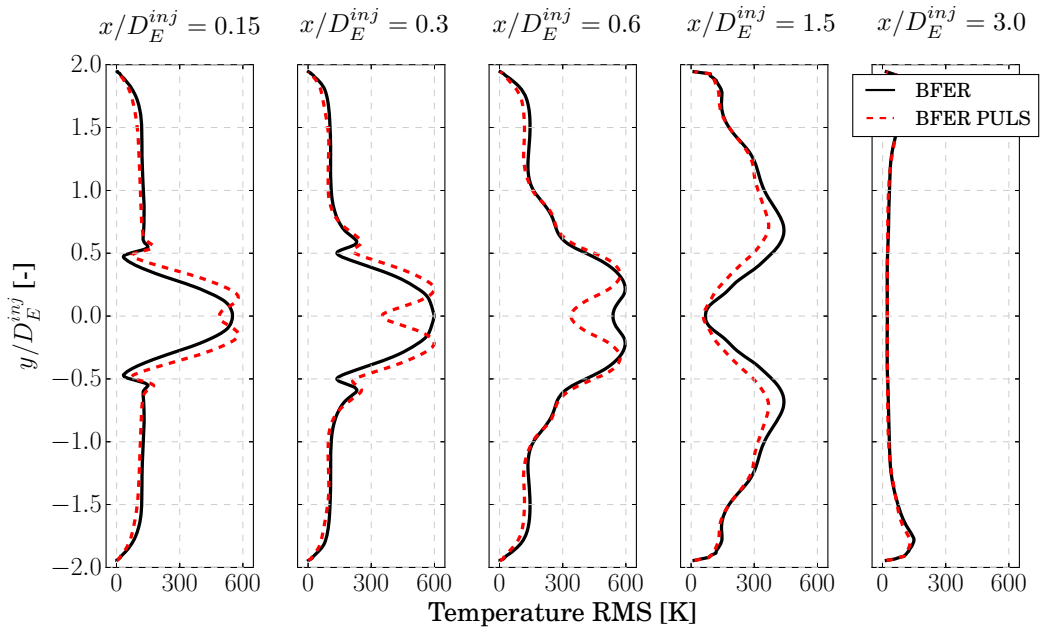


Figure 7.50: 1D temperature RMS profiles at different axial positions. Comparison between unforced and forced simulation.

t is divided by the period $T = 1/160 \text{ Hz} = 6.25 \text{ ms}$. As confirmed also by means of Fig. 7.52, where the mean heat release rate power spectral density is shown, the flame dynamics is completely controlled by the acoustic forcing and all the natural frequencies which have been found in the unforced case (see Fig. 7.29) are no longer present. The

7. LES OF A PREMIXED SWIRL-STABILIZED BURNER

acoustic forcing is, in this case, responsible for a mean heat release rate variability with minimum and maximum values which can be different by a factor higher than 2.5. A high cycle-to-cycle variability of the maximum and minimum values is found. In order

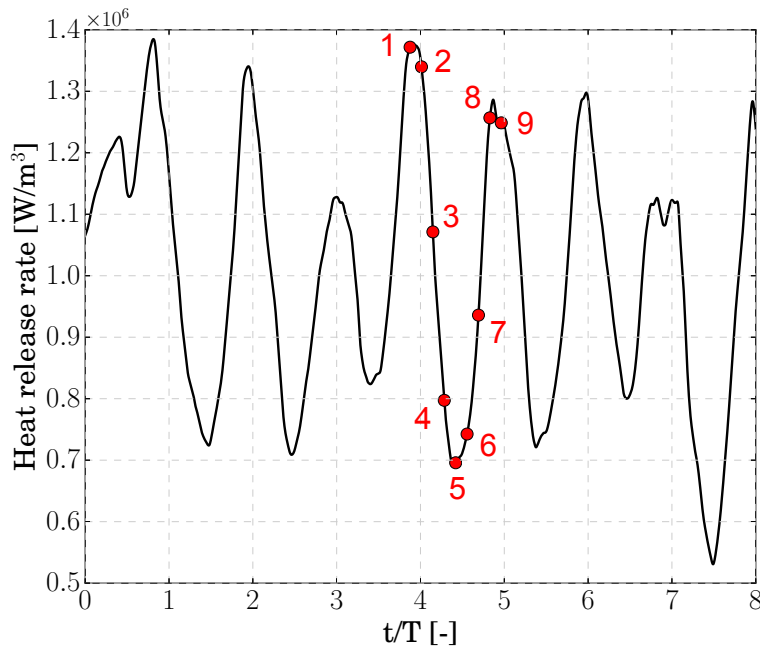


Figure 7.51: Temporal evolution of the mean heat release rate as a function of the forcing cycle. Red dots: states at which the snapshots of Figs. 7.53 and 7.54 have been taken.

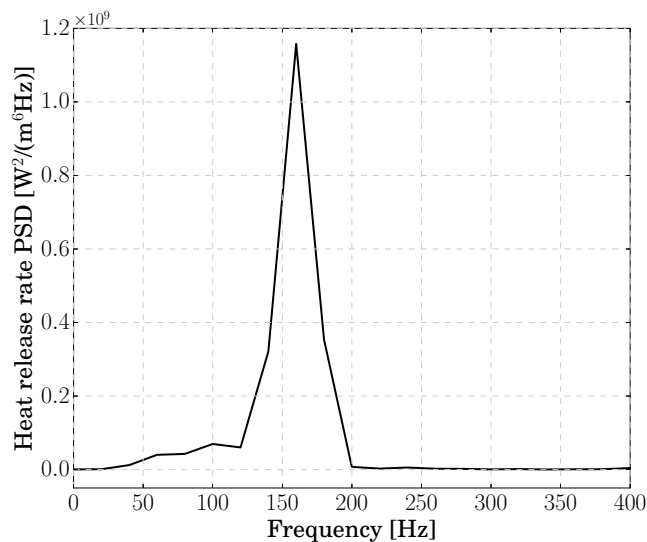


Figure 7.52: Power spectral density of mean heat release rate applying an acoustic forcing at 160 Hz.

to understand the physics driving the burner response to the acoustic forcing, various snapshots of temperature and axial velocity are presented in Figs. 7.53 and 7.54.

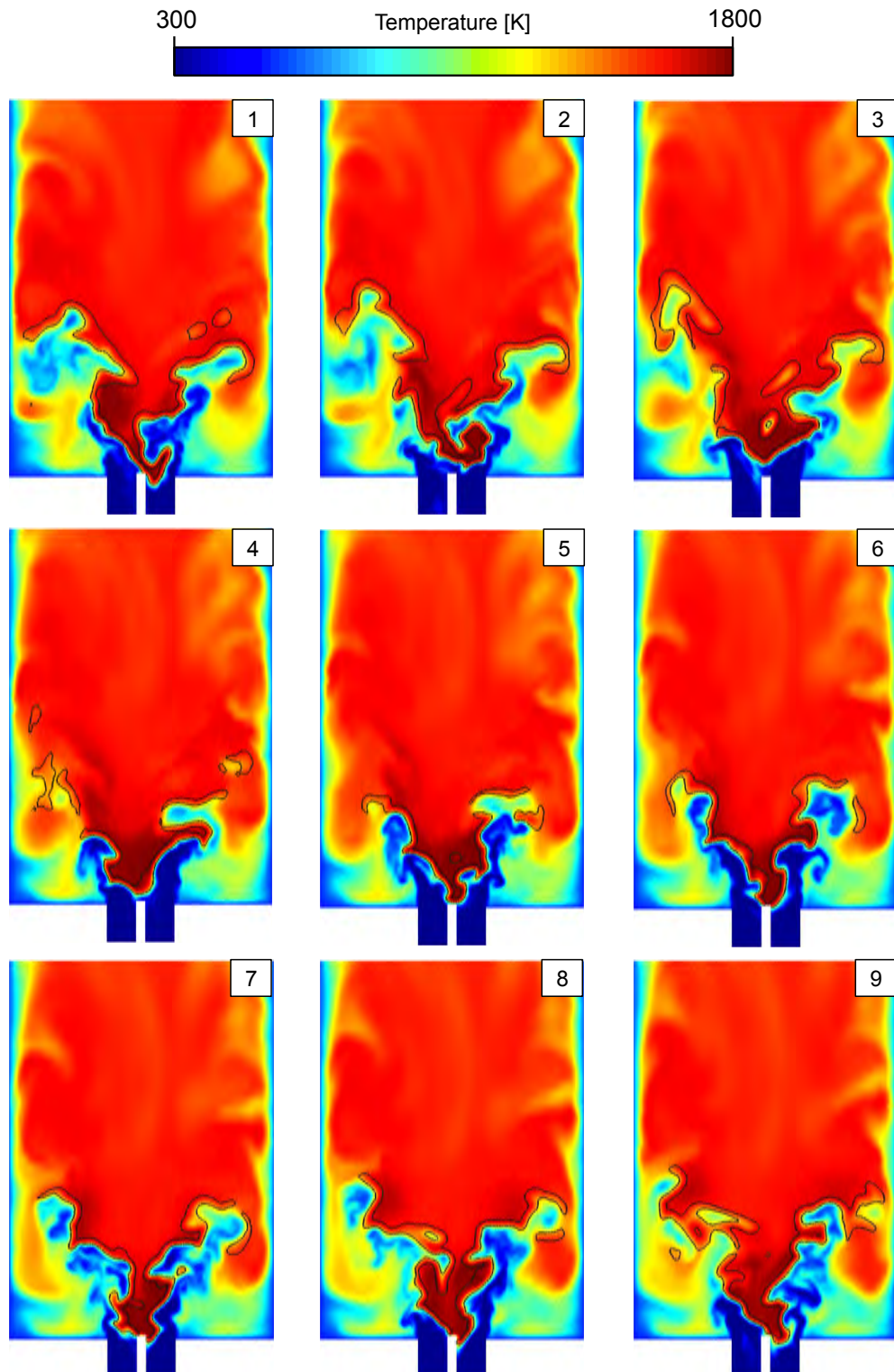


Figure 7.53: Instantaneous fields of temperature on a 2D cut at $z=0$. Black line: iso-line of heat release rate ($1 \times 10^8 \text{ W/m}^3$). The number in the white box represents the red dot of Fig. 7.51.

7. LES OF A PREMIXED SWIRL-STABILIZED BURNER

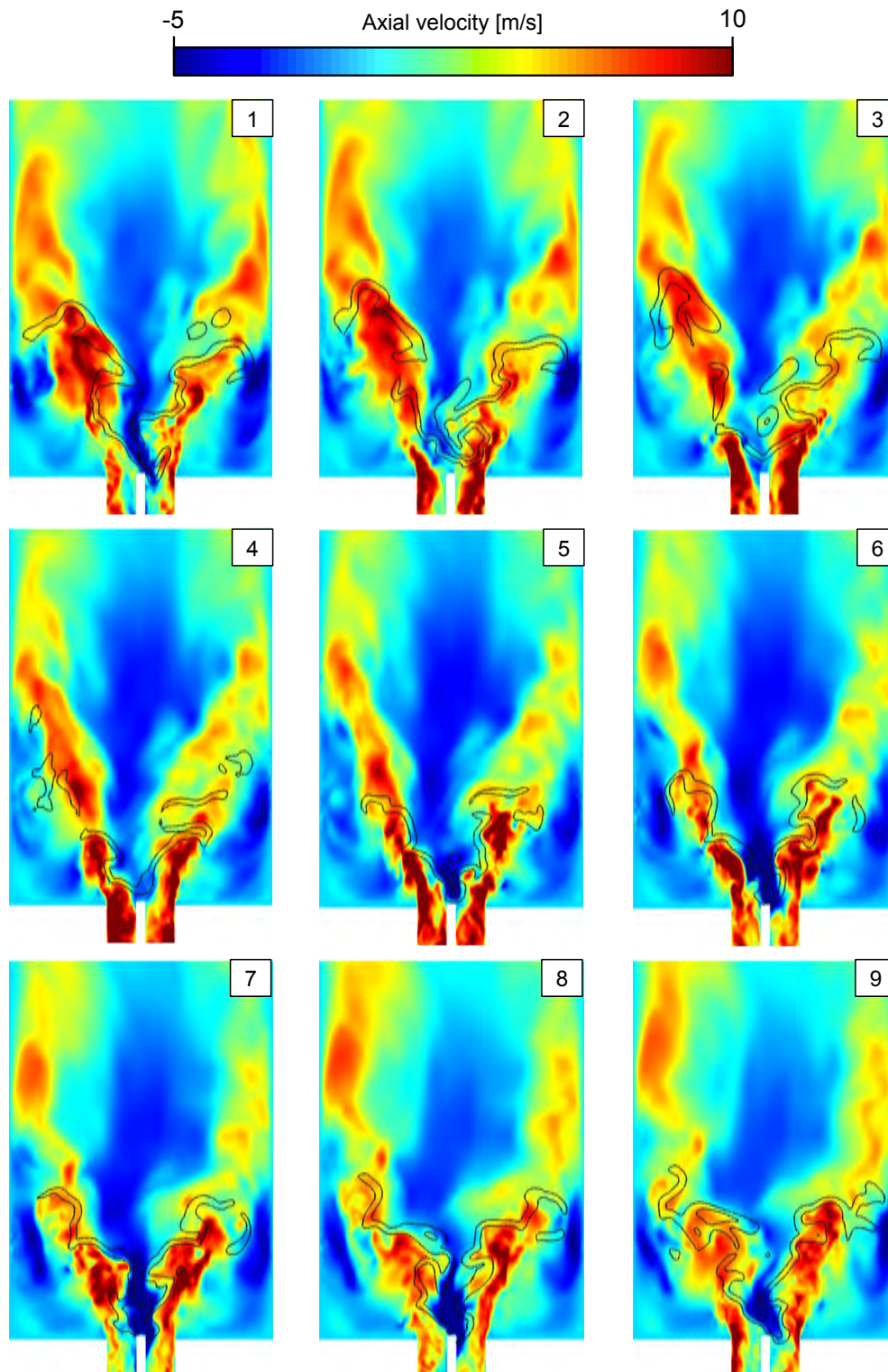


Figure 7.54: Instantaneous fields of axial velocity on a 2D cut at $z=0$. Black line: iso-line of heat release rate ($1 \times 10^8 \text{ W/m}^3$). The number in the white box represents the red dot of Fig. 7.51.

The snapshots have been taken along the fifth cycle at a fixed temporal distance. They have been chosen to describe the evolution from a local maximum towards a local minimum and subsequent way back to a new local maximum. The corresponding states are marked on the mean heat release rate evolution by means of red marks.

The states responsible for a maximum of heat released by the flame (snapshot 1 and 8-9) are the ones in which there is a contemporary coexistence of several positive factors for the flame. First, the axial velocity at the chamber inlet is relatively slow, permitting to the central recirculation zone to penetrate inside the injection tube, leading to a flame attached to the rod.

The central recirculation zone is in this case characterized by relatively strong negative values of axial velocity. At the same time, the higher velocities caused by the previous acoustic cycle have reached the flame zone situated a little more downstream. Here they stretch and wrinkle the flame, causing a vortex roll-up and a consequent increase in flame surface. This simultaneous extension of the flame both upstream and downstream leads to a maximum in flame length, and corresponding heat release rate. From these states, the velocity at the exit of the injection tube increases, pushing the flame and leading to a slight lifting of the latter (snapshot 3). At the same time, the high velocities present downstream are gone and this area is now characterized by the slower velocities which were at the chamber inlet previously. This leads to a decrease in the flame surface and a diminution of the heat release rate.

The state in which the heat release rate is minimum (snapshot 5) corresponds to the one in which the flame is less extended axially. Then, the fluid at high velocity propagates downstream, generating a new vortex roll-up and leading to a new increase in flame length. At the same time the velocity at the chamber inlet has decreased and the flame root attaches to the rod, slightly penetrating in the injection tube and the process repeats. This flame behavior is similar to the one observed, among others, by Palies et al. [2010].

7.4.2.d Flame Transfer Function evaluation

The Flame Transfer Function can be evaluated as mentioned in subsection 7.4.1 by using the reference velocity and mean heat release rate signals recorded in the LES. The reference velocity is recorded by means of a probe situated near the inlet of the domain, upstream of the swirler, where plane waves can be considered and no radial or azimuthal oscillation is present (Fig. 7.55). This corresponds to the position of the hot wire used in the experimental setup (see Fig. 7.1) to measure the velocity fluctuation induced by the acoustic forcing. The recorded signals of velocity and heat release rate are shown in Fig. 7.56. The first forcing cycle is needed to establish the burner response and is not considered in the evaluation of the FTF. Starting from the second forcing cycle, the FTF is evaluated considering 7 cycles. The resulting values are summarized in Tab. 7.6.

A qualitative comparison with experimental data is not possible in this case, since the forcing amplitude is different. To have a reference, the values found in the experimental campaign using a frequency of 160 Hz and applying a forcing amplitude of 10 % are the following: gain $N = 1.12$ and time delay $\tau = 3.9$ ms. An underestimation of the gain and overestimation of the time delay at the local maximum has been found

7. LES OF A PREMIXED SWIRL-STABILIZED BURNER

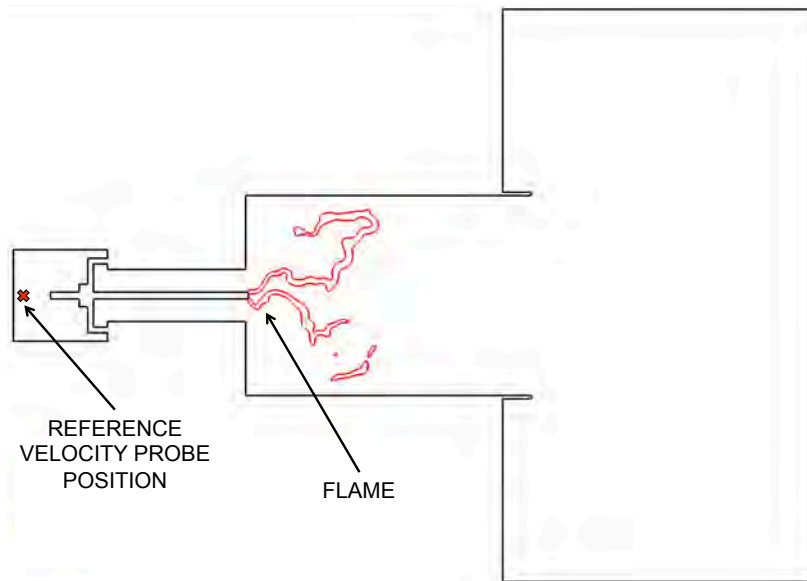


Figure 7.55: Schematic of the probe position for the FTF evaluation. Flame position represented by the red line: iso-line of heat release rate ($1 \times 10^8 \text{ W/m}^3$).

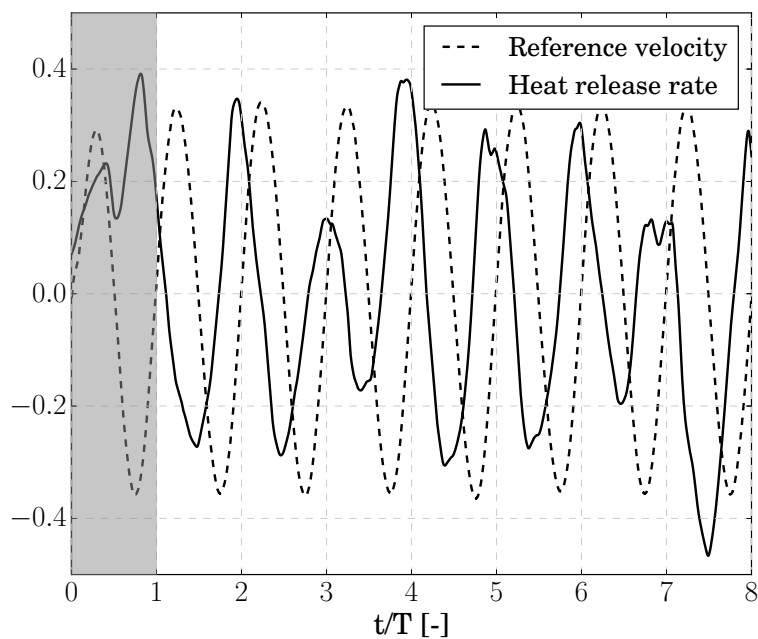


Figure 7.56: Temporal evolution of the reference velocity and mean heat release rate as a function of the forcing cycle.

also in the works of [Hermeth et al. \[2013\]](#) and [Ghani et al. \[2016\]](#). This has to be the subject of further studies and here only a comparison between LES with and without NRP discharges at the chosen equal conditions is presented.

	LES
N [-]	0.748
τ [ms]	4.426

Table 7.6: Gain and time delay of the FTF at 160 Hz and forcing amplitude 40 %.

7.4.2.e Few words about CPU time

The CPU cost associated to this numerical simulation (50 ms of physical time) on 15 nodes (360 CPUs) using the CERFACS in-house cluster NEMO is about 22 kh.

7.5 Conclusion

LES of the PACCI swirl stabilized premixed burner have been performed and presented. The whole series of LES has been performed in order to validate the numerical setup and provide base cases to check the influence of the use of NRP discharges in flame stabilization.

First, a cold simulation has been performed in order to validate the prediction of the swirling flow. Comparisons with experimental data have shown a global good agreement, with a slight overestimation of the azimuthal velocity and jet opening.

Then, reacting simulations have been performed. Two kinetic schemes (BFER and LU13) have been beforehand validated for the burner operating conditions. The flame shape and dynamics have been analyzed in order to know the natural behavior of the unforced flame. The flame has been found to alternate between states in which it is attached to the central rod and states in which it is completely lifted. The flame shape has been validated against experimental visualization of the OH* chemiluminescence showing a good agreement. The two kinetic schemes have been compared, showing minor differences.

Using the BFER scheme, an acoustically pulsed LES at 160 Hz has been performed. The flame natural dynamics has been found to completely disappear: the flame is modified by the acoustic excitation and completely "follows" the forcing oscillation. The oscillation in heat release rate is due to flame surface oscillation and, in particular, to vortex roll-up at the flame tip. The flame response has been quantitatively evaluated by means of the Flame Transfer Function approach.

The next chapters show how NRP discharges are modeled in AVBP and how they modify the flame response to acoustic waves.

Phenomenological model for NRP discharges

Contents

8.1 Building up a phenomenological model	163
8.2 Test case setup	166
8.2.1 Model calibration using the BFER kinetic scheme	170
8.3 Increasing the complexity of the kinetic scheme: from BFER to LU13	176
8.3.1 Influence of the deposit size	179
8.3.2 Influence of the number of consecutive discharges	183
8.4 Influence of the plasma chemistry	185
8.4.1 The PLASMA-LU kinetic scheme	187
8.5 Few words about CPU time	194
8.6 Conclusion	195

In this chapter the phenomenological model developed to model NRP discharges in AVBP is presented and validated. The development of the model has been done according to data provided by the team of Prof. Lacoste (KAUST) and is fitted on the experimental configuration studied in chapter 7. In order to facilitate the development of the NRP discharges model and to validate it, a test case has been set up and parametric studies have been performed. The phenomenological model has been developed using the BFER kinetic scheme. Then the influence of the kinetic scheme is evaluated by using the LU13 mechanism and by developing a new kinetic scheme which includes the plasma phase.

8.1 Building up a phenomenological model

The parameters and the NRP discharge behaviors provided by KAUST and used for the development of the phenomenological model can be classified in two categories. First, technical parameters, as used in the experiment and which are retained also for the model are:

8. PHENOMENOLOGICAL MODEL FOR NRP DISCHARGES

- The repetition frequency of the pulse f_p , which is 30 kHz. This means the appearance of one plasma discharge every $33 \mu\text{s}$ approximatively.
- The total power of the plasma $P_p = 40 \text{ W}$. This means an energy E_p supplied by each plasma discharge of about 1.3 mJ. No losses are accounted for.
- The time duration Δt_p of the plasma discharges, which is 10 ns.

The temporal evolution of the energy supplied by the NRP discharges is then schematically represented as in Fig 8.1.

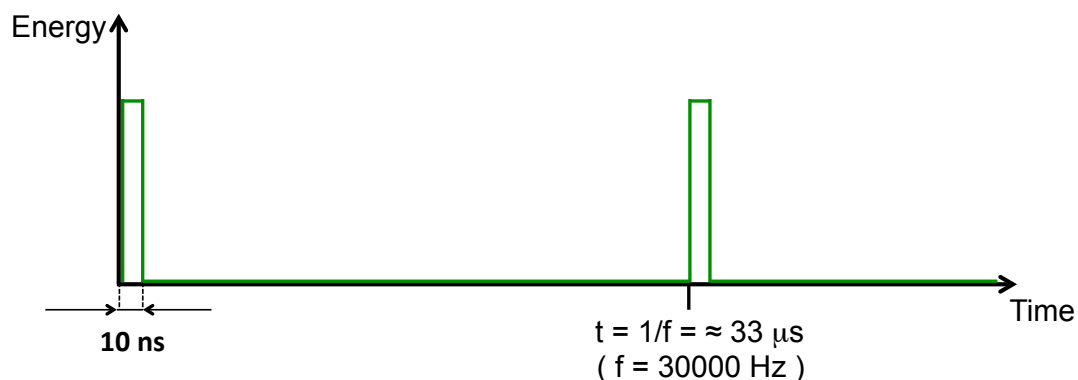


Figure 8.1: Schematic of the temporal evolution of the energy deposited by the NRP.

The second series of parameters which must be set have been come from observations made at KAUST. The first key parameter is the shape of the energy deposit zone. Based on experimental data, the energy deposit has been fixed as cylindrical (Fig. 8.2), with a 2D Gaussian distribution in the cross section of the cylinder (plane y - z in Fig. 8.2). The cylinder "diameter" has been fixed based on the Gaussian full width

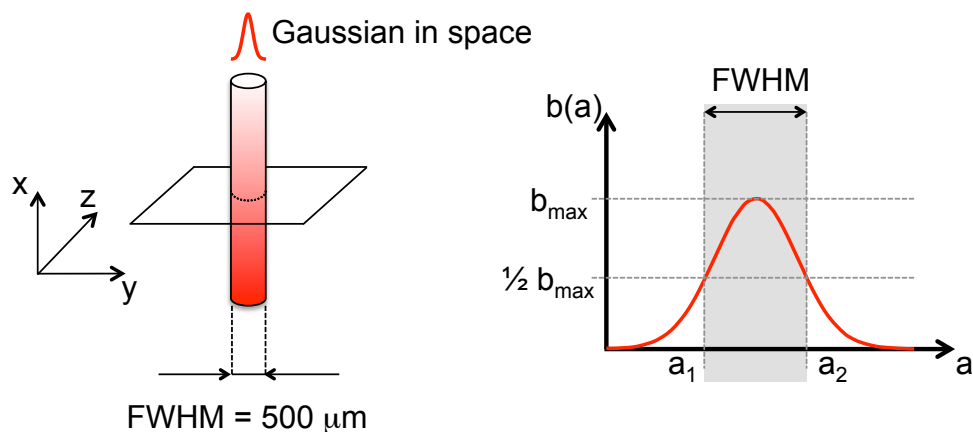


Figure 8.2: Left: schematic of the spatial distribution of the plasma channel. Right: definition of the gaussian Full Width at Half Maximum (amplitude b as a function of the generic spatial coordinate a)

at half maximum (FWHM), which has been set to $500 \mu\text{m}$. This values comes from

8.1 Building up a phenomenological model

experimental observations and is of the order of magnitude of the results of [Rusterholtz et al. \[2013\]](#). The distribution in the y - z plane reads:

$$\varphi(y, z) = \frac{1}{2\pi\sigma^2} \cdot \exp\left[-\frac{1}{2}\left(\frac{y-y_0}{\sigma}\right)^2\right] \cdot \exp\left[-\frac{1}{2}\left(\frac{z-z_0}{\sigma}\right)^2\right] \quad (8.1)$$

where σ is the standard deviation $\sigma = \text{FWHM}/2\sqrt{2\ln(2)}$ and (y_0, z_0) the deposition center.

The energy distribution has been kept constant along the axis of the cylinder (x axis in Fig. 8.2), and is smoothed at both ends by means of an hyperbolic tangent profile. The total length of the plasma channel is equal to the distance between anode and cathode in the PACCI configuration (approximately 8 mm). It results a 3D distribution $\psi(x, y, z)$, characterized by an integrated value Ψ and by a volume V_ψ .

Two perpendicular 2D cuts of the 3D field of the energy deposited by a discharge, non-dimensionalized by its maximum value, are shown in Fig. 8.3.

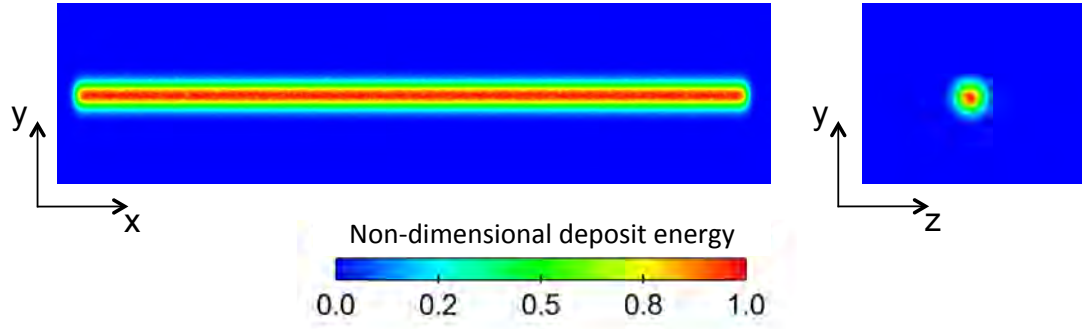


Figure 8.3: Field of the energy deposited by an NRP discharge, non-dimensionalized by its maximum value

Energy is supplied directly to the gas by means of a source term in the energy equation (\dot{Q}_{sp} in Eq. 2.8). It writes:

$$\dot{Q}_{sp}(x, y, z) = \frac{E_p}{\Psi V_\psi \Delta t_p} \cdot \psi(x, y, z) \quad (8.2)$$

This means that, once the energy amount to supply and its spatial non-dimensional distribution are fixed, the source term applied to each mesh node depends on the total deposit volume V_ψ . The size of the deposit is crucial in determining the effects on the gas, as will be shown in section 8.3.1, and has been found to be the most sensitive parameter of the model.

A key point in the model construction has been to choose where the NRP discharges have to be positioned, considering that they could potentially appear anywhere between the pin steel electrode and the cylindrical inner wall of the injection tube. It has been experimentally observed (Fig. 8.4) that the first discharge appears in the inter-electrodes zone of lowest gas density, creating an OH^* filament. Then successive discharges (usually between 2 and 5) at close location increase the OH^* filament in-

8. PHENOMENOLOGICAL MODEL FOR NRP DISCHARGES

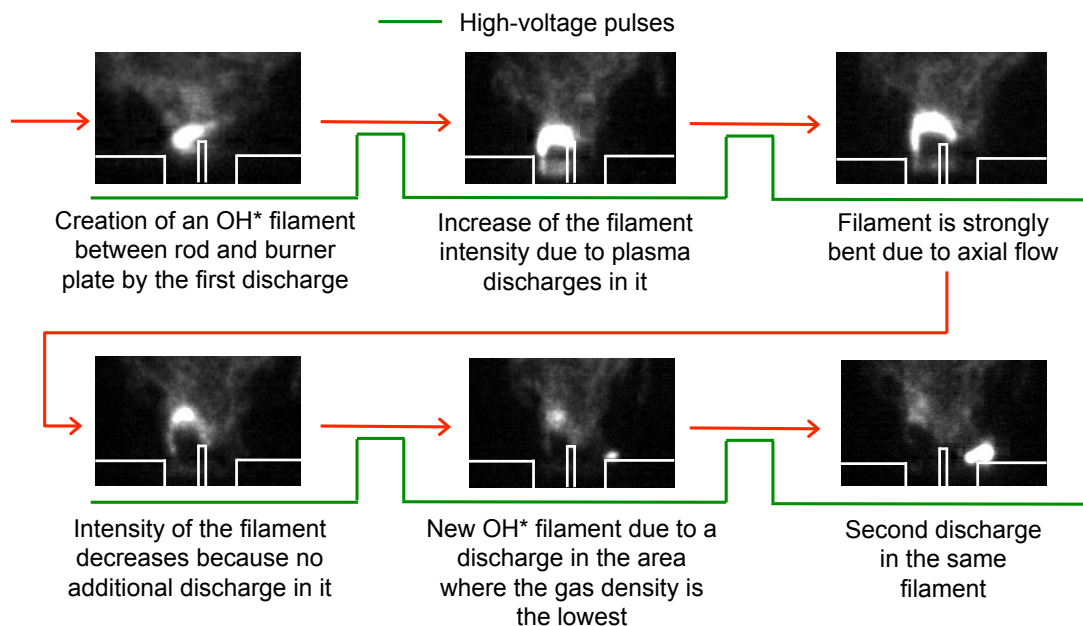


Figure 8.4: Experimental observation of the position of the NRP discharges. Courtesy of D. Lacoste (KAUST).

tensity, until the latter is too bent by the axial flow to sustain. When this happens, the next discharge takes place at a completely different position, again in the inter-electrodes zone of lowest gas density, and the sequence repeats. Similarly to the flame, the plasma discharges statistically rotate with the swirl. Ignition of the fresh gases is locally observed.

Following these observations, the numerical discharges model makes them turn around the burner axis as follows: three consecutive discharges take place next to each other, moving by an angle (ϑ in Fig. 8.5) equal to the one of the circle arc traveled by the fluid at the mean azimuthal speed at the exit of the injection tube. After three discharges a random jump in ϑ appears, in order to mimic the new sudden change of position of the new filament observed experimentally. The next three consecutive discharges stay close to each other, moving with the flow exactly as the first motion series. Then another jump appears, and so on. The number of three close consecutive discharges has been chosen because it is in the experimental range of 2 to 5. It is also the number that in validation test cases provides the final gas temperature closest to the experiment (≈ 2500 K). The jump in ϑ has been limited between 0 and 180 degrees, to have a statistical rotational motion in the direction of the swirl rotation.

8.2 Test case setup

In order to tune the NRP discharge model, a 3D simple channel equipped with an NRP system has been used as test case. A schematic view is presented in Fig. 8.6.

The channel is designed in order to have flow conditions as close as possible as the ones in the discharge zone of the PACCI burner. The square cross section of $l \times l$, with

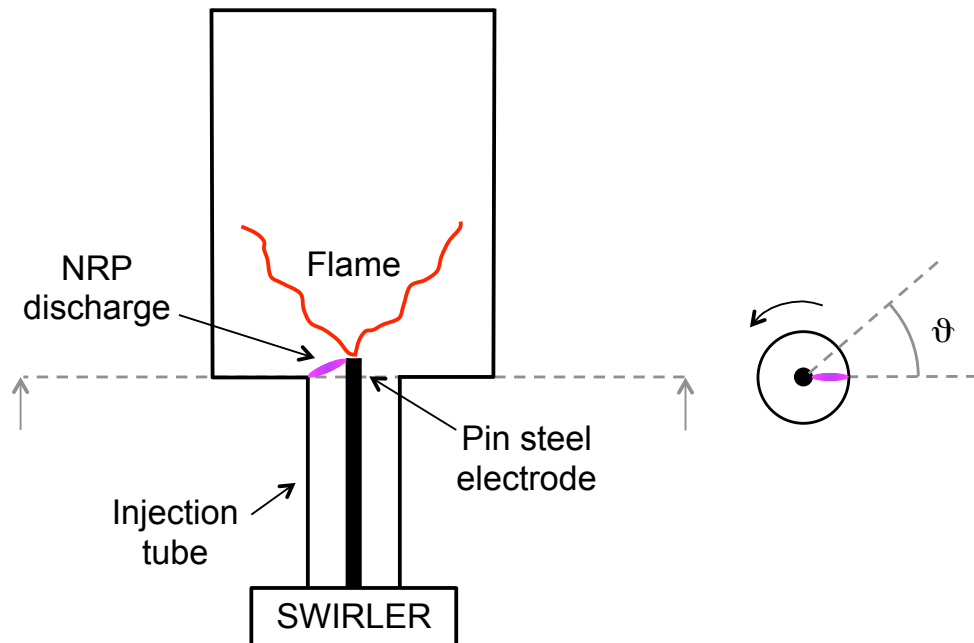


Figure 8.5: Position of the NRP discharges in the phenomenological model developed in this work.

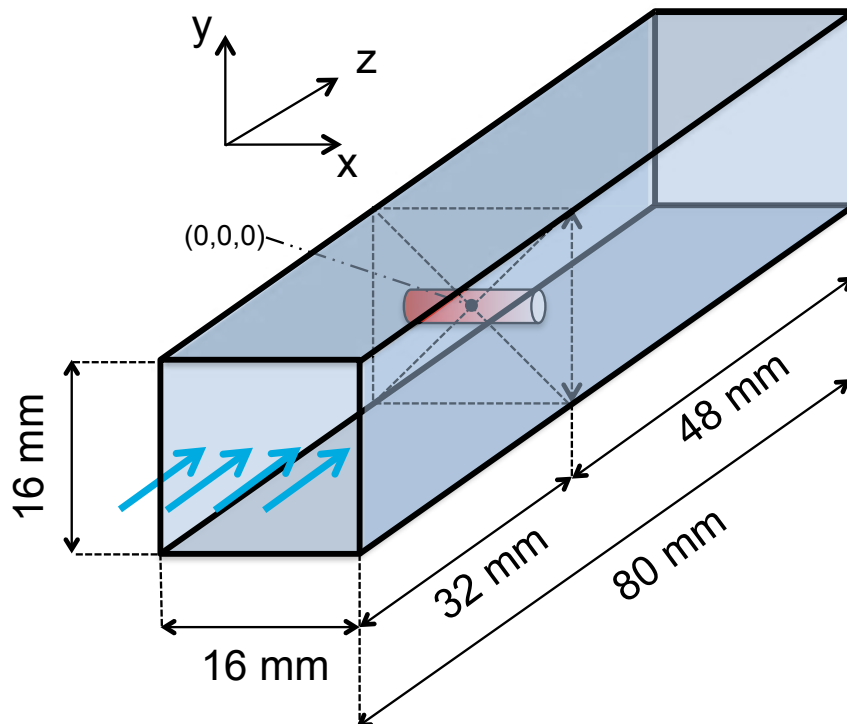


Figure 8.6: Schematic of the channel used as a test case for the building of the NRP discharge model.

8. PHENOMENOLOGICAL MODEL FOR NRP DISCHARGES

$l = 16$ mm, has been fitted in order to have an area and a Reynolds number $Re \approx 7500$ close to the ones at the exit of the injection tube. A total channel length of $5l$ has been used. $z = 0$ is the discharge position and the inlet has been positioned at $z = -2l$, in order to be sufficiently far from it. The remaining distance of $3l$ from the outlet permits to eventually study the convection of the heated gas for a distance sufficiently long. The position of the discharges on the y axis is variable.

Operating and boundary conditions

The operating conditions are summarized in Tab 8.1. The mass flow rate is prescribed

Mass flow rate \dot{m}	Mixture composition	Temperature
1.960 g/s	CH ₄ /Air at $\phi = 0.67$	300 K

Table 8.1: Operating conditions.

at the inlet by means of an NSCBC boundary condition. Its value and the species composition are the same as in the PACCI burner. The outlet is set to atmospheric conditions by means of an NSCBC outlet which imposes pressure. The walls are treated as adiabatic and a wall law is used, as in the injection tube of the PACCI configuration.

All the test cases performed in this chapter assume that in the energy deposit area, only fresh gases at 300 K are present before the first pulse. In the PACCI configuration, as shown in the following, this is not always the case. The energy deposit can take place in a hotter fluid which contains burnt gases too. This changes drastically the final state of the fluid, leading to different ignition mechanisms and different final gas temperatures.

Mesh characteristics

A fully tetrahedral unstructured mesh is used. The whole domain is discretized with cells having a characteristic size of 0.4 mm, the same as in the injection tube of the PACCI configuration. In the discharge zone a very refined mesh is used, with a minimum cell size of 50 μm , in order to have a sufficient number of grid points in the plasma channel and correctly capture the gas heating, as well as the pressure wave which develops. A fine grid (typical cell size of 100 μm) is kept in the zone downstream of the deposit zone, in order to have a good resolution of the flame kernel development and propagation for the convective time simulated. The resulting mesh is about 5.4 M cells. A schematic of the mesh is given in Fig. 8.7. In the y direction, the refinement is limited around $y = 0$, but it has to be extended progressively to higher positive and negative values of y depending on the number of the pulses to study. In the x direction, since the plasma channel extends for about 8 mm, the mesh has been refined between $x = -5$ mm and $x = 5$ mm.

One point to notice here is that the refinement is sufficient in the discharge zone in order to capture the formation and early development of the pressure wave. As the mesh coarsens, the latter is not properly resolved anymore and dissipates. This choice has been done in order to limit the computational cost and because the development of the pressure wave is not of interest in this test case.

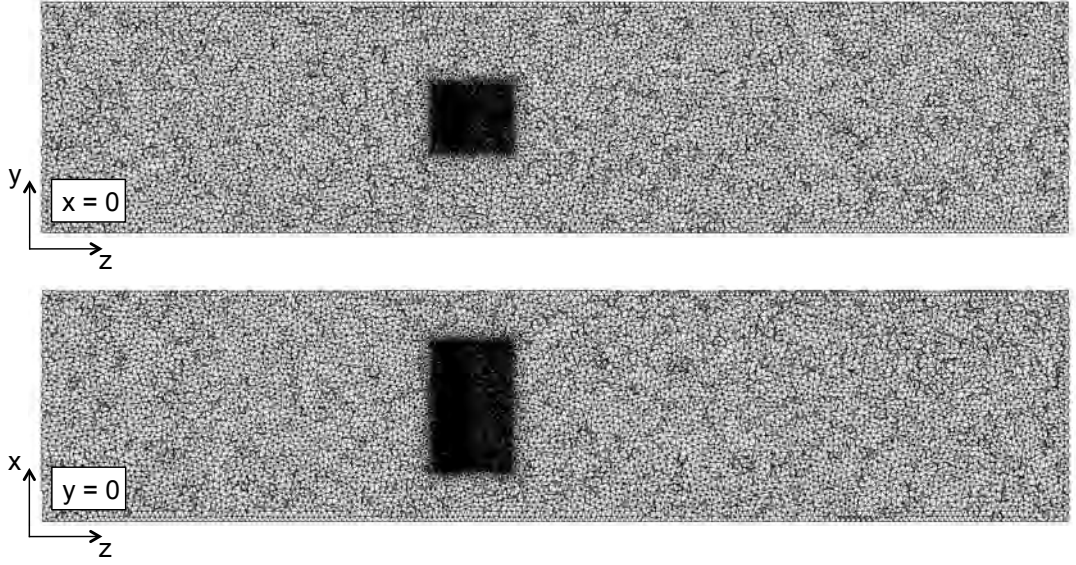


Figure 8.7: 2-D cuts of the channel mesh. Top: y - z plane, bottom: x - z plane.

Numerical setup

The numerical simulations have been run with the same numerical setup as the PACCI reactive case. The numerical scheme used for the simulations is TTGC [Colin and Rudgyard, 2000], third order accurate in space and time. The sub-grid stress tensor is closed using the SIGMA [Nicoud et al., 2011] model. The turbulence-chemistry interaction is modeled using a Thickened Flame LES model [Colin et al., 2000; Légier et al., 2000] approach. Note that the TFLES model is deactivated during the energy deposit and the possible ignition (until reaching a temperature of 1600 K) in order to avoid quenching due to artificial diffusivity. This is obtained via the mesh refinement in the discharge zone, which naturally leads to no thickening in this zone. The laminar viscosity and thermal conductivity are modeled according to D'Angola et al. [2008], which is accurate at low and very high temperatures. The kinetic scheme used to tune the model is the BFER [Franzelli et al., 2012] scheme, with 6 species and 2 global steps. The scheme has been built and validated for combustion simulations and has been used as is in this study. The choice of this simple kinetic scheme to tune the model is a first step before including more complex chemistry, as shown in section 8.3. The numerical simulations are run using a fixed time step of 10 ns: the energy is entirely supplied during a single time step.

Simulations initialization

The convective time of the channel is defined as

$$\tau_{conv} = \frac{\bar{\rho} \cdot V_c}{\dot{m}} \quad (8.3)$$

with $\bar{\rho}$ the mean density, V_c the channel volume and \dot{m} the mass flow rate. For the considered test case the convective time is about 12 ms. The simulation has been run for a total of two convective times before applying the NRP discharges, in order to

8. PHENOMENOLOGICAL MODEL FOR NRP DISCHARGES

evacuate the initial condition and establish the flow.

Discharges characteristics

The discharges channel is always centered in $(x_0, z_0) = (0, 0)$ and its axis is always oriented as the x axis. The y position of the discharge zone is instead variable. When applying multiple discharges, the distance Δy between them has been set to 0.15 mm, a distance representative of the circle arc traveled by the fluid at the mean azimuthal speed measured at the exit of the injection tube in the PACCI LES. The series of NRP discharges is always centered at $y_0 = 0$: the y position is therefore comprised between $-0.15 \text{ mm} \cdot n$ and $0.15 \text{ mm} \cdot n$, where $2n+1$ is the total number of pulses simulated.

In the following, the model is calibrated using the BFER kinetic scheme. Then, the influence of the choice of the kinetic scheme is analyzed by means of switching from the BFER to the LU13 mechanism. Based on this second kinetic scheme, a parametric study is performed and the influence of several parameters on the final gas state is studied.

8.2.1 Model calibration using the BFER kinetic scheme

The BFER 2-step global scheme is well tuned and extensively used for combustion calculations, but it is not adapted to high temperatures and to plasma phases of the gas. It is however behind the scope of this work to correctly reproduce plasma chemistry, since the contribution of plasma chemistry to combustion initiation is marginal [Collin-Bastiani et al. \[2018\]](#). The aim is here to reproduce NRP effects and BFER mechanism is very convenient thanks to its low computational cost and is used as the basis to study the thermal effect of the energy deposit on the gas. Starting from experimental observation, the objective of the model is to have, at the end of the discharge series in the same zone, (1) a temperature of $\approx 2500 \text{ K}$, (2) re-ignition of the mixture.

This can be achieved by means of three consecutive discharges, moving from a y -coordinate of $y = -0.15 \text{ mm}$ to $y = 0.15 \text{ mm}$, as shown in Figs. 8.8, 8.9 and 8.10. The discharge series starts at a time $t = 0$, where the first pulse causes an ultrafast increase of temperature of about 600 K and an ultrafast increase of pressure of about 2.5 bar. This first pulse is not sufficient to ignite and the temperature stays low after the pulse. The increase in temperature and pressure caused by the second pulse are of the same order of magnitude than for the first one. Its added effect causes a temperature rise of about 1000 K. The maximum heat release rate grows due to the higher temperature, but is still not sufficient to ignite the mixture and create a flame front. This is achieved on the contrary with the third pulse. The temperature rise in this case is about 2000 K, as a combination of the ultrafast heating caused by the energy deposit and the chemical source term which leads to a drastic increase of the heat release rate. The order of magnitude of the ultrafast increase in gas temperature is in accordance with what found by [Rusterholtz et al. \[2013\]](#) ($\approx 1000 \text{ K}$) and [Castela et al. \[2016\]](#) ($\approx 1000 \text{ K}$ when taking into account O production by the plasma and up to 2000 K when not taking it into account).

With this procedure, the objective of igniting the mixture is achieved, but the maximum temperature is about 3350 K, higher than the desired one of 2500 K. This

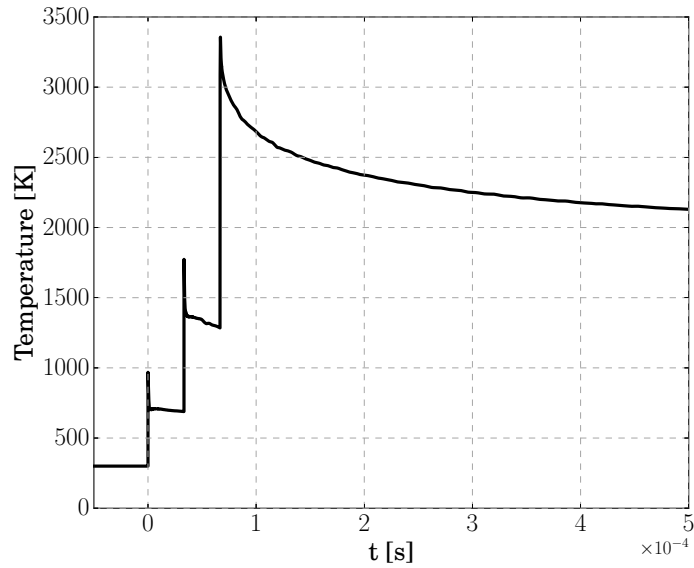


Figure 8.8: Temporal evolution of maximum temperature (BFER kinetic scheme).

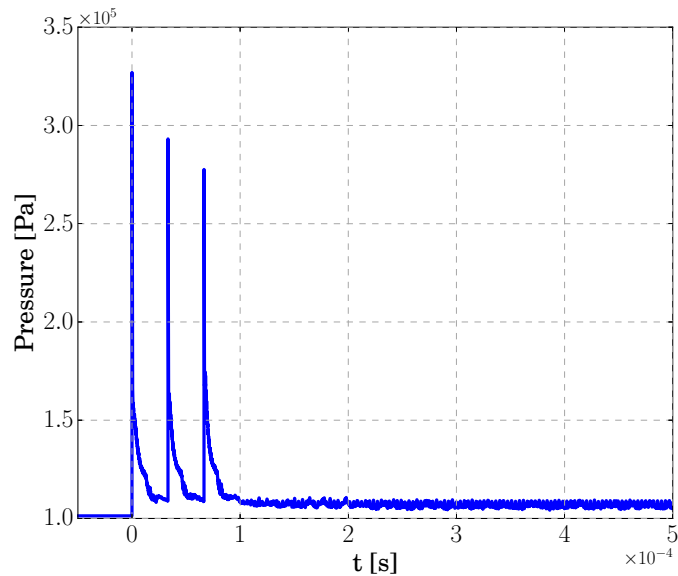


Figure 8.9: Temporal evolution of maximum pressure (BFER kinetic scheme).

is due to the fact that the endothermic reactions linked to species dissociations are not taken into account. This effect will be studied in section 8.3. It is also probable that the BFER scheme does not answer well in term of reaction rates to temperatures higher than the operating range for which it has been developed, overestimating the heat release rate and leading consequently to a too high temperature. This effect can partially be avoided using a more adapted kinetic scheme (see section 8.3) or tuning

8. PHENOMENOLOGICAL MODEL FOR NRP DISCHARGES

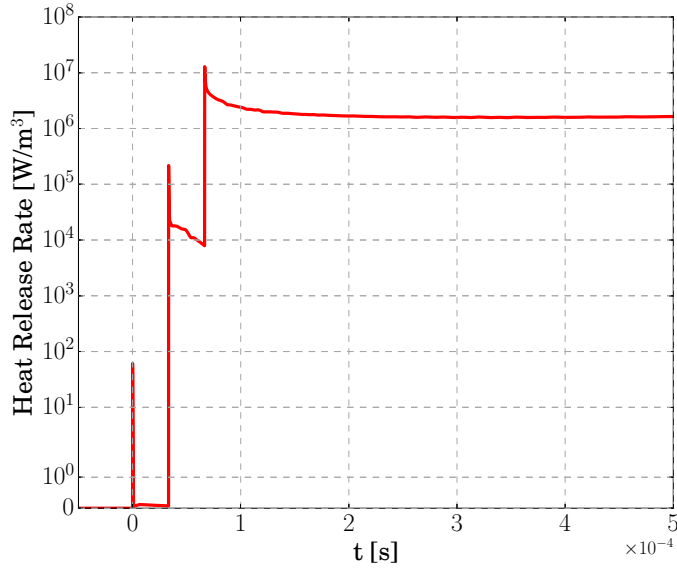


Figure 8.10: Temporal evolution of mean heat release rate (BFER kinetic scheme). Logarithmic scale.

the deposit size (see subsection 8.3.1). Such tuning has not been done with the BFER scheme, since this kinetic scheme does not give much flexibility: for example if only two discharges are used, the mixture does not ignite, with four discharges the final temperature would be too high (and the response of the kinetic scheme not accurate).

Once the mixture ignited, a flame kernel is convected by the flow and the maximum temperature tends to the adiabatic flame temperature. The mean heat release rate stabilizes to a constant value. The pressure decreases towards the atmospheric one, even if some oscillations remain. The numerical simulations are run here for a total time of 0.5 ms, which is sufficient to analyze the flame kernel development and early propagation of the flame. Fig. 8.8 shows that, at the end of the simulation the maximum temperature of the ignited kernel is about 2100 K. The sequence of 3 discharges is illustrated in Figs. 8.11 and 8.12, where instantaneous fields of temperature and heat release rate are shown respectively. The fields are extracted on a 2-dimensional $y - z$ plane cut, in an area close to the plasma discharge. Six different temporal instants are shown: the fields of the top row correspond to the end of the three discharges, while the bottom row presents the flame kernel creation and development.

In order to analyze the chemical effect of the energy deposit, species profiles are plotted in Fig. 8.13 at four different temporal instants: at the end of each one of the three discharges and at the end of the simulation time, when the flame kernel is established and convected towards the main flame. The profiles have been taken on the $x = 0$ plane, at the y position corresponding to the analyzed discharge. The fourth profile is taken at the y position of the last discharge. The profiles are taken along the z -axis, from a position of $z = -1$ mm, at the left to the discharge, to a position $z = 6$ mm.

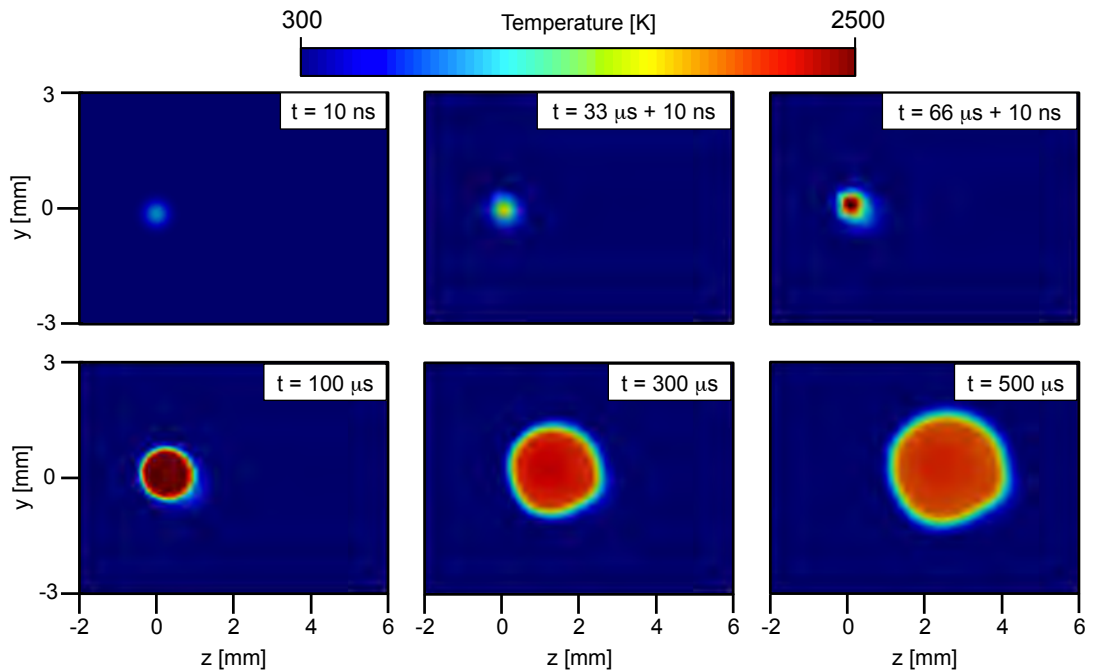


Figure 8.11: 2-D cut of the instantaneous temperature field at different temporal instants in a region close to the discharge (BFER kinetic scheme).

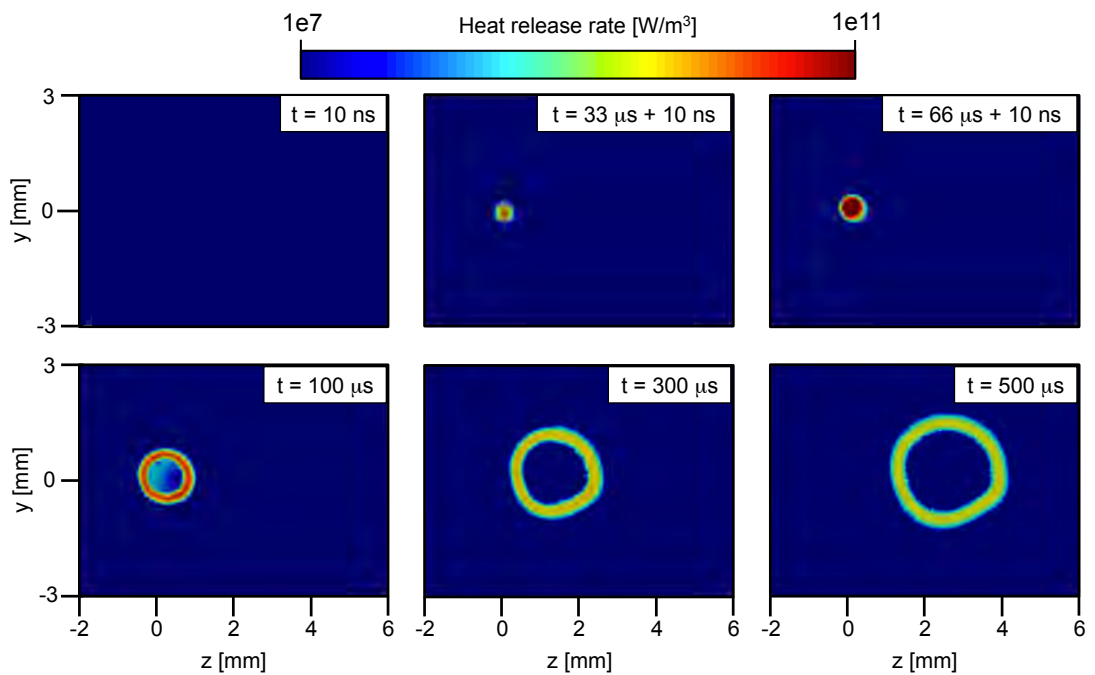


Figure 8.12: 2-D cut of the instantaneous heat release rate field at different temporal instants in a region close to the discharge (BFER kinetic scheme). Logarithmic scale.

8. PHENOMENOLOGICAL MODEL FOR NRP DISCHARGES

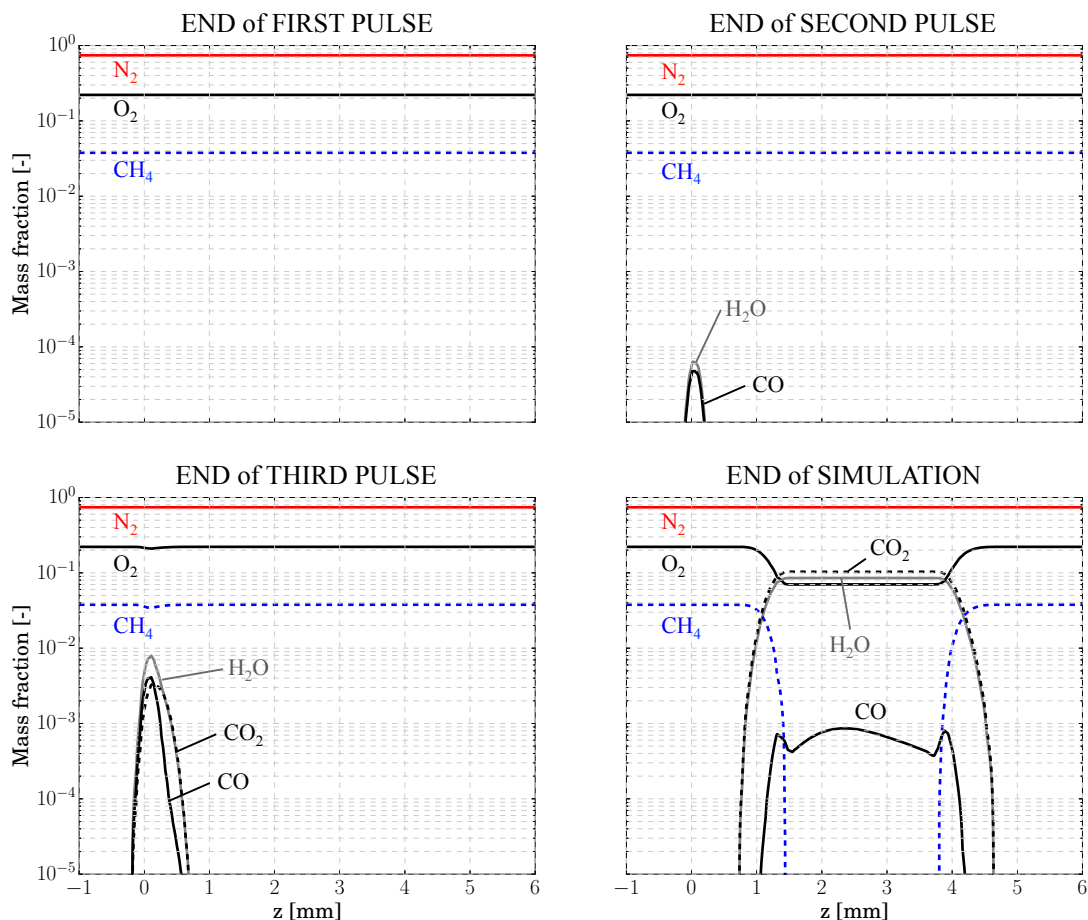


Figure 8.13: Species profile at different temporal instants (BFER kinetic scheme). Logarithmic scale.

It can be clearly seen how the first discharge has no effect on the species composition: apart from negligible fractions, the mixture is still composed only by heated air and fuel. This is in agreement with Fig. 8.10, where for the first discharge the mean heat release is nearly zero. The second pulse causes a triggering of some reactions, with a production of small quantities of CO and H₂O. The reaction rate is however quite weak and does not lead to ignition. This is different after applying the third pulse, at the end of which final products can already be found. From there ignition occurs, a flame kernel develops and is convected downstream.

As shown experimentally by Xu et al. [2011], a pressure wave develops as a consequence of the energy deposition and its behavior is shown in Fig. 8.14 for the first discharge. Pressure is plotted along a line in the plane $x = 0$, at a y position corresponding to the first discharge. The axial coordinate $z = 0$ corresponds to the center of the deposit: at the end of the energy deposit, pressure increases in the entire deposit zone, featuring a Gaussian shape in the z -direction. As found in Fig. 8.9, the maximum pressure is about 3 bar. A pressure wave detaches after $0.4 \mu\text{s}$ (see Fig. 8.15, where

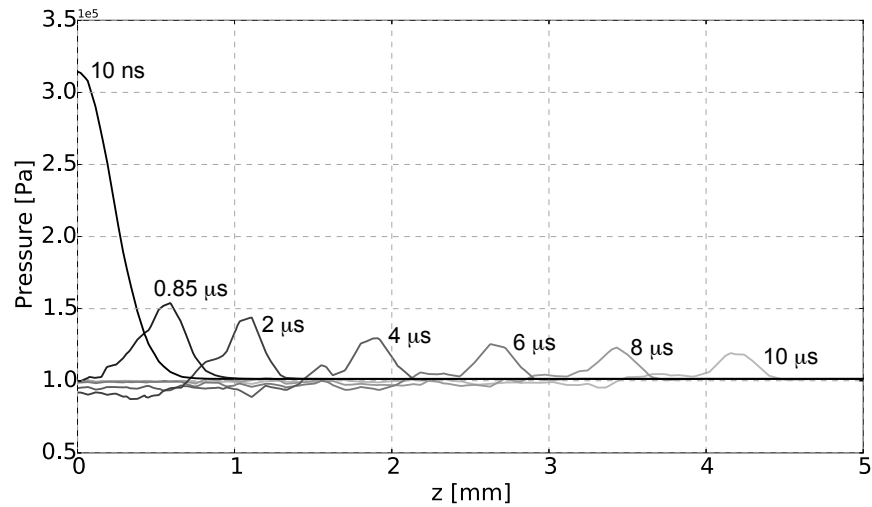


Figure 8.14: Pressure profiles at different temporal instants ($x = 0$, $y = -0.15$ mm). First NRP discharge, BFER kinetic scheme.

the pressure wave position versus time is shown) and propagates outwards through the surrounding mixture at a speed close to the sound speed (≈ 340 m/s). Because the external source of energy ceases after the pulse and because the energy must be spread over an ever-increasing radius, the wave strength diminishes due to both expansion and viscous dissipation. As a consequence of the wave strength attenuation, after $1 \mu\text{s}$ the maximum of pressure has already fallen to about 1.5 bar. After $10 \mu\text{s}$ the maximum is even weaker, with a maximum of pressure of about 1.2 bar. The pressure wave has traveled at this stage about 4 mm.

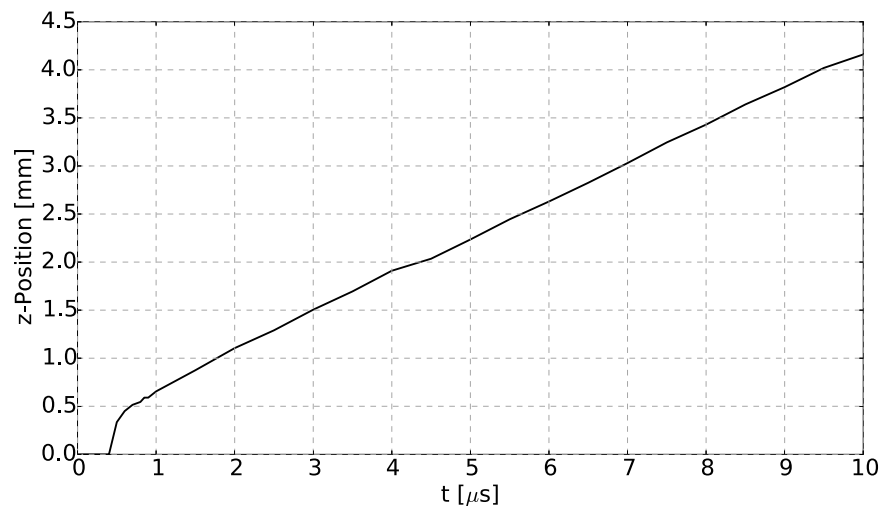


Figure 8.15: Pressure wave position versus time. First NRP discharge, BFER kinetic scheme.

Fig. 8.16 shows that the pressure wave is associated to a "temperature wave" which travels with it. Here the temperature is plotted along the same line in the plane $x = 0$,

8. PHENOMENOLOGICAL MODEL FOR NRP DISCHARGES

at a y position corresponding to the first discharge. The temperature faces an ultrafast decrease of nearly 200 K in less than $1 \mu\text{s}$, after which the shape of the heated channel and its maximum values remain practically constant. This quota of the deposit energy is lost from the point of view of gas heating and it corresponds to about 30 % of the temperature increase. The amplitude of the "temperature wave" is relatively low, of about 30 K after $2 \mu\text{s}$ and reduced to around 13 K after $10 \mu\text{s}$. The speed of the wave remains close to the sound speed (340 m/s) showing that combustion is not driving it (no detonation mode at any time).

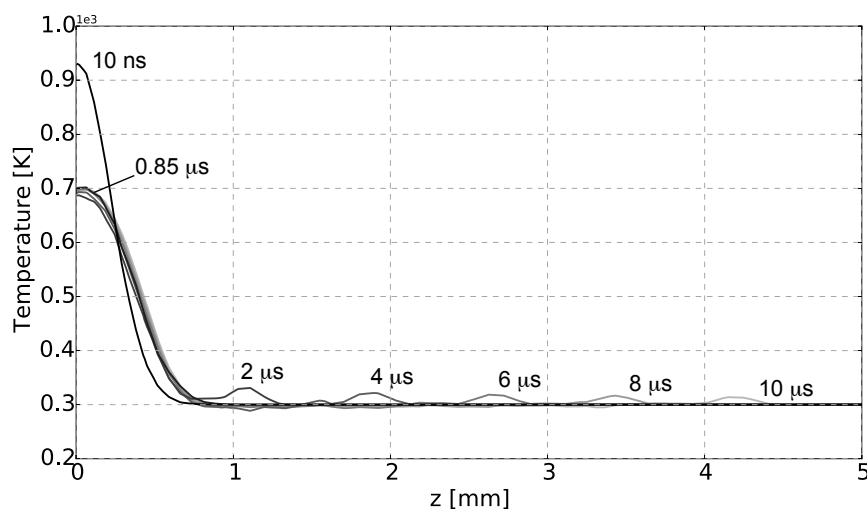


Figure 8.16: Temperature profiles at different temporal instants ($x = 0$, $y = -0.15$ mm). First NRP discharge, BFER kinetic scheme.

8.3 Increasing the complexity of the kinetic scheme: from BFER to LU13

In this section the objective is to move one step forward and analyze the influence of the kinetic scheme on the overall results of the model developed during this work. To do so a more complex scheme which is still usable in LES computations, the LU13 in this specific case, is used. Being more adaptive, this kinetic scheme permits in addition to perform a parametric study on the model parameters.

The influence of the kinetic scheme is analyzed by performing the same simulation as in subsection 8.2.1, only switching from the BFER to the LU13 kinetic scheme. It has been shown in subsection 7.3.1 that the behavior of the two schemes for autoignition delay is different, so that differences are expected on the ignition of the mixtures. Moreover, the LU13 scheme contains some of the species involved in high temperature dissociation (O for instance) and endothermic reactions associated to dissociation can appear.

Figures 8.17, 8.18 and 8.19 show the temporal evolution of the maximum temperature, maximum pressure and mean heat release rate obtained with the LU13 mechanism, compared to the ones obtained with the BFER one.

8.3 Increasing the complexity of the kinetic scheme: from BFER to LU13

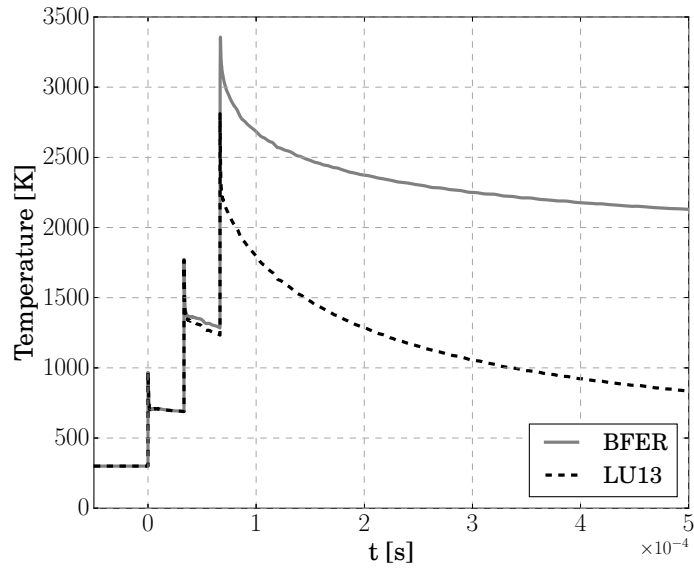


Figure 8.17: Temporal evolution of maximum temperature (LU13 vs BFER kinetic scheme).

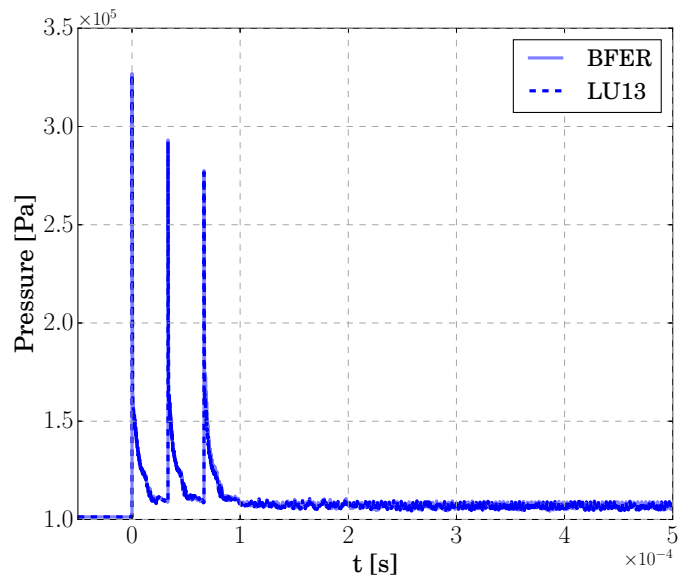


Figure 8.18: Temporal evolution of maximum pressure (LU13 vs BFER kinetic scheme).

If the rise in temperature is very similar for the first and second discharges (Fig. 8.17), the behavior is completely different for the third one: with the LU13 kinetic scheme, the increase in temperature associated to the third energy deposit triggers endothermic reactions with negative heat release rate (Fig. 8.19), which quickly cool down the mixture. The maximum temperature recorded is about 2800 K, more than 500 K lower

8. PHENOMENOLOGICAL MODEL FOR NRP DISCHARGES

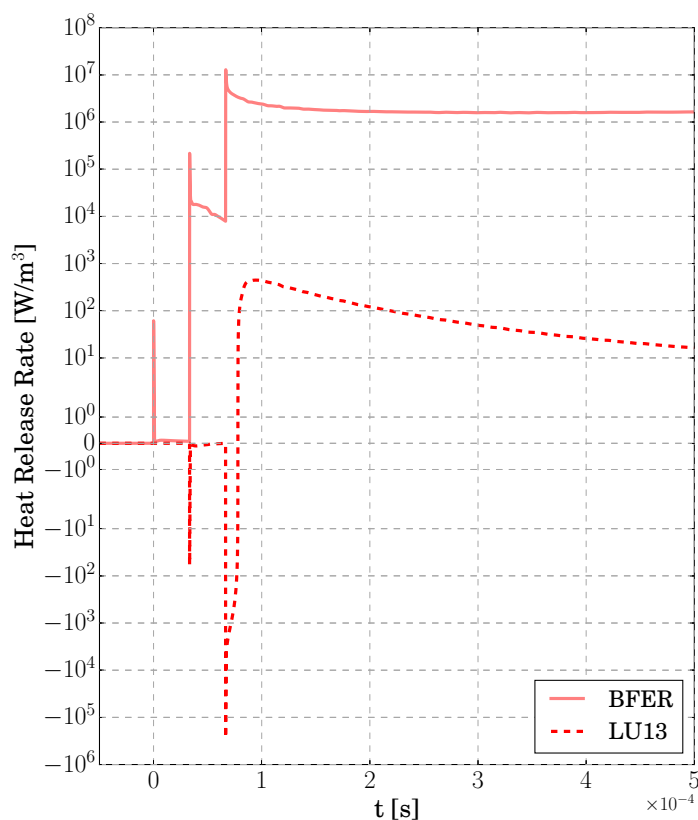


Figure 8.19: Temporal evolution of mean heat release rate (LU13 vs BFER kinetic scheme). Linear scale around zero and logarithmic scale elsewhere.

than using the BFER mechanism. With this temperature behavior, the hot kernel does not stay long enough at high temperatures to ignite before being diffused. As an example, at 2000 K, the autoignition time is about 0.1 ms with the LU13 mechanism, while in the numerical simulation this temperature is kept for no more than 0.015 ms. It is also clear that the under-estimation of the autoignition time typical of the BFER scheme can lead in this case to false ignition.

Once the sequence of pulses has ended, and because of the absence of ignition, the pocket of heated gases is convected and diffused. Since the chemical source term is negligible, the gas cools down and, at the end of the simulation, the maximum temperature is about 800 K, around 1300 K lower than with the BFER mechanism. No major differences are visible on the pressure evolution, with pressure waves of the same amplitude in both cases. This is not surprising as the energy deposit is identical in both cases. The mean heat release rate tends rapidly to zero.

Regarding the species composition of the mixture, radicals are produced mainly by the third pulse but their amount is very low. Their mass fraction is always lower than 1×10^{-5} and is not sufficient to branch chemical reactions in LU13 which lead to the

8.3 Increasing the complexity of the kinetic scheme: from BFER to LU13

fuel oxidation.

In order to check the influence of the calibrated model parameters, a parametric study is now performed using the LU13 mechanism.

8.3.1 Influence of the deposit size

One key model parameter is the deposit volume. For a fixed total energy E_p (see section 8.1), the volume is directly proportional to the source term. Avoiding bending effects, which are however present as shown in section 8.1, and considering the cylinder length as fixed (equal to the inter-electrodes gap), the parameter which can be modified to vary the deposit volume is the cylinder diameter. The value of the gaussian FWHM, fixed in the standard case to $500 \mu\text{m}$, is now varied. Using higher values of FWHM will lead to a lighter heating of the fluid and eventually to a pocket of colder gases delivered to the main flame, stepping away to the objective of igniting the mixture. On the contrary, using lower values of FWHM could produce a sufficient increase of temperature and/or radical concentration to lead to ignition. Therefore, an additional value of FWHM = $400 \mu\text{m}$ is chosen. In order to illustrate the effect of changing the

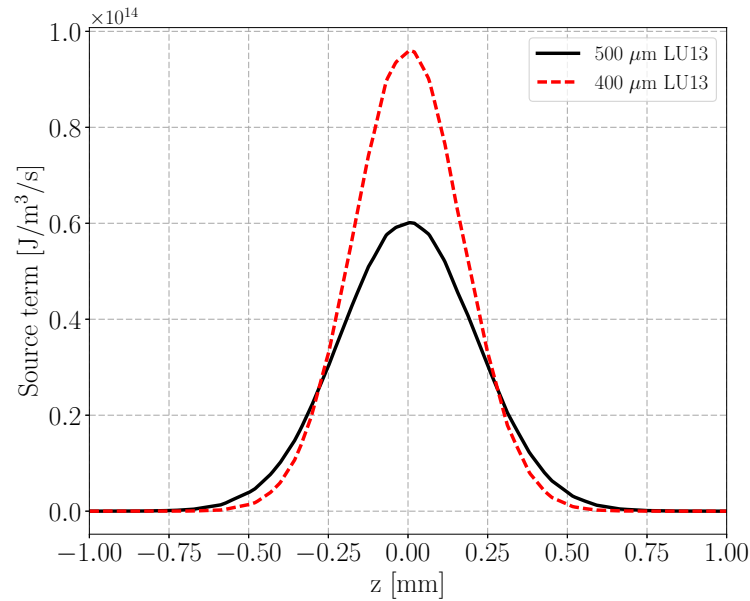


Figure 8.20: Effect of the FWHM of the energy deposit on the source term applied to the fluid.

deposit volume on the source term, the 1-D profile of the deposit energy is shown in Fig. 8.20. The profile is extracted from the numerical simulation on a line at $x = 0 \text{ mm}$ and $y = -0.15 \text{ mm}$, corresponding to the y -position of the first discharge.

A variation of FWHM of 20 % leads to an increase of the maximum of the source term of more than 50 %: the grid nodes at which the maximum of the source term is applied will experience a much higher temperature increase.

8. PHENOMENOLOGICAL MODEL FOR NRP DISCHARGES

The temporal evolution of the maximum temperature, maximum pressure and mean heat release rate are presented for the two cases in Figs. 8.21, 8.22 and 8.23 respectively.

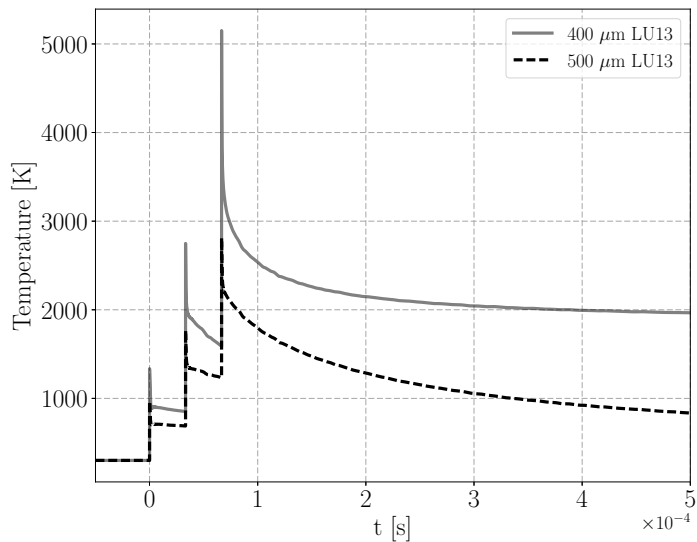


Figure 8.21: Temporal evolution of maximum temperature for different values of the energy deposit FWHM.

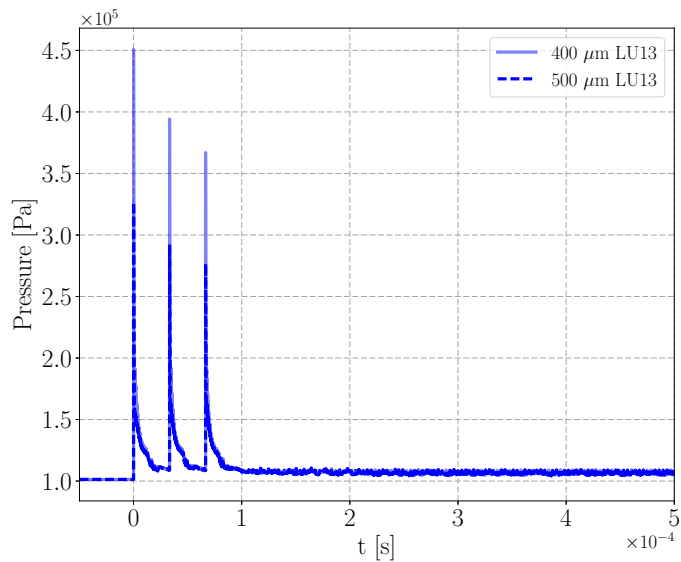


Figure 8.22: Temporal evolution of maximum pressure for different values of the energy deposit FWHM.

As expected, a higher value of the term source leads to higher temperature. The

8.3 Increasing the complexity of the kinetic scheme: from BFER to LU13

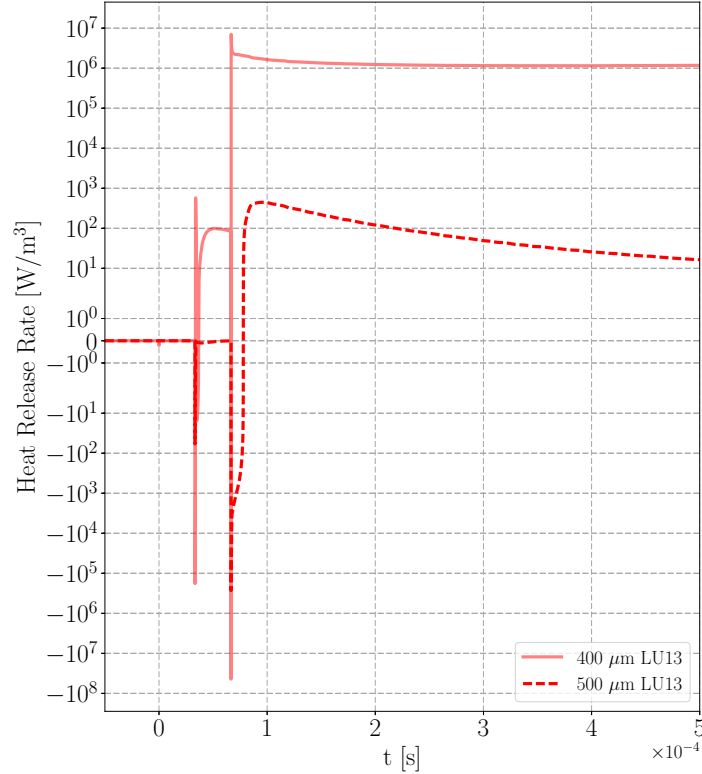


Figure 8.23: Temporal evolution of mean heat release rate for different values of the energy deposit FWHM. Linear scale around zero and logarithmic scale elsewhere.

first pulse produces an ultrafast heating of about 900 K, leading to a maximum gas temperature of 1200 K. The second pulse brings already the gas to temperatures close to the maximum expected, and close to the one obtained after three pulses using a FWHM of 500 μm . As it happened in the previous case, no ignition is present at these temperatures, since they are maintained for a too short time. The third pulse features two main phenomena: first, a strong negative heat release rate (Fig. 8.23) and right after, the branching of chemical reactions activation, leading to ignition. The ultrafast increase of temperature is in this case of about 3400 K, much higher than in the previous case. This is the result of the energy deposit and the chemical reactions. The very high temperature of about 5000 K is however maintained for a very short time, of the order of magnitude of nanoseconds, and falls rapidly to more expected values of about 3000 K. Note that, since the LU13 mechanisms contains, in part, dissociation reactions, its behavior at high temperatures is expected to be less inaccurate than the one obtained with the BFER scheme.

After ignition, the evolution of the flame kernel is similar to the one observed with the BFER mechanism, with a maximum temperature which progressively decreases

8. PHENOMENOLOGICAL MODEL FOR NRP DISCHARGES

towards the adiabatic flame temperature and with the mean heat release rate which stabilizes to similar values. At the end of the simulation the maximum temperature is about 2000 K, i.e., 100 K lower than with the BFER mechanism.

The maximum pressure is also affected by the higher value of the energy deposit source term, with an increase in pressure which goes from 2.5 to 3.5 bar. Even if the maximum value is affected, the temporal evolution of the latter is very similar in both cases.

The species composition is now analyzed. Only the species profiles at the end of the third discharge and at the end of the simulation are presented in Fig. 8.24, since the first and second discharge do not lead to a significant production of radicals and products. This is coherent with the simulation run using a FWHM of 500 μm , where

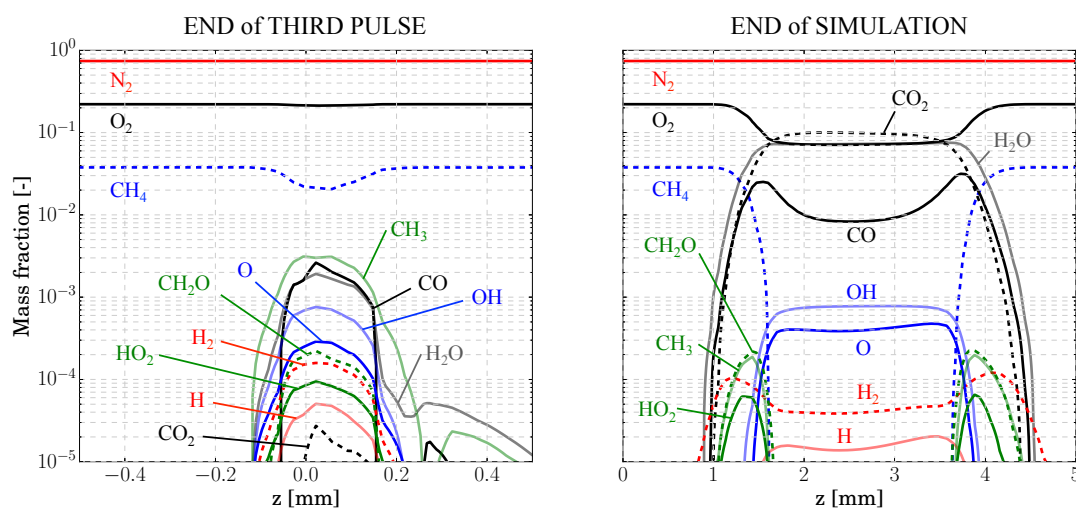


Figure 8.24: Species profiles at different temporal instants (LU13 kinetic scheme). Logarithmic scale.

the mixture fraction of the species other than fuel and air were found to be negligible. At the end of the third discharge, the mixture is composed by a pool of radicals resulting from the oxygen dissociation and other intermediate combustion species. This means that CH_4 is already partially oxidized and that the chain branching reactions have begun. The mixture fraction of CH_4 is lower in this case than the one obtained with the BFER mechanism, denoting a higher reactivity of the mixture. At the same time, due to the higher concentration in radicals, the mixture fractions of final products are lower than the one obtained using the BFER mechanism.

At the end of the simulation a flame structure similar to the one obtained with the BFER mechanism is obtained. A higher mixture fraction is observed for CO, whose conversion to CO_2 is slow and generally too fast with the BFER mechanism. Moreover, not all intermediate species are converted into final products, denoting a flame which is still not at its final steady state. This indicates that the flame kernel which will merge to the main flame in plasma-assisted combustion configurations may have different species compositions depending on the mechanism used.

Due to the very high temperature reached using an energy deposit FWHM of 400 μm , the standard power law used for the modeling of laminar viscosity and thermal conductivity in chapter 7 is not valid anymore and one has to switch to more precise

8.3 Increasing the complexity of the kinetic scheme: from BFER to LU13

laws, like the D'Angola one [D'Angola et al., 2008]. The importance of using this kind of laws will be shortly presented now by means of Fig. 8.25, where the evolution of the maximum temperature is plotted against time using the standard Power Law and the D'Angola approach.

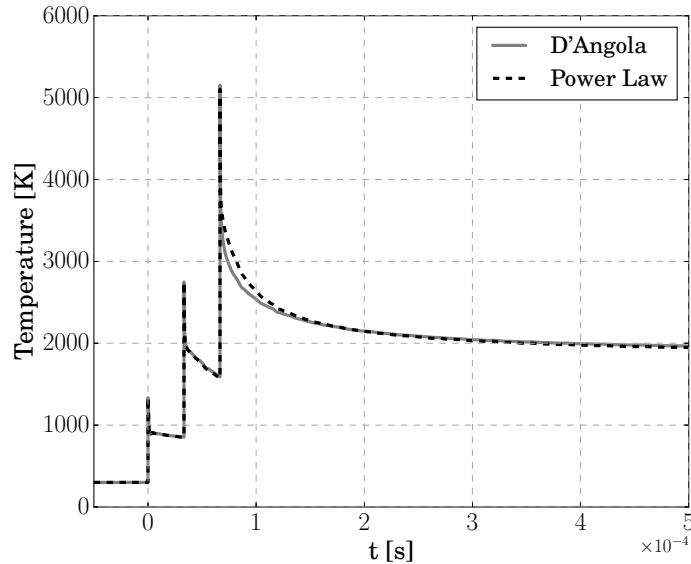


Figure 8.25: Temporal evolution of maximum temperature for different laminar viscosity and thermal conductivity laws (LU13).

Even if the differences are not of leading order, as soon as the temperature begins to be high, they can be noticed in the temporal evolution of the maximum temperature. This can be critical if the maximum temperature rises even more, as in the cases which will be presented in section 8.3.2. The D'Angola law has been used for all the simulations run in this chapter, since its validity is ensured either at low and high temperature.

8.3.2 Influence of the number of consecutive discharges

The second important parameter which has been fixed by the calibration of the phenomenological model is the number of consecutive plasma discharges in the same zone. It has been found experimentally that, depending on the gas conditions, 2 to 5 consecutive discharges take place in the same plasma channel. This variability has not been included in this first version of the phenomenological model and the number of consecutive discharges has been fixed and maintained constant for the entire simulation time.

Starting from the base setup of three consecutive discharges and an energy deposit FWHM of $500 \mu\text{m}$, the number of successive discharges is increased in order to check its effect. Moreover, the total number of consecutive discharges has not been limited to 5 in order to mimic the effect of a continuous series of discharges and check the need of the statistically jump in azimuthal direction which has been adopted in the model. The simulation is run with 15 consecutive discharges. The discharge position follows

8. PHENOMENOLOGICAL MODEL FOR NRP DISCHARGES

the same principle as in the base test case, with a displacement in the y direction of 0.15 mm at each discharge.

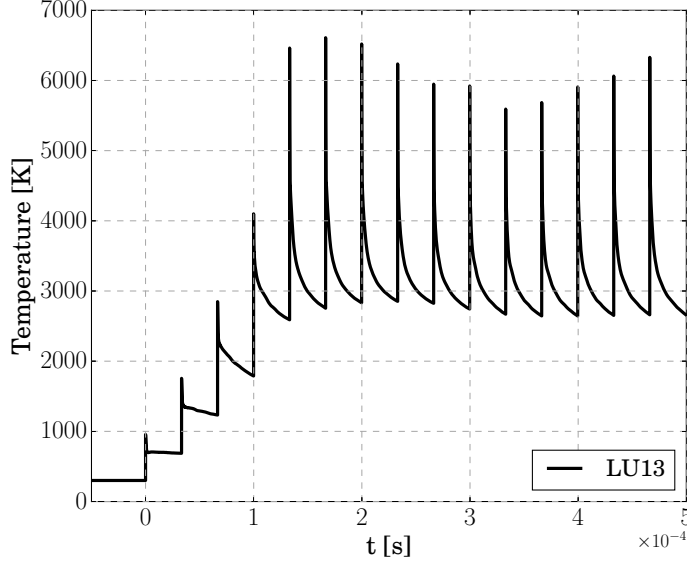


Figure 8.26: Temporal evolution of maximum temperature applying more than three consecutive discharges (LU13 kinetic scheme).

In order to keep the series of discharges centered in $y = 0$, the first discharge has a y coordinate of $y = -1.05$ mm, while the last one of $y = 1.05$ mm.

The evolution of maximum temperature is presented in Fig. 8.26.

After the fourth discharge, ignition occurs, with an ultrafast increase of temperature of about 2200 K. The fifth discharge, which is applied in a fluid at a very high temperature, leads to an even higher increase in temperature (of more than 3000 K), which reaches in this case values higher than 6000 K. From there the maxima and minima of the curve stabilize, due to an equilibrium between diffusive fluxes and the heat released by the discharge. The temperature does not go below 2700 K anymore. The behavior here found is in qualitative accord with what found by [Castela et al. \[2016\]](#) for NRP discharges in air. This suggests that a continuous series of pulses could sustain a flame at these flow conditions, acting like a flame holder.

The mechanism is shown in Fig. 8.27, where instantaneous temperature fields are shown. It can be seen how the fourth discharge is the one which triggers ignition and how a flame kernel is already present when applying the fifth discharge. All the successive discharges take place mostly in burnt gases and provide a very high temperature source which acts as a flame holder. After the last discharge, the flame kernel is convected by the flow, identically to the case in which only three discharges were used.

In the experiment the number of consecutive discharges varies naturally, depending on the local fluid and flow condition. This can be achieved in the numerical simulation only by using a more sophisticated model which takes into account the plasma phase, as well as the electrodes behavior. The bending of the plasma channel can also lead to different results, since the discharge will follow exactly the heated channel. Such effects

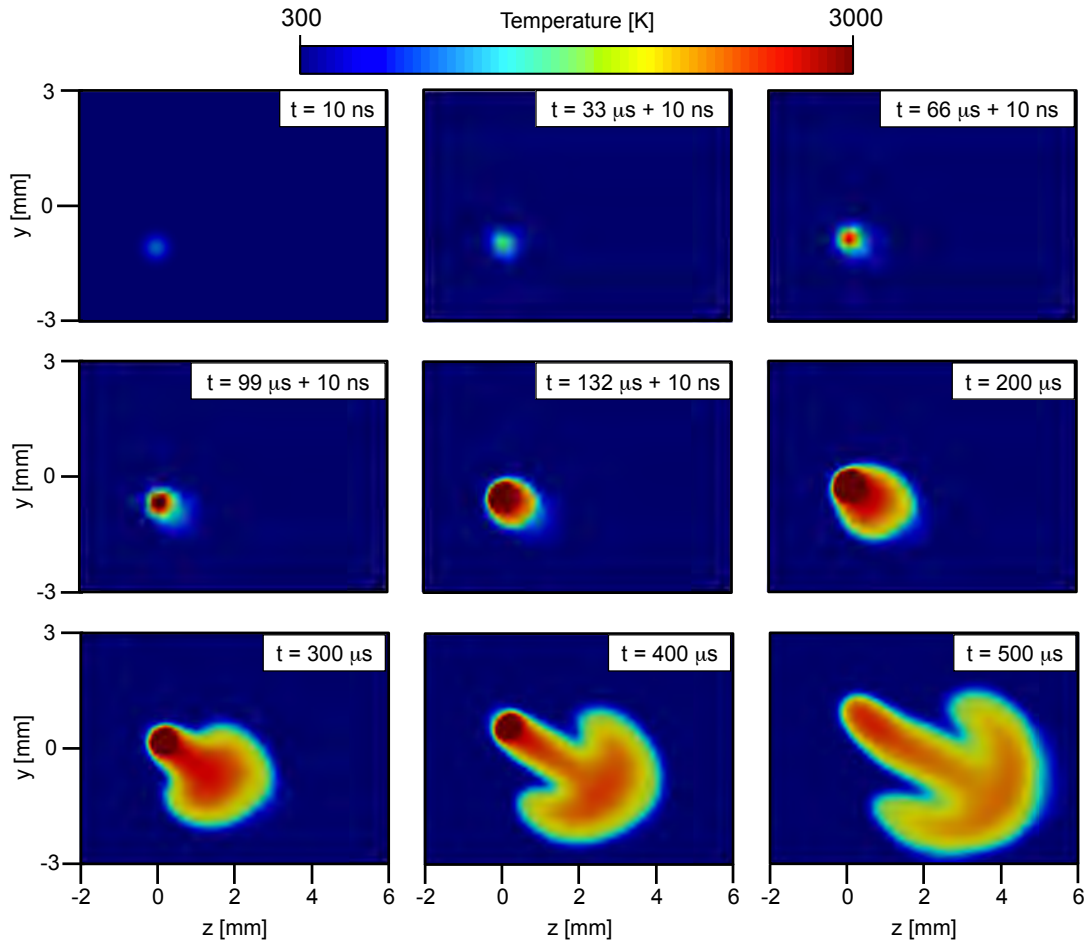


Figure 8.27: 2-D cut of the instantaneous temperature field at different temporal instants in a region close to the discharge (LU13 kinetic scheme).

will be studied in future work and are not considered here.

8.4 Influence of the plasma chemistry

All results presented until now have been obtained with kinetic schemes developed for combustion and which are sufficiently light to be used in a LES code. However none of these kinetic schemes takes into account the plasma chemistry generated by the NRP discharge. Even if such plasma is in non-equilibrium, the ionized species, as well as the N_2 and fuel dissociations can play a role. In order to check if this is of leading order, a new kinetic scheme is proposed here, following the approach proposed by [Collin-Bastiani et al. \[2018\]](#). This new kinetic scheme, which will be called PLASMA-LU in the following, is the result of the merging of the LU13 combustion scheme with the plasma kinetic scheme of [Teulet et al. \[2009a\]](#). The kinetic scheme is presented and validated in subsection 8.4.1. It has to be pointed out here that the decision to follow the approach of [Collin-Bastiani et al. \[2018\]](#) has been made in order to have

8. PHENOMENOLOGICAL MODEL FOR NRP DISCHARGES

a methodology ready to be applied, since the detailed modeling of the plasma phase is beyond the scope of this work. However, Collin-Bastiani et al. [2018] focused on equilibrium plasmas and the validity of the plasma kinetic scheme for non-equilibrium plasmas has to be further validated.

Before presenting the kinetic scheme it has to be mentioned that the numerical simulations performed in this section have been run with the Lax-Wendroff (LW) kinetic scheme instead of the TTGC one. This has been necessary due to numerical problems encountered when using the PLASMA-LU kinetic scheme combined with the TTGC numerical scheme. The problem has not been investigated into details and must be the object of further studies. In order to compare the PLASMA-LU kinetic scheme with the LU13 one, it has been first verified that the influence of the numerical scheme on the results obtained with the LU13 kinetic scheme is not of leading order. To do so, two identical simulations have been run with LU13, applying 3 successive discharges and with a deposit FWHM of $400 \mu\text{m}$ to have ignition.

The temporal evolution of the maximum temperature, maximum pressure and mean heat release rate obtained with LW and TTGC are shown in Figs. 8.28, 8.29 and 8.30 respectively.

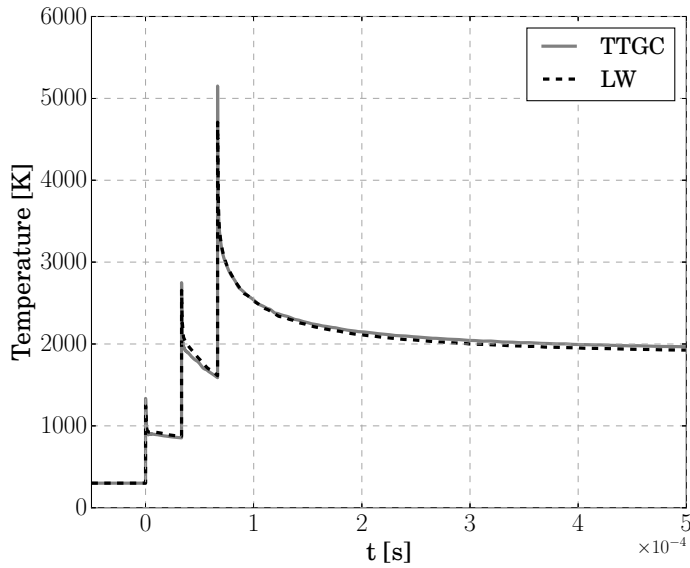


Figure 8.28: Temporal evolution of maximum temperature for different numerical schemes. LU13 kinetic scheme, deposit FWHM of $400 \mu\text{m}$.

LW is more dissipative and the maximum temperature reached using this scheme is slightly lower than using the TTGC one. This difference is very low (around 35 K) when comparing the values at the end of the simulation ($t = 0.5 \mu\text{s}$). As a result of the lower maximum temperature, the maximum pressure is slightly lower at the end of the three discharges, denoting a slightly weaker pressure wave. Thanks to its more dissipative behavior, LW permits to better dissipate the acoustics resulting from the pressure waves and at the end of the simulation time the maximum pressure value has fallen to the atmospheric one. Regarding the mean heat release temporal evolution, despite

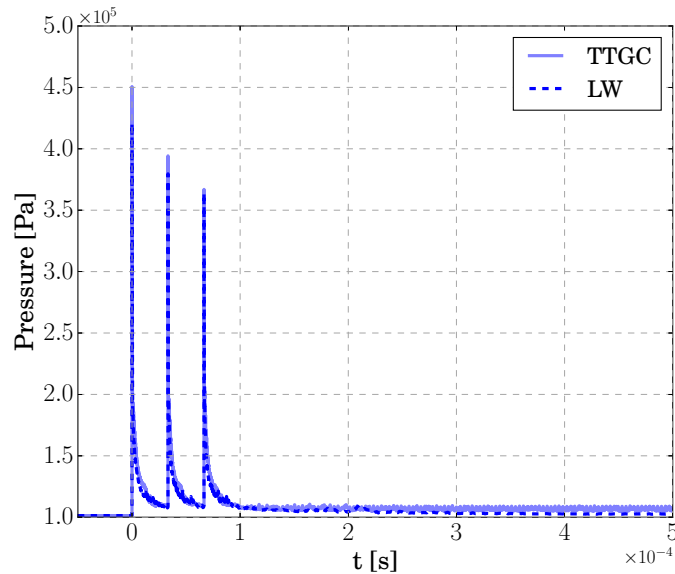


Figure 8.29: Temporal evolution of maximum pressure for different numerical schemes. LU13 kinetic scheme, deposit FWHM of $400 \mu\text{m}$.

the differences in the branching of chemical reactions due to the second discharge, the overall behavior is very similar in both cases.

This suggests that, in this case, the LW scheme can be used to compare the LU13 and PLASMA-LU kinetic schemes.

8.4.1 The PLASMA-LU kinetic scheme

The PLASMA-LU kinetic scheme (Fig. 8.31) is obtained by merging the plasma kinetic scheme of Teulet et al. [2009a], which contains 38 species and 183 reversible reactions, and the LU13 ARC combustion scheme, which contains 13 transported species, 4 QSS species and 73 reversible reactions. All the charged species contained in the plasma mechanism are treated as QSS, since they are very reactive. The resulting PLASMA-LU scheme contains 22 transported species. Among them 9 come from the plasma chemistry, 1 comes from the combustion chemistry and 12 are common and permit the coupling between the plasma and the gas. A total of 19 species are treated with the QSS approximation. The kinetic scheme contains 215 reversible reactions.

8.4.1.a PLASMA-LU scheme validation

The PLASMA-LU kinetic scheme is validated in canonical test cases using the Cantera software. Equilibrium temperature and species mass fractions obtained with PLASMA-LU are compared with the results of the GRI30 kinetic scheme and the LU13 one in Tab. 8.2. Only the species mass fractions greater than 1×10^{-6} are considered. The equilibrium calculation is performed starting from a mixture at an equivalence ratio $\phi = 0.67$, a temperature of 300 K and atmospheric pressure (inlet conditions of the PACCI burner). The PLASMA-LU kinetic scheme provides very good results, generally

8. PHENOMENOLOGICAL MODEL FOR NRP DISCHARGES

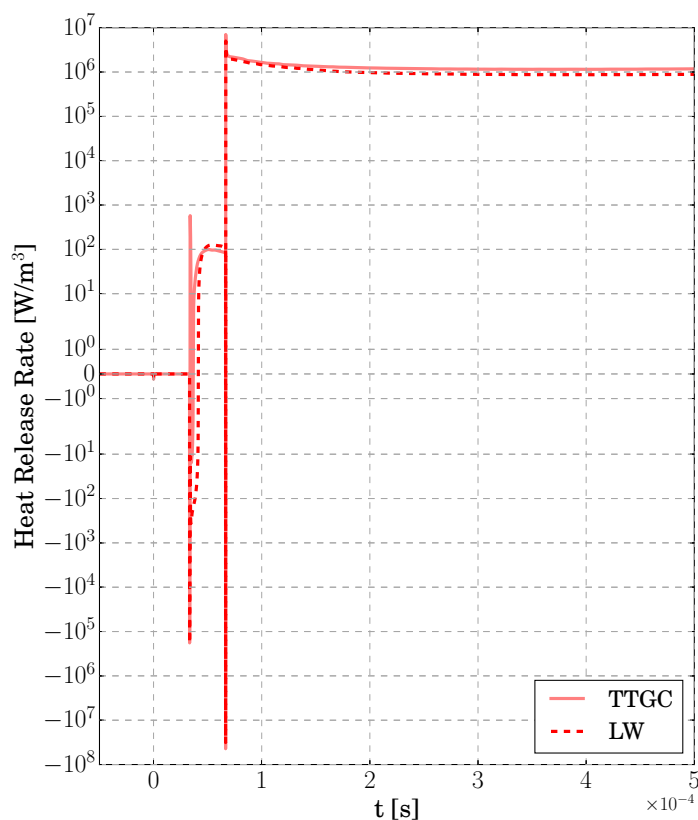


Figure 8.30: Temporal evolution of mean heat release rate for different numerical schemes. LU13 kinetic scheme, deposit FWHM of 400 μm . Linear scale around zero and logarithmic scale elsewhere.

slightly better than the LU13 one. It can be seen in particular how the only species which is present at equilibrium and is not considered by the LU13 scheme is NO.

Keeping the equivalence ratio equal to the one encountered in the PACCI configuration ($\phi = 0.67$), the flame structure is now compared in Fig. 8.32, where the temperature and heat release rate profiles are shown. The agreement is good between the different kinetic schemes.

A crucial point for the NRP discharges has been found to be the autoignition behavior. The autoignition time is shown in Fig 8.33 for the PLASMA-LU mechanism and compared to the LU13 and GRI30 kinetic schemes. The initial mixture is set to an equivalence ratio $\phi = 0.67$ and to atmospheric pressure: the PLASMA-LU kinetic scheme has a behavior almost identical to the LU13 one. This is coherent with the fact that the PLASMA-LU mechanism is an extension of the LU13 one and that the additional set of species and reactions which it contains are mostly prone to change its behavior at high temperatures. At temperatures typical of ignition in NRP discharges

8.4 Influence of the plasma chemistry

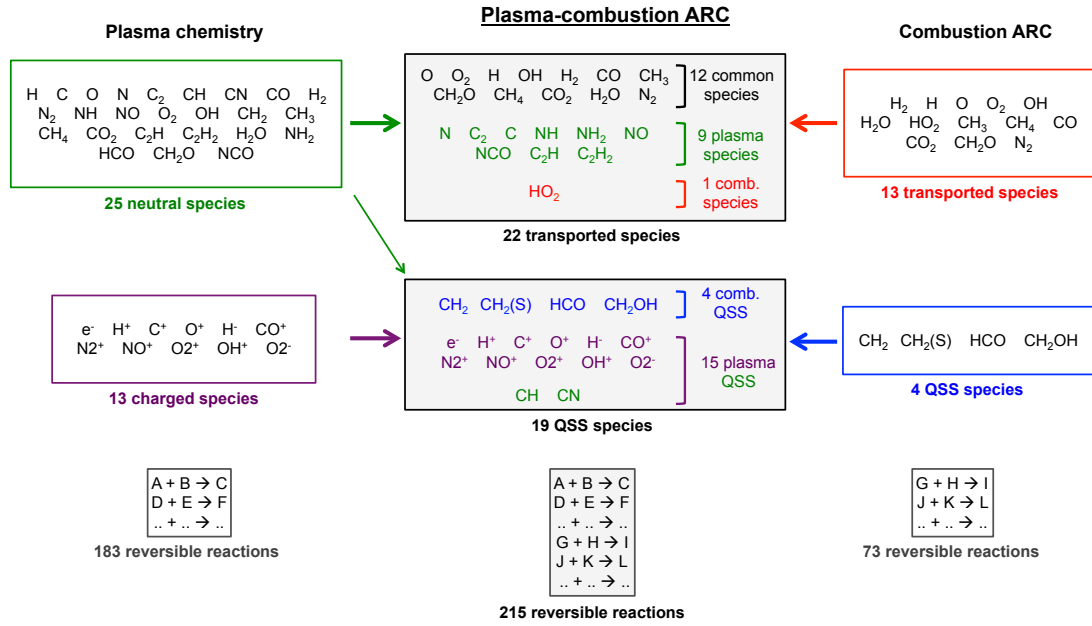


Figure 8.31: Building methodology of the PLASMA-LU kinetic scheme.

	GRI30	LU13	PLASMA-LU
Mass fraction [-]			
H ₂	1.81×10^{-6}	1.88×10^{-6}	1.79×10^{-6}
O	1.57×10^{-5}	1.65×10^{-5}	1.55×10^{-5}
O ₂	7.26×10^{-2}	7.39×10^{-2}	7.26×10^{-2}
OH	3.31×10^{-4}	3.42×10^{-4}	3.81×10^{-4}
H ₂ O	8.44×10^{-2}	8.44×10^{-2}	8.44×10^{-2}
CO	4.74×10^{-5}	4.94×10^{-5}	4.68×10^{-5}
CO ₂	1.03×10^{-1}	1.03×10^{-1}	1.03×10^{-1}
NO	2.29×10^{-3}	-	2.30×10^{-3}
NO ₂	4.98×10^{-6}	-	-
N ₂	7.37×10^{-1}	7.38×10^{-1}	7.37×10^{-1}
Temperature [K]	1788	1793	1788

Table 8.2: Equilibrium temperature and species mass fractions for different kinetic schemes.

($2.5 < 10000/T < 4$), the accordance between the ARC mechanisms and the detailed one is excellent.

In order to check the overall mechanism behavior, the evolution of the laminar flame speed and of the adiabatic flame temperature with the equivalence ratio is also evaluated and presented in Fig. 8.34. This has been performed for an unstrained premixed flame with a mixture at initial temperature of 300 K and atmospheric pressure: the PLASMA-

8. PHENOMENOLOGICAL MODEL FOR NRP DISCHARGES

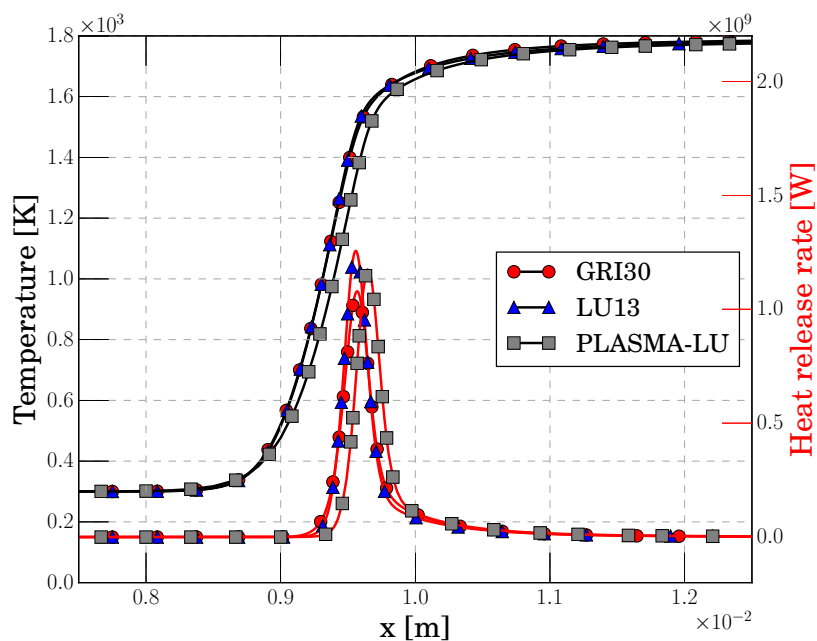


Figure 8.32: Temperature and heat release rate profiles for a 1D unstrained premixed flame using various kinetic schemes.

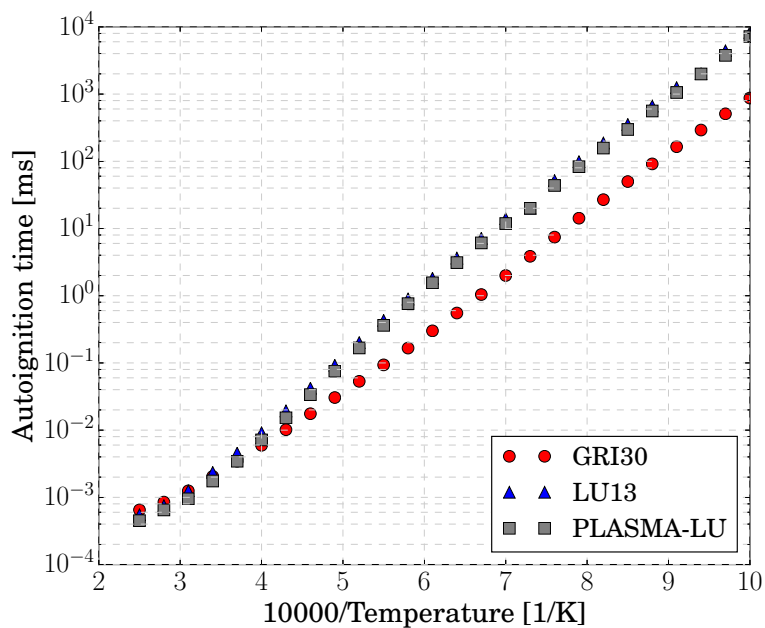


Figure 8.33: Autoignition time as a function of the mixture temperature. Logarithmic scale.

LU kinetic scheme behaves like the LU13 one and, at the equivalence ratio of the PACCI experimental configuration, the agreement is excellent with the detailed kinetic scheme.

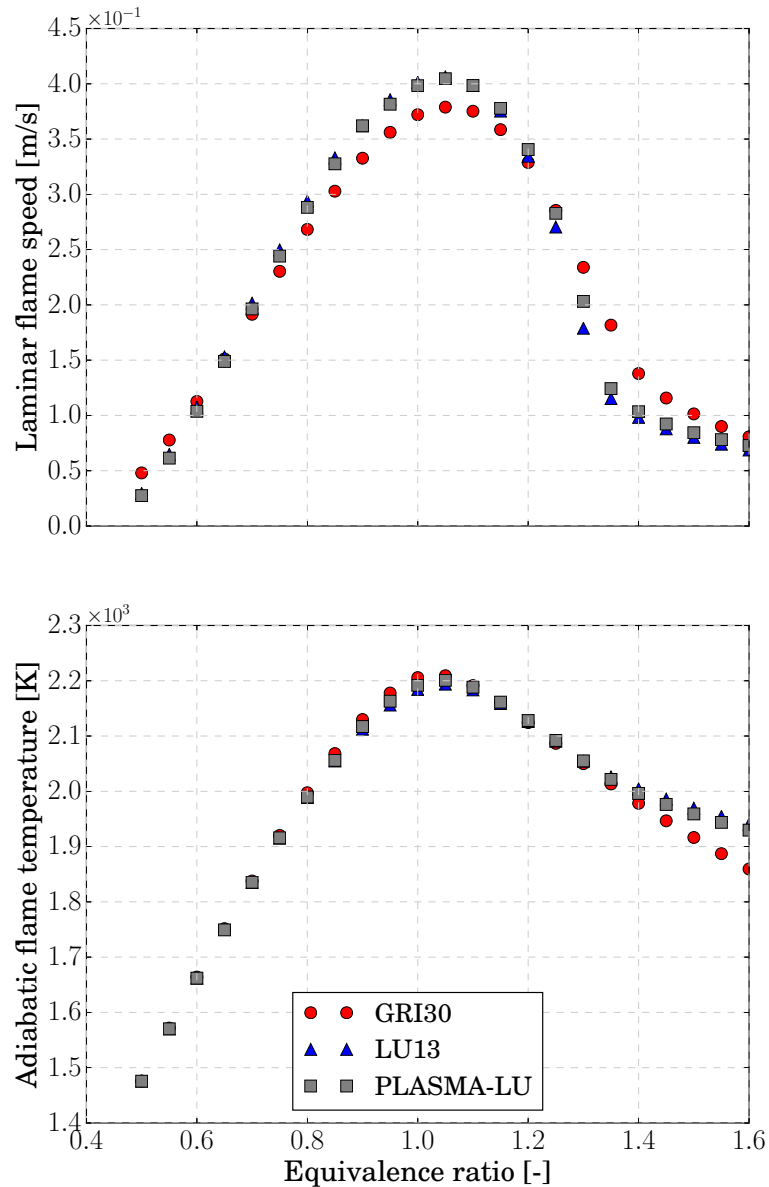


Figure 8.34: Laminar flame speed (top) and adiabatic flame temperature (bottom) as a function of the mixture equivalence ratio.

Once stated that the PLASMA-LU mechanism has the correct behavior in a typical combustion environment, the question of how to validate it for the non-equilibrium plasma phase rises. The plasma chemistry has already been validated in [Teulet et al. \[2009a,b\]](#). It has been decided in a first step to assume that the plasma phase is independent of the coupling with the combustion scheme, which does not modify it. Moreover, it is assumed that the mechanism, built for equilibrium plasmas, has the right behavior for non-equilibrium plasmas too. It will however need to be validated by further studies.

8. PHENOMENOLOGICAL MODEL FOR NRP DISCHARGES

8.4.1.b Application to the test case setup

The temporal evolution of the maximum temperature, maximum pressure and mean heat release rate are shown in Figs. 8.35, 8.36 and 8.37 respectively.

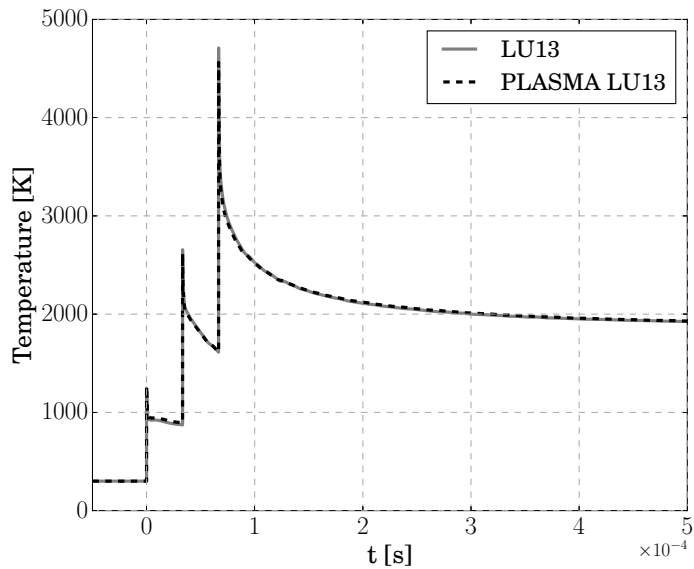


Figure 8.35: Temporal evolution of maximum temperature for different kinetic schemes. Deposit FWHM of $400 \mu\text{m}$.

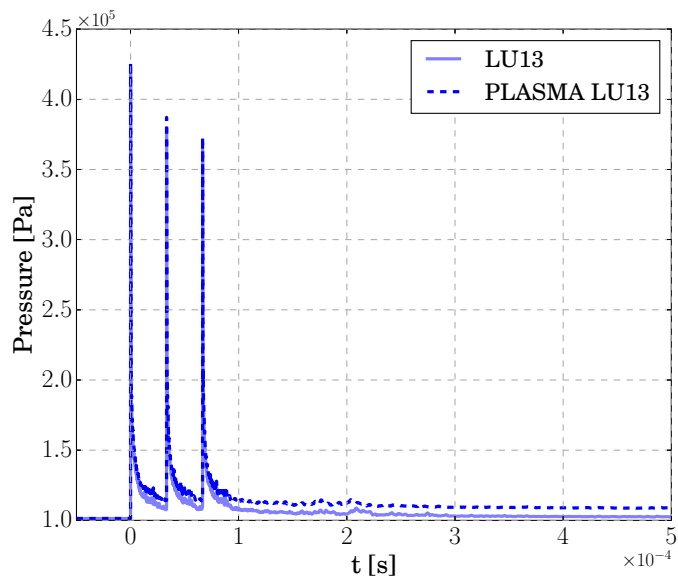


Figure 8.36: Temporal evolution of maximum pressure for different kinetic schemes. Deposit FWHM of $400 \mu\text{m}$.

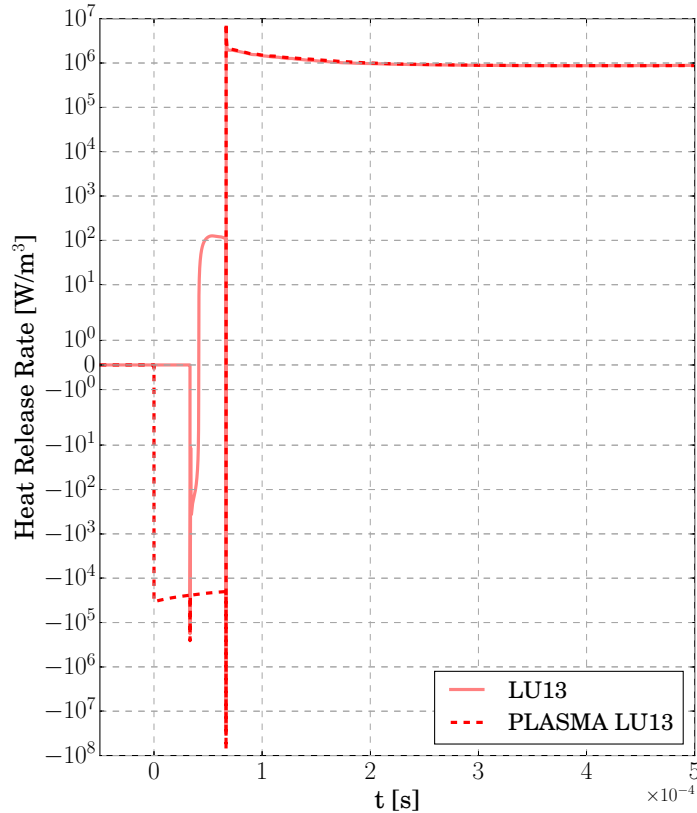


Figure 8.37: Temporal evolution of mean heat release rate for different kinetic schemes. Deposit FWHM of $400 \mu\text{m}$. Linear scale around zero and logarithmic scale elsewhere.

The evolutions of maximum temperature and pressure do not show significant differences between the two kinetic schemes. The maximum temperature obtained at the end of the third pulse with the PLASMA-LU kinetic scheme is around 200 K lower than the one obtained with the LU13 one. However, at the end of the simulation time, this difference is reduced to only 30 K. The largest differences can be seen on the mean heat release rate curves. The first discharge triggers stronger endothermic reaction when using the PLASMA-LU kinetic scheme, due to the larger number of possible dissociative reactions taken into account in the mechanism. The second pulse, which with the LU13 kinetic scheme caused a weakly positive mean heat release rate, does not trigger a global exothermic reaction when using the PLASMA-LU mechanism. Despite these differences, the behavior of the kinetic scheme to the third pulse is globally identical.

This suggests that the LU13 kinetic scheme is sufficient for these conditions, since it contains already the species and reactions responsible for the kinetics at temperatures typical of NRP discharges. For instance the oxygen dissociation is already taken into account. At the same time, other dissociation mechanisms, like the nitrogen one, which is known to be of leading order for equilibrium plasmas, is weakly encountered in this

8. PHENOMENOLOGICAL MODEL FOR NRP DISCHARGES

non-equilibrium plasma condition.

Species profiles (Fig. 8.38) at the end of the third discharge confirm the differences between the PLASMA-LU and the LU13 kinetic scheme: the species profiles for the

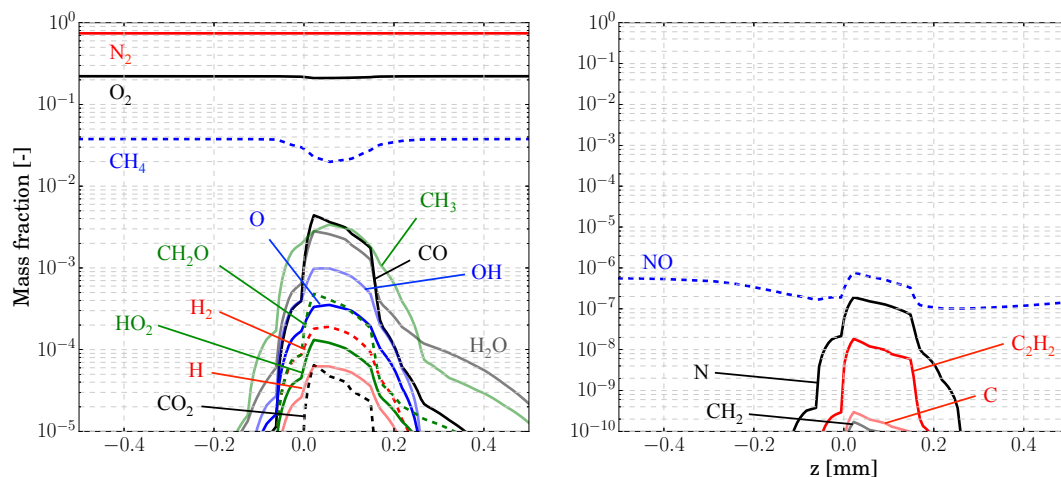


Figure 8.38: Species profiles at the end of the third discharge. Left: common species between LU13 and PLASMA-LU kinetic scheme. Right: additional species present using PLASMA-LU kinetic scheme. Logarithmic scale.

species present in both mechanisms are very similar to the ones of Fig. 8.24. The PLASMA-LU additional species (right side) have a very low concentration, with mixture fractions always below 10^{-5} . A dissociation of nitrogen is present, but with a N concentration very low when compared to equilibrium plasmas [see for example [Collin-Bastiani et al., 2018](#)]. This confirms that the influence of the species typical of the plasma phase is very low and not of leading order for the final state of the gas which will merge to the main flame in plasma-assisted combustion.

However, it is not taken here into account the ultrafast O_2 dissociation directly caused by the electrical discharge. Its impact on the gas temperature and chain-branching of chemical reactions has been found to be not negligible, as shown by [Castela et al. \[2016\]](#). This has to be taken into account in future work.

8.5 Few words about CPU time

It has been shown that ARC mechanism is more accurate to simulate NRP discharges. However, the higher number of species transported, as well as the heavier source terms computation, makes them quite more expensive in CPU time. As an example, Tab. 8.3 summarizes the CPU time needed to perform 0.5 ms of physical time on 15 nodes (360 CPUs) using the CERFACS in-house cluster NEMO. The LU13 kinetic scheme demands

Table 8.3: CPU time for different kinetic schemes.

	BFER	LU13	PLASMA-LU
CPU hours	850	1325	1490

55 % additional CPU time when compared to the BFER one, while the PLASMA-LU demands up to 75 % additional CPU time. In complex configurations, this difference can become even larger due to the different needs the kinetic schemes can have (i.e. mesh size). This explains our choice to continue the study with the simpler BFER mechanism, keeping in mind the limitations shown in this chapter.

8.6 Conclusion

A phenomenological model for NRP discharges has been developed and validated in this chapter. The model is built following experimental data provided by KAUST, as well as experimental observations. The parametrization of the model is strongly dependent on the final result desired (especially regarding whether or not the mixture ignites) and on the kinetic scheme used. The 2-step BFER mechanism has been found to be suitable for NRP discharges applications, but can lead to unphysical ignition due to its underestimation of the autoignition time. On the contrary, the LU13 kinetic scheme is a good candidate for plasma-assisted combustion due to its very good behavior when compared to a new kinetic scheme specifically built to include the plasma phase.

The most sensitive parameter is the size of the energy deposit, since it is directly linked to the source term responsible for the temperature increase. The other discriminating parameter is whether the mixture ignites or not, since the resulting fluid has a completely different behavior if this happens. Experimental re-ignition has been observed. Numerically, depending on the kinetic scheme used and on the energy deposit size, ignition does not always happen.

The final parameters chosen here are kept constant for all kinetic mechanisms used and are a compromise which can be improved when choosing to focus on a single mechanism (the LU13 one seems a good candidate for further studies). The phenomenological model parameters are the following:

- Repetition frequency of the pulse: $f_p = 30$ kHz.
- Total power of the plasma: $P_p = 40$ W. Energy supplied by each plasma discharge: $E_p = 1.3$ mJ.
- Time duration of the plasma discharges: $\Delta t_p = 10$ ns.
- Cylindrical shape, with a Gaussian distribution in the plane normal to the plasma channel axis. Gaussian FWHM: $500 \mu\text{m}$.
- Three consecutive discharges moving at the mean azimuthal velocity of the flow. After three discharges a random jump is applied to change the azimuthal position of the following discharge and the process repeats.

Chapter 9

LES of plasma assisted combustion for a premixed swirl-stabilized burner

Contents

9.1	LES of the PACCI burner with NRP discharges	197
9.1.1	LES using the BFER 2-steps global chemistry	197
9.1.2	Impact of the kinetic scheme: LES using the LU13 ARC chemistry	211
9.1.3	Few words about CPU cost	221
9.1.4	Concluding remarks	222
9.2	Acoustically pulsating the PACCI burner with NRP discharges	222
9.2.1	Dynamic response of the PACCI burner	222
9.3	Conclusion	232

In this chapter the phenomenological model developed in chapter 8 is applied to the LES of the PACCI configuration performed in chapter 7 to perform the first LES simulations of plasma assisted combustion.

The model has been first applied to the cases without acoustic forcing, which are presented in section 9.1. Here the influence of the use of NRP discharges on the flame shape and dynamics is analyzed. Moreover, the influence of the kinetic mechanism is evaluated.

Section 9.2 presents then an LES of the PACCI configuration when applying an acoustic forcing and NRP discharges simultaneously. The role of the NRP discharges on the flame dynamics is investigated.

9.1 LES of the PACCI burner with NRP discharges

9.1.1 LES using the BFER 2-steps global chemistry

9.1.1.a Numerical setup

The numerical simulation has been run starting from the reacting simulation presented in subsection 7.3.2 and share with it the entire numerical setup, except for the viscos-

9. LES OF PLASMA ASSISTED COMBUSTION FOR A PREMIXED SWIRL-STABILIZED BURNER

ity law and for the mesh used. The viscosity law has been switched indeed from the Power Law to the D'Angola one due to the high temperature reached, as explained in chapter 8. Due to the application of NRP discharges, the mesh had to be refined indeed in the discharge zone. Following the needs defined in chapter 8, a new mesh, which will be called M3 in the following, has been generated. A schematic is presented in Fig. 9.1. A very fine mesh is used in the discharge zone, with a characteristic cell size of $50 \mu\text{m}$, and a coarsening is applied in the surrounding area until reaching a cell size of $100 \mu\text{m}$ in correspondence of the white dashed line of Fig. 9.1. This permits to correctly capture the plasma channel and the shock wave early development. The

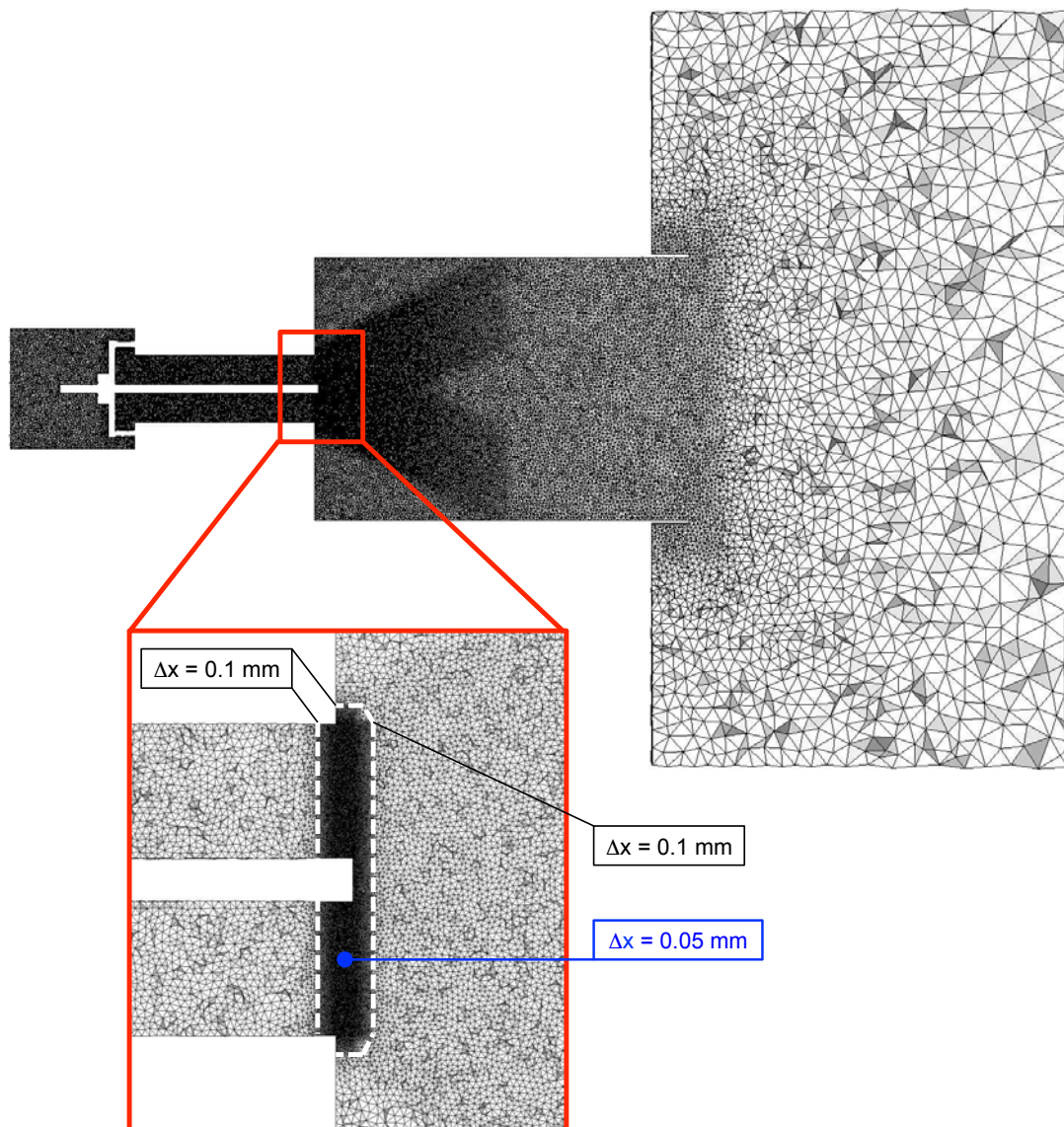


Figure 9.1: 2-D cut of the mesh M3 in the plane $z = 0$.

entire zone outside the white dashed line features the same cell sizes of the mesh M1 (Fig. 7.4). This modification in cell size causes an important increase in the mesh size,

which is of 34M of cells for the mesh M3.

The time step has been fixed to 1×10^{-8} s, equal to the deposit time of the NRP discharges. This is the value also used in the test cases of chapter 8. Such a small time step is necessary for the energy deposit and the shock wave early development. Once this critical phase has passed, the time step could be increased up to the one corresponding to $CFL = 0.7$. This is a possible path for efficiency improvement which can be studied in the future.

The NRP discharges are applied according to the final parameters listed in section 8.6. Their spatial position is shown in Fig. 9.2, where a zoom on the NRP discharges zone is represented. On the left hand side, a cut at $z = 0$ is presented. The white dashed line revolution surface around the x axis is visible on the right hand side and represents the surface on which the NRP channel axis always lies. This surface extends from the edge of the top end of the central rod to the edge formed by the injection tube and the chamber faceplate. The azimuthal motion of consecutive discharges

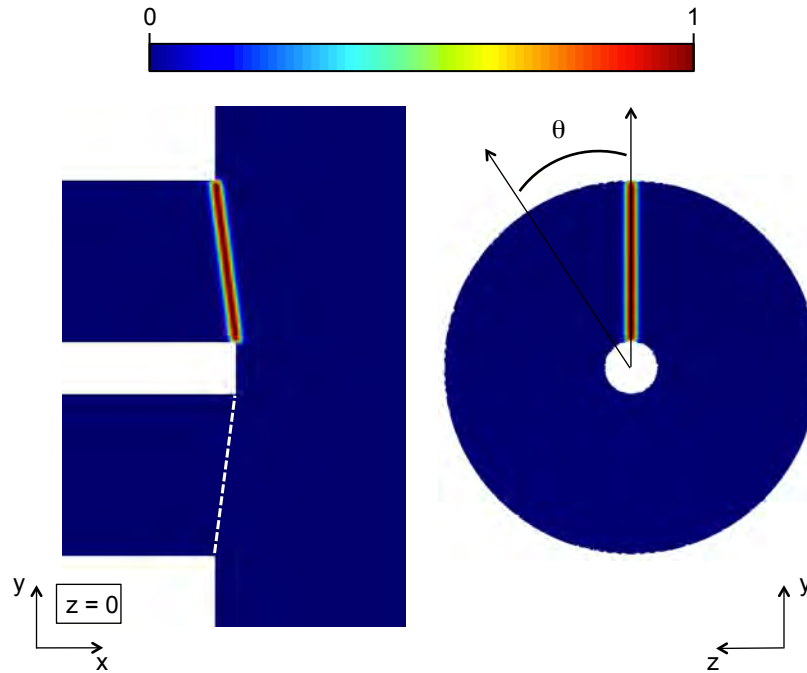


Figure 9.2: Schematic of the NRP discharges position. Fields of energy deposit non-dimensionalized by their maximum value.

is represented by means of the angle ϑ . If the mean azimuthal velocity in the discharge zone is about 5 m/s, considering the arc circle that the fluid travels between two consecutive discharges (at a frequency of 30 kHz), the jump in ϑ between two consecutive discharges has been fixed to 1.5° . After three consecutive discharges a random jump with $0 < \vartheta < 180^\circ$ is applied, in order to have a statistically random motion of the discharges with the swirling flow. It has been arbitrarily decided to place the first NRP discharge at $\vartheta = 0^\circ$.

9. LES OF PLASMA ASSISTED COMBUSTION FOR A PREMIXED SWIRL-STABILIZED BURNER

As it will be shown, the energy deposit leads in some cases to very high temperatures, which are not well handled by the BFER mechanism. For this reason, in order to help the code to manage the resulting source terms, chemical sub-iterations are used around the energy deposit. This consists in computing the chemical source term using a smaller time step and n sub-iterations during a single simulation iteration.

Due to the heavier mesh and to the small time step, the current LES has a high CPU cost. Because of this, only 7.5 ms of physical time have been simulated, corresponding to one tenth of one convective time. After the first 3.75 ms the effects of NRP discharges on the flame are indeed already visible. The resting 3.75 ms are used to average the fields and extract mean solutions. The simulation time is not enough to have statistically converged data and a longer simulation time is desirable for further studies.

9.1.1.b Impact of the NRP discharges on the flame shape and dynamics

Starting from an instantaneous solution from the case without plasma discharges, the physical time is reset to zero and the NRP model is activated. The effect of the NRP discharges on the fluid is explained in Fig. 9.3 and 9.4, where snapshots of temperature and heat release rate are shown in the discharge zone on a plane at $z = 0$.

Both figures are separated in two parts by means of a vertical black line. On the left hand side of the line the snapshot corresponds to the end of an NRP pulse, which number is indicated. On the right hand side, intermediate states between two consecutive pulses are represented: the snapshots have been taken at 1/3 and 2/3 of the time interval between two pulses. The first pulse heats up the gas in the discharge zone, but it is not sufficient to ignite the fresh gases mixture. This is highlighted by the absence of heat release rate in the discharge zone immediately after the discharge as well as after a certain delay. The channel of heated gases diffuses and starts to be slowly convected away.

The second discharge heats up the fluid ulteriorly in this zone, where the mixture reaches temperatures higher than 2000 K, and leads to ignition. This is visible on the snapshots of the heat release rate fields (Fig. 9.4): no heat release rate is present at the end of the energy deposit but a trace of it can be found when looking at the next snapshot. A small flame kernel is created near the electrode.

The third pulse happens in an already heated fluid and leads to a further increase of temperature which causes ignition in a larger zone of fluid. The maximum temperature reached in this case is about 5000 K.

We can see here a first difference from the test case presented in chapter 8 where, with the calibrated parameters, ignition always happened at the third pulse and the final temperature was around 3000 K. This is due to the fact that the initial temperature of the fluid in the discharge zone is not 300 K everywhere, due to hot gases recirculation and due to heating caused by the electrode, which is treated as isothermal. Contrarily to the test case, in the PACCI configuration the discharge can happen in cold fresh gases at 300 K, hotter fresh gases, burnt gases at around 1800 K or a mixture of them. Since the model is independent of the gas composition and temperature in the

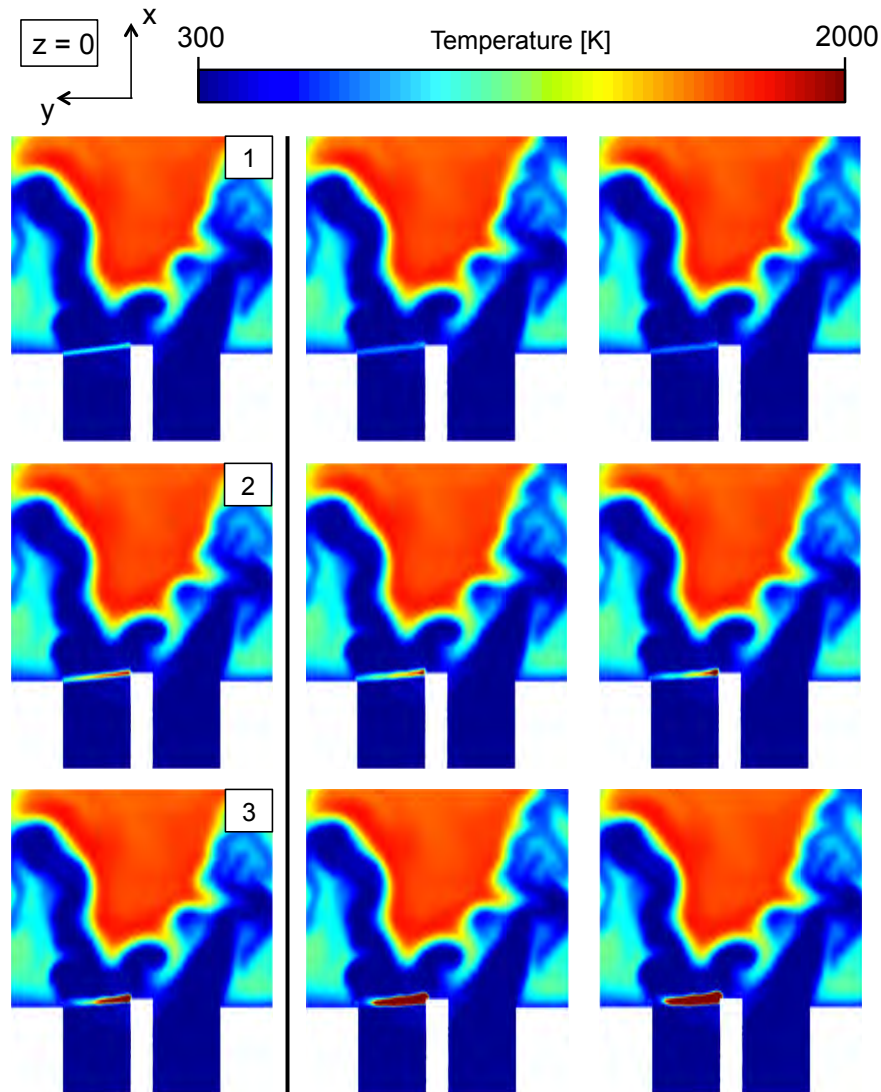


Figure 9.3: Snapshots of the temperature field in the discharge zone on the plane $z = 0$ for the first 3 discharges, with intermediate states. The number in the white box indicates the overall discharge number.

discharge zone, for each one of these cases the final temperature is different. Choosing a discharge position varying in a random way, implies to consider the fresh cold gases as the reference scenario. Another choice could have been made and a parametric study could be made in the future to have an idea of the sensitivity to this parameter.

In order to visualize how the hot flame kernel generated by the series of pulses is convected towards the flame, as well as to visualize the azimuthal motion of the discharges, another series of snapshots is presented in Figs. 9.5 and 9.6. In Fig. 9.5 snapshots of the temperature fields at the end of each pulse in a plane at $z = 0$ in the discharge zone are shown. On the top row, the three snapshots already shown on

9. LES OF PLASMA ASSISTED COMBUSTION FOR A PREMIXED SWIRL-STABILIZED BURNER

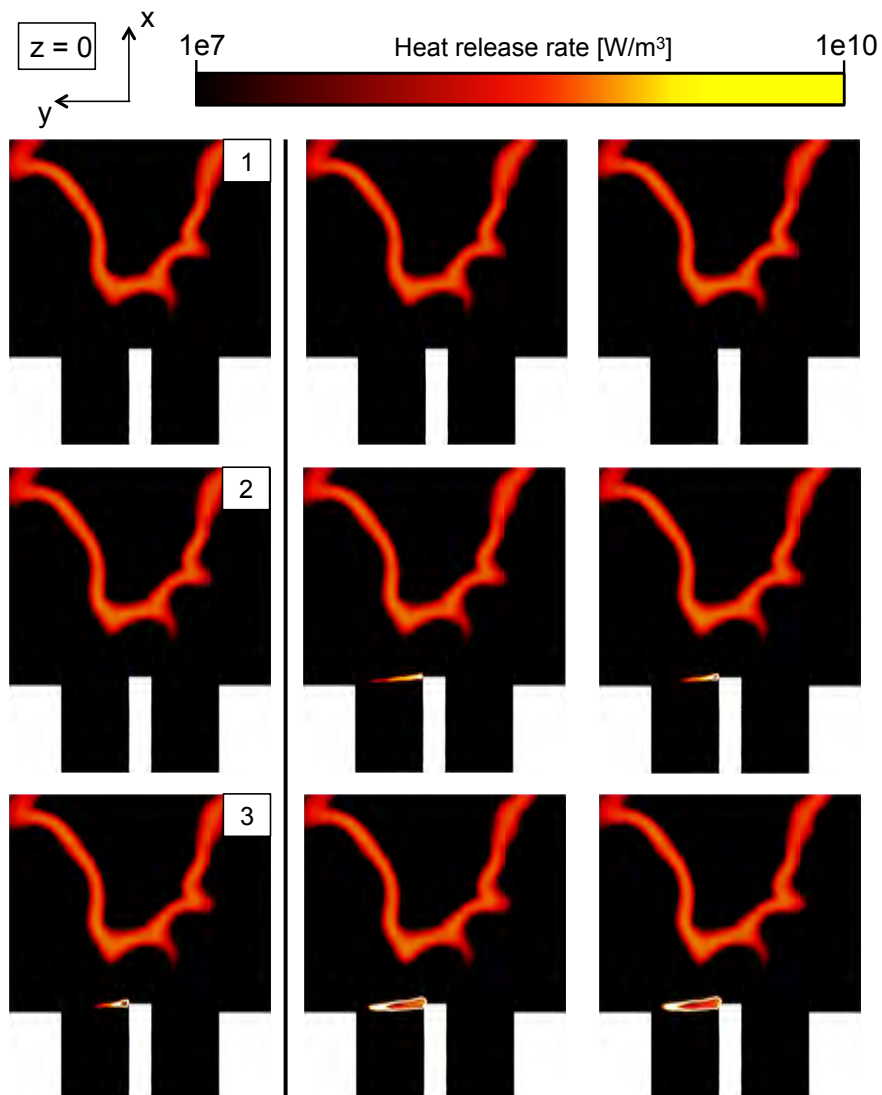


Figure 9.4: Snapshots of the heat release rate field in the discharge zone on the plane $z = 0$ for the first 3 discharges, with intermediate states. Logarithmic scale. The number in the white box indicates the overall discharge number.

the left hand side of Fig. 9.3 can be recognized. The mid and bottom line show the next NRP discharges. If one looks at the left side of the entire series of snapshots, the evolution of the hot pocket of burnt gases generated by the first three pulses can be tracked. The hot pocket is slowly convected downstream towards the main flame by the flow. Starting from the fifth pulse, a new hot pocket appears on the right side of the snapshots. This is the result of a new series of pulses which takes place at a different azimuthal position and can not be viewed on the plane shown in Figs. 9.5 and 9.7.

This is shown in Fig. 9.6, where the temperature field is extracted on the discharge axis revolution surface around the x axis. After the first three discharges (top row), a jump in the angle ϑ is applied. The second series of three consecutive discharges (mid

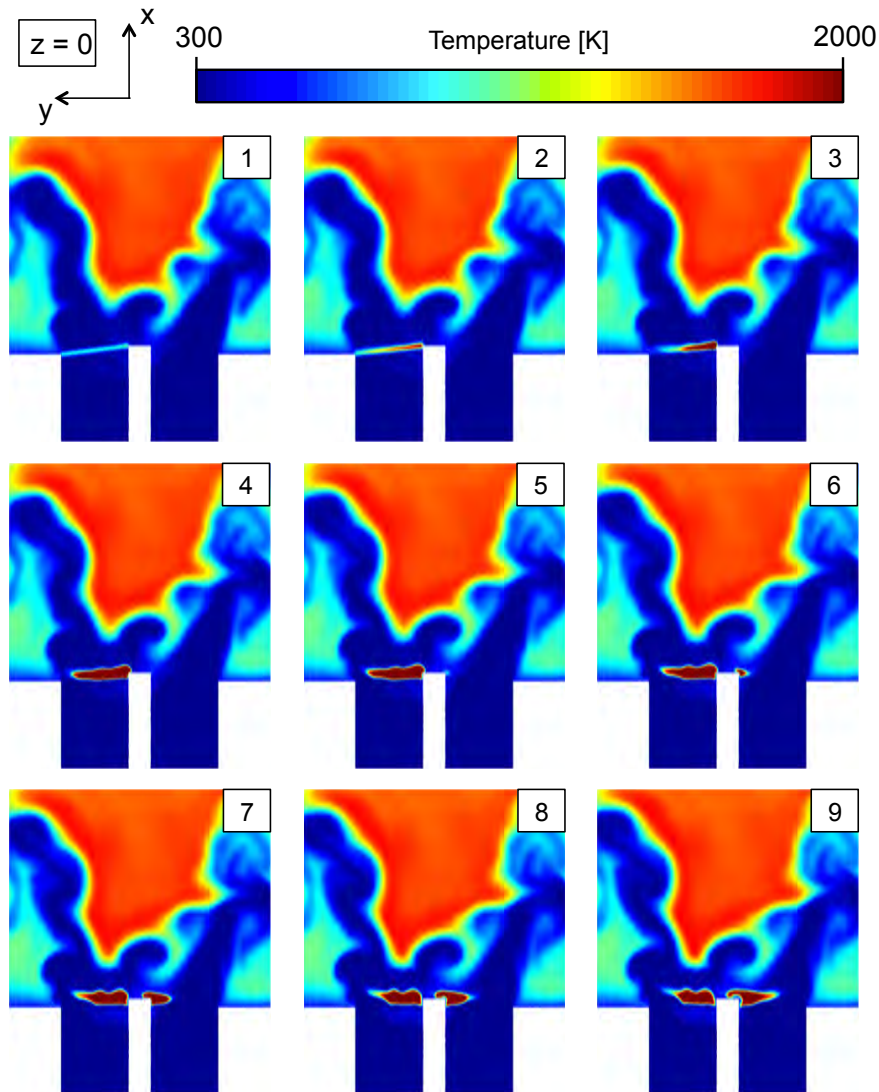


Figure 9.5: Snapshots of the temperature field in the discharge zone on the plane $z = 0$ for the first 9 discharges. The number in the white box indicates the overall discharge number.

row) takes place in a completely different position, having however a similar effect on the fresh gases mixture. The new hot pocket of hot gases is partially present on the plane $z = 0$, explaining the hot pocket visible on the right hand side of the snapshots of Fig. 9.5. The jump in angle ϑ is applied again for the next series of consecutive discharges (bottom row). Then the process repeats.

The random nature of the jump in angle ϑ is also visible: in this case it is of around 160° between the first and second series of pulses and of around 60° between the second and third one.

Ignition (and the resulting hot kernel) happens generally in the area close to the pin steel electrode rather than close to the chamber faceplate. This is due on one side to

9. LES OF PLASMA ASSISTED COMBUSTION FOR A PREMIXED SWIRL-STABILIZED BURNER

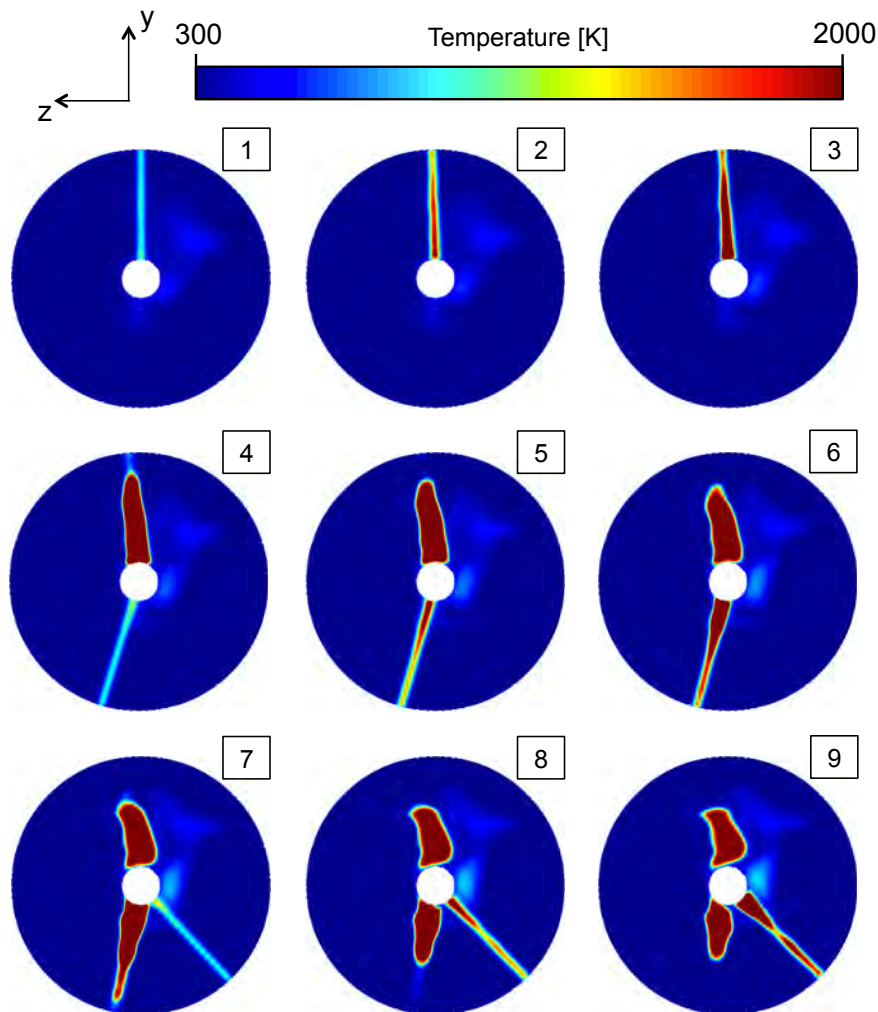


Figure 9.6: Snapshots of the temperature field on the discharge axis revolution surface around the x axis for the first 9 discharges. The number in the white box indicates the overall discharge number.

the minor axial velocity in this zone: the hot gases move less between one pulse and the next one. At the same time, being the discharge position movement fixed in terms of angle, the arc cord between two consecutive channel axis is smaller close to the pin steel electrode: this causes a greater overlap of the energy deposit channels.

The process just described for few discharges has a "cumulative effect" when continuing to applying plasma pulses to the system. The discharges enrich the zone near the top end of the rod with small flame kernels filled by hot gases. These small kernels merge between them and, later on, with the main flame. The phenomenon is described in Fig. 9.7 with snapshots of the temperature field in the combustion chamber. After 15 pulses, the kernels are still separated between them. On the contrary, a local merging of the hot pockets is already visible after 30 pulses. It is after about 60 pulses that the merging with the main flame takes place. After this moment, the flame always stays

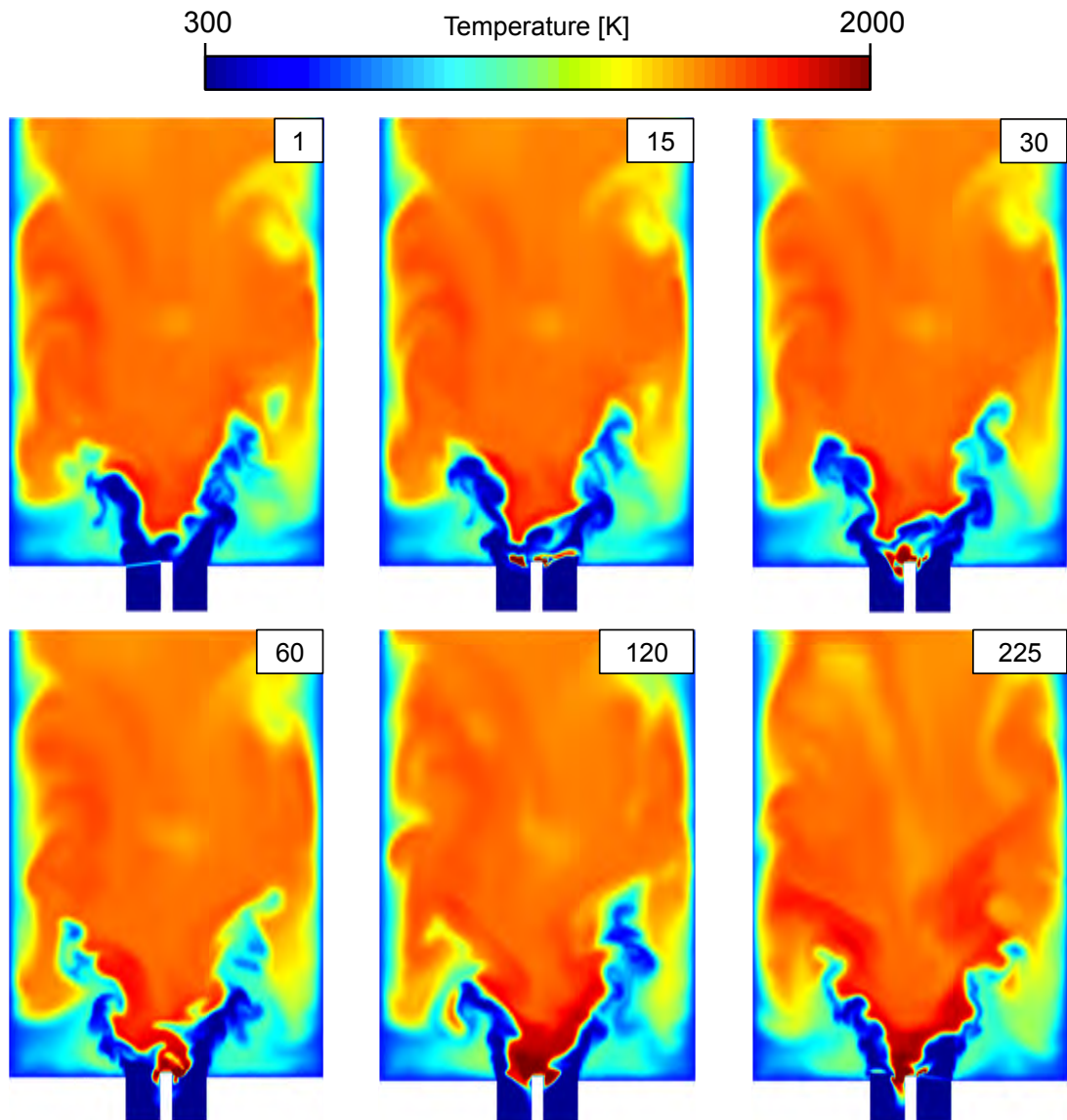


Figure 9.7: Snapshots of the temperature field after a different number of NRP pulses. Cut of the combustion chamber with a plane at $z = 0$. The number in the white box indicates the overall discharge number.

attached to the rod and the alternating lifted-attached movement described in Fig. 7.27 is completely suppressed. This is visible by means of the fields extracted after 120 and 225 pulses (which corresponds to 7.5 ms of physical time).

The NRP discharges change notably the flame shape and dynamics. They act indeed as a flame holder, providing to the fresh gases the conditions necessary to combustion. The flame stabilization seems in this case to be not only due to the central recirculation zone but also to the energy source which is supplied to the flame by means of the NRP discharges. The effect that the plasma has on the fluid is, in this case, only of thermal nature, since the kinetic scheme used does not contain neither any species typical of

9. LES OF PLASMA ASSISTED COMBUSTION FOR A PREMIXED SWIRL-STABILIZED BURNER

the plasma phase nor any species produced by high temperature dissociation. Moreover, no significant mechanical effect caused by the pressure waves which propagate as a result of the ultrafast gas expansion is found. An effect is visible upstream of the discharge position, since the pressure wave tends to modify the local velocity, which is nevertheless unchanged in its mean value. Downstream, the velocity modification is dissipated very fast and does not have a significant effect on the flame. Indeed the propagation of the acoustic wave through the flame generates a fluctuation of the heat release rate which is very small compared to its mean value. Moreover, the acoustic wave which reaches the flame is quickly dissipated in small vortices, not strong enough to perturb significantly the flame surface.

Such change in the flame stabilization position, towards the discharges zone, was also found in literature regarding experimental work. See for example [Moeck et al. \[2013\]](#) and [Lacoste et al. \[2013b\]](#).

9.1.1.c Mean fields

The flow pattern is illustrated in Fig. 9.8 where the time and azimuthal averaged field of axial velocity is shown, compared to the one obtained with the BFER kinetic scheme. Streamlines are superimposed in white: the flow pattern changes drastically, with a central recirculation zone which is not attached anymore to the top end of the central rod. The recirculation zone is completely lifted instead, pushed downstream by the gas acceleration due to the heating of the mixture in the discharge zone: this zone between the top end of the electrode and the central recirculation zone is fully filled by hot gases coming from the NRP discharges. Downstream, the recirculation zone closes notably upstream when applying NRP discharges. This could be linked to the insufficient averaging time, as it will be shown in the following. The corner recirculation zones are on the contrary similar in both cases.

This flow pattern shows that, in this case, the central recirculation zone is not anymore the only responsible for flame stabilization, as it is usually found in swirl-stabilized configuration. This is confirmed by analyzing Fig. 9.9, where time and azimuthal averaged fields of temperature and heat release rate are presented.

The temperature field of Fig. 9.9 shows that there is a zone (bounded by the yellow line) situated at the top end of the rod in which the gas temperature is always higher than the adiabatic flame temperature. This denotes necessarily that the gas which fills this zone comes from the pockets of hot gases generated by the NRP discharges. The downstream end of this very hot zone is situated at $x/D_E^{inj} \approx 0.65$. Only downstream this axial position the central recirculation zone (white line) can exist, filled by combustion products (at a temperature lower or equal the adiabatic flame one). The resulting flame is a V-shaped flame stabilized both by the hot gases generated by the NRP discharges and by the central recirculation zone.

The heat release rate field shows that the flame root is more stable and crosses the burner axis only very close to the rod, contrarily to the case without NRP discharges. Heat release is obviously not zero in the NRP discharge zone, where it takes high values due to the high temperatures reached in this zone. The heat release rate is

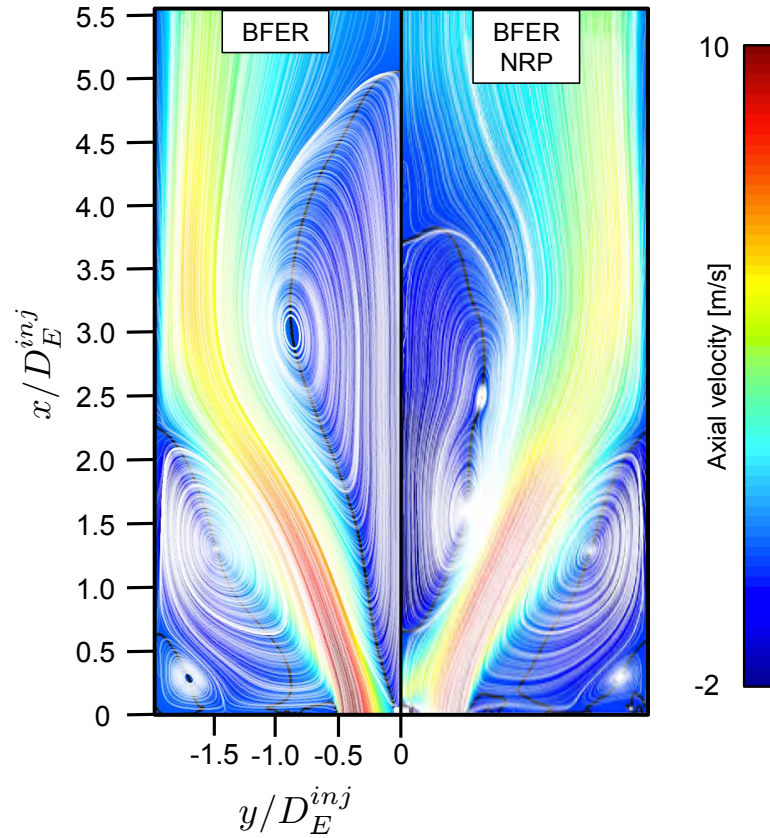


Figure 9.8: Mean flow pattern in the combustion chamber. White: time and azimuthal averaged streamlines. Black line: zero axial (x-axis) velocity iso-line. Comparison between LES without and with NRP discharges.

quite higher when applying NRP discharges, due to two different causes. First, the very high temperatures reached due to the energy deposit heat up the gases and cause an increase in reaction rates. Second, the flame is less dispersed in space so that the averaging procedure leads directly to higher values. This is another proof that the flame moves less.

No significant difference is seen on flame length. This could be linked to the insufficient averaging time, as shown in the following.

Analyzing now Fig. 9.10, one can notice how the field of RMS axial velocity is characterized by higher values in the discharge zone, due to the gas acceleration through the flame kernels which form in this zone.

Interesting differences can be found when looking at the RMS temperature fields. As expected, the RMS temperature takes higher values in the discharge zone, when compared to the case without NRP discharges: this is an obvious effect of the intermittent gas heating in this area. Moreover, looking at the main flame zone, it can be seen how, using NRP discharges the zones in which the RMS temperature is high are limited to the shear zones. On the contrary, the central zone is characterized by low values, confirming a limited movement of the flame root. This might suggest a more

9. LES OF PLASMA ASSISTED COMBUSTION FOR A PREMIXED SWIRL-STABILIZED BURNER

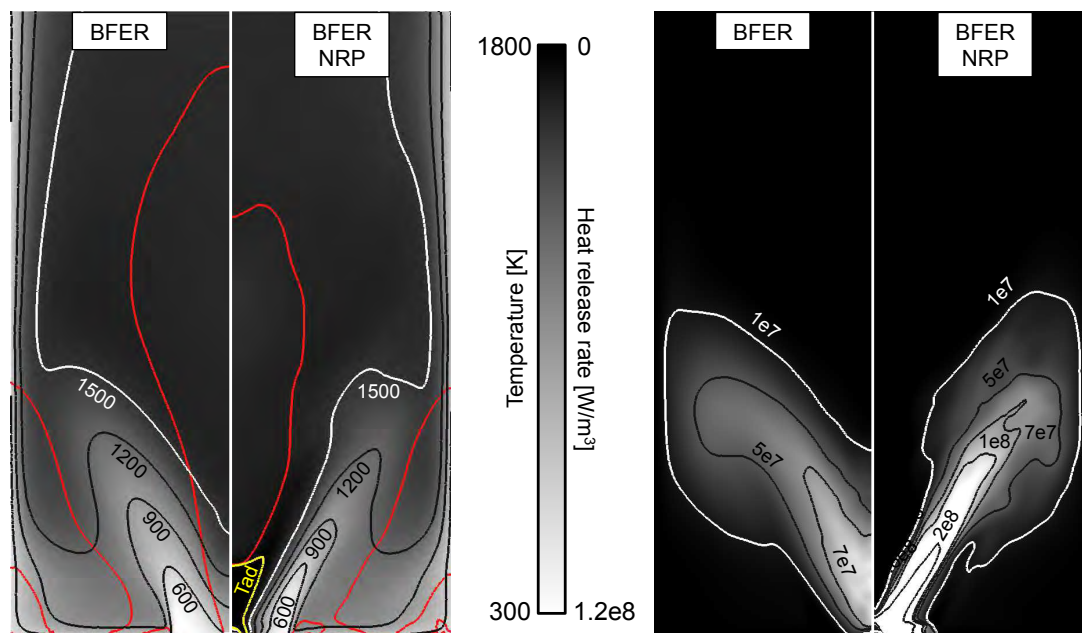


Figure 9.9: Time and azimuthal averaged flow field of temperature (left) and heat release rate (right) in the combustion chamber. Comparison between LES without and with NRP discharges. Yellow line: isoline at adiabatic flame temperature; red line: isoline at zero axial velocity.

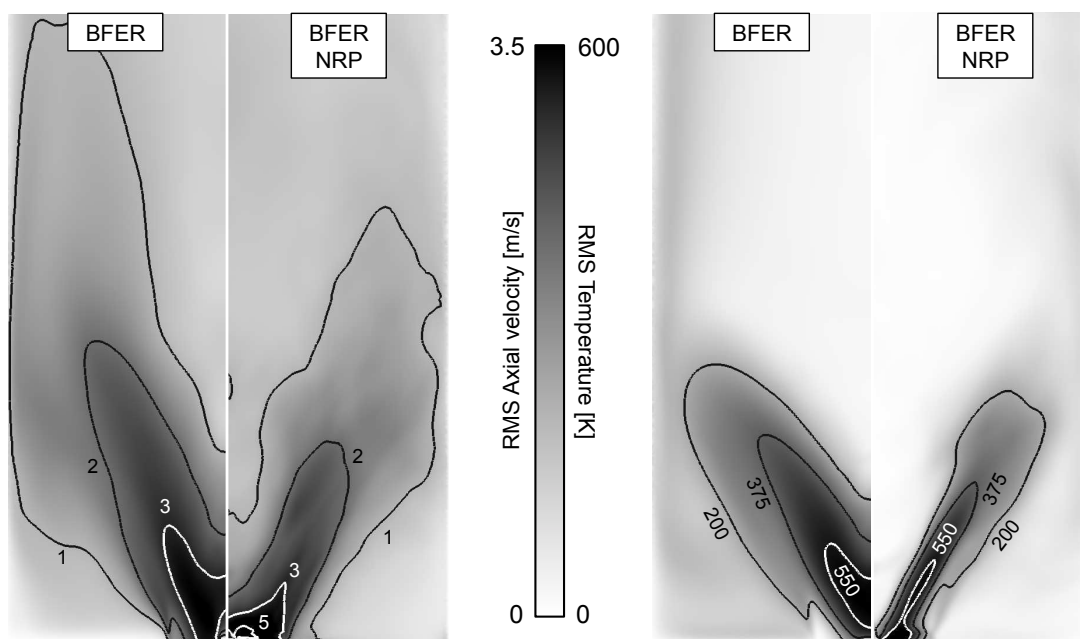


Figure 9.10: Time and azimuthal averaged flow field of RMS axial velocity (left) and RMS temperature (right) in the combustion chamber. Comparison between LES without and with NRP discharges.

stable flame and will be analyzed in the following.

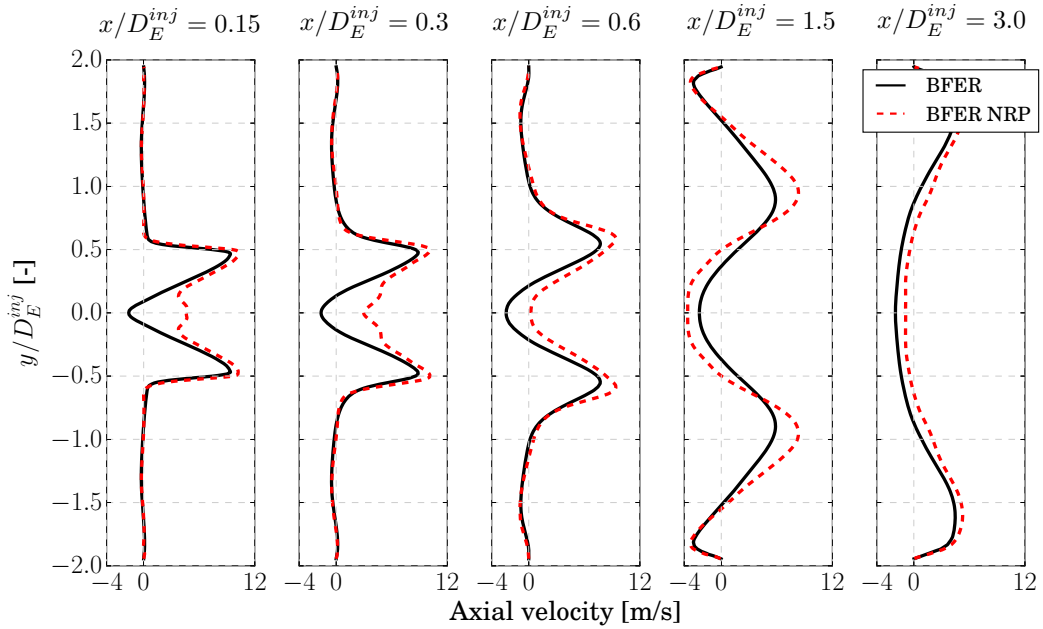


Figure 9.11: 1D axial velocity mean profiles at different axial positions. Comparison between LES without and with NRP discharges.

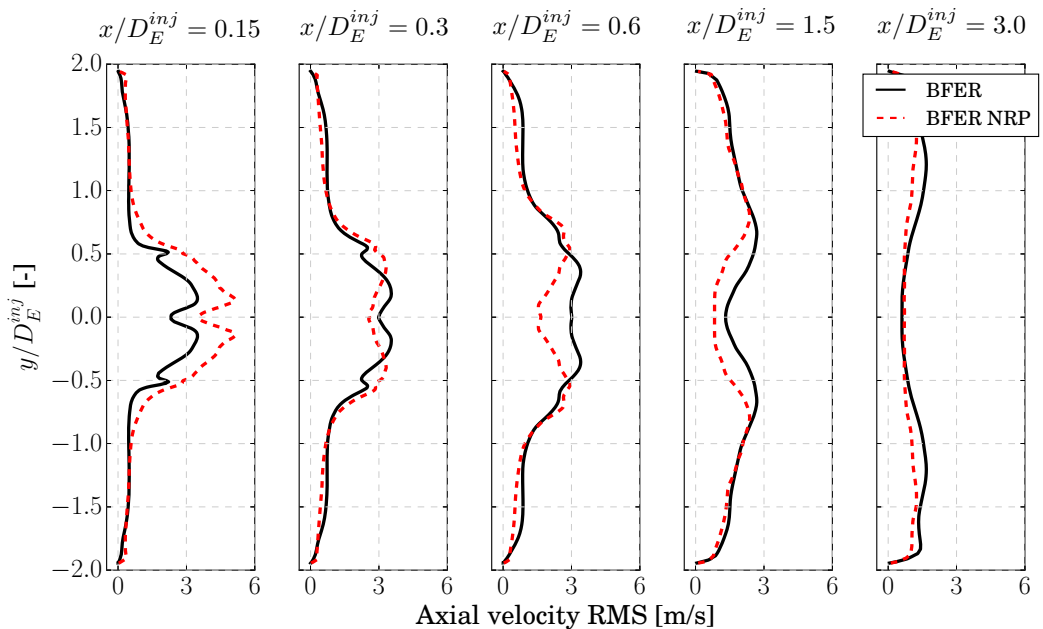


Figure 9.12: 1D axial velocity RMS profiles at different axial positions. Comparison between LES without and with NRP discharges.

9. LES OF PLASMA ASSISTED COMBUSTION FOR A PREMIXED SWIRL-STABILIZED BURNER

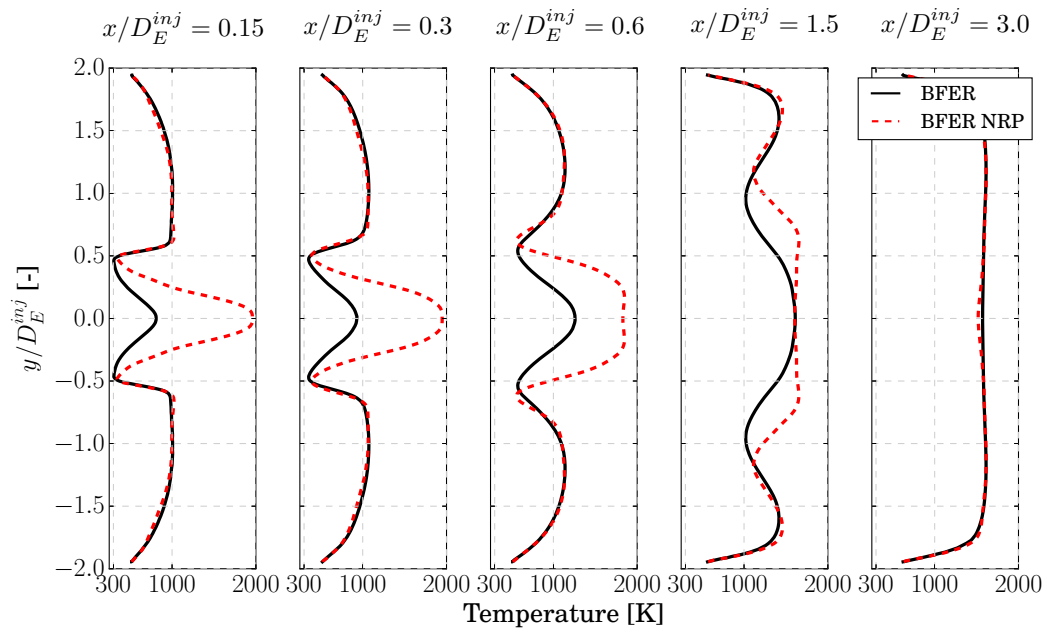


Figure 9.13: 1D temperature mean profiles at different axial positions. Comparison between LES without and with NRP discharges.

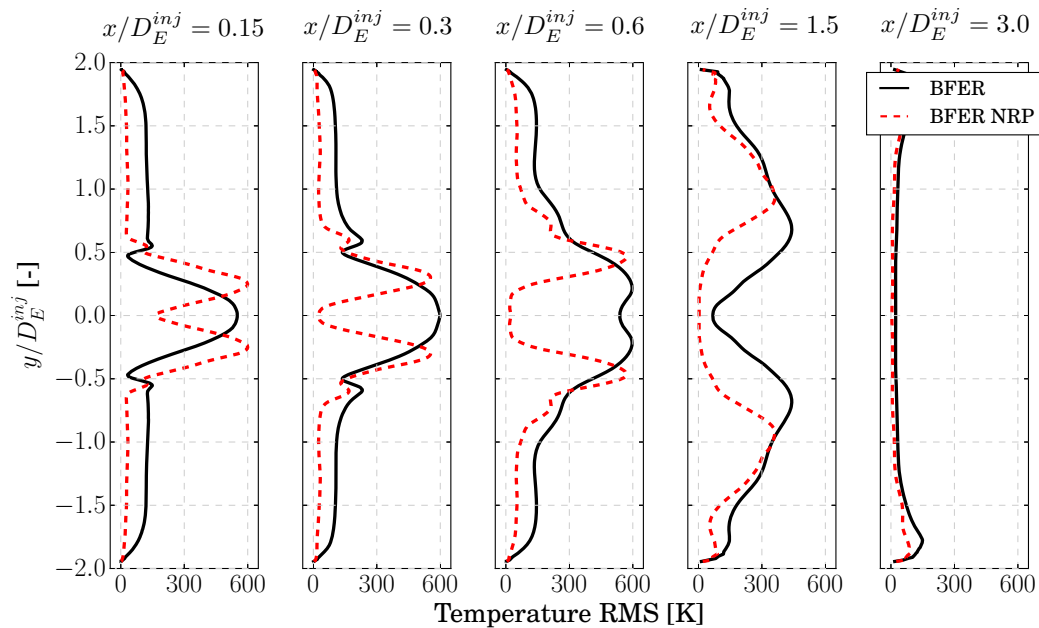


Figure 9.14: 1D temperature RMS profiles at different axial positions. Comparison between LES without and with NRP discharges.

The effects of the NRPs are also evaluated quantitatively by means of 1D profiles at 5 different axial positions, corresponding to $x/D_E^{inj} = 0.15, 0.3, 0.6, 1.5$ and 3.0 (Fig. 7.36). Profiles of mean and root-mean-square values of axial velocity and temperature are shown respectively in Figs. 9.11, 9.12, 9.13 and 9.14.

The slight increase in axial velocity is caused by the NRP discharges, as well as the already mentioned increase in RMS axial velocity. The temperature in the zone between the top end of the rod and the central recirculation zone reaches 2000 K, about 200 K higher than the adiabatic flame temperature. The overall reduction of RMS temperature is also evident, except from the shear zone.

This work did not analyze the inverse transient phase, when the NRP generation system is switched off. The transition from a flame stabilized by means of NRP discharges to a flame stabilized again by the central recirculation zone generated by the swirling flow can be the subject of further studies. This has to be investigated in order to be sure that the flame is able to come back to its initial configuration and is not blown off.

9.1.2 Impact of the kinetic scheme: LES using the LU13 ARC chemistry

The NRP discharges model has been activated also in the numerical simulation run with the LU13 mechanism, in order to evaluate the effect of the differences between the two kinetic schemes observed in chapter 8 on the PACCI configuration.

9.1.2.a Numerical setup

The numerical simulation has been run starting from the reacting simulation presented in subsection 7.3.3 and share with it the entire numerical setup, except for the mesh used. Similarly to the mesh M3, a refinement is applied to the mesh M2 in the discharge zone. The refinement parameters are the same used for the mesh M3 with a minimum cell size of 50 μm . The resulting mesh, which will be called mesh M4, is composed of 39M of cells.

The NRP discharges are applied in the same way as in the LES with the BFER kinetic scheme. The time step used, as well as the physical time simulated are the same one used with the BFER mechanism.

Due to the better behavior that the LU13 kinetic scheme has at high temperatures, no chemical sub-cycling is necessary in this case.

9.1.2.b Impact of the NRP discharges on the flame shape and dynamics

Starting from an instantaneous solution from the case without plasma discharges, the physical time is reset to zero and the NRP model is activated. The effect of the NRP discharges on the fluid is explained by means of Figs. 9.15 and 9.16, where snapshots of temperature and heat release rate are shown in the discharge zone on a plane at $z = 0$.

In this case, the initial fluid state in the discharge zone is different from the one we had when using the BFER mechanism. A branch of the flame with hot gases partially occupy the zone where NRPs take place.

The first pulse heats up the gas in the discharge zone. The portion of the plasma channel which crosses the hot zone is heated, enhancing chemistry and increasing locally the heat released by the flame. Outside of this zone, the fluid heats up slightly, but no

9. LES OF PLASMA ASSISTED COMBUSTION FOR A PREMIXED SWIRL-STABILIZED BURNER

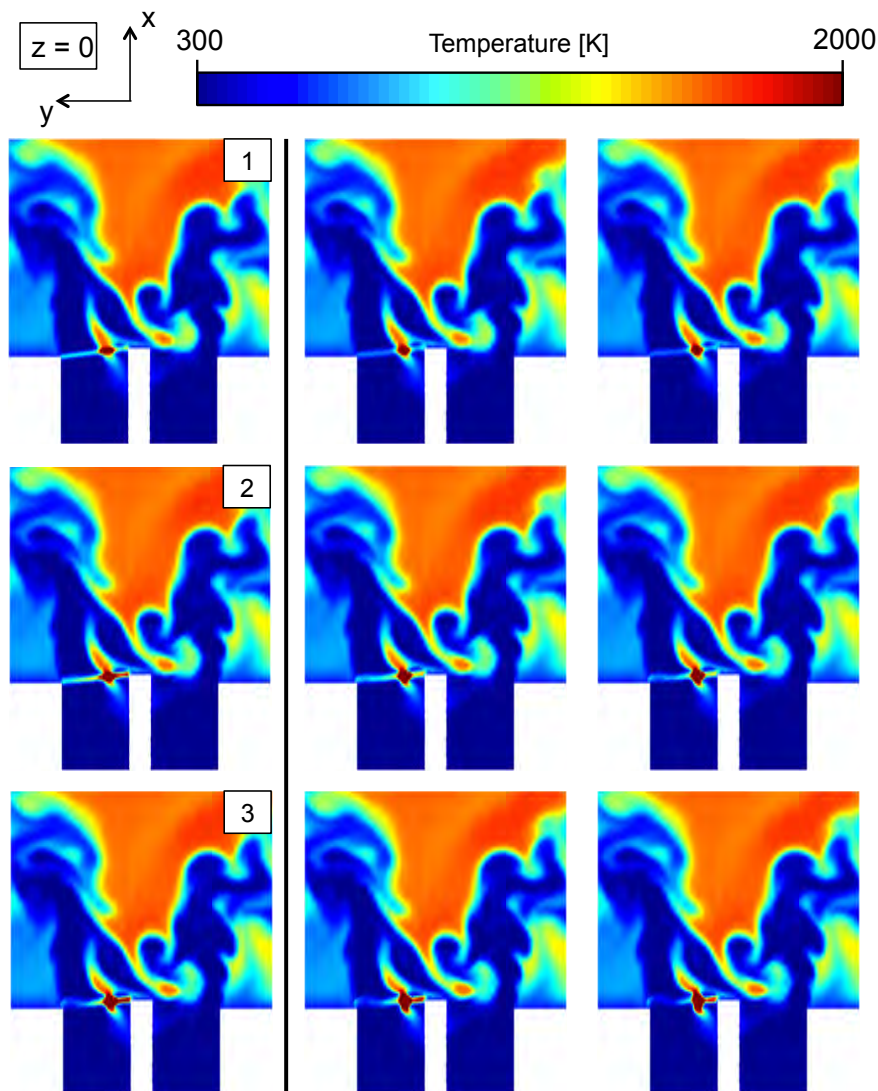


Figure 9.15: Snapshots of the temperature field in the discharge zone on the plane $z = 0$ for the first 3 discharges, with intermediate states. The number in the white box indicates the overall discharge number. LU13 kinetic scheme.

ignition is observed. Here the heated gases diffuse and start to be slowly convected away.

Contrarily to what was seen using the BFER mechanism, the second and third pulse have in this case an effect similar to the first one. They both heat up the fluid in the discharge channel, but an effect on the heat release rate can be seen only in the zone which already contains hot gases. Elsewhere the temperature increase is not sufficient to trigger ignition and the hot gas diffuses while it is convected away. Only in the zone very close to the rod, where the fluid is slightly heated up by the isothermal boundary condition, a weak trace of heat release rate is visible after the third pulse and rapidly vanishes.

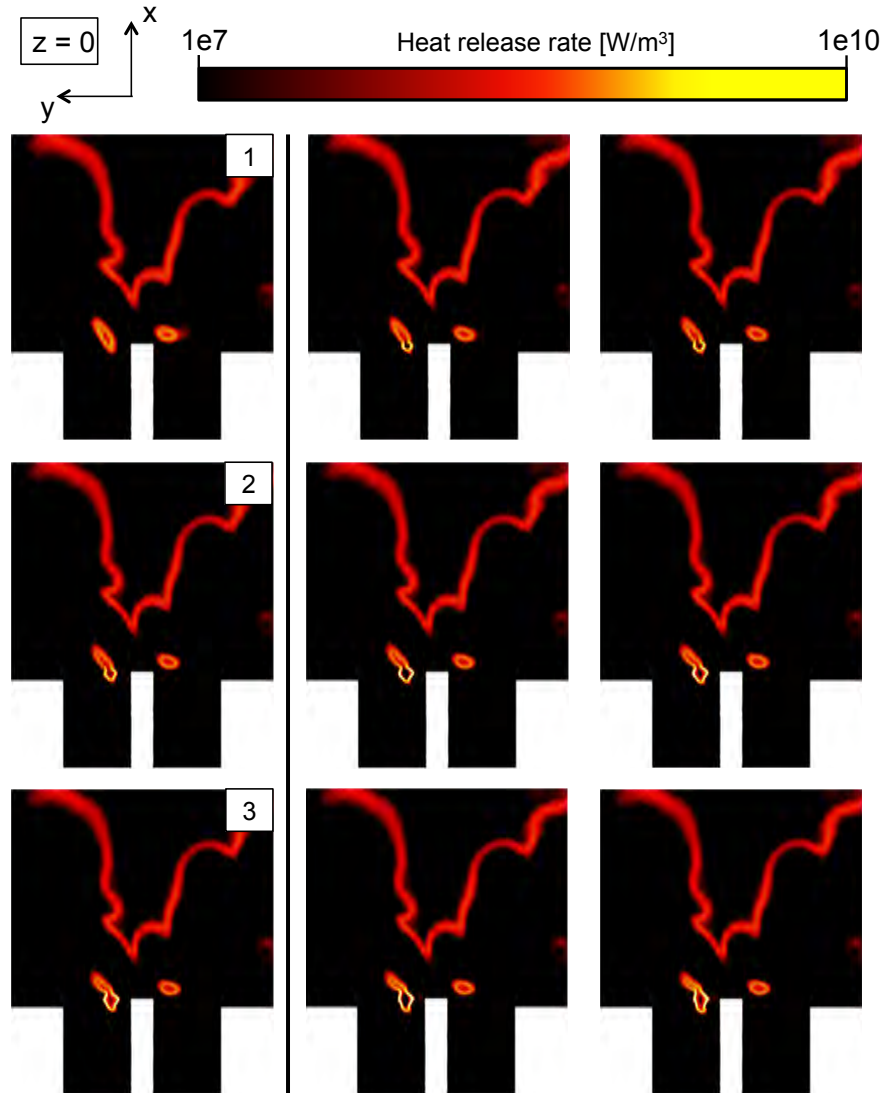


Figure 9.16: Snapshots of the heat release rate field in the discharge zone on the plane $z = 0$ for the first 3 discharges, with intermediate states. Logarithmic scale. The number in the white box indicates the overall discharge number. LU13 kinetic scheme.

This behavior is not surprising when remembering what has been shown in section 8.3 which showed that, when using the LU13 mechanism together with the model parameters tuned with the BFER mechanism, no ignition was observed. It was also shown how, when applying a discharge in an already hot fluid, the maximum temperature was strongly rising, reaching a maximum of over 6000 K. The maximum temperature found in this case is of the same order of magnitude.

This behavior of the model when using the LU13 kinetic scheme introduces a new degree of freedom, with a final state of the fluid strongly dependent on the initial temperature of the gas in which the discharge takes place. When the fluid is cold, the

9. LES OF PLASMA ASSISTED COMBUSTION FOR A PREMIXED SWIRL-STABILIZED BURNER

final state is of pre-heated fresh gases which will be convected towards the main flame. On the contrary, if the fluid is already pre-heated by the main flame or by burnt gases, ignition is triggered.

It appears then that the effect of NRP discharges on the flame is somehow weakened by this mechanism. Similarly to what was observed by using the BFER mechanism,

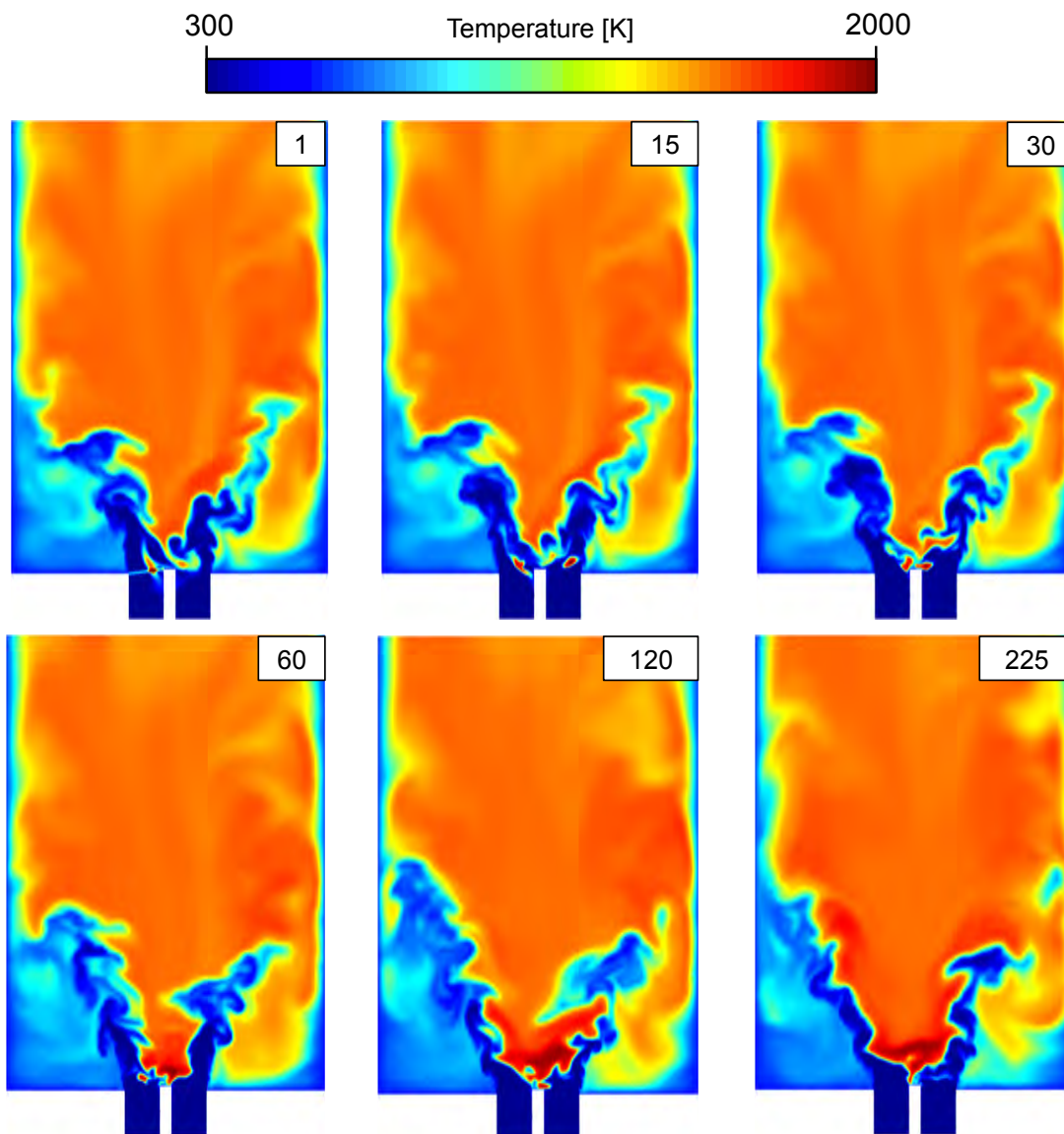


Figure 9.17: Snapshots of the temperature field after a different number of NRP pulses. Cut of the combustion chamber with a plane at $z = 0$. The number in the white box indicates the overall discharge number. LU13 kinetic scheme.

successive plasma discharges enrich the zone near the top end of the rod with pre-heated gases and/or small flame kernels filled by hot gases. The phenomenon is described in Fig. 9.17 with snapshots of the temperature field in the combustion chamber.

The effect on the flame is the same one found when using the BFER mechanism,

but slower and weaker. After 15 and 30 pulses, few kernels are formed, which are still separated between them. It is after about 60 pulses that the merging with the main flame takes place. After this moment, thanks to the continue source of heating represented by the NRP discharges, the flame is anchored close to the rod and the alternating lifted-attached movement described in Fig. 7.27 is completely suppressed. This is visible by means of the fields extracted after 120 and 225 pulses (which corresponds to 7.5 ms of physical time).

It is however noticeable how the anchoring of the flame to the rod is weaker in this case than when using the BFER mechanism, with a flame which stabilizes at the very top end of the rod and is eventually slightly lifted sometimes. Similarly to when using the BFER mechanism, the flame stabilization seems to be not only due to the central recirculation zone but also to the energy source which is supplied to the flame by means of the NRP discharges. The effect that the plasma has on the fluid is, in this case, both of thermal and chemical nature, since the burner zone above the top end of the rod contains high concentration of radicals, as it will be shown in the following.

The mechanical effect due the pressure wave which develops because of the energy deposit is found to be not of first order in this case too.

9.1.2.c Mean fields

The flow pattern is illustrated in Fig. 9.18 where the time and azimuthal averaged field of axial velocity is shown, compared to the one obtained with the BFER kinetic scheme. Streamlines are superimposed in white. The flow pattern shows the same qualitative features using both kinetic scheme, with some quantitative differences. In both cases the central recirculation zone is not attached to the top end of the central rod, but lifted instead. This is the result of the gas acceleration due to the heating of the mixture in the discharge zone. However, the central recirculation zone is less lifted when using the LU13 mechanism, which seems to suggest how the mean acceleration of the gases by the NRP discharges is lower in this case. Downstream, the recirculation zone closes upstream when using the BFER mechanism. The corner recirculation zones are on the contrary similar in both cases.

These differences in flow pattern are analyzed by means of Fig. 9.19, where time and azimuthal averaged fields of temperature and heat release rate are presented.

The temperature field shows that in both cases there is a zone (bounded by the yellow line) situated at the top end of the rod in which the gas temperature is always higher than the adiabatic flame temperature. As already mentioned, this denotes necessarily that the gas which fills this zone comes from the pockets of hot gases generated by the NRP discharges. The extension of this zone is however quite different depending on the kinetic scheme used. When using the LU13 mechanism, the volume occupied by gases hotter than the adiabatic flame temperature is smaller indeed. This confirms what has been mentioned before: the temperature increase caused by the NRP discharges is, in average, lower. The limited extension of the "very hot" zone has an effect on the central recirculation zone, which closes upstream when using the LU13 mechanism (at $x/D_E^{inj} \approx 0.6$). Moreover, the flame is more lifted in average when using the ARC kinetic scheme.

9. LES OF PLASMA ASSISTED COMBUSTION FOR A PREMIXED SWIRL-STABILIZED BURNER

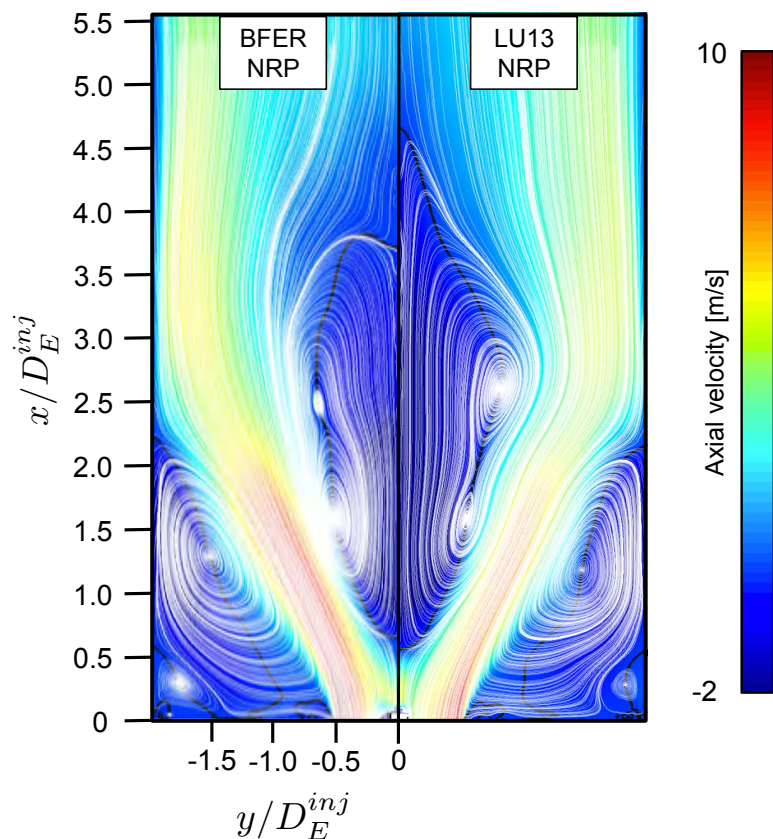


Figure 9.18: Mean flow pattern in the combustion chamber when applying NRP discharges. White: time and azimuthal averaged streamlines. Black line: zero axial (x-axis) velocity iso-line. Comparison between BFER and LU13 mechanisms.

It is anyway confirmed how in both cases the resulting flame is a V-shaped flame stabilized both by the hot gases generated by the NRP discharges and by the central recirculation zone.

The heat release rate field (Fig. 9.19) reveals a slight lifting on the flame, denoted by high values of the heat release rate in the chamber axis zone, above the top end of the rod. Comparing the results obtained with the LU13 mechanism to what has been obtained without the use of NRP discharges (Fig. 7.33) shows that the mean lifting of the flame is also reduced in this case.

In both cases, heat release is not zero in the NRP discharge zone, where it takes high values due to the high temperatures reached in this zone.

As already found comparing the LES without NRP discharges, the flame is longer using the LU13 mechanism.

Looking at data available from [Lacoste et al. \[2013a\]](#), a qualitative comparison with the experimental observations can be done. This has to be taken as a purely qualitative comparison and no conclusion can directly be taken, since the current geometry and operating conditions correspond to a modified version of the setup studied during that work. The time-averaged Abel-inverted images of the CH* emission without and

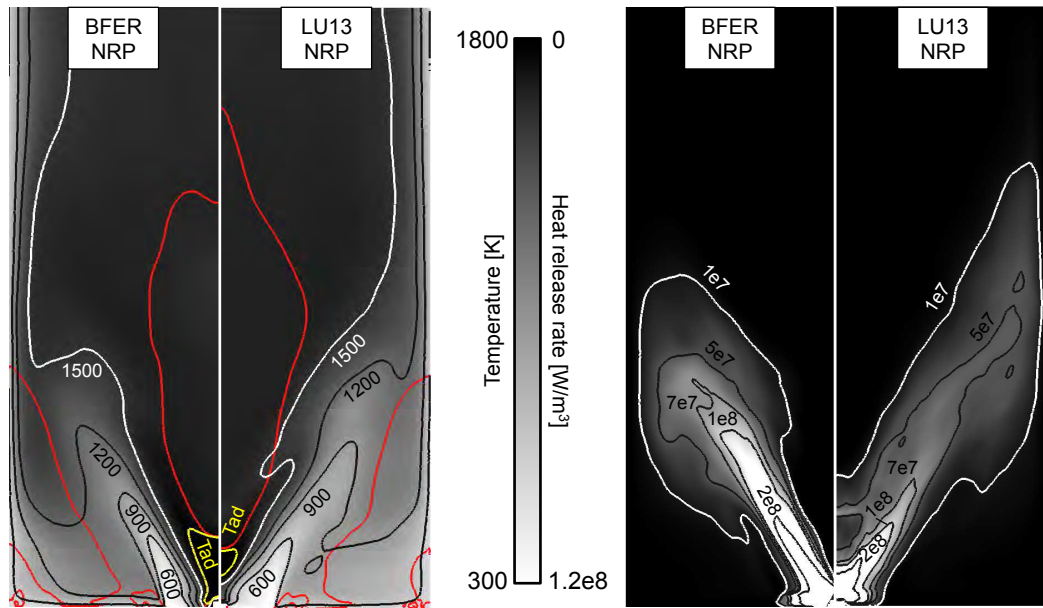


Figure 9.19: Time and azimuthal averaged flow field of temperature (left) and heat release rate (right) in the combustion chamber when applying NRP discharges. Comparison between BFER and LU13 mechanisms. Yellow line: isoline at adiabatic flame temperature; red line: isoline at zero axial velocity.

with NRP discharges are reproduced in Fig. 9.20. It can be seen how the increase in

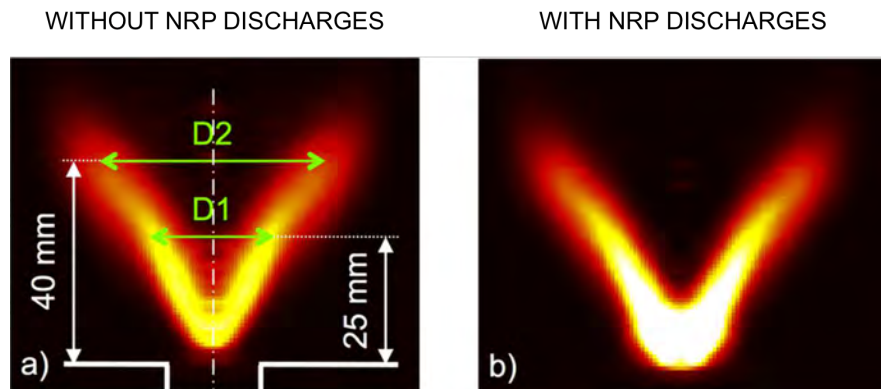


Figure 9.20: Time-averaged Abel-inverted images of the CH^* emission without (a) and with (b) NRP discharges [Lacoste et al., 2013a].

heat release rate when using NRP discharges is found also in experimental observation, together with a shift of the flame towards the chamber inlet. The mean flame lifting is reduced but not completely suppressed: from this point of view it seems that the LU13 mechanism leads to a more realistic result than the BFER one.

Fig. 9.21 shows that the field of RMS axial velocity is characterized by higher values in a larger zone above the top end of the rod when using the LU13 mechanism. This

9. LES OF PLASMA ASSISTED COMBUSTION FOR A PREMIXED SWIRL-STABILIZED BURNER

is coherent with the presence of the flame root in this zone.

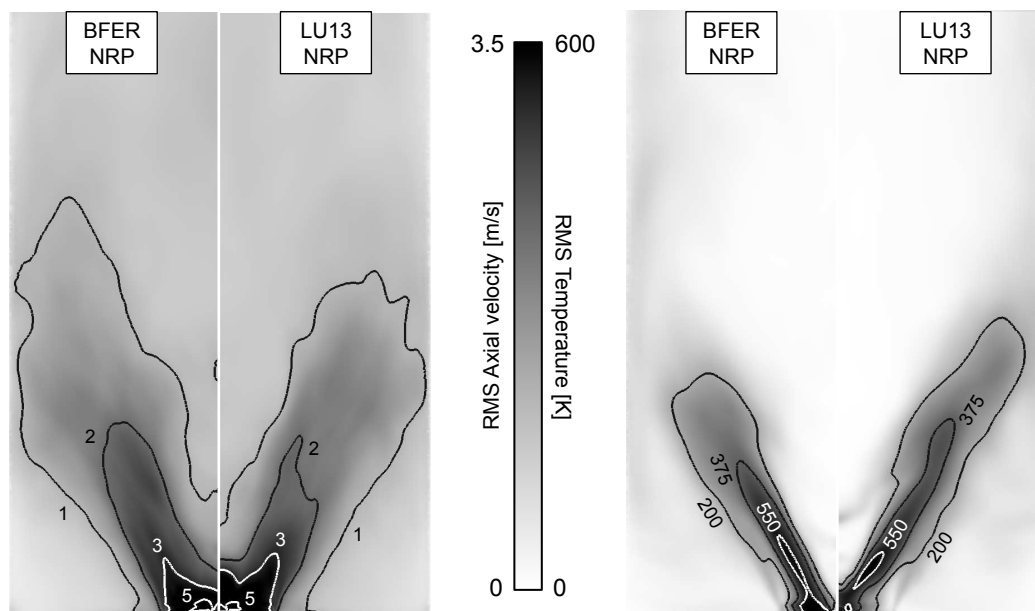


Figure 9.21: Time and azimuthal averaged flow field of RMS axial velocity (left) and RMS temperature (right) in the combustion chamber when applying NRP discharges. Comparison between BFER and LU13 mechanisms.

When looking at the RMS temperature fields, two main features can be underlined. First, the use of the LU13 kinetic scheme leads to higher values above the top end of the rod, coherently to what seen for temperature and axial velocity. Second the comparison of the LU13 results with the one obtained without NRP discharges (Fig. 7.35) shows that the area in which the RMS temperature takes high values is smaller. This identifies a globally lower flame root movement, confirming what found using the BFER mechanism.

All the above mentioned differences are also evaluated quantitatively by means of 1D profiles at 5 different axial positions, corresponding to $x/D_E^{inj} = 0.15, 0.3, 0.6, 1.5$ and 3.0 (Fig. 7.36). Profiles of mean and root-mean-square values of axial velocity and temperature are shown respectively in Figs. 9.22, 9.23, 9.24 and 9.25.

The increase in axial velocity caused by the NRP discharges is lower when using the LU13 mechanism, due to the fact that the acceleration is lower in average. Regarding temperature, the overall behavior is the same in both cases, with however a less marked increase in temperature when using the LU13 mechanism. The RMS temperature plots show that the use of the LU13 mechanism produces a lighter reduction in maximum values when compared to the LES without NRP discharges.

As previously mentioned, the plasma discharges can have a thermal but also chemical effect on the flame. Since the plasma phase is not computed in the present LES, its chemical effect can not be evaluated quantitatively in this case. On the other side, the energy supplied to the gas is not divided into quotas responsible for different phenomena like for example in the model developed by [Castela et al. \[2016\]](#). Here the full

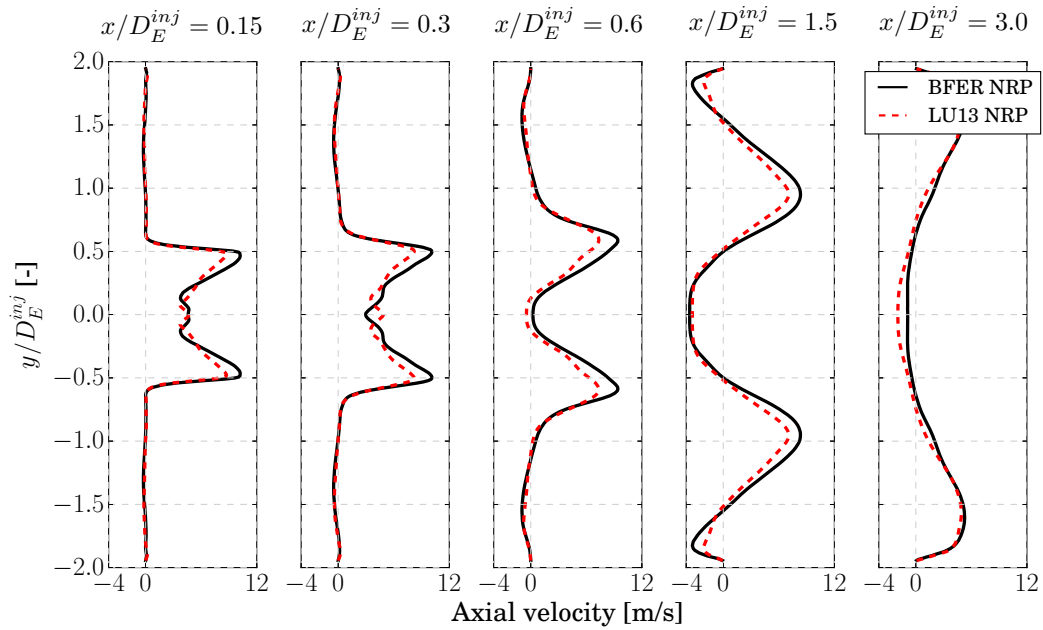


Figure 9.22: 1D axial velocity mean profiles at different axial positions when applying NRP discharges. Comparison between BFER and LU13 mechanisms.

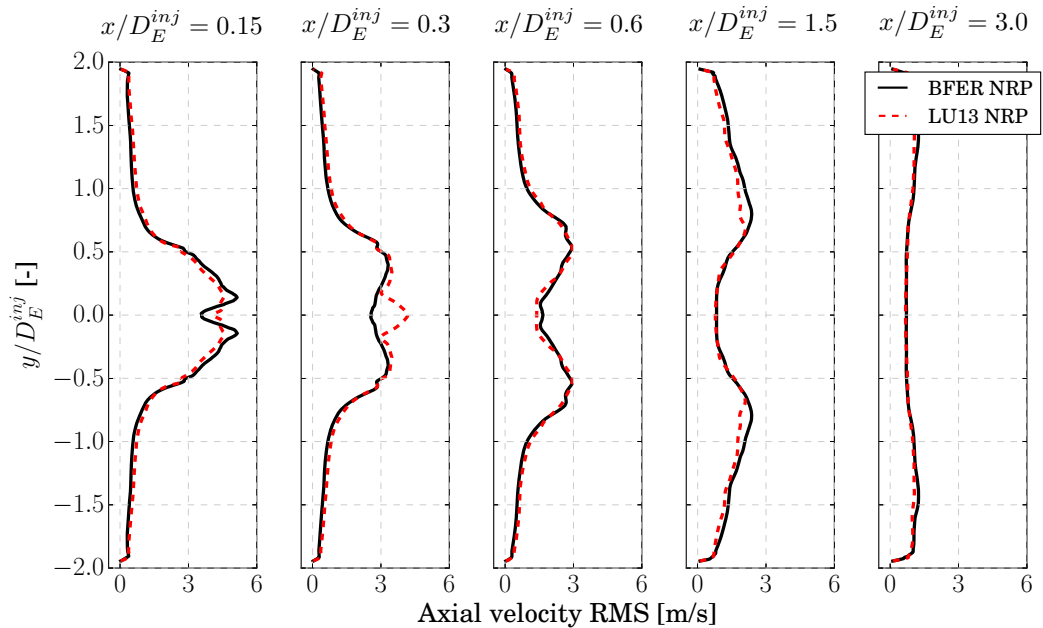


Figure 9.23: 1D axial velocity RMS profiles at different axial positions when applying NRP discharges. Comparison between BFER and LU13 mechanisms.

amount of energy is supplied to the gas and any species production is determined only by the reaction associated to the current kinetic scheme. However, a high concentration of species which can have a role in combustion enhancement, like O, H and OH, is

9. LES OF PLASMA ASSISTED COMBUSTION FOR A PREMIXED SWIRL-STABILIZED BURNER

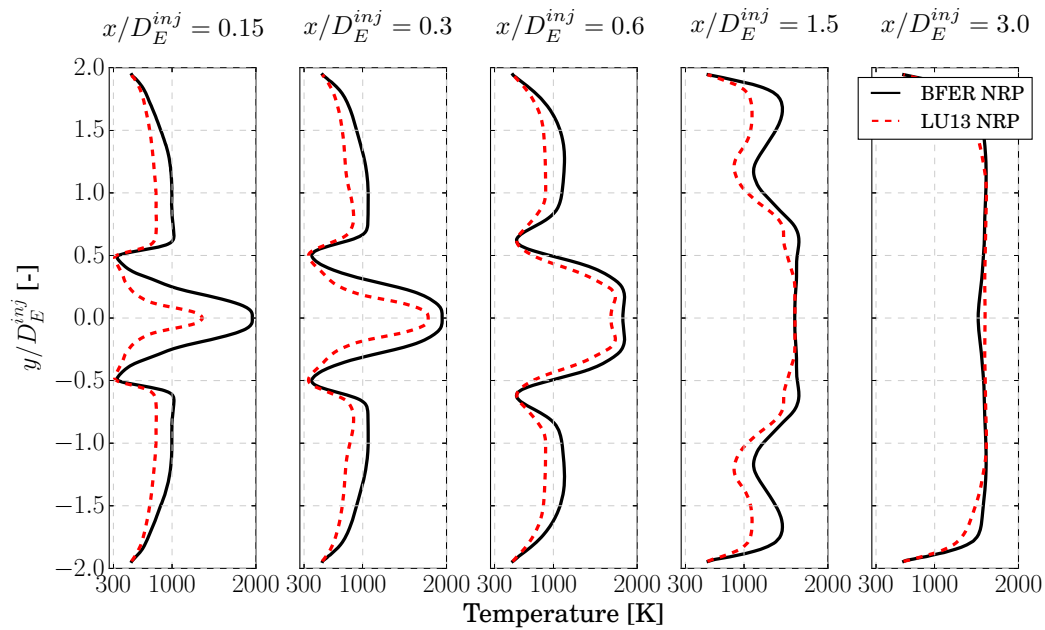


Figure 9.24: 1D temperature mean profiles at different axial positions when applying NRP discharges. Comparison between BFER and LU13 mechanisms.

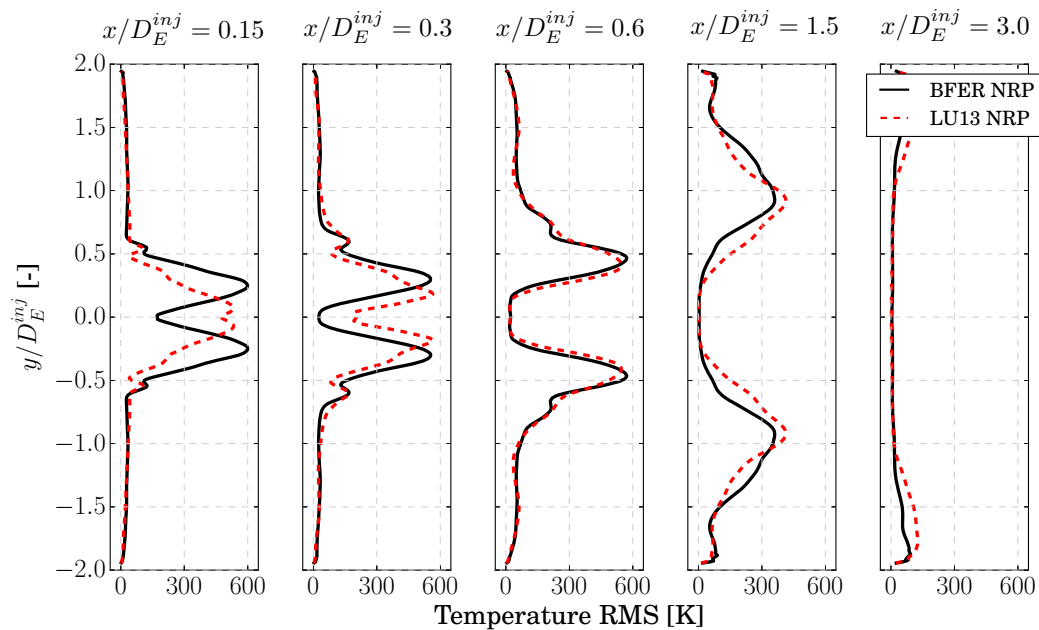


Figure 9.25: 1D temperature RMS profiles at different axial positions when applying NRP discharges. Comparison between BFER and LU13 mechanisms.

found in the zone at very high temperature situated above the top end of the rod. This was not the case in the LES without NRP discharges, where the mass fractions of these species were strongly lower. These species are produced in a significant amount in the plasma channels due to high temperatures and could have a role in flame stabilization

which has to be deeper investigated in future studies. As an example the time and azimuthal averaged field of O mass fraction is shown in Fig. 9.26.

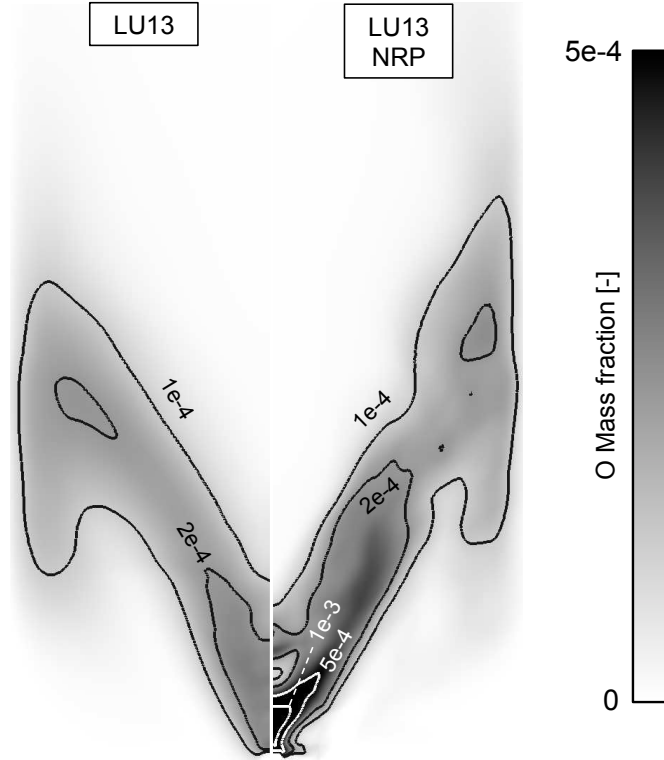


Figure 9.26: Time and azimuthal averaged flow field of O mass fraction in the combustion chamber when using the LU13 mechanism. Comparison between LES without and with NRP discharges.

9.1.3 Few words about CPU cost

The heavy mesh, as well as the small time step, make the simulation performed in this study very expensive in CPU time. Table 9.1 summarizes the CPU time needed to perform 7.5 ms of physical time on 15 nodes (360 CPUs) using the CERFACS in-house cluster NEMO (or equivalent). The LU13 kinetic scheme demands 22.5 %

Table 9.1: CPU time for different PACCI cases with NRP discharges.

	BFER	LU13
CPU hours	~110k	~135k

additional CPU time when compared to the BFER one. This value is lower than the one found when running the LES without NRP discharges because of the need, in this case, to apply a sub-cycling of chemistry around the discharge when using the BFER mechanism. The chemical sub-cycling is very CPU expensive indeed.

9.1.4 Concluding remarks

The effect of applying NRP plasma discharges to the flame shape and dynamics has been studied using LES. The NRP discharges seem to have a major impact on the flame, leading to a more stable flame by means of a complete change of its anchoring position and mechanisms. The two kinetic schemes used show qualitatively similar results, but also quantitative differences: the effect produced using the LU13 scheme is weaker and this seems to be closer to the experimental visualizations.

In the next section an acoustic forcing of the flame is presented, in order to quantitatively establish the effect of the NRP discharges on the flame dynamics. For time and CPU cost reasons, this study has been performed using only the BFER mechanism.

9.2 Acoustically pulsating the PACCI burner with NRP discharges

Starting from an instantaneous solution of the LES run with the BFER mechanism and with the NRP discharges model, acoustic forcing is applied to the inlet boundary condition. The initial solution corresponds to a physical time of 7.5 ms, being $t = 0$ the temporal instant at which the NRP discharges model is activated.

The mesh used is the mesh M3 and the entire numerical setup is the one used in the LES without acoustic forcing of section 9.1. The time step has been set to 1×10^{-8} s.

The acoustic forcing is introduced, as in subsection 7.4.2, by generating a harmonic acoustic perturbation at the domain inlet (Fig. 7.5) using the inlet wave modulation method. The forcing amplitude has been chosen to be of around 40 % of the mean mass flow rate. The forcing frequency is of 160 Hz.

The numerical simulation has been run for a total of 8 forcing cycles. Discarding the first cycle, needed to establish the burner response, the FTF can be evaluated using 7 forcing cycles. The total simulation time is of 50 ms, corresponding to 2/3 of a burner convective time.

9.2.1 Dynamic response of the PACCI burner

9.2.1.a Mean fields

Time and azimuthal averaged flow fields of main flow variables during acoustic excitation at 160 Hz are shown in Fig. 9.27 and 9.28 and compared to the ones obtained in the simulation without NRP discharges.

Figure 9.27 shows how, similarly to what was seen in the unforced case, the NRP discharges completely change the flame and flow topology. The central recirculation zone, which was attached to the top end of the central rod in the simulation without NRP discharges, is pushed downstream and takes a lifted position when the NRP model is activated. The zone between the top end of the electrode and the bottom end of the central recirculation zone is filled with very hot gases, at a temperature higher than the adiabatic flame temperature. This hot gas is generated by the plasma discharges. The central recirculation zone closes downstream at the same axial position in both cases.

9.2 Acoustically pulsating the PACCI burner with NRP discharges

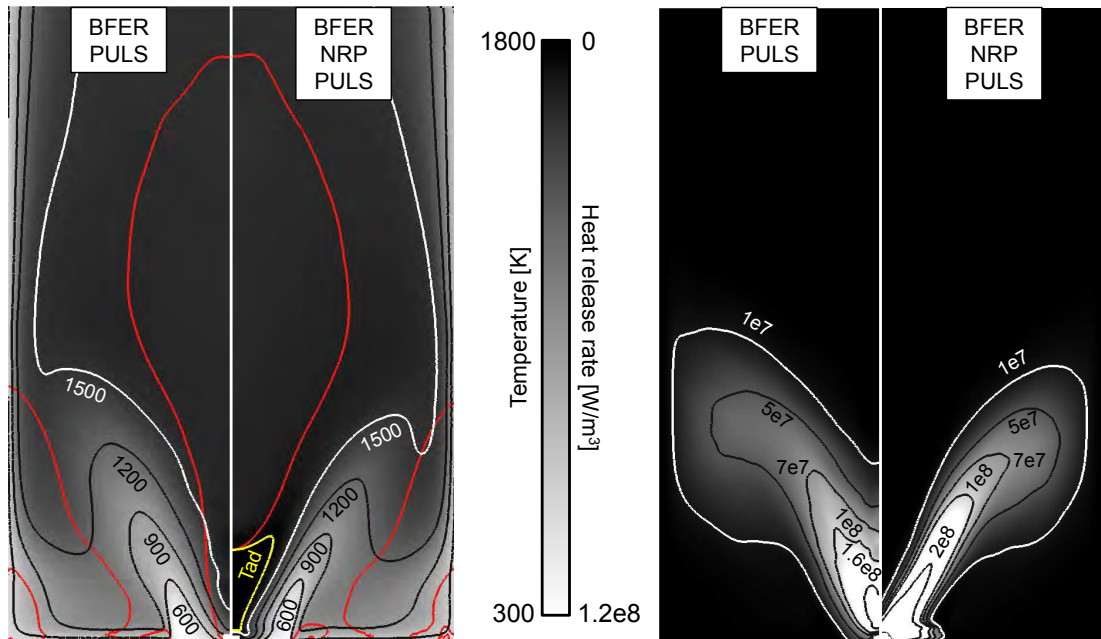


Figure 9.27: Time and azimuthal averaged flow field of temperature (left) and heat release rate (right) in the combustion chamber when applying acoustic forcing. Comparison between numerical simulations without and with NRP discharges.

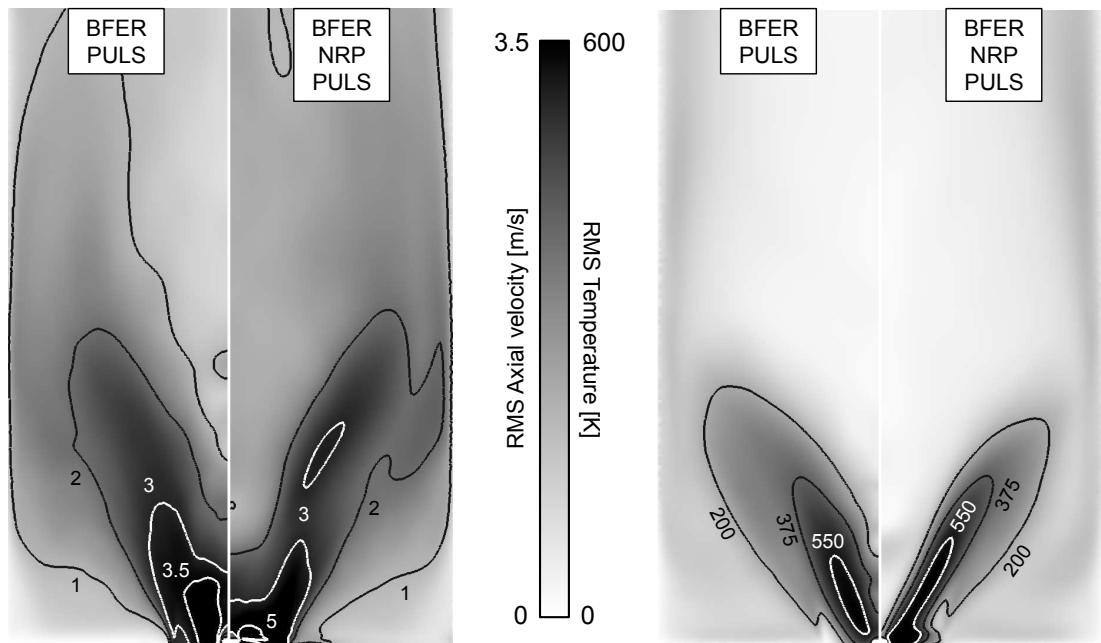


Figure 9.28: Time and azimuthal averaged flow field of RMS axial velocity (left) and RMS temperature (right) in the combustion chamber when applying acoustic forcing. Comparison between numerical simulations without and with NRP discharges. Black line: iso-line of adiabatic flame temperature. White line: iso-line of zero axial velocity.

9. LES OF PLASMA ASSISTED COMBUSTION FOR A PREMIXED SWIRL-STABILIZED BURNER

The corner recirculation zone, on the contrary, seems to close upstream when applying NRP discharges.

The heat release rate field shows that the use of NRP discharges generates a shorter flame, which is also less extended in the radial direction. The shorter flame can be the consequence of the increase in flame speed caused by the heating of the fresh gas stream. Both these characteristics have been observed experimentally in the work of [Lacoste et al. \[2013a\]](#). Overall, when applying NRP discharges, the flame moves less. The flame root is also found to be more stable, since it crosses the burner axis only very close to the central rod.

We focus now on the RMS fields presented in Fig. 9.28. The RMS field shows similar values in both cases. However, higher values are found at the chamber inlet, due to the plasma discharges. At the same time, along the chamber axis, the field shows values decreasing in a faster way when using NRP discharges. This is due to the lifted recirculation zone which does never penetrate the area close to the top end of the rod, in which velocity is always positive.

The RMS temperature field confirms the higher compactness and less movement of the flame, being the field of non-zero values less extended both axially and radially. As expected, values are higher in the discharge zone and in the shear layer, due to the generation of hot spots by the NRPs and their convection and merging with the main flame.

All the above mentioned differences are also evaluated quantitatively by means of 1D profiles at the 5 different axial positions, corresponding to $x/D_E^{inj} = 0.15, 0.3, 0.6, 1.5$ and 3.0 (Fig. 7.36). Profiles of mean and root-mean-square values of axial velocity and temperature are shown respectively in Figs. 9.29, 9.30, 9.31 and 9.32.

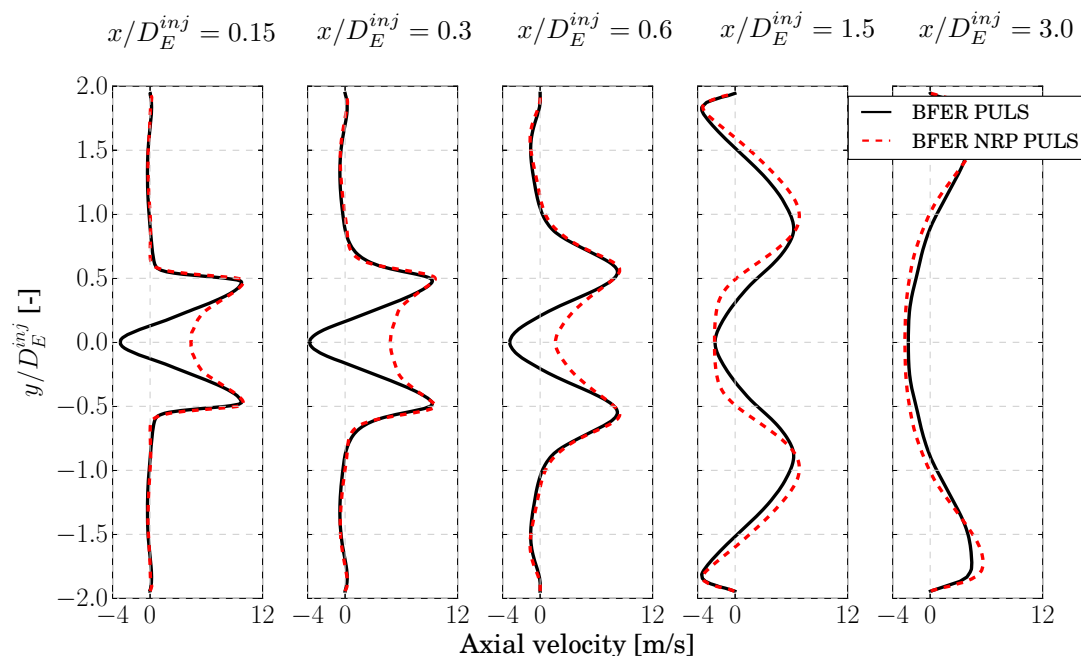


Figure 9.29: 1D axial velocity mean profiles at different axial positions when acoustically forcing the flame. Comparison between LES without and with NRP discharges.

9.2 Acoustically pulsating the PACCI burner with NRP discharges

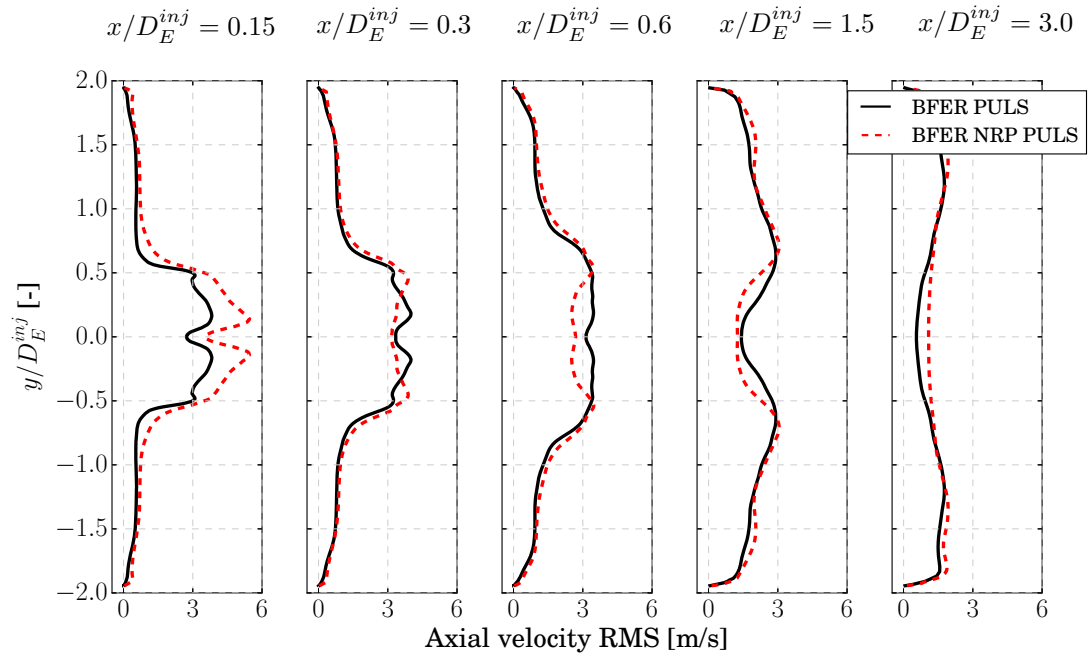


Figure 9.30: 1D axial velocity RMS profiles at different axial positions when acoustically forcing the flame. Comparison between LES without and with NRP discharges.

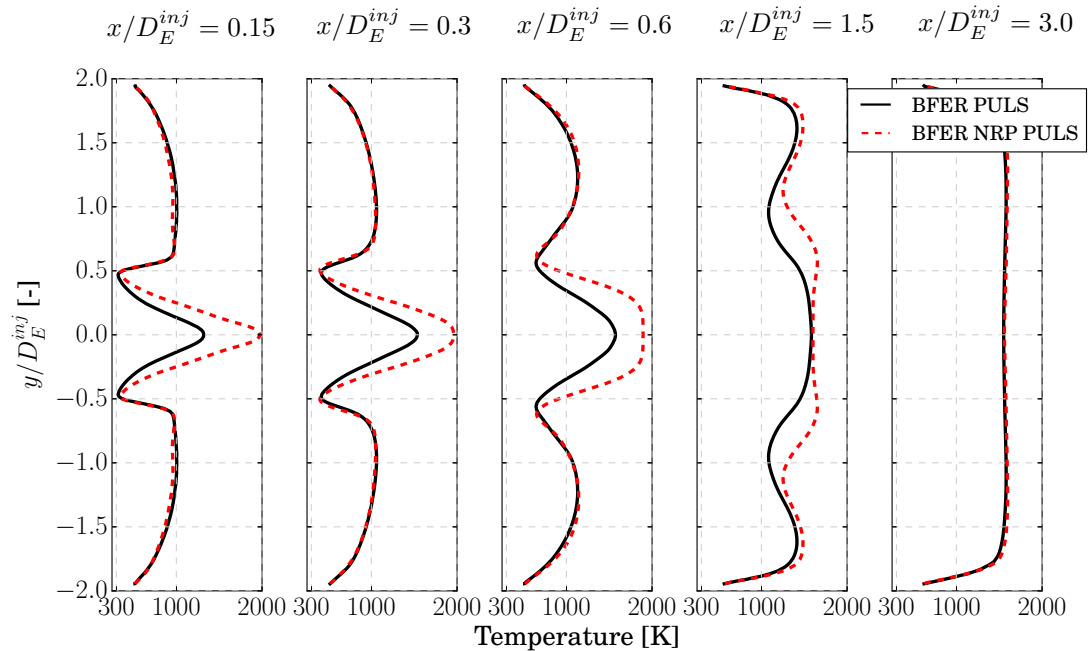


Figure 9.31: 1D temperature mean profiles at different axial positions when acoustically forcing the flame. Comparison between LES without and with NRP discharges.

9. LES OF PLASMA ASSISTED COMBUSTION FOR A PREMIXED SWIRL-STABILIZED BURNER

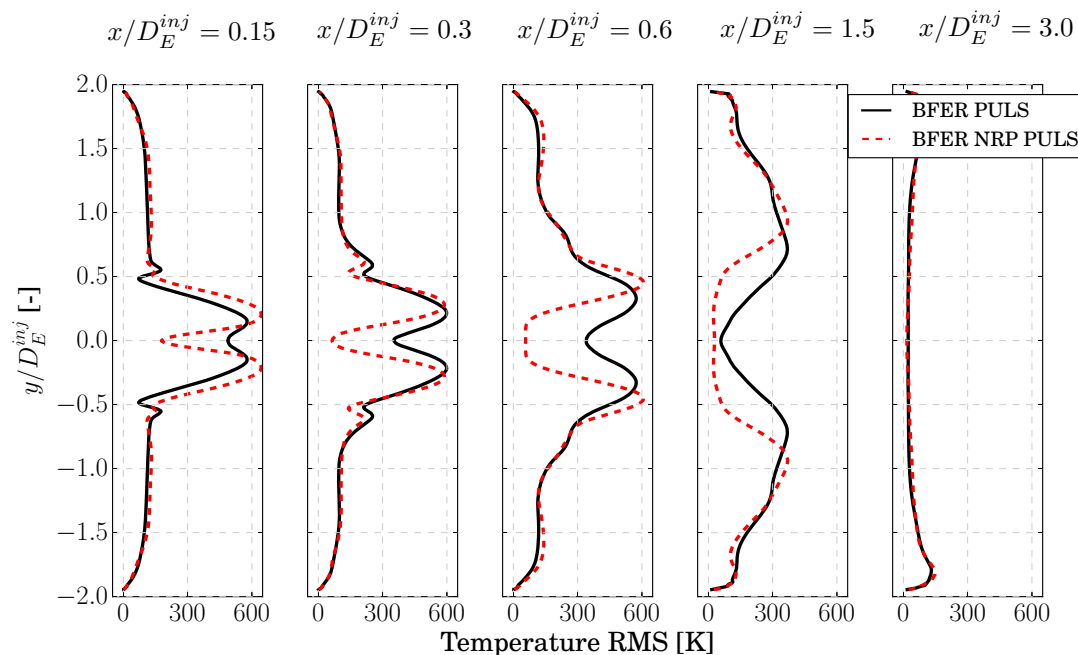


Figure 9.32: 1D temperature RMS profiles at different axial positions when acoustically forcing the flame. Comparison between LES without and with NRP discharges.

9.2.1.b Flame dynamics

The flame dynamics is here analyzed in Fig. 9.33, where the evolution of the mean heat release rate is plotted as a function of the forcing cycle. A low pass filter has been applied to the temporal signal recorded in LES, in order to clean it up from high frequency variations caused by the NRP discharges. As it can be confirmed also by means of Fig. 9.34, where the mean heat release rate power spectral density is shown, the flame dynamics is completely controlled by the acoustic forcing. The cycle-to-cycle variability of the maximum and minimum values seems to be lower than in the acoustically forced simulation without NRP discharges (see Fig. 7.51). Moreover, the peak is weaker when applying NRP discharges, denoting a decrease in oscillation amplitude.

Similarly to subsection 7.4.2, various snapshots of temperature and axial velocity are presented in Fig. 9.35 and 9.36. The snapshots have been taken at a fixed temporal distance. They have been chosen in order to describe the evolution from a local maximum towards a local minimum and subsequent way back to a new local maximum. The corresponding states are marked on the mean heat release rate evolution by means of red marks.

The flame dynamics is overall very similar to the one observed in the LES without NRP discharges (Fig. 7.53 and 7.54). The states corresponding to maximum values of heat release rate (snapshots 1-2 and 9) are the ones in which the flame length is maximum and a vortex roll-up appears. At these states, the axial velocity is maximum

9.2 Acoustically pulsating the PACCI burner with NRP discharges

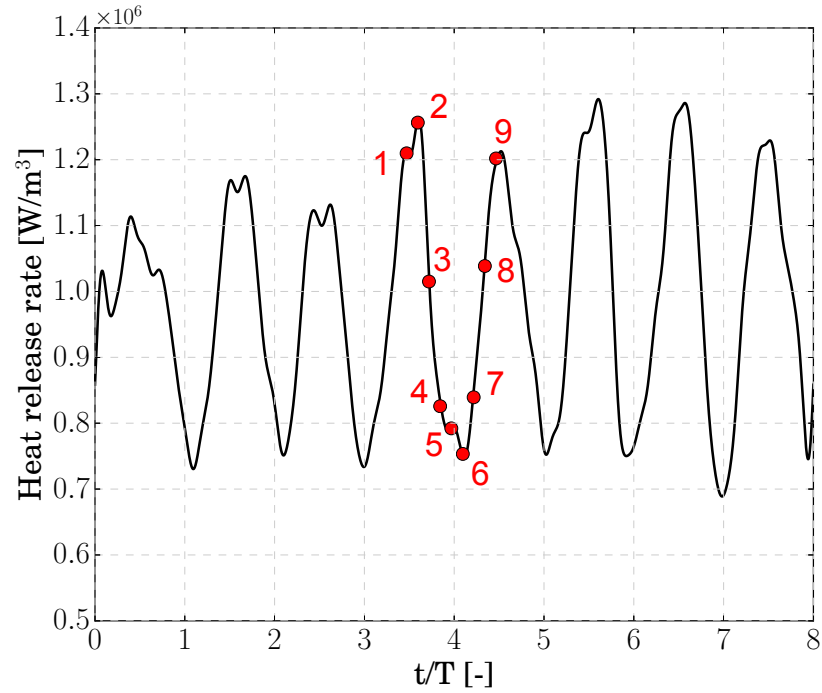


Figure 9.33: Temporal evolution of the mean heat release rate as a function of the forcing cycle when using NRP discharges. Red dots: states at which the snapshots of Fig. 9.35 and 9.36 have been taken.

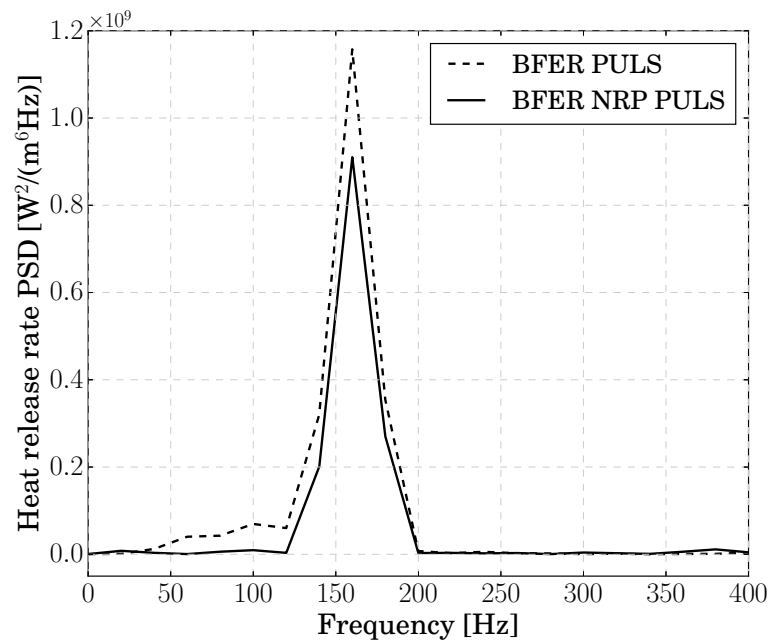


Figure 9.34: Power spectral density of mean heat release rate applying an acoustic forcing at 160 Hz. Comparison between LES without and with NRP discharges.

9. LES OF PLASMA ASSISTED COMBUSTION FOR A PREMIXED SWIRL-STABILIZED BURNER

in the vortex roll-up zone and relatively low at chamber inlet. Here the flame root slightly penetrates into the injection tube, where the flame stabilizes.

On the contrary, the heat release rate is minimum when the axial velocity is maximum at chamber inlet, pushing the flame and slightly lifting it. At these states, due to the low velocity present further downstream, the flame is less stretched and more compact. No vortex roll-up is present.

The wrinkling of the flame is strongly different in the two cases. In the numerical simulation run without NRP discharges (Fig. 7.53), additionally to the flame wrinkling due to the vortex roll-up at the flame tip, the flame is strongly wrinkled at its root. A large vortical motion at flame root can be seen indeed for example in the snapshots 1-2 of Fig. 7.53. In the same way, snapshots 7-8 show how the two opposite flame fronts almost collapse in the burner axis zone. This denotes a high radial motion of the flame in its lower part, associated to higher radial flame wrinkling. When looking at the LES with NRP discharges, this radial motion seems on the contrary to be much less present. The snapshots of Fig. 9.35 reveal that the central zone is always filled by very hot gases and that the flame is always V-shaped around it. The radial movement of the flame front is strongly attenuated and the flame is much less wrinkled.

This can be explained by the fact that, when using NRP discharges, the behavior of the zone situated just above the top end of the rod is controlled by the NRP discharges and not anymore by the flow dynamics linked to the central recirculation zone. This prevents the zone to be subject to the flow dynamics visible in the case without NRP discharges. The resulting flame front always develops around this zone and never penetrates it. This has the effect of reducing the flame wrinkling in the flame root zone induced by the acoustic forcing.

The flow dynamics just described can also be identified in Fig. 9.36: the flow field is strongly different without or with NRP discharges. The very low velocity zone which can be observed at the rod tip in snapshots 1-2 of Fig. 7.54 is not present in the respective snapshots of Fig. 9.36. In the latter case, the velocity is indeed positive as a result of the acceleration of the fluid due to gas heating. This makes the flow more difficult to destabilize and promotes the flame V-shape stabilization around it, reducing so the flame wrinkling at flame root.

The acoustics generated by the NRP discharges is clearly visible in Fig. 9.36, both in the discharge zone and in the center of the burner, where traveling waves can be recognized.

The flame behavior observed in the LES seems to be in accordance to what observed experimentally by [Lacoste et al. \[2013a\]](#). They found how, using NRP discharges, the radial oscillation of the flame front responding to the velocity forcing was partially suppressed. They suggested moreover that the reduction of flame wrinkling in radial direction was associated with a reduction of FTF gain. This is now analyzed.

9.2.1.c Flame Transfer Function evaluation

The flame transfer function is evaluated using the mean heat release rate in the burner and the reference velocity on a probe situated near the inlet of the domain, upstream of the swirler (see Fig. 7.55).

9.2 Acoustically pulsating the PACCI burner with NRP discharges

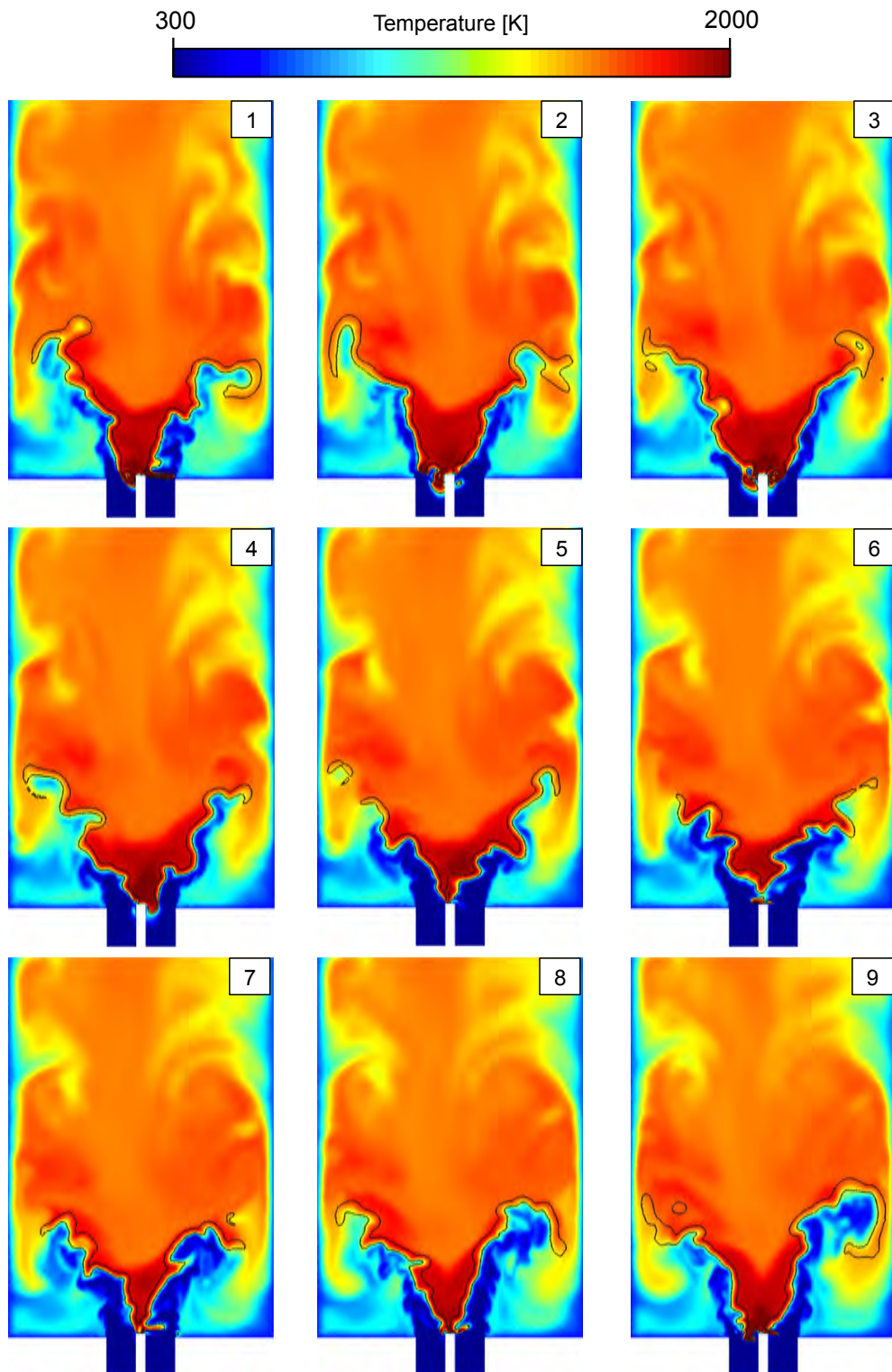


Figure 9.35: Instantaneous fields of temperature on a 2D cut at $z = 0$ when using NRP discharges. Black line: iso-line of heat release rate ($1 \times 10^8 \text{ W/m}^3$). The number in the white box represents the red dot of Fig. 9.33.

9. LES OF PLASMA ASSISTED COMBUSTION FOR A PREMIXED SWIRL-STABILIZED BURNER

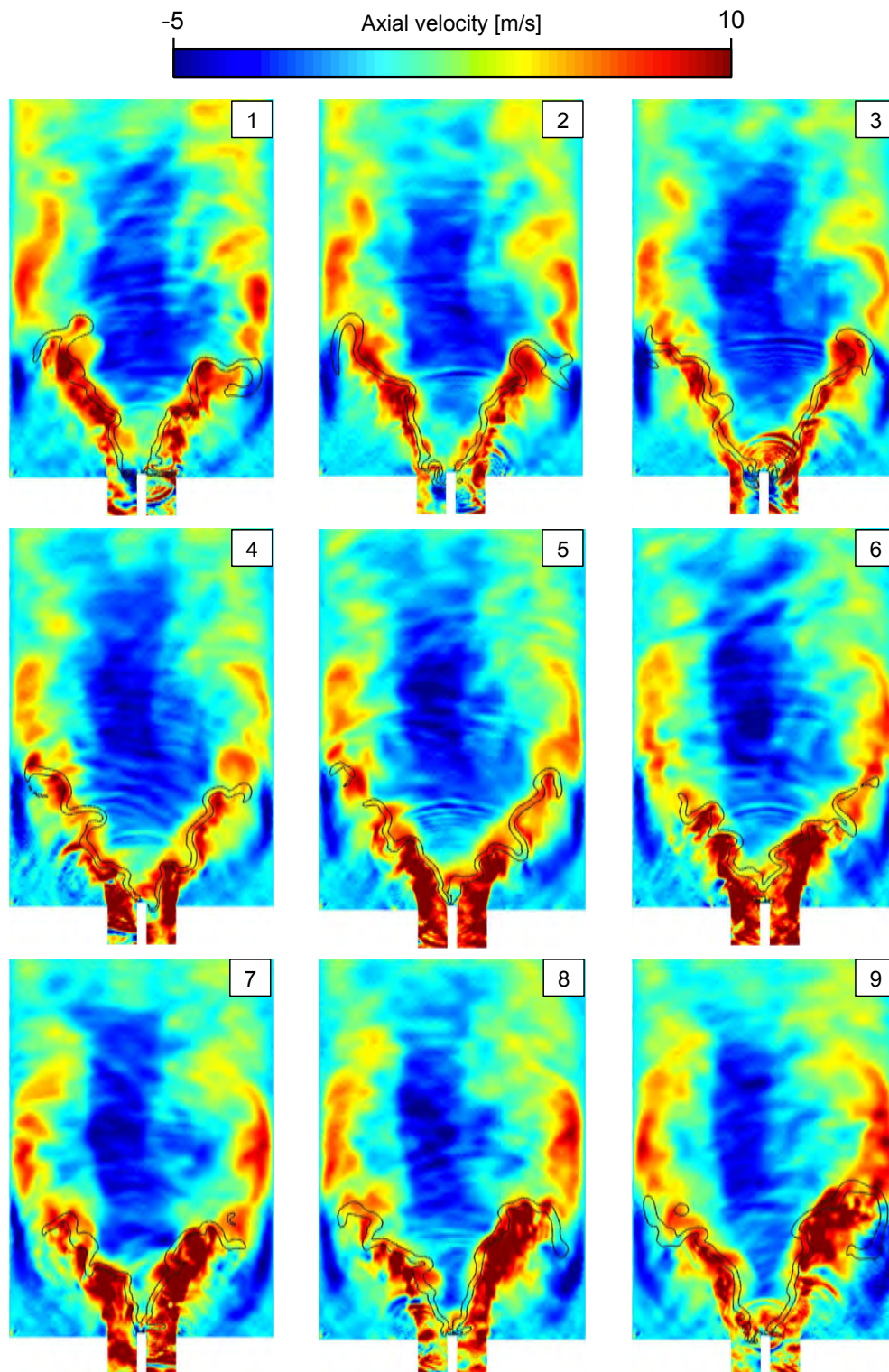


Figure 9.36: Instantaneous fields of axial velocity on a 2D cut at $z = 0$ when using NRP discharges. Black line: iso-line of heat release rate ($1 \times 10^8 \text{ W/m}^3$). The number in the white box represents the red dot of Fig. 9.33.

9.2 Acoustically pulsating the PACCI burner with NRP discharges

The recorded signals of velocity and heat release rate are shown in Fig. 9.37. Both signals have been treated using a low-pass filter, in order to eliminate high frequency fluctuation caused by the NRP discharges and permit a clear visualization.

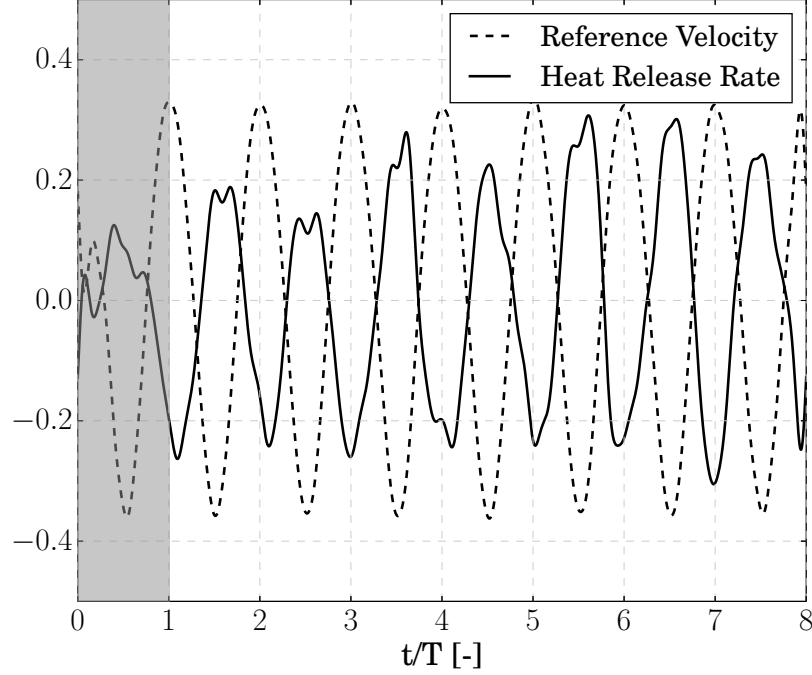


Figure 9.37: Temporal evolution of the reference velocity and mean heat release rate as a function of the forcing cycle when using NRP discharges.

The first forcing cycle is needed to establish the burner response and is not considered in the evaluation of the FTF. Starting from the second forcing cycle, the FTF is evaluated considering 7 cycles, alike to what did for the LES without NRP discharges. The resulting values are summarized in Tab. 9.2 and compared to the case without NRP discharges.

	LES w/o NRPs	LES w/ NRPs
N [-]	0.748	0.702
τ [ms]	4.426	3.237

Table 9.2: Gain and time delay of the FTF for the cases without and with NRP discharges.

The FTF gain decreases of around 6.15 % when applying NRP discharges, according to what was found in the experimental observations of Lacoste et al. [2013a]. The time delay is also found to decrease. This can be the consequence of the increase in flame speed caused by the heating of the fresh gas stream, as shown by Duchaine et al. [2011]. However, this is found in the experimental observation of Lacoste et al. [2013a] only for frequencies above 304 Hz.

9. LES OF PLASMA ASSISTED COMBUSTION FOR A PREMIXED SWIRL-STABILIZED BURNER

9.2.1.d Few words about CPU time

The CPU cost associated to this numerical simulation (50 ms of physical time) on 15 nodes (360 CPUs) using the CERFACS in-house cluster NEMO (or equivalent) is of about 735 kh.

9.3 Conclusion

The phenomenological model developed in chapter 8 to model the effect of NRP discharges has been applied to the PACCI configuration.

A significant modification of the flame shape and dynamics when applying NRP discharges has been found: the central recirculation zone takes a lifted position. The zone between the top end of the rod and the recirculation zone is filled with gases coming from the discharges zone, at a temperature higher than the adiabatic flame temperature. The flame anchoring mechanism changes: the flame is stabilized by both the central recirculation zone and the NRP discharges.

Qualitatively, the same results have been found when using the BFER or the LU13 mechanism. Quantitatively, the effect found using the LU13 mechanism is weaker.

An acoustic forcing has been applied to the LES run with the BFER mechanism in order to analyze the flame response at 160 Hz. It has been found how the overall flame dynamics does not change but how, applying NRP discharges, the resulting flame is shorter and moves less radially. This seems to depend to the anchoring mechanism provided by the NRP discharges. The effect on the FTF has been evaluated, showing a reduction both in gain and time delay.

Conclusions and perspectives

This PhD work aimed at study via Large Eddy Simulations some of the interactions between flames and thermal phenomena which can appear in burners. Flames generate heat indeed, but can also be affected by it. This multi-physical environment has been investigated with a focus on two main topics: wall heat transfer and combustion control.

In a first part, wall heat transfer has been studied in the context of rocket engines. In this field cost reduction and launchers re-usability are major challenges: new propellant combination are considered and wall heat fluxes have to be precisely predicted. In this framework, the single-element sub-scale CH_4/O_2 rocket combustor experimentally studied by the team of Prof. Haidn at the Technische Universität München (Germany) has been numerically simulated. In order to perform this LES, various challenges had to be faced: (i) the CH_4/O_2 chemistry at high pressure, (ii) the highly confined environment in which flame and walls are very close, (iii) the turbulence-combustion interaction in a non-premixed flame environment, (iv) the evaluation of the heat fluxes at walls in an environment characterized by very high ratios between gas and walls temperature. This resulted in a delicate balance between the heat released by the flame, the heat lost at walls, the gas acceleration and the chamber pressure evolution. Everything had to be correctly predicted at the same time in order to have a reliable LES. This required the set-up of an "ad hoc" methodology which takes advantage of the know-how available at CERFACS and has the aim of be re-usable in future LES of similar configurations. Regarding chemistry, Analytically Reduced Chemistry, has been used. Infinitely fast chemistry can be in this case inadequate, since the gas is often out of thermal equilibrium. Moreover, a kinetic scheme with a certain amount of radical species is necessary in order to take into account low activation energy reactions. The LU13 [Sankaran et al., 2007] mechanism has been chosen and validated for high pressure and oxi-combustion. The vicinity between the walls and the flame brought a non-negligible problem in controlling the radial expansion of the flame. It has been found indeed how the LES mesh has the tendency to artificially thicken the flame, causing an early convection of hot gases towards the walls. In order to overcome this problem, it has been found that the use of a fine grid is mandatory close to the injector, in order to retrieve the correct flow pattern and to avoid a too large thickening of the flame. A first version of a turbulence-combustion interaction model for diffusion flames has been applied, following the work of Shum-Kivan [2017].

Stated the impossibility of resolving the boundary layer, for which too many cells would

CONCLUSIONS AND PERSPECTIVES

be needed, wall laws have been used. Due to the very high temperature ratio between the gas and the walls (> 5), an improved version of the classical wall law, called coupled wall law [Cabrit, 2009], has been used.

Results showed a good agreement in chamber pressure and wall heat flux evolution predictions in the first half of the combustion chamber and a slight difference in the second half. The possible causes for these differences have been investigated, showing a leading order influence of the interaction between wall law and sub-grid-scale turbulence model. An energetic balance showed the link between heat released by the flame, heat lost at walls and wall heat fluxes and chamber pressure evolution.

Regarding future work, several actions can be conducted. Taking advantage of the ARC methodology already used and validated, a new kinetic scheme could be derived, in order to fully adapt to this combustion environment. Moreover, a study of the role of radicals could be carried on, with the aim of reducing the number of transported species and consequently of the CPU cost. The turbulence-combustion interaction model has to be further developed, in order to be able to directly obtain the required parameters from the LES, without setting it manually. This has also to be done in order to try to coarsen the grid in the flame zone: this will help in saving CPU time, still correctly predicting the flame opening and length. A deeper understanding in the interaction between the wall laws and the SGS model is also mandatory, since it has been shown to be responsible of first order differences in the wall heat fluxes prediction. Finally, the setup developed during this work has to be tested on similar configurations.

In a second part, combustion control by means of Nanosecond Repetitively Pulsed plasma discharges has been studied in the context of gas turbine combustors. Gas turbines run usually fuel lean, in order to control fuel consumption and pollutant emission. Lean combustion is however known to be prone to combustion instabilities: combustion control is a major challenge in this field. Among other techniques, NRP plasma discharges seem to be a promising technique to control combustion, thanks to their thermal and chemical effects on the gas. In this work a phenomenological model which considers the plasma discharges as a heat source has been developed. The model has been tuned to experimental observations made by the team of Prof. Lacoste at the King Abdulla University of Science and Technology (Saudi Arabia) on the experimental bench PACCI. The model has been tuned using the global 2-step kinetic scheme BFER [Franzelli, 2011], which has been used for the majority of the LES performed. The PACCI configuration has been numerically studied in this work: it consists of a lean premixed swirl-stabilized CH_4/Air combustor run at atmospheric pressure. The non reacting and reacting flows without the use of NRP discharges have been simulated showing an overall good agreement with the experimental observations. An acoustical forcing has been introduced in order to study the flame response to acoustics and the Flame Transfer Function has been evaluated. The flame dynamics was found to be driven by the acoustical perturbation. Large variations in flame surface, associated to vortex roll up, caused large variation of the total heat released by the flame. The phenomenological model has then been applied to the PACCI configuration, both in the case without and with acoustic forcing. In the case without acoustic forcing it has been found how the application of NRP discharges completely changed the flame

anchoring mechanism. Due to local re-ignition and fresh gas preheating, a zone of very hot gases was formed at the chamber inlet and the central recirculation zone was pushed downstream. The anchoring of the flame was found to be due not anymore to the central recirculation zone alone but to the contemporaneous effect of the NRP discharges and the central recirculation zone.

An effect of the NRP discharges on the flame dynamics was also found when acoustically pulsating the incoming flow. The anchoring mechanism provided by the NRP discharges constrained indeed the flame root zone to move less than in the case where NRPs were not used. This resulted in a lower radial movement of the flame and an associated lower peak-to-peak fluctuation of the flame heat release rate. It resulted also a decrease in values of the gain and time delay of the FTF.

In order to evaluate the effect of the kinetic scheme used, which is rather simple, the reacting simulation without and with NRP discharges (without acoustical forcing) has been re-run using the LU13 kinetic scheme. The use of a more complex kinetic scheme suggested that using a kinetic scheme like the BFER one could lead to an over-prediction of the NRP discharges effect. This has also been done in order to prepare the field to further studies which will be performed in the context of the French ANR Program "GECCO".

Regarding future work, much can be done. For the PACCI configuration, the main improvement path is that just one frequency has been simulated and with a perturbation amplitude higher than the experimental one. This has been done for time reasons and further studies have to be performed in order to have a complete acoustical characterization of the burner.

It is regarding the phenomenological model that many improvement can be implemented. First of all, it has been found how, when fixing the deposited energy per pulse, a completely different final state of the gas can result. The final state changes when changing the deposit size, the number and relative position of consecutive discharges, the initial temperature and composition of the gas, the kinetic mechanism used. It will be very important to know more precisely the deposit size and spatial position of the plasma channels. It could so be built a model in which the plasma channel changes position following the local gas characteristics instead of a random movement. It would also be important to take into account the bending of the gas channel in which the discharges take place. Regarding the response of chemistry to the energy deposit, a switch from the BFER to the LU13 kinetic scheme is advisable, due to the differences observed. Moreover, for the PACCI configuration with NRP discharges, the additional cost associated to the switch from the BFER to the LU13 kinetic scheme was only about 20 %. Another point which is still to be accounted for is the energy discharge repartition, as done by [Castela et al. \[2016\]](#). This has to be done in order to consider the entirety of phenomena caused by the non-equilibrium plasma, i.e. the molecular oxygen ultrafast production and the energy storage in vibrational states of the gas which provide a slower heat source.

Publications and Communications

1. D. MAESTRO, L. SELLE, AND B. CUENOT *Thermally chained LES of a GCH_4/GOX single element combustion chamber*. Proceedings of the 2015 Summer Program, 2015.
2. C. ROTH, O. HAIDN, H. RIEDMANN, B. IVANCIC, D. MAESTRO, B. CUENOT, L. SELLE, Y. DAIMON, A. CHEMNITZ, R. KELLER, ET AL. *Comparison of different modeling approaches for CFD simulations of a single-element GCH_4/GOX rocket combustor*. Proceedings of the 2015 Summer Program, 2015.
3. D. MAESTRO, B. CUENOT, A. CHEMNITZ, T. SATTELMAYER, C. ROTH, O. HAIDN, Y. DAIMON, R. KELLER, P. M GERLINGER, G. FRANK, ET AL. *Numerical investigation of flow and combustion in a single-element GCH_4/GOX rocket combustor: Chemistry modeling and turbulence-combustion interaction*. In 52nd AIAA/SAE/ASEE Joint Propulsion Conference, 2016.
4. H. MÜLLER, J. ZIPS, M. PFITZNER, D. MAESTRO, B. CUENOT, S. MENON, R. RANJAN, P. TUDISCO, AND L. SELLE. *Numerical investigation of flow and combustion in a single-element GCH_4/GOX rocket combustor: A comparative les study*. In 52nd AIAA/SAE/ASEE Joint Propulsion Conference, 2016.
5. C. ROTH, O. HAIDN, A. CHEMNITZ, T. SATTELMAYER, G. FRANK, H. MÜLLER, J. ZIPS, R. KELLER, P. GERLINGER, D. MAESTRO, L. SELLE, B. CUENOT, AND H. RIEDMANN *Numerical investigation of flow and combustion in a single element GCH_4/GOx rocket combustor*. In 52nd AIAA/SAE/ASEE Joint Propulsion Conference, 2016.
6. D. MAESTRO, B. CUENOT, AND L. SELLE *Large eddy simulation of flow and combustion in a single-element GCH_4/GOX rocket combustor*. In 7th European Conference for Aeronautics and Space Sciences (EUCASS), 2017.
7. D. MAESTRO, F. DI SABATINO, D. LACOSTE AND B. CUENOT *Large Eddy Simulation of Nanosecond Repetitively Pulsed Discharges for the Control of Thermoacoustic Instabilities*. In 4e Colloque du réseau d'INitiative en Combustion Avancée (INCA), 2017.

PUBLICATIONS AND COMMUNICATIONS

8. D. MAESTRO, B. CUENOT, AND L. SELLE *Large Eddy Simulation of combustion and heat transfer in a single-element GCH_4/GOX rocket combustor*. Prepared for publication in the Int. J. Heat Mass Transfer, 2018.

Bibliography

- N. L. Aleksandrov, F. I. Vysikailo, R. S. Islamov, I. V. Kochetov, A. P. Napartovich, and V. G. Pevgov. Electron distribution function in 4: 1 n₂-o₂ mixture. High Temperature Science, 19:22–27, 1981. [99](#)
- T. Alshaalan and C. J. Rutland. Turbulence, scalar transport and reaction rates in flame wall interaction. Proc. Combust. Inst., 27:793–799, 1998. [13](#)
- C. A. Armitage, R. Balachandran, E. Mastorakos, and R. Cant. Investigation of the non-linear response of turbulent premixed flames to imposed inlet velocity oscillations. Combust. Flame, 146:419–436, 2006. [150](#)
- R. Arnold, D. Suslov, and O. J. Haidn. Film cooling of accelerated flow in a subscale combustion chamber. Journal of propulsion and power, 25(2):443–451, 2009. [56](#)
- M. S. Bak, H. Do, M. G. Mungal, and M. A. Cappelli. Plasma-assisted stabilization of laminar premixed methane/air flames around the lean flammability limit. Combustion and Flame, 159(10):3128–3137, 2012. [99](#), [107](#), [108](#)
- R. Balachandran, B. O. Ayoola, C. F. Kaminski, A. P. Dowling, and E. Mastorakos. Experimental investigation of the nonlinear response of turbulent premixed flames to imposed inlet velocity oscillations. Combust. Flame, 143(1-2):37 – 55, 2005. [150](#)
- S. Barbosa, G. Pilla, P. Scouffaire, S. Ducruix, C. O. Laux, and D. Veynante. Influence of nanosecond repetitively pulsed discharges on the stability of a swirled propane/air burner representative of an aeronautical combustor. Phil. Trans. R. Soc. A, 373 (2048):20140335, 2015. [102](#), [103](#)
- M. Bauerheim, G. Staffelbach, N.A. Worth, J.R. Dawson, L.Y.M. Gicquel, and T. Poinsot. Sensitivity of les-based harmonic flame response model for turbulent swirled flames and impact on the stability of azimuthal modes. Proc. Combust. Inst., 35(3):3355 – 3363, 2015. [12](#)
- B. D. Bellows, M. K. Bobba, J. M. Seitzman, and T. Lieuwen. Nonlinear flame transfer function characteristics in a swirl-stabilized combustor. Journal of Engineering for Gas Turbines and Power, 129(4):954–961, 2007a. [140](#)

- M. K. Bellows, B. D. Bobba, A. Forte, J. M. Seitzman, and T. Lieuwen. Flame transfer function saturation mechanisms in a swirl-stabilized combustor. Proceedings of the combustion institute, 31(2):3181–3188, 2007b. 140
- S. Berger, S. Richard, F. Duchaine, and L. Gicquel. Variations of anchoring pattern of a bluff-body stabilized laminar premixed flame as a function of the wall temperature. In ASME Turbo Expo 2016: Turbomachinery Technical Conference and Exposition, pages V05BT17A004–V05BT17A004. American Society of Mechanical Engineers, 2016. 10, 11
- R. W. Bilger. Turbulent diffusion flames. Ann. Rev. Fluid Mech. , 21:101, 1989. 33, 35
- P. Billant, J.-M. Chomaz, and P. Huerre. Experimental study of vortex breakdown in swirling jets. J. Fluid Mech. , 376:183–219, 1998. 119
- A.L. Birbaud, D. Durox, and S. Candel. Upstream flow dynamics of a laminar premixed conical flame submitted to acoustic modulations. Combust. Flame, 146(3):541–552, 2006. 12
- S. T. Bose and G. I. Park. Wall-modeled large-eddy simulation for complex turbulent flows. Annual Review of Fluid Mechanics, 50(1), 2018. 57
- D. Breden, L. L. Raja, C. A. Idicheria, P. M. Najt, and S. Mahadevan. A numerical study of high-pressure non-equilibrium streamers for combustion ignition application. Journal of Applied Physics, 114(8):083302, 2013. 106
- U. Brummund, A. Cessou, and A. Vogel. Plif imaging measurements of a co-axial rocket injector spray at elevated pressure. In Symposium (International) on Combustion, volume 26, pages 1687–1695. Elsevier, 1996. 56
- G. Bruneaux, K. Akselvoll, T. Poinot, and J. Ferziger. Flame-wall interaction in a turbulent channel flow. Combust. Flame, 107(1/2):27–44, 1996. 13
- G. Bruneaux, T. Poinot, and J. H. Ferziger. Premixed flame-wall interaction in a turbulent channel flow: budget for the flame surface density evolution equation and modelling. J. Fluid Mech. , 349:191–219, 1997. 13
- O. Cabrit. Modelisation des flux parietaux sur les tuyeres des moteurs a propergol solide. PhD thesis, 2009. 51, 57, 58, 59, 234
- S. Candel. Combustion instabilities coupled by pressure waves and their active control. In 24th Symp. (Int.) on Combustion, pages 1277–1296. The Combustion Institute, Pittsburgh, 1992. 3
- S. Candel. Combustion dynamics and control: progress and challenges. Proc. Combust. Inst. , 29(1):1–28, 2002. 3, 91, 94, 95
- S. Candel, G. Herding, R. Synder, P. Scouffaire, C. Rolon, L. Vingert, M. Habiballah, F. Grisch, M. Pé, Bouchardy P., Stepowski D., Cessou A., and Colin P. Experimental investigation of shear coaxial cryogenic jet flames. Journal of Propulsion and Power, 14(5):826–834, 1998. 56

- S. Candel, M. Juniper, G. Singla, P. Scoufflaire, and C. Rolon. Structure and dynamics of cryogenic flames at supercritical pressure. Combustion Science and Technology, 178(1-3):161–192, 2006. [56](#)
- S. Candel, T. Durox, D. Schuller, J.-F. Bourgoignie, and J. P. Moeck. Dynamics of Swirling Flames. Ann. Rev. Fluid Mech., 46(1):147–173, January 2014. [151](#)
- M. Castela. Direct numerical simulations of plasma-assisted ignition in quiescent and turbulent flow conditions. PhD thesis, CentraleSupélec, 2016. [109](#)
- M. Castela, B. Fiorina, A. Coussement, O. Gicquel, N. Darabiha, and C. O. Laux. Modelling the impact of non-equilibrium discharges on reactive mixtures for simulations of plasma-assisted ignition in turbulent flows. Combust. Flame, 166:133–147, 2016. [109](#), [110](#), [170](#), [184](#), [194](#), [218](#), [235](#)
- M. Castela, S. Stepanyan, B. Fiorina, A. Coussement, O. Gicquel, N. Darabiha, and C. O. Laux. A 3-d dns and experimental study of the effect of the recirculating flow pattern inside a reactive kernel produced by nanosecond plasma discharges in a methane-air mixture. Proceedings of the Combustion Institute, 36(3):4095–4103, 2017. [109](#), [110](#)
- M. P. Celano, S. Silvestri, G. Schlieben, C. Kirchberger, and O. J. Haidn. Injector characterization for a gox-gch4 single element combustion chamber. In 5th European Conference For Aeronautics And Space Sciences (EUCASS), 2013. [56](#)
- M. P. Celano, S. Silvestri, G. Schlieben, C. Kirchberger, O. J. Haidn, T. Dawson, R. Ranjan, and S. Menon. Experimental and numerical investigation of GOX-GCH4 shear-coaxial injector element. In SP-2014-2969417, 2014. [56](#)
- M.P. Celano, S. Silvestri, J. Pauw, N. Perakis, F. Schily, D. Suslov, and O. J. Haidn. Heat flux evaluation methods for a single element heat-sink chamber. In 6th European Conference of Aeronautics and Space Science, Krakow, Poland, 2015. [56](#)
- D. R. Chapman. Computational aerodynamics development and outlook. AIAA Journal, 17(12):1293–1313, December 1979. doi: 10.2514/3.61311. [57](#)
- F. Charlette, D. Veynante, and C. Meneveau. A power-law wrinkling model for LES of premixed turbulent combustion: Part I - non-dynamic formulation and initial tests. Combust. Flame, 131:159–180, 2002. [47](#), [127](#)
- J. H. Chen, A. Choudhary, B. deSupinski, M. DeVries, E. R. Hawkes, S. Klasky, W. K. Liao, K. L. Ma, J. Mellor-Crummey, N. Podhorszki, R. Sankaran, S. Shende, and C. S. Yoo. Terascale direct numerical simulations of turbulent combustion using s3d. Comput. Sci. Disc., 2(015001), 2009. [40](#)
- J. M. Cohen and A. Banaszuk. Factors affecting the control of unstable combustors. Journal of propulsion and power, 19(5):811–821, 2003. [96](#)
- O. Colin and M. Rudgyard. Development of high-order taylor-galerkin schemes for unsteady calculations. J. Comput. Phys., 162(2):338–371, 2000. [50](#), [117](#), [169](#)

- O. Colin, F. Ducros, D. Veynante, and T. Poinso. A thickened flame model for large eddy simulations of turbulent premixed combustion. Phys. Fluids , 12(7):1843–1863, 2000. [46](#), [47](#), [169](#)
- F. Collin-Bastiani, O. Vermorel, C. Lacour, B. Lecordier, and B. Cuenot. Dns of spark ignition using analytically reduced chemistry including plasma kinetics. Proceedings of the Combustion Institute, 2018. [170](#), [185](#), [186](#), [194](#)
- L. Crocco. Aspects of combustion instability in liquid propellant rocket motors. Part I. J. American Rocket Society , 21:163–178, 1951. [150](#)
- L. Crocco. Aspects of combustion instability in liquid propellant rocket motors. part II. J. American Rocket Society , 22:7–16, 1952. [150](#)
- B. Cuenot and T. Poinso. Effects of curvature and unsteadiness in diffusion flames. implications for turbulent diffusion flames. Proc. Combust. Inst. , 25:1383–1390, 1994. [37](#)
- F. E. C. Culick and P. Kuentzmann. Unsteady Motions in Combustion Chambers for Propulsion Systems. NATO Research and Technology Organization, 2006. [90](#), [95](#), [97](#)
- F. Cuoco, B. Yang, and M. Oschwald. Experimental investigation of lox/h₂ and lox/ch₄ sprays and flames. In 24th International Symposium on Space Technology and Science, 2004. [56](#)
- A. D’Angola, G. Colonna, C. Gorse, and M. Capitelli. Thermodynamic and transport properties in equilibrium air plasmas in a wide pressure and temperature range. The European Physical Journal D-Atomic, Molecular, Optical and Plasma Physics, 46(1):129–150, 2008. [22](#), [169](#), [183](#)
- J. Daou and M. Matalon. Influence of conductive heat-losses on the propagation of premixed flames in channels. Combustion and Flame, 128(4):321–339, 2002. [10](#)
- M. De Rosa, J. Sender, H. Zimmermann, and M. Oschwald. Cryogenic spray ignition at high altitude conditions. In 42nd AIAA/ASME/SAE/ASEE Joint Propulsion Conference & Exhibit, page 4539, 2006. [56](#)
- A. C. DeFilippo and J.-Y. Chen. Modeling plasma-assisted methane–air ignition using pre-calculated electron impact reaction rates. Combustion and Flame, 172:38–48, 2016. [106](#)
- A. Delataillade, F. Dabireau, B. Cuenot, and T. Poinso. Flame/wall interaction and maximum heat wall fluxes in diffusion burners. Proc. Combust. Inst. , 29:775–780, 2002. [14](#)
- A. Di Vita. On Rayleigh’s criterion of thermo-acoustics. PhD thesis, Università degli Studi di Genova, 2016. [97](#)
- M. DiCicco and J. Buckmaster. Role of slip in the generation of acoustic instabilities in gas turbines. Journal of propulsion and power, 12(1):34–40, 1996. [94](#)

- N. Docquier and S. Candel. Combustion control and sensors: a review. Progress in energy and combustion science, 28(2):107–150, 2002. 3, 95
- J. Donea and A. Huerta. Finite Element Methods for Flow Problems. John Wiley & Sons Inc, New York, 2003. 50
- L. H. Dorey, P. Grenard, L. Matuszewski, and L. Selle. Experimental and numerical study of a cooled rocket combustion chamber. In 15th International Heat Transfer Conference IHTC15-9238, 2014. 57
- A. Dreizler and B. Böhm. Advanced laser diagnostics for an improved understanding of premixed flame-wall interactions. Proceedings of the Combustion Institute, 35(1): 37–64, 2015. 13
- F. Duchaine, F. Boudy, D. Durox, and T. Poinsot. Sensitivity analysis of transfer functions of laminar flames. Combust. Flame, 158(12):2384–2394, 2011. 151, 231
- F. Ducros, F. Nicoud, and T. Poinsot. Wall-adapating local eddy-viscosity models for simulations in complex geometries. In ICFD, pages 293–300. Baines M. J., 1998. 44
- D. Durox, T. Schuller, N. Noiray, and S. Candel. Experimental analysis of nonlinear flame transfer functions for different flame geometries. Proc. Combust. Inst., 32(1): 1391–1398, 2009. 150
- A. Duvvur, C.H. Chiang, and W.A. Sirignano. Oscillatory fuel droplet vaporization-driving mechanism for combustion instability. Journal of Propulsion and Power, 12(2):358–365, 1996. 94
- R. R. Erickson and M. C. Soteriou. The influence of reactant temperature on the dynamics of bluff body stabilized premixed flames. Combustion and Flame, 158(12): 2441–2457, 2011. 8
- O. A. Ezekoye, R. Greif, and D. Lee. Increased surface temperature effects on wall heat transfer during unsteady flame quenching. In 24th Symp. (Int.) on Combustion, pages 1465–1472. The Combustion Institute, Pittsburgh, 1992. 13
- B. Franzelli. Impact of the chemical description on direct numerical simulations and Large Eddy Simulations of turbulent combustion in industrial aero-engines - TH/CFD/11/101. PhD thesis, Université de Toulouse, France - MeGeP Dynamique des Fluides, 2011. 48, 234
- B. Franzelli, E. Riber, L.Y.M. Gicquel, and T. Poinsot. Large eddy simulation of combustion instabilities in a lean partially premixed swirled flame. Combust. Flame, 159(2):621 – 637, 2012. ISSN 0010-2180. doi: <http://dx.doi.org/10.1016/j.combustflame.2011.08.004>. URL <http://www.sciencedirect.com/science/article/pii/S0010218011002525>. 49, 127, 169
- M. Frenklach, H. Wang, M. Goldenberg, G. P. Smith, D. M. Golden, C. T. Bowman, R. K. Hanson, W. C. Gardiner, and V. Lissianki. GRI-mech: an optimized detailed chemical reaction mechanism for methane combustion. Technical Report GRI-Report GRI-95/0058, Gas Research Institute, 1995. 50

- J. Fritz, M. Kröner, and T. Sattelmayer. Flashback in a swirl burner with cylindrical premixing zone. In ASME Turbo Expo 2001: Power for Land, Sea, and Air, pages V002T02A021–V002T02A021. American Society of Mechanical Engineers, 2001. 13
- M. Germano, U. Piomelli, P. Moin, and W. Cabot. A dynamic subgrid-scale eddy viscosity model. Phys. Fluids, 3(7):1760–1765, 1991. 44
- A. Ghani. LES of self-excited transverse combustion instabilities in perfectly-premixed and swirling spray flames. PhD thesis, Institut National Polytechnique de Toulouse, 2016. 133, 151, 152
- A. Ghani and T. Poinso. Flame quenching at walls: A source of sound generation. Flow, Turbulence and Combustion, pages 1–12, 2017. 14
- A. Ghani, T. Poinso, L. Gicquel, and J.-D. Muller. Les study of transverse acoustic instabilities in a swirled kerosene/air combustion chamber. Flow, Turb. and Combustion, 96:207–226, 2016. 160
- A. Giauque, L. Selle, T. Poinso, H. Buechner, P. Kaufmann, and W. Krebs. System identification of a large-scale swirled partially premixed combustor using LES and measurements. J. Turb., 6(21):1–20, 2005. 151
- N. Gourdain, L. Gicquel, M. Montagnac, O. Vermorel, M. Gazaix, G. Staffelbach, M. Garcia, J.F. Boussuge, and T. Poinso. High performance parallel computing of flows in complex geometries: I. methods. Comput. Sci. Disc., 2:015003, 2009. 14
- C. J Goy, S. R. James, and S. Rea. Monitoring combustion instabilities: E. on uk’s experience. Progress in Astronautics and Aeronautics, 210:163, 2005. 90
- S. Gröning, J. S. Hardi, D. Suslov, and M. Oswald. Injector-driven combustion instabilities in a hydrogen/oxygen rocket combustor. Journal of Propulsion and Power, (0):560–573, 2016. 56
- S. Gröning, J. S. Hardi, D. Suslov, and M. Oswald. Influence of hydrogen temperature on the stability of a rocket engine combustor operated with hydrogen and oxygen. CEAS Space Journal, 9(1):59–76, 2017. 56
- A. Gruber, R. Sankaran, E. R. Hawkes, and J. Chen. Turbulent flame–wall interaction: a direct numerical simulation study. J. Fluid Mech., 658:5–32, 2010. 14
- T. F. Guiberti, P. Durox, D. Scouffaire, and T. Schuller. Impact of heat loss and hydrogen enrichment on the shape of confined swirling flames. Proceedings of the Combustion Institute, 35(2):1385–1392, 2015. 7
- O. Gurliat, V. Schmidt, O. J. Haidn, and M. Oswald. Ignition of cryogenic h₂/lox sprays. Aerospace Science and Technology, 7(7):517–531, 2003. 56
- L. C. Haber, U. Vandsburger, W. R. Saunders, and V. K. Khanna. An examination of the relationship between chemiluminescent light emissions and heat release rate under non-adiabatic conditions. In ASME Turbo Expo 2000: Power for Land, Sea, and Air, pages V002T02A041–V002T02A041. American Society of Mechanical Engineers, 2000. 150

- M. Habiballah, M. Orain, F. Grisch, L. Vingert, and P. Gicquel. Experimental studies of high-pressure cryogenic flames on the mascotte facility. Combustion Science and Technology, 178(1-3):101–128, 2006. 56
- C. L. Hackert, J. L. Ellzey, and O. A. Ezekoye. Effects of thermal boundary conditions on flame shape and quenching in ducts. Combustion and Flame, 112(1-2):73–84, 1998. 10
- O. J. Haidn, V. Schmidt, and J. Sender. Flow visualization of interacting cryogenic coaxial jets. 14th ILASS-Europe'98, pages 602–608, 1998. 56
- L. Hakim, T. Schmitt, S. Ducruix, and S. Candel. Dynamics of a transcritical coaxial flame under a high-frequency transverse acoustic forcing: Influence of the modulation frequency on the flame response. Combust. Flame, 162(10):3482 – 3502, 2015. 56
- J. Han, S. Dutta, and S. Ekkad. Gas turbine heat transfer and cooling technology. CRC Press, 2012. 8
- J. S. Hardi, S. K. Beinke, M. Oswald, and B. B. Dally. Coupling of cryogenic oxygen–hydrogen flames to longitudinal and transverse acoustic instabilities. Journal of Propulsion and Power, 30(4):991–1004, 2014a. 56
- J. S. Hardi, H. C. G. Martinez, M. Oswald, and B. B. Dally. Lox jet atomization under transverse acoustic oscillations. Journal of propulsion and power, 30(2):337–349, 2014b. 56
- U.G. Hegde, D. Reuter, B.R. Daniel, and B.T. Zinn. Flame driving of longitudinal instabilities in dump type ramjet combustors. Combustion Science and Technology, 55(4-6):125–138, 1987. 94
- G. Heid, Lecourt R. Pilla, G., and D. Lacoste. Assisted combustion of air kerosene mixture by repetitive impulse nanosecond plasma discharges. In Proc. ISABE, 2009. 104
- G. Herding, R. Snyder, C. Rolon, and S. Candel. Investigation of cryogenic propellant flames using computerized tomography of emission images. Journal of propulsion and power, 14(2):146–151, 1998. 56
- J. Hermann and S. Hoffmann. Implementation of active control in a full-scale gas-turbine combustor. Combustion Instabilities in Gas Turbine Engines: Operational Experience, Fundamental Mechanisms, and Modeling, 2004. 97
- S. Hermeth, G. Staffelbach, L.Y.M. Gicquel, and T. Poinso. LES evaluation of the effects of equivalence ratio fluctuations on the dynamic flame response in a real gas turbine combustion chamber. Proc. Combust. Inst. , 34(2):3165 – 3173, 2013. 151, 152, 160
- J. O. Hirschfelder, C. F. Curtiss, and R. B. Bird. Molecular theory of gases and liquids. John Wiley & Sons, New York, 1969. 21

- G. Im Hong, J. H. Chen, and J.-Y. Chen. Chemical response of methane/air diffusion flames to unsteady strain rate. Combustion and Flame, 118(1):204–212, 1999. 31
- Y. Huang and V. Yang. Dynamics and stability of lean-premixed swirl-stabilized combustion. Prog. Energy Comb. Sci. , 35(4):293–364, 2009. 94, 95, 96
- I. R. Hurle, R. B. Price, T. M. Sudgen, and A. Thomas. Sound emission from open turbulent premixed flames. Proc. R. Soc. Lond. , 303:409–427, 1968. 94
- A. Iannetti, N. Girard, Ni. Ravier, E. Edeline, and D. Tchou-Kien. Prometheus, a low cost lox/ch4 engine prototype. In 53rd AIAA/SAE/ASEE Joint Propulsion Conference, page 4750, 2017. 3, 4
- M. Ihme. Combustion and engine-core noise. Annual Review of Fluid Mechanics, 49:277–310, 2017. 14
- U. Ingard and V. K. Singhal. Effect of flow on the acoustic resonances of an open-ended duct. J. Acous. Soc. Am. , 58(4):788–793, 1975. 95
- T. Jaravel, E. Riber, B. Cuenot, and G. Bulat. Large eddy simulation of an industrial gas turbine combustor using reduced chemistry with accurate pollutant prediction. Proc. Combust. Inst. , pages –, 2016. 47, 117, 127
- J. Jarosiński. Flame quenching by a cold wall. Combustion and Flame, 50:167–175, 1983. 10
- J. Jarosinski. A survey of recent studies on flame extinction. Combust. Sci. Technol. , 12:81–116, 1986. 13
- W. P. Jones and R. P. Lindstedt. Global reaction schemes for hydrocarbon combustion. Combust. Flame, 73:222–233, 1988. 48
- Y. Ju and W. Sun. Plasma assisted combustion: Dynamics and chemistry. Progress in Energy and Combustion Science, 48:21–83, 2015. 3, 97, 98, 99, 100
- M. Juniper, A. Tripathi, P. Scoufflaire, J.-C. Rolon, and S. Candel. Structure of cryogenic flames at elevated pressures. Proceedings of the Combustion Institute, 28(1):1103–1109, 2000. 56
- R. Kaess, W. Polifke, T. Poinso, N. Noiray, D. Durox, T. Schuller, and S. Candel. Cfd-based mapping of the thermo-acoustic stability of a laminar premix burner. In Proc. of the Summer Program , pages 289–302, Center for Turbulence Research, NASA AMES, Stanford University, USA, 2008. 11
- N. Karimi, M.J. Brear, S.-H. Jin, and J.P. Monty. Linear and non-linear forced response of a conical, ducted, laminar premixed flame. Combust. Flame, pages 2201–2212, 2009. 91, 150
- A. Kaufmann, F. Nicoud, and T. Poinso. Flow forcing techniques for numerical simulation of combustion instabilities. Combust. Flame, 131:371–385, 2002. 151

- W.M. Kays, M.E. Crawford, and B. Weigand. Convective heat and mass transfer. McGraw-Hill Inc., New York, 2004. 58
- A. Kazakov and M. Frenklach. 107
- K.S. Kedia and A.F. Ghoniem. Mechanisms of stabilization and blowoff of a premixed flame downstream of a heat-conducting perforated plate. Combust. Flame, 159(3): 1055–1069, 2012. 10
- K.S. Kedia and A.F. Ghoniem. The anchoring mechanism of a bluff-body stabilized laminar premixed flame. Combust. Flame, 161(9):2327–2339, 2014. 10
- K.S. Kedia and A.F. Ghoniem. The response of a harmonically forced premixed flame stabilized on a heat-conducting bluff-body. Proceedings of the Combustion Institute, 35(1):1065–1072, 2015. 10
- D. W. Kendrick, T. J. Anderson, and W. A. Sowa. Acoustic sensitivities of lean-premixed fuel injectors in a single nozzle rig. American Society of Mechanical Engineers, 98-GT-382, 1998. 93
- J. S. Kim. Effects of turbulence on linear acoustic instability: Spatial inhomogeneity. PROGRESS IN ASTRONAUTICS AND AERONAUTICS, 169:431–454, 1995. 95
- K. T. Kim, J. G. Lee, B. D. Quay, and D. A. Santavicca. Response of partially premixed flames to acoustic velocity and equivalence ratio perturbations. Combust. Flame, 157(9):1731 – 1744, 2010. 150
- S. Kobayashi, Z. Bonaventura, F. Tholin, N. Popov, and A. Bourdon. Study of nanosecond discharges in h₂–air mixtures at atmospheric pressure for plasma assisted combustion applications. Plasma Sources Science and Technology, 2017. 106
- A. N. Kolmogorov. The local structure of turbulence in incompressible viscous fluid for very large reynolds numbers. C. R. Acad. Sci. , USSR, 30:301, 1941. 27, 39, 44
- V. Kornilov, R. Rook, J. ten Thijsse Boonkcamp, and L. de Goeij. Experimental and numerical investigation of the acoustic response of multi-slit bunsen burners. Combust. Flame, pages 1957–1970, 2009. 150, 151
- I. N. Kosarev, N. L. Aleksandrov, S. V. Kindysheva, S. M. Starikovskaia, and A. Starikovskii. Kinetics of ignition of saturated hydrocarbons by nonequilibrium plasma: Ch 4-containing mixtures. Combustion and flame, 154(3):569–586, 2008. 106
- C. H. Kruger, C. O. Laux, L. Yu, D. M. Packan, and L. Pierrot. Nonequilibrium discharges in air and nitrogen plasmas at atmospheric pressure. Pure and App. Chem., 74(3):337–347, 2002. ISSN 0033-4545. 99
- D. Kuhl, A. Woschnak, and O. J. Haidn. Coupled heat transfer and stress analysis of rocket combustion chambers. AIAA Paper, (1998-3373), 1998. 9

- K. K. Kuo. Principles of combustion. John Wiley & Sons, Inc., Hoboken, New Jersey, 2005 Second Edition. [19](#), [23](#), [27](#)
- D. A. Lacoste, J. P. Moeck, D. Durox, C. O. Laux, and T. Schuller. Effect of nanosecond repetitively pulsed discharges on the dynamics of a swirl-stabilized lean premixed flame. J. Eng. Gas Turb. and Power , 135(10):101501, 2013a. ISSN 0742-4795. [105](#), [107](#), [112](#), [113](#), [114](#), [216](#), [217](#), [224](#), [228](#), [231](#)
- D. A. Lacoste, D. A. Xu, J. P. Moeck, and C. O. Laux. Dynamic response of a weakly turbulent lean-premixed flame to nanosecond repetitively pulsed discharges. Proc. Combust. Inst. , 34(2):3259–3266, 2013b. ISSN 15407489. [104](#), [206](#)
- B. Lakshminarayana. Fluid dynamics and heat transfer of turbomachinery. John Wiley & Sons, 1995. [8](#)
- S. H. Lam and D. A. Goussis. The csp method for simplifying kinetics. International Journal of Chemical Kinetics, 26(4):461–486, 1994. [49](#)
- N. Lamarque. Schémas numériques et conditions limites pour la simulation aux grandes échelles de la combustion diphasique dans les foyers d’hélicoptère. Phd thesis, INP Toulouse, 2007. [50](#)
- S. Lamige, J. Min, C. Galizzi, F. André, F. Baillet, D. Escudié, and K. M. Lyons. On preheating and dilution effects in non-premixed jet flame stabilization. Combustion and Flame, 160(6):1102–1111, 2013. [8](#)
- W. Lang, T. Poinso, and S. Candel. Active control of combustion instability. Combust. Flame, 70:281–289, 1987. [3](#)
- J. Larsson, S. Kawai, J. Bodart, and I. Bermejo-Moreno. Large eddy simulation with modeled wall-stress: recent progress and future directions. Mechanical Engineering Reviews, 3(1):15–00418, 2016. [57](#)
- C. O. Laux, et al., G. D. Stancu, D. Rusterholtz, and D. A. Xu. Nanosecond repetitively pulsed discharges in plasma-assisted combustion. 31st ICPIG, page 4, 2013. [101](#), [103](#)
- P. D. Lax and B. Wendroff. Systems of conservation laws. Commun. Pure Appl. Math. , 13:217–237, 1960. [50](#)
- A. H. Lefebvre. Gas turbine combustion: alternative fuels and emissions. CRC press, 2010. [2](#), [5](#), [7](#)
- A. H. Lefebvre, A. R. A. F. Ibrahim, and N. C. Benson. Factors affecting fresh mixture entrainment in bluff-body stabilized flames. Combustion and Flame, 10(3):231–239, 1966. [6](#)
- J.-Ph. L gier. Simulations num riques des instabilit s de combustion dans les foyers a ronautiques. Phd thesis, INP Toulouse, 2001. [49](#), [127](#)

- J.-Ph. L egier, T. Poinso, and D. Veynante. Dynamically thickened flame LES model for premixed and non-premixed turbulent combustion. In Proc. of the Summer Program, pages 157–168. Center for Turbulence Research, NASA Ames/Stanford Univ., 2000. [46](#), [47](#), [61](#), [127](#), [169](#)
- D. C. Leslie and G. L. Quarini. The application of turbulence theory to the formulation of subgrid modelling procedures. Journal of fluid mechanics, 91(1):65–91, 1979. [44](#)
- H. Liang and T. Maxworthy. An experimental investigation of swirling jets. J. Fluid Mech., 525:115–159, 2005. [125](#)
- P. A. Libby and F. A. Williams. Turbulent combustion: fundamental aspects and a review. In Turbulent Reacting Flows, pages 2–61. Academic Press London, 1994. [34](#)
- T. Lieuwen. Modeling premixed combustion-acoustic wave interactions: A review. J. Prop. Power, 19(5):765–781, 2003. [3](#)
- T. Lieuwen and V. Yang. Combustion Instabilities in Gas Turbine Engines. Operational Experience, Fundamental Mechanisms and Modeling. Prog. in Astronautics and Aeronautics AIAA Vol 210, 2005. [91](#), [93](#), [94](#)
- T. Lieuwen, H. Torres, C. Johnson, and B. Zinn. A mechanism of combustion instability in lean premixed gas turbine combustors. J. Eng. Gas Turb. and Power, 123(1):182–189, 2001. [93](#)
- T. Lieuwen, R. Rajaram, Y. Neumeier, and S. Nair. Measurements of incoherent acoustic wave scattering from turbulent premixed flames. Proceedings of the Combustion Institute, 29(2):1809–1815, 2002. [95](#)
- D. K. Lilly. The representation of small-scale turbulence in numerical simulation experiments. In Proceedings of the IBM Scientific Computing Symposium on Environmental Sciences, Yorktown Heights, USA, 1967. [44](#)
- D. K. Lilly. A proposed modification of the germano sub-grid closure method. Phys. Fluids, 4(3):633–635, 1992. URL [LES](#). [44](#)
- A. Linan. The asymptotic structure of counterflow diffusion flames for large activation energies. Acta Astronautica, 1:1007, 1974. [34](#)
- J. P. Longwell, E. E Frost, and M. A. Weiss. Flame stability in bluff body recirculation zones. Industrial & Engineering Chemistry, 45(8):1629–1633, 1953. [5](#)
- T. Lu and C. Law. A directed relation graph method for mechanism reduction. Proceedings of the Combustion Institute, 30(1):1333–1341, 2005. [49](#), [50](#)
- T. Lu, Y. Ju, and C. Law. Complex csp for chemistry reduction and analysis. Combustion and Flame, 126(1):1445–1455, 2001. [50](#)
- O. Lucca-Negro and T. O’Doherty. Vortex breakdown: a review. Prog. Energy Comb. Sci., 27:431–481, 2001. [119](#)

- J. Lux and O.J. Haidn. Flame stabilization in high-pressure liquid oxygen/methane rocket engine combustion. Journal of Propulsion and Power, 25(1):15–23, 2009. 56
- U. Maas and S. B. Pope. Implementation of simplified chemical kinetics based on low-dimensional manifolds. Proc. Combust. Inst., 24:719–729, 1992. 49
- D. Maestro, L. Selle, and B. Cuenot. Thermally chained LES of a GCH₄/GOX single element combustion chamber. Proceedings of the 2015 Summer Program, 2015. 61
- D. Maestro, B. Cuenot, A. Chemnitz, T. Sattelmayer, C. Roth, O. Haidn, Y. Daimon, R. Keller, P. M Gerlinger, G. Frank, et al. Numerical investigation of flow and combustion in a single-element gch₄/gox rocket combustor: Chemistry modeling and turbulence-combustion interaction. In 52nd AIAA/SAE/ASEE Joint Propulsion Conference, 2016. 61
- D. Maestro, B. Cuenot, and L. Selle. Large eddy simulation of flow and combustion in a single-element gch₄/gox rocket combustor. In 7th European Conference for Aeronautics and Space Sciences (EUCASS), 2017. 61
- R. Mari. Influence of heat transfer on high pressure flame structure and stabilization in liquid rocket engines. PhD thesis, 2015. 56
- M. Masquelet, S. Menon, Y. Jin, and R. Friedrich. Simulation of unsteady combustion in a lox-gh₂ fueled rocket engine. Aerospace Science and Technology, 13(8):466–474, 2009. 56, 57
- S. Matsuyama, J. Shinjo, Y. Mizobuchi, and S. Ogawa. A numerical investigation on shear coaxial lox/gh₂ jet flame at supercritical pressure. In 44th AIAA Aerospace Sciences Meeting and Exhibit, page 761, 2006. 56
- W. Mayer and H. Tamura. Propellant injection in a liquid oxygen/gaseous hydrogen rocket engine. Journal of Propulsion and Power, 12(6):1137–1147, 1996. 56
- W. Mayer, B. Ivancic, A. Schik, and U. Hornung. Propellant atomization and ignition phenomena in liquid oxygen/gaseous hydrogen rocket combustors. Journal of Propulsion and Power, 17(4):794–799, 2001. 56
- K. McManus, T. Poinot, and S. Candel. A review of active control of combustion instabilities. Prog. Energy Comb. Sci., 19:1–29, 1993. 3, 95
- D. Mejia, L. Selle, R. Bazile, and T. Poinot. Wall-temperature effects on flame response to acoustic oscillations. Proc. Combust. Inst., 35(3201-3208):3, August 2014. 12
- D. Mejia, M. Miguel-Brebion, A. Ghani, T. Kaiser, F. Duchaine, L. Selle, and T. Poinot. Influence of flame-holder temperature on the acoustic flame transfer functions of a laminar flame. Combustion and Flame, 188:5–12, 2018. 13
- C. Mockett, M. Fuchs, and F. Thiele. Progress in des for wall-modelled les of complex internal flows. Computers & Fluids, 65:44–55, 2012. 57

- J. Moeck, D. A. Lacoste, C. O. Laux, and C. O. Paschereit. Control of combustion dynamics in a swirlstabilized combustor with nanosecond repetitively pulsed discharges. 51st AIAA Aerospace Sciences Meeting, (January):AIAA-2013-565, 2013. [104](#), [105](#), [106](#), [206](#)
- V. Moureau, G. Lartigue, Y. Sommerer, C. Angelberger, O. Colin, and T. Poinso. Numerical methods for unsteady compressible multi-component reacting flows on fixed and moving grids. J. Comput. Phys. , 202(2):710–736, 2005. [51](#)
- H. Müller, M. Pfitzner, and S. Matheis, J. and Hickel. Large-eddy simulation of coaxial H_2/O_2 injection at trans-and supercritical conditions. Journal of Propulsion and Power, 32(1):46–56, 2015. [56](#)
- H. Müller, J. Zips, M. Pfitzner, D. Maestro, B. Cuenot, S. Menon, R. Ranjan, P. Tudisco, and L. Selle. Numerical investigation of flow and combustion in a single-element CH_4/O_2 rocket combustor: A comparative LES study. In 52nd AIAA/SAE/ASME Joint Propulsion Conference, 2016. [61](#)
- S. Nagaraja, W. Sun, and V. Yang. Effect of non-equilibrium plasma on two-stage ignition of n-heptane. Proceedings of the Combustion Institute, 35(3):3497–3504, 2015. [107](#)
- J. Natarajan, T. Lieuwen, and J. Seitzman. Laminar flame speeds of H_2/CO mixtures: Effect of CO_2 dilution, preheat temperature, and pressure. Combust. Flame, 151(1-2):104–119, 2007. [7](#)
- F. Nicoud, H. Baya Toda, O. Cabrit, S. Bose, and J. Lee. Using singular values to build a subgrid-scale model for large eddy simulations. Phys. Fluids , 23(8):085106, 2011. [45](#), [83](#), [117](#), [169](#)
- W. L. Nighan. Electron energy distributions and collision rates in electrically excited N_2 , CO , and CO_2 . Physical Review A, 2(5):1989, 1970. [99](#)
- N. Noiray, D. Durox, T. Schuller, and S. Candel. Passive control of combustion instabilities involving premixed flames anchored on perforated plates. Proc. Combust. Inst. , 31:1283–1290, 2007. [12](#)
- J. C. Oefelein. Thermophysical characteristics of shear-coaxial O_2 - H_2 flames at supercritical pressure. Proceedings of the Combustion Institute, 30(2):2929–2937, 2005. [56](#)
- J. C. Oefelein and V. Yang. Comprehensive review of liquid-propellant combustion instabilities in F-1 engines. J. Prop. Power , 9(5):657–677, 1993. [90](#)
- M. Oswald, R. Lecourt, U. Brummund, A. Cessou, and O. J. Haidn. Optical diagnostics of atomization and combustion for cryogenic liquid rocket propulsion. International Journal of Energetic Materials and Chemical Propulsion, 4(1-6), 1997. [56](#)

- D. Z. Pai, et al., and C. O. Laux. Nanosecond repetitively pulsed discharges in air at atmospheric pressure—the spark regime. Plasma Sources Science and Technology, 19(6):065015, 2010. [99](#)
- P. Palies, D. Durox, T. Schuller, and S. Candel. The combined dynamics of swirler and turbulent premixed swirling flames. Combust. Flame, 157:1698–1717, 2010. [151](#), [159](#)
- P. Palies, T. Schuller, D. Durox, L. Y. M. Gicquel, and S. Candel. Acoustically perturbed turbulent premixed swirling flames. Phys. Fluids, 23(3):037101–15, 2011. [151](#)
- S. V. Pancheshnyi, et al., A. Bourdon, and C. O. Laux. Ignition of propane-air mixtures by a repetitively pulsed nanosecond discharge. IEEE Trans. on Pl. Sci., 34(6):2478–2487, 2006. ISSN 00933813. [100](#)
- C. O. Paschereit, E. Gutmark, and W. Weisenstein. Control of thermoacoustic instabilities and emissions in an industrial-type gas-turbine combustor. In Symposium (International) on Combustion, volume 27, pages 1817–1824. Elsevier, 1998. [94](#)
- C. Pera and J. Reveillon. Direct numerical simulation of spray flame/acoustic interactions. Proceedings of the Combustion Institute, 31(2):2283–2290, 2007. [94](#)
- N. Perakis, M. P. Celano, and O. J. Haidn. Heat flux and temperature evaluation in a rectangular multi-element gox/gch4 combustion chamber using an inverse heat conduction method. In 7th European Conference for Aeronautics and Space Sciences (EUCASS), 2017. [56](#)
- N. Peters. Turbulent combustion. Cambridge university press, 2000. [27](#), [32](#), [33](#), [60](#)
- G. Pilla, D. Galley, et al., F. Lacas, D. Veynante, and C. O. Laux. Stabilization of a turbulent premixed flame using a nanosecond repetitively pulsed plasma. IEEE Transactions on Plasma Science, 34(6):2471–2477, 2006. [101](#), [104](#)
- G. L. Pilla, et al., D. Veynante, and C. O. Laux. Stabilization of a swirled propane-air flame using a nanosecond repetitively pulsed plasma. IEEE Trans. on Pl. Sci., 36(4 PART 1):940–941, 2008. ISSN 00933813. [102](#)
- U. Piomelli. Wall-layer models for large-eddy simulations. Prog. Aerospace Sci., 44(6):437–446, 2008. doi: 10.1016/j.paerosci.2008.06.001. [57](#)
- H. Pitsch. Large eddy simulation of turbulent combustion. Ann. Rev. Fluid Mech., 38:453–482, 2006. [46](#)
- T. Poinot. Controle actif indirect des instabilites de combustion. Centralien, 1991. [51](#)
- T. Poinot. Prediction and control of combustion instabilities in real engines. Proceedings of the Combustion Institute, 36(1):1–28, 2017. [3](#)
- T. Poinot and S. Lele. Boundary conditions for direct simulations of compressible viscous flows. J. Comput. Phys., 101(1):104–129, 1992. doi: 10.1016/0021-9991(92)90046-2. [116](#)

- T. Poinso and D. Veynante. Theoretical and Numerical Combustion. Third Edition (www.cerfacs.fr/elearning), 2011. [13](#), [19](#), [25](#), [27](#), [29](#), [31](#), [36](#), [46](#), [92](#)
- T. Poinso, A. Trouvé, D. Veynante, S. Candel, and E. Esposito. Vortex driven acoustically coupled combustion instabilities. J. Fluid Mech., 177:265–292, 1987. [94](#)
- T. Poinso, D. Veynante, F. Bourienne, S. Candel, E. Esposito, and J. Surjet. Initiation and suppression of combustion instabilities by active control. In 22nd Symp. (Int.) on Combustion, pages 1363–1370. The Combustion Institute, Pittsburgh, 1988. [92](#)
- T. Poinso, W. Lang, F. Bourienne, S. Candel, and E. Esposito. Suppression of combustion instabilities by active control. J. Prop. Power, 5:14–20, 1989. [3](#)
- T. Poinso, D. Veynante, B. Yip, A. Trouvé, J.-M. Samaniego, and S. Candel. Active control methods and applications to combustion instabilities. J. Phys. III, July: 1331–1357, 1992. [3](#)
- T. Poinso, D. Haworth, and G. Bruneaux. Direct simulation and modelling of flame-wall interaction for premixed turbulent combustion. Combust. Flame, 95(1/2):118–133, 1993. [13](#)
- W. Polifke and C. Lawn. On the low-frequency limit of flame transfer functions. Combustion and flame, 151(3):437–451, 2007. [150](#)
- S. B. Pope. Turbulent flows. Cambridge University Press, 2000. [26](#), [44](#), [57](#)
- N. A. Popov. Investigation of the mechanism for rapid heating of nitrogen and air in gas discharges. Plasma Physics Reports, 27(10):886–896, 2001. [99](#)
- N. A. Popov. Fast gas heating in a nitrogen–oxygen discharge plasma: I. kinetic mechanism. Journal of Physics D: Applied Physics, 44(28):285201, 2011. [99](#)
- L Potier. Large Eddy Simulation of the combustion and heat transfer in sub-critical rocket engines. PhD thesis, Institut National Polytechnique de Toulouse, 2018. [56](#), [57](#), [58](#), [59](#)
- W. H. Press, B. P. Flannery, S. A. Teukolsky, and W. T. Vetterling. Numerical recipes: The art of scientific computing. Cambridge U. Press, Cambridge, MA, 1986. [59](#)
- A. A. Putnam. Combustion driven oscillations in industry. American Elsevier, J.M. Beer editor, Fuel and Energy Science Series, 1971. [95](#)
- Y. P. Raizer and J. E. Allen. Gas discharge physics, volume 2. Springer Berlin, 1997. [97](#)
- L. Rayleigh. The explanation of certain acoustic phenomena. Nature, July 18:319–321, 1878. [89](#)
- L. Rayleigh. The Theory of Sound. Mac Millan (reprinted by Dover, New York, 1945), 1894. [91](#)

- D.M. Reuter, U.G. Hegde, and B.T. Zinn. Flowfield measurements in an unstable ramjet burner. Journal of Propulsion and Power, 6(6):680–685, 1990. 94
- L. F. Richardson. Weather Prediction by Numerical Process. Cambridge University Press, cambridge edition, 1922. 27
- J.-P. Rocchi. Simulations aux grandes échelles de la phase d’allumage dans un moteur fusée cryotechnique. PhD thesis, Institut National Polytechnique de Toulouse, 2014. 56
- C. Roth, O. Haidn, H. Riedmann, B. Ivancic, D. Maestro, B. Cuenot, L. Selle, Y. Daimon, A. Chemnitz, R. Keller, et al. Comparison of different modeling approaches for CFD simulations of a single-element GCH₄/GOX rocket combustor. Proceedings of the 2015 Summer Program, 2015. 61
- C. Roth, O. Haidn, A. Chemnitz, T. Sattelmayer, G. Frank, H. Müller, J. Zips, R. Keller, P. Gerlinger, D. Maestro, L. Selle, B. Cuenot, and H. Riedmann. Numerical investigation of flow and combustion in a single element gch₄/gox rocket combustor. In 52nd AIAA/SAE/ASEE Joint Propulsion Conference, 2016. 61
- S. Roux, G. Lartigue, T. Poinso, U. Meier, and C. Bérat. Studies of mean and unsteady flow in a swirled combustor using experiments, acoustic analysis and large eddy simulations. Combust. Flame, 141:40–54, 2005. 125
- M. Rudgyard. Cell vertex methods for steady inviscid flow. In Von Karman Institute for Fluid Dynamics, editor, Lectures Series 1993-04, volume 1993-04. Von Karman Institute for Fluid Dynamics, 1993. 50
- M. Rudgyard, T. Schönfeld, and I. D’Ast. A parallel library for cfd and other grid-based applications. In International Conference on High-Performance Computing and Networking, pages 358–364. Springer, 1996. 83
- A. Ruiz. Unsteady numerical simulations of transcritical turbulent combustion in liquid rocket engines. PhD thesis, Institut National Polytechnique de Toulouse, 2012. 56
- D. L. Rusterholtz, D. Z. Pai, G. D. Stancu, et al., and C. O. Laux. Ultrafast heating in nanosecond discharges in atmospheric pressure air. In 50th Aerospace Sciences Meeting, 2012. 99
- D. L. Rusterholtz, D. A. Lacoste, G. D. Stancu, D. Z. Pai, and C. O. Laux. Ultrafast heating and oxygen dissociation in atmospheric pressure air by nanosecond repetitively pulsed discharges. Journal of Physics D: Applied Physics, 46(46):464010, 2013. 165, 170
- P. Sagaut. Large eddy simulation for incompressible flows. Springer, 2002. 44
- J.-M. Samaniego, B. Yip, T. Poinso, and S. Candel. Low-frequency combustion instability mechanism in a side-dump combustor. Combust. Flame, 94(4):363–381, 1993. 93

- R. Sankaran, E. Hawkes, J. Chen, T. Lu, and C. K. Law. Structure of a spatially developing turbulent lean methane–air bunsen flame. Proc. Combust. Inst., 31: 1291–1298, 2007. 50, 127, 233
- S. Sanquer, P. Bruel, and B. Deshaies. Some specific characteristics of turbulence in the reactive wakes of bluff bodies. AIAA journal, 36(6):994–1001, 1998. 5
- K.C. Schadow and E. Gutmark. Combustion instability related to vortex shedding in dump combustors and their passive control. Progress in Energy and Combustion Science, 18(2):117–132, 1992. 94
- T. Schmitt. Simulation des grandes échelles de la combustion turbulente en régime supercritique. PhD thesis, Université de Toulouse - Ecole doctorale MEGeP, CER-FACS - CFD Team, Toulouse, June 2009. 56
- T. Schmitt, Y. Méry, M. Boileau, and S. Candel. Large-eddy simulation of oxygen/methane flames under transcritical conditions. Proceedings of the Combustion Institute, 33(1):1383–1390, 2011. 56
- T. Schmitt, G. Staffelbach, S. Ducruix, S. Gröning, J. Hardi, and M. Oswald. Large-eddy simulations of a sub-scale liquid rocket combustor: influence of fuel injection temperature on thermo-acoustic stability. In 7th European Conference for Aeronautics and Space Sciences (EUCASS), 2017. 56
- T. Schönfeld and T. Poinso. Influence of boundary conditions in LES of premixed combustion instabilities. In Annual Research Briefs, pages 73–84. Center for Turbulence Research, NASA Ames/Stanford Univ., 1999. 14
- T. Schönfeld and M. Rudgyard. Steady and unsteady flows simulations using the hybrid flow solver avbp. AIAA Journal, 37(11):1378–1385, 1999. 50
- T. Schuller, D. Durox, and S. Candel. A unified model for the prediction of laminar flame transfer functions: comparisons between conical and v-flames dynamics. Combust. Flame, 134:21–34, 2003. 150
- L. Selle, G. Lartigue, T. Poinso, R. Koch, K.-U. Schildmacher, W. Krebs, B. Prade, P. Kaufmann, and D. Veynante. Compressible large-eddy simulation of turbulent combustion in complex geometry on unstructured meshes. Combust. Flame, 137(4): 489–505, 2004. 133
- F. Shum-Kivan. Simulation des Grandes Echelles de flammes de spray et modélisation de la combustion non-prémélangée. PhD thesis, Institut National Polytechnique de Toulouse, 2017. 26, 46, 60, 61, 233
- S. Silvestri, M. P. Celano, G. Schlieben, C. Kirchberger, and O. J. Haidn. Characterization of a gox-gch4 single element combustion chamber. In 4th Space Propulsion Conference, Köln (Germany), 2014. 56
- S. Silvestri, M. P. Celano, O. J. Haidn, and O. Knab. Comparison of single element rocket combustion chambers with round and square cross sections. In 6th European Conference for Aeronautics and Space Sciences (EUCASS), 2015. 56

- S. Silvestri, M. P. Celano, C. Kirchberger, G. Schlieben, O. J. Haidn, and O. Knab. Investigation on recess variation of a shear coax injector for a single element gox-gch4 combustion chamber. TRANSACTIONS OF THE JAPAN SOCIETY FOR AERONAUTICAL AND SPACE SCIENCES, AEROSPACE TECHNOLOGY JAPAN, 14(ists30):Pa_13–Pa_20, 2016a. 56
- S. Silvestri, M. P. Celano, G. Schlieben, and O. J. Haidn. Characterization of a multi-injector gox/ch4 combustion chamber. In 52nd AIAA/SAE/ASEE Joint Propulsion Conference, page 4992, 2016b. 56
- S. Silvestri, F. Winter, M. Garulli, M. P. Celano, G. Schlieben, O. J. Haidn, and O. Knab. Investigation on recess variation of a shear coaxial injector in a gox-gch4 rectangular combustion chamber with optical access. In 7th European Conference for Aeronautics and Space Sciences (EUCASS), 2017. 56
- G. Singla, P. Scouffaire, C. Rolon, and S. Candel. Transcritical oxygen/transcritical or supercritical methane combustion. Proceedings of the combustion institute, 30(2): 2921–2928, 2005. 56
- G. Singla, P. Scouffaire, C. Rolon, and S. Candel. Planar laser-induced fluorescence of oh in high-pressure cryogenic lox/gh2 jet flames. Combustion and Flame, 144(1-2): 151–169, 2006. 56
- G. Singla, P. Scouffaire, J.-C. Rolon, and S. Candel. Flame stabilization in high pressure lox/gh2 and gch4 combustion. Proceedings of the Combustion Institute, 31(2):2215–2222, 2007. 56
- J. Smagorinsky. General circulation experiments with the primitive equations: 1. the basic experiment. Mon. Weather Rev., 91:99–164, 1963. 44, 83
- C. H. Smith, D. I. Pineda, and J. L. Ellzey. Syngas production from burner-stabilized methane/air flames: The effect of preheated reactants. Combustion and Flame, 160(3):557–564, 2013. 7
- G. P. Smith, D. M Golden, M. Frenklach, N. W. Moriarty, B. Eiteneer, M. Goldenberg, C. T. Bowman, R. K. Hanson, S. Song, W. C. Gardiner Jr, et al. Gri-mech 3.0. URL: http://www.me.berkeley.edu/gri_mech, 51:55, 1999. 49
- R. Snyder, G. Herding, J.-C. Rolon, and S. Candel. Analysis of flame patterns in cryogenic propellant combustion. Combustion science and technology, 124(1-6):331–370, 1997. 56
- S. M. Starikovskaia. Plasma assisted ignition and combustion. Journal of Physics D: Applied Physics, 39(16):R265, 2006. 98
- A. Starikovskiy and N. Aleksandrov. Plasma-assisted ignition and combustion. Progress in Energy and Combustion Science, 39(1):61–110, 2013. 3, 97, 99, 100
- R. C. Steele, L. H. Cowell, S. M. Cannon, and Cl. E. Smith. Passive control of combustion instability in lean premixed combustors. In ASME 1999 International

- Gas Turbine and Aeroengine Congress and Exhibition, pages V002T02A004–V002T02A004. American Society of Mechanical Engineers, 1999. [96](#)
- W. Strahle. Combustion noise. Prog. Energy Comb. Sci. , 4:157–176, 1978. [94](#)
- W. Strahle. A more modern theory of combustion noise. In C. Casci and C. Bruno, editors, Recent Advances in the Aerospace Sciences, pages 103–114. Plenum Press, New York, 1985. [94](#)
- W. C. Strahle. On combustion generated noise. J. Fluid Mech. , 49:399–414, 1971. [94](#)
- W. C. Strahle. Some results in combustion generated noise. J. Sound Vib. , 23(1): 113–125, 1972. [91](#), [94](#)
- W. Sun, M. Uddi, S. H. Won, T. Ombrello, C. Carter, and Y. Ju. Kinetic effects of non-equilibrium plasma-assisted methane oxidation on diffusion flame extinction limits. Combustion and Flame, 159(1):221–229, 2012. [99](#), [100](#)
- M.S. Sweeney, S. Hochgreb, and R.S. Barlow. Cambridge stratified swirl burner technical drawings, 2012. [26](#)
- N. Syred. A review of oscillation mechanisms and the role of the precessing vortex core in swirl combustion systems. Prog. Energy Comb. Sci. , 32(2):93–161, 2006. [125](#)
- L. Tay-Wo-Chong and W. Polifke. Large eddy simulation-based study of the influence of thermal boundary condition and combustor confinement on premix flame transfer functions. J. Eng. Gas Turb. and Power , 135:021502, 2013. [12](#)
- L. Tay Wo Chong, R. Kaess, T. Komarek, S. Foller, and W. Polifke. Identification of flame transfer functions using LES of turbulent reacting flows. In Siegfried Wagner, Matthias Steinmetz, Arndt Bode, and Markus Michael Muller, editors, High Performance Computing in Science and Engineering, Garching/Munich 2009, pages 255–266. Springer Berlin Heidelberg, 2010. ISBN 978-3-642-13872-0. [151](#)
- S. Temkin. Elements of acoustics. Wiley New York, 1981. [94](#)
- A. Terzis. Detailed heat transfer distributions of narrow impingement channels for integrally cast turbine airfoils. PhD thesis, 2014. [8](#), [9](#)
- P. Teulet, J. Gonzalez, A. Mercado-Cabrera, Y. Cressault, and A. Gleizes. One-dimensional hydro-kinetic modelling of the decaying arc in air–pa66–copper mixtures: I. chemical kinetics, thermodynamics, transport and radiative properties. Journal of Physics D: Applied Physics, 42(17):175201, 2009a. [185](#), [187](#), [191](#)
- P. Teulet, J. Gonzalez, A. Mercado-Cabrera, Y. Cressault, and A. Gleizes. One-dimensional hydro-kinetic modelling of the decaying arc in air–pa66–copper mixtures: II. study of the interruption ability. Journal of Physics D: Applied Physics, 42(17): 175201, 2009b. [191](#)
- D. Thibaut and S. Candel. Numerical study of unsteady turbulent premixed combustion. application to flashback simulation. Submitted to Combust. Flame, 1997. [90](#)

- F. Tholin, D. A. Lacoste, and A. Bourdon. Influence of fast-heating processes and o atom production by a nanosecond spark discharge on the ignition of a lean h₂-air premixed flame. Combust. Flame, (5):1235–1246, 2014. ISSN 15562921. 106
- S. K. Thumuluru, H.-H. Ma, and T. Lieuwen. Measurements of the flame response to harmonic excitation in a swirl combustor. In 45th AIAA Aerospace Sciences Meeting and Exhibit, page 845, 2007. 140
- A. S. Tomlin, M. J. Pilling, T. Turányi, J. H. Merkin, and J. Brindley. Mechanism reduction for the oscillatory oxidation of hydrogen: sensitivity and quasi-steady-state analyses. Combustion and Flame, 91(2):107–130, 1992. 49
- A. Tripathi, M. Juniper, P. Scoufflaire, J.-C. Rolon, D. Durox, and S. Candel. Lox tube recess in cryogenic flames investigated using oh and h₂o emission. In 35th Joint Propulsion Conference and Exhibit, page 2490, 1999. 56
- P. Tudisco, R. Ranjan, and S. Menon. Numerical investigation of transverse forcing in a multi-element, shear-coaxial, high pressure combustor. In 54th AIAA Aerospace Sciences Meeting, page 2155, 2016. 56
- A. Urbano, L. Selle, G. Staffelbach, B. Cuenot, T. Schmitt, S. Ducruix, and S. Candel. Exploration of combustion instability triggering using large eddy simulation of a multiple injector liquid rocket engine. Combustion and Flame, 169:129–140, 2016. 56
- K. Venkataraman, L. Preston, D. Simons, B. Lee, J. Lee, and D. Santavicca. Mechanism of combustion instability in a lean premixed dump combustor. J. Prop. Power , 15 (6):909–918, Nov 1999. 94
- D. Veynante and L. Vervisch. Turbulent combustion modeling. Prog. Energy Comb. Sci. , 28:193 – 266, 2002. 46
- Z. Wei, H.S Zhen, C.W Leung, C.S Cheung, and Z. Huang. Heat transfer characteristics and the optimized heating distance of laminar premixed biogas- hydrogen bunsen flame impinging on a flat surface. 40:15723–15731, 11 2015. 26
- I. Wichman and G. Bruneaux. Head on quenching of a premixed flame by a cold wall. Combust. Flame, 103(4):296–310, 1995. 13
- F. A. Williams. Combustion Theory. Benjamin Cummings, Menlo Park, CA, 1985. 35
- F. Winter, S. Silvestri, M. P. Celano, G. Schlieben, and O. Haidn. High-speed and emission imaging of a coaxial single element gox/gch₄ rocket combustion chamber. In 7th European Conference for Aeronautics and Space Sciences (EUCASS), 2017. 56
- P. Wolf, G. Staffelbach, A. Roux, L. Gicquel, T. Poinsot, and V. Moureau. Massively parallel LES of azimuthal thermo-acoustic instabilities in annular gas turbines. C. R. Acad. Sci. Mécanique, 337(6-7):385–394, 2009. 90

- N.A. Worth and J.R. Dawson. Self-excited circumferential instabilities in a model annular gas turbine combustor: global flame dynamics. In Proc. Combust. Inst., volume 34, pages 3127–3134, 2013. 12
- P. Xavier, A. Ghani, D. Mejia, M. Miguel-Brebion, M. Bauerheim, L. Selle, and T. Poinso. Experimental and numerical investigation of flames stabilised behind rotating cylinders: interaction of flames with a moving wall. Journal of Fluid Mechanics, 813:127–151, 2017. 13
- D. A. Xu, et al., D. L. Rusterholtz, P.-Q. Elias, G. D. Stancu, and C. O. Laux. Experimental study of the hydrodynamic expansion following a nanosecond repetitively pulsed discharge in air. Applied Physics Letters, 99(12):121502, 2011. 100, 109, 174
- D. A. Xu, M. N. Shneider, et al., and C. O. Laux. Thermal and hydrodynamic effects of nanosecond discharges in atmospheric pressure air. Journal of Physics D: Applied Physics, 47(23):235202, 2014. 100, 109
- D. A. Xu, et al., and C. O. Laux. Ignition of quiescent lean propane–air mixtures at high pressure by nanosecond repetitively pulsed discharges. Plasma Chemistry and Plasma Processing, 36(1):309–327, 2016. 100, 109
- B. Yang, F. Cuoco, and M. Oswald. Atomization and flames in lox/h₂-and lox/ch₄-spray combustion. Journal of Propulsion and Power, 23(4):763–771, 2007. 56
- Z. Yin, A. Montello, C. D. Carter, W. R. Lempert, and I. V. Adamovich. Measurements of temperature and hydroxyl radical generation/decay in lean fuel–air mixtures excited by a repetitively pulsed nanosecond discharge. Combustion and Flame, 160(9):1594–1608, 2013. 106
- J. B. Zeldowitsch and D. A. Frank-Kamenetzki. A theory of thermal propagation of flame. 1938. 28, 29
- J. Zips, H. Müller, M. Pfitzner, J. Hardi, and M. Oswald. Large-eddy simulation of multi-element lox/h₂ combustion at transcritical conditions. In 7th European Conference for Aeronautics and Space Sciences (EUCASS), 2017. 56
- E. E. Zukoski. The aerothermodynamics of aircraft turbines. In G.G. Oates, editor, Afterburners, pages AFAPL-TR-78-52. 1978. 93
- E. E. Zukoski and F. E. Marble. Combustion researches and reviews. page 167. Butterworths Scientific Publications, Paris, 1955. 5